Design and Construction of a Molecular Beamline for Cluster Catalysis Studies

By

Zachary A. Hicks

A dissertation submitted to Johns Hopkins University in conformity with the requirements for the degree of Doctor of Philosophy.

Baltimore, Maryland

May, 2019

Abstract

Metal and metal oxide nanoparticles are widely used in heterogeneous catalysis. In order to determine how these catalysts function and in order to find new catalysts, model systems can be used to provide experimental and computational insight. One such model system is a cluster which contains <100 atoms allowing for ease of calculation. In this work a molecular beamline was constructed in order to produce a wide range of these clusters and control their composition on an atom-by-atom level. These clusters could then be deposited onto a substrate in vacuum and studied via multiple techniques including TPD, XPS, UPS, LEED, and STM, allowing for the study of not only the cluster's composition but their reactivity to a range of reactants in a range of reaction environments. In the process of designing the instrument, novel tools and parts were developed and manufactured to push the capabilities of the instrument forward and are discussed in detail. The instrument was tested and found to meet the three design goals of a molecular beamline that can 1) produce a large range of clusters varying in size and composition of a magnitude that can be deposited and studied in a timely fashion, 2) mass select the clusters with a resolution capable of resolving the elements in the cluster, and 3) bring to bear a variety of analytical techniques to study the cluster's composition and catalytic capabilities.

Acknowledgments

First, I would like to thank my research advisor, Dr. Kit H. Bowen. If not for him I would not have had this opportunity. He was always there guiding me forward and engaging in both scholarly and more vigorous debate, never letting me move forward without having defended my thoughts and proposed actions to an acceptable level. In the end I have become a better scientist for it.

Next, I would like to thank my sub-group as I did not build this instrument alone, and if I had, I never would have finished. Linjie Wang was always there with a clever question or insight that would force me to reevaluate what we were doing. And for the times I couldn't decide where to progress towards in the next push of research, she always had a solid opinion. Nicolas Blando is a man who can get things done. For anyone who has worked on a complicated project with many moving parts they would understand when I say that the ability to give a half-thought out task to someone and have them finish it in a manner that not only works well but that you needed to be minimally involved in helping them through it is a godsend and Nic did that all the time. Michael Denchy is one of the most careful and thoughtful people I know who can do the most delicate and complicated tasks in a way that works wonderfully. Also, he never let me get away with giving a half-way explanation for anything.

I would like to thank the others I have worked with throughout my time in the Bowen lab. Xin Tang for teaching me the ins-and-outs of many skills I used throughout graduate school. Evan Collins for always being willing to answer any question I posed about instrument design and always being willing to brainstorm with me about solutions to a problem. Mary Marshall for always working on something interesting and putting up with my ideas, as well as being as into football as I am. Sandy Ciborowski and Goaxiang Liu for always allowing me to go through their instrument's parts looking for the one part I needed. And finally, the newer people Zhaoguo Zhu, Chalynette

Martinez-Martinez, Rachel Harris, Marica Dipalo, and Mortiz Blankenhorn for being receptive listeners as the more you say something the better it sticks in your head.

I would also like to thank my graduate research committee, Dr. Art Bragg and Dr. Howard Fairbrother.

My unofficial undergraduate advisor, Dr. Daniel Havey, who showed me there was more to chemistry than glassware and balances.

Remsen's building manager Boris Steinburg is a man who knows how to do everything that involves making something with your hands and is always willing to help. His talents and kindheartedness have been invaluable throughout the years.

Michael Kratfel of Consolidated Instruments, made almost all of the custom parts on my instrument, but what earns him a spot in the acknowledgements is the advice he freely gave about any kind of machining project whether it was something we were going to pay him to make or if it was a project I thought I could do myself. His insights and experience were invaluable.

My parents for always making sure I had the opportunities in life to get to where I am today. They may not understand what I do but they're the reason I can do it.

Most importantly my fiancé, Jessica, who is there when I am highest and lowest.

Table of Contents

List of Figures

I Introduction

Catalysts are used in many industrial processes and just in 2016 alone accounted for $23.08 billion in the global market.[1] The reason for this is their ability to reduce the reaction barrier between the reactants and products of a given reaction resulting in the need for less heating and improved kinetics of the reaction making the whole process occur faster.[2] Further, catalysts can be tuned to be selective towards certain products resulting in the desired product being primarily produced. All of this results in a high demand for improving both the activity and selectivity of catalysts.

Catalysts can be broken down into two types: heterogeneous and homogeneous. Homogeneous catalysts exist in the same phase as the reactants, while heterogeneous exist in a different phase from the reactants.[3] While homogeneous catalysts are generally more effective, there are challenges in separating the products from the catalyst after the reaction has progressed. Heterogeneous catalysts are more often used in industry for this reason. This work will focus exclusively on heterogeneous catalysts.

In heterogeneous catalysis only the surface of the catalysts can be utilized in the reaction process, and as such, using a surface-to-volume argument, it is more ideal for the catalyst to be smaller as less wasted bulk is present. As the size of the nanoparticle is reduced more surface atoms appear, and as the particle gets smaller the curvature of its surface increases placing more of these surface atoms into a low-coordination environment where they are potentially more reactive. To this end many industrial catalysts are supported nanoparticles ranging in size from a few nanometers to hundreds of nanometers.[4]

In order to study catalysis on a fundamental level, model systems are required. One such system is supported, soft-landed, size-selected clusters as produced by molecular beam techniques.

Compared to normal synthesis techniques, clusters produced by molecular beam are free of stabilizers, such as ligands and surfactants, that crowd the surface of the cluster and effects from solvents used in standard synthesis methods. Further, these clusters can be produced with very precise control of their structure and chemical composition on an atom-by-atom level allowing for exacting definition of the clusters being studied. This exacting composition makes clusters produced via this method ideal models for high-level computational studies allowing for easier determination of reactive sites and reaction pathways.[5]

Size effects of clusters used for catalysis have been studied extensively.[6-43] An example is the study of CO oxidation on size-selected Au_n clusters supported on magnesia performed by Ueli Heiz.[44] In this work it was determined that the cluster size had a strong effect on the reactivity of the cluster where Au_{2-7} were inactive, while Au_8 shows an increase in catalytic activity. (**Figure II.1.1-1**)

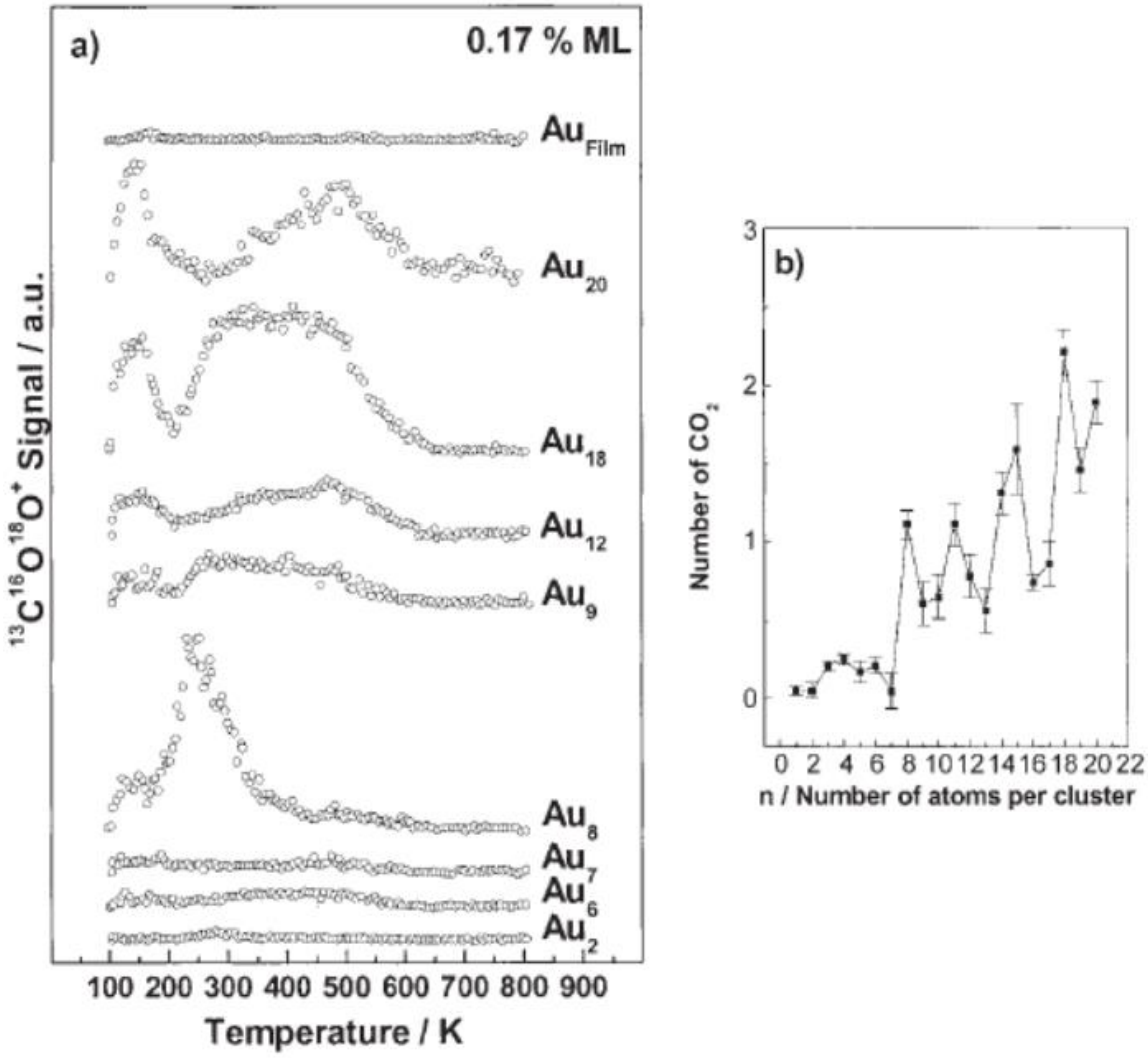

Figure II.1.1-1: Au_n/MgO Catalytic activity for CO Oxidation

Highlighting the fact that these clusters are not in an isolated environment, there was also a support dependency wherein the Au_8 clusters supported on a defect-rich MgO(001) substrate were much more catalytically active than a defect-poor surface, which Heiz attributes to a partial positive charging of the Au_8 by F-center defects in the surface. (**Figure II.1.1-2**) This is also an effect of reduced cluster size, where, as the cluster gets smaller, there is reinforced cluster-support interactions.[45]

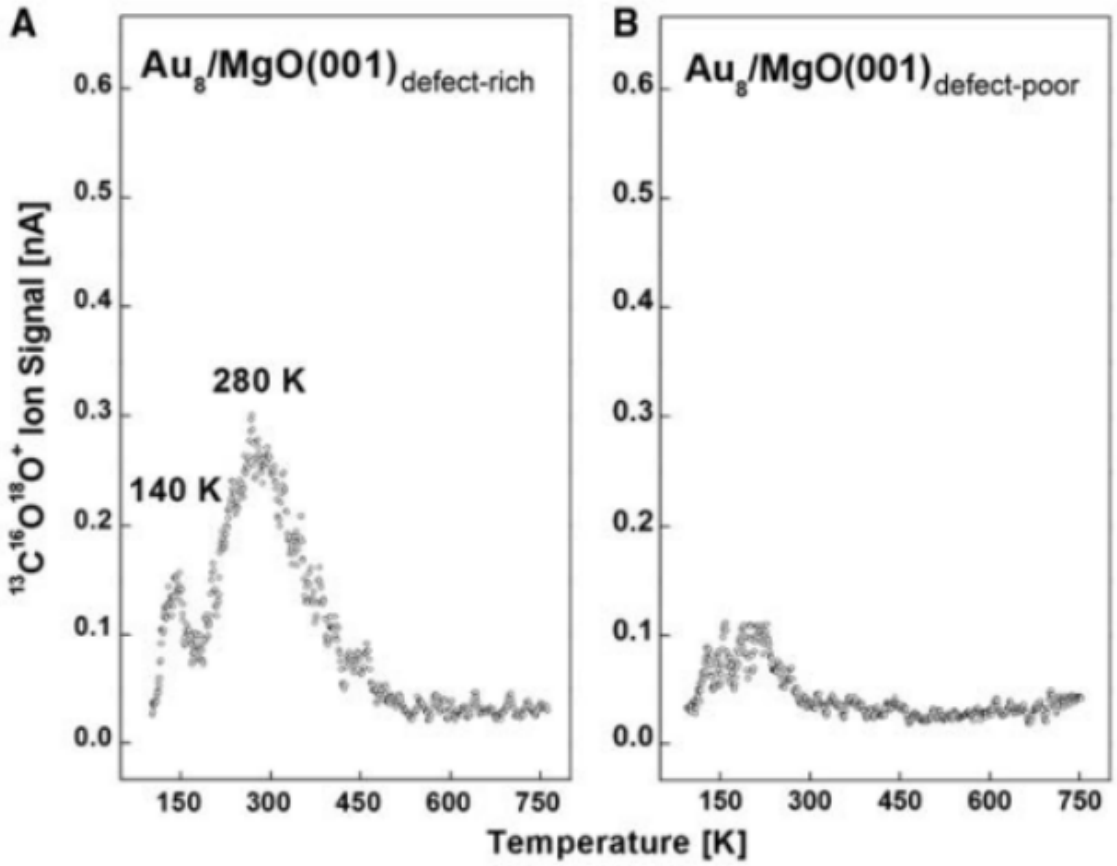

Figure II.1.1-2: Defect effects on CO oxidation reaction.

From this work it is shown that not only does the cluster size change the catalytic activity of the cluster but also the chemical environment of the cluster. In this case the chemical environment resulted in a partial positive charge on the cluster, i.e. a slight oxidation. This is incongruent with the fact that the most extensive studies for size-selected clusters have been on precious metal clusters. If the chemical environment of the cluster is important towards its reactivity, then size-selected metal oxides, nitrides, sulfides, carbides, and mixed-metals (alloys) should be studied as well, however the share of the literature on these clusters is much smaller. Also, overall metal oxide catalysts are very present in industrial processes, as one-quarter of the top 20 chemical production processes uses metal oxides as catalysts.[46]

Metal oxides have been used in a range of reactions from redox to acid-base reactions as summarized in the figure below. (**Figure II.1.1-3**)

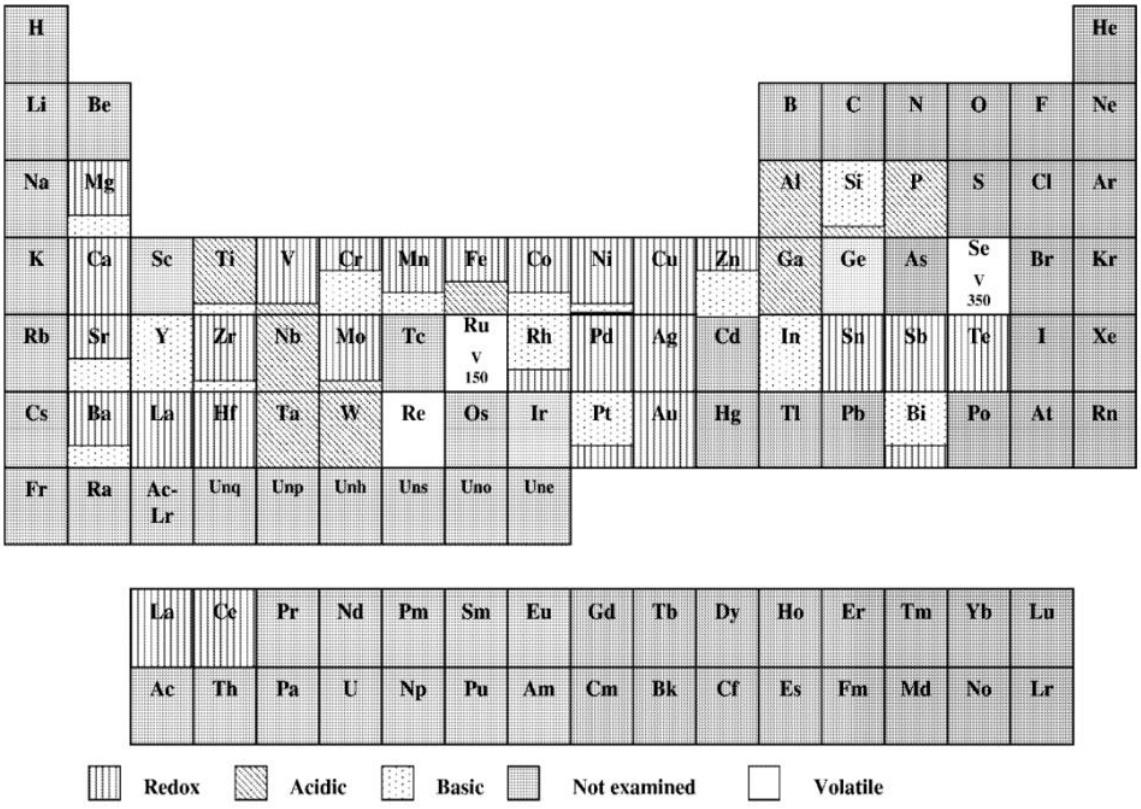

Figure II.1.1-3: Reaction Properties of Metal Oxides[47]

The differences between the different metal oxides can be explained by the differences in bonding character between the metals and oxygens. While some clusters may have a more reducible metal center which affects redox catalysts, others may have a range of different oxo groups that result in changes in the Lewis activity of the clusters. For example, it was found that in $(MO_3)_n$ clusters (M=Mo,W), di-oxo groups had a higher Lewis acidity than either the mono-oxo or bridging oxygen sites.[48,49] Not only does changing the metal center effect the properties of the cluster, but by modifying the cluster with defects such as an oxygen vacancy, overoxidation, or adding hydroxyls, the catalytic properties can be changed.

Adding a further layer of depth, mixed-metal oxides (MMOs) can be studied as well, where there is a synergistic effect between the metal centers. This greatly broadens the field of metal oxides that have yet to be studied adding another dimension to the possibilities.

As established above, the size of the cluster plays a critical role, and as the size of the cluster decreases the surface to volume ratio increases thereby increasing the ratio of possible active-sites per gram of catalyst. This efficiency per amount is critical to the use of expensive catalysts such as gold, iridium, rhodium, and platinum. If one were to take these clusters to the extreme size limit and study the effects of single atoms on catalysis, there is no greater surface to volume ratio.

These single atom catalysts (SACs) consist of individual metal atoms anchored to a support. SACs have the most optimal surface area per gram that can be achieved, and since they consist of a single atom, they can contain only one active site allowing for potentially near perfect selectivity.[45] These SACs must be anchored onto a substrate in order to prevent aggregation of the SACs into larger clusters when heated to reaction temperatures, and losing the SAC effects. As such, any interaction with a substrate has to be strong enough to bind to the SAC, and such a strong interaction modifies the SAC giving SACs a strong substrate dependence.[45] In fact, most of the studies of SACs have been about changing the substrate the SAC is supported on rather than changing the SAC itself. Much of this has to do with the complexity of producing a SAC; it is simply easier to keep the method the same and change the substrate.

SAC has been studied with a narrow range of metals (M=Fe, Pt, Pd, Au, Rh, Ru, Ir) on a wide range of substrates including metals and metal oxides (FeO_x, Al_2O_3, TiO_2, CeO_2, Co_3O_4, ZnO, SiO_2, Au, Cu, graphene) for a range of reactions (CO oxidation, formaldehyde oxidation, cinnamyl and Crotyl alcohol oxidation, methane oxidation, Ullmann reactions, hydrogenation of styrene and acetylene, reduction of nitric oxide with hydrogen, photocatalytic evolution of H_2, water gas shift

reaction, electro catalysis).[50-63,] In some cases the catalyst performed 20 times better than previously reported catalysts.[60] Furthermore, the SACs are stable enough to undergo catalytic cycles, a testament to the strength of the atom-surface interaction preventing the SACs from aggregating. This strong interaction also plays a role in catalysis, as much of the literature reports a small cationic character being applied to the single atom by the metal oxide surface.

The large breath of reactions these SACs have been used in and the large field of possible combinations of single atoms and surfaces makes this an interesting area to explore. However, as mentioned previously, these catalysts are hard to prepare, and as a result the studies are slow. A possible solution to this problem is molecular-beam-deposited, size-selected clusters. If a beam of a mixed-metal oxide cluster containing only one atom of a given metal were to be produced and was small enough such that that single metal was located on the surface of the cluster rather than inside the cluster that beam could be deposited onto a non-reactive surface and studied. Upon potential aggregation of these clusters, the likelihood that the clusters were to aggregate such that the single atoms on two clusters were to be the aggregation point of clusters is low. Hence, a beam of size-selected MMOs with a single atom of one of the two metals on the surface can be deposited and annealed into a surface consisting of many SACs sites. As compared to current SAC production techniques, the single atom is already in its surface site when produced and does not need to migrate around the surface looking for a defect site that was added to the surface via sputtering. A high intensity beam of clusters could allow for a potential SAC to be formed in a single day.

With a versatile molecular beam deposition instrument a very large field of model catalysts can studied. Such an instrument would need to be able to; 1) produce any of the desired clusters with intensities that allow for reasonable deposition times, 2) mass select the clusters with a high enough resolution to differentiate the cluster compositions, and 3) bring to bear a range of

techniques to study the chemical composition and catalytic efficiency of the resulting clusters. In this work such an instrument was designed, constructed, and tested.

---

[1] "Catalyst Market Size, Share & Trends Analysis Report By Raw Material (Metal, Chemical Compounds), By Product (Heterogeneous, Homogeneous), By Application (Polymers & Petrochemicals, Environmental), And Segment Forecasts, 2019 – 2025", Grand View Research, 2019.

[2] U. Heiz, U. Landman, "Nanoscience and Technology: Nanocatalysis", Springer, 2008. ISBN: 978-3-540-74551-8

[3] R. Günther., W. Christian, Journal of Physics: Condensed Matter, 2008, **20**, 184019.

[4] D. Astruc, F. Lu, J. R. Aranzaes, Angew. Chem. Int. Ed. Engl., 2005, **44**, 7852.

[5] C. Harding, V. Habibpour, S. Kunz, A. N. Farnbacher, U. Heiz, B. Yoon, U. Landman, J. Am. Chem. Soc., 2009, **131**, 538.

[6] M. D. Kane, F. S. Roberts, S. L. Anderson, Faraday Discuss 2013.

[7] M. D. Kane, F. S. Roberts, S. L. Anderson, Int. J. Mass. Spectrom., 2014, **370**, 1.

[8] A. von Weber, E. T. Baxter, S. Proch, M. D. Kane, M. Rosenfelder, H. S. White, S. L. Anderson,, Phys. Chem. Chem. Phys., 2015, **17**, 17601.

[9] S. Proch, M. Wirth, H. S. White, S. L. Anderson, J. Am. Chem. Soc., 2013, 135, 3073.

[10] F. S. Roberts, M. D. Kane, E. T. Baxter, S. L. Anderson, Phys. Chem. Chem. Phys., 2014, **16**, 26443.

[11] A. von Weber, E. T. Baxter, H. S. White, S. L. Anderson, J. Phys. Chem. C., 2015, **119**, 11160.

[12] W. E. Kaden, T. P. Wu, W. A. Kunkel, S. L. Anderson, Science, 2009, **326**, 826.

[13] W. E. Kaden, W. A. Kunkel, F. S. Roberts, M. Kane, S. L. Anderson, Surf. Sci., 2014, **621**, 40.

[14] S. S. Lee, C. Y. Fan, T. P. Wu, S. L. Anderson, J. Am. Chem. Soc., 2004, **126**, 5682.

[15] S. S. Lee, C. Y. Fan, T. P. Wu, S. L. Anderson, J. Chem. Phys., 2005, 123.

[16] C. Y. Fan, T. P. Wu, W. E. Kaden, S. L. Anderson, Surf. Sci. 2006, **600**, 461.

[17] S. S. Lee, B. Lee, S. Seifert, R. E. Winans, S. Vajda, J. Phys. Chem. C., 2015, **119**, 11210.

[18] S. S. Lee, B. Lee, F. Mehmood, S. Seifert, J. A. Libera, J. W. Elam, J. Greeley, P. Zapol, L. A. Curtiss, M. J. Pellin, P. C. Stair, R. E. Winans, S. Vajda, J. Phys. Chem. C., 2010, **114**, 10342.

[19] G. Kwon, G. A. Ferguson, C. J. Heard, E. C. Tyo, C. R. Yin, J. DeBartolo, S. Seifert, R. E. Winans, A. J. Kropf, J. Greeley, R. L. Johnston, L. A. Curtiss, M. J. Pellin, S. Vajda, Acs. Nano. 2013, **7**, 5808.

[20] V. Habibpour, C. R. Yin, G. Kwon, S. Vajda, R. E. Palmer, J. Exp. Nanosci., 2013, **8**, 993.

[21] Y. Lei, F. Mehmood, S. Lee, J. Greeley, B. Lee, S. Seifert, R. E. Winans, J. W. Elam, R. J. Meyer, P. C. Redfern, D. Teschner, R. Schlogl, M. . Pellin, L. A. Curtiss, S. Vajda, Science ,2010, **328**, 224.

[22] S. Vajda, M. J. Pellin, J. P. Greeley, C. L. Marshall, L. A. Curtiss, G. A. Ballentine, J. W. Elam, S. Catillon-Mucherie, P. C. Redfern, F. Mehmood, P. Zapol, Nat. Mater., 2009, **8**, 213.

[23] C. Liu, B. Yang, E. Tyo, S. Seifert, J. DeBartolo, B. von Issendorff, P. Zapol, S. Vajda, L. A. Curtiss, J. Am. Chem. Soc., 2015, **137**, 8676.

[24] S. Abbet, U. Heiz, A. M. Ferrari, L. Giordano, C. Di Valentin, G. Pacchioni, Thin Solid Films, 2001, **400**, 37.

[25] U. Heiz, A. Sanchez, S. Abbet, W. D. Schneider, J. Am. Chem. Soc., 1999, **121**, 3214

[26] M. Nesselberger, M. Roefzaad, R. F. Hamou, P. U. Biedermann, F. F. Schweinberger, S. Kunz, K. Schloegl, G. K. Wiberg, S. Ashton, U. Heiz, K. J. Mayrhofer, M. Arenz, Nat. Mater., 2013, **12**, 919.

[27] F. F. Schweinberger, M. J. Berr, M. Doblinger, C. Wolff, K. E. Sanwald, A. S. Crampton, C. J. Ridge, F. Jackel, J. Feldmann, M. Tschurl, U. Heiz, J. Am. Chem. Soc., 2013, **135**, 13262.

[28] A. S. Crampton, M. D. Rotzer, C. J. Ridge, F. F. Schweinberger, U. Heiz, B. Yoon, U. Landman, Nat. Commun., 2016, 7.

[29] U. Heiz, A. Sanchez, S. Abbet, W. D. Schneider, Chem. Phys., 2000, **262**, 189.

[30] X. Tang, J. Schneider, A. Dollinger, Y. Luo, A. S. Worz, K. Judai, S. Abbet, Y. D. Kim, G. F. Gantefor, D. H. Fairbrother, U. Heiz, K. H. Bowen, S. Proch, Phys. Chem. Chem. Phys., 2014, **16**, 6735.

[31] M. Moseler, M. Walter, B. Yoon, U. Landman, V. Habibpour, C. Harding, S. Kunz, U. Heiz, J. Am. Chem. Soc., 2012, **134**, 7690.

[32] B. Yoon, U. Landman, V. Habibpour, C. Harding, S. Kunz, U. Heiz, M. Moseler, M. J. Walter, J. Phys. Chem. C., 2012, **116**, 9594.

[33] K. Judai, S. Abbet, A. S. Worz, A. M. Ferrari, L. Giordano, G. Pacchioni, U. Heiz, J. Mol. Cat. Chem., 2003, **199**, 103.

[34] S. Bonanni, K. Ait-Mansour, W. Harbich, H. J. Brune, J. Am. Chem. Soc., 2012, **134**, 3445.

[35] S. Bonanni, K. Ait-Mansour, W. Harbich, H. J. Brune, J. Am. Chem. Soc., 2014, **136**, 8702.

[36] X. Tong, L. Benz, P. Kemper, H. Metiu, M. T. Bowers, S. K. Buratto, J. Am. Chem. Soc., 2005, **127**, 13516.

[37] S. P. Price, X. Tong, C. Ridge, H. L. Neilson, J. W. Buffon, J. Robins, H. Metiu, M. T. Bowers, S. K. Buratto, J. Phys. Chem. A., 2014, **118**, 8309.

[38] X. Tong, L. Benz, S. Chretien, P. Kemper, A. Kolmakov, H. Metiu, M. T. Bowers, S. K. Buratto, J. Chem. Phys., 2005, 123.

[39] V. Habibpour, M. Y. Song, Z. W. Wang, J. Cookson, C. M. Brown, P. T. Bishop, R. E. Palmer, J. Phys. Chem. C., 2012, **116**, 26295.

[40] K. J. Hu, S. R. Plant, P. R. Ellis, C. M. Brown, P. T. Bishop, R. E. Palmer, J. Am. Chem. Soc., 2015, **137**, 15161.

[41] N. Isomura, X. Y. Wu, Y. J. Watanabe, J. Chem. Phys., 2009, 131.

[42] Y. Watanabe, X. Y. Wu, H. Hirata, N. Isomura, Catal. Sci. Technol., 2011, **1**, 1490.

[43] M. Nakayama, M. Xue, W. An, P. Liu, M. G. White, J. Phys. Chem. C., 2015, **119**, 14756

[44] B. Yoon, H. Hakkinen, U. Landman, A. S. Worz, J. M. Antonietti, S. Abbet, K. Judai, U. Heiz, Science, 2005, **307**, 403.

[45] S. Liang, C. Hao, Y. Shi, Chem. Cat. Chem, 2015, **17**, 2559.

[46] I. M. Campbell, "Catalysis at surfaces", Chapman and Hall, 1988.

[47] M. Badlani, I. E. Wachs, Catalysis Letters, 2001, **75**, 137.

[48] Z. Li, B. Smid, Y. K. Kim, V. Matolin, B. D. Kay, R. Rousseau, Z. Dohnalek, J. Phys. Chem. Lett., 2012, **3**, 2168.

[49] R. Rousseau, D. A. Dixon, B. D. Kay, Z. Dohnalek, Chem. Soc. Rev., 2014, **43**, 7664.

[50] B. Qiao, A. Wang, X. Yang, L. F. Allard, Z. Jiang, Y. Cui, J. Liu, J. Li, T. Zhang, Nat. Chem., 2011, **3**, 634–641.

[51] M. Moses-DeBusk, M. Yoon, L. F. Allard, D. R. Mullins, Z. Wu, X. Yang, G. Veith, G. M. Stocks, C. K. Narula, J. Am. Chem. Soc., 2013, **135**, 12634–12645.

[52] C. Zhang, F. Liu, Y. Zhai, H. Ariga, N. Yi, Y. Liu, K. Asakura, M. Flytzani-Stephanopoulos, H. He, Angew. Chem. Int. Ed., 2012, **51**, 9628–9632.

[53] S. Hackett, R. Brydson, M. Gass, I. Harvey, A. Newman, K. Wilson, A. Lee, Angew. Chem. Int. Ed., 2007, **46**, 8593.

[54] W. Tang, Z. Hu, M. Wang, G. D. Stucky, H. Metiu, E. W. McFarland, J. Catal., 2010, **273**, 125–137.

[55] L. Zhang, A. Wang, J. T. Miller, X. Liu, X. Yang, W. Wang, L. Li, Y. Huang, C. Mou, T. Zhang, ACS Catal., 2014, **4**, 1546–1553.

[56] Y. Li, Z. Zhou, G. Yu, W. Chen, Z. Chen, J. Phys. Chem. C, 2010, **114**, 6250–6254.

[57] P. Wu, P. Du, H. Zhang, C. Cai, Phys. Chem. Chem. Phys., 2015, **17**, 1441–1449.

[58] G. Kyriakou, M. B. Boucher, A. D. Jewell, E. A. Lewis, T. J. Lawton, A. E. Baber, H. L. Tierney, M. Flytzani-Stephanopoulos, E. C. H. Sykes, Science, 2012, **335**, 1209–1212.

[59] L. Wang, S. Zhang, Y. Zhu, A. Patlolla, J. Shan, H. Yoshida, S. Takeda, A. I. Frenkel, F. Tao, ACS Catal., 2013, **3**, 1011–1019.

[60] L. Wang, S. Zhang, Y. Zhu, A. Patlolla, J. Shan, H. Yoshida, S. Takeda, A. I. Frenkel, F. Tao, ACS Catal., 2013, **3**, 1011–1019.

[61] G. Pei, X. Liu, A. Wang, L. Li, Y. Huang, T. Zhang, J. W. Lee, B. W. L. Jang, C. Mou, New J. Chem., 2014, **38**, 2043–2051.

[62] G. Pei, X. Liu, A. Wang, L. Li, Y. Huang, T. Zhang, J. W. Lee, B. W. L. Jang, C. Mou, New J. Chem., 2014, **38**, 2043–2051.

[63] X. Gu, B. Qiao, C. Huang, W. Ding, K. Sun, E. Zhan, T. Zhang, J. Liu, W. Li, ACS Catal., 2014, **4**, 3886–3890.

II Experimental

The production of mass selected clusters at an intensity where they can be studied either on surfaces or with spectroscopic or spectrometric techniques involves the use of a molecular beamline. At their core molecular beamlines consist of four sections: an ion source, ion transport, mass selection, and analytics, all of which are held under vacuum ranging from a couple torr to ultra-high vacuum (UHV, $<10^{-8}$ torr) conditions.

Ion sources are where the cluster of interest is produced and given a charge which allows for manipulation of the cluster in the rest of the beamline. *Ion transport* consists of metal devices of a range of form-factors with either DC or oscillating voltages applied to them creating an electric field that directs the charged cluster down the beamline. *Mass selection* is where a condition is made such that a cluster of only a singly chosen mass to charge ratio (m/z) is allowed to continue through. The *analytics* are the region where the study of the cluster is performed.

This work consists of the construction of such a beamline allowing for the production of a range of clusters and the ability to study their reactivity on surfaces. The four sections mentioned above are discussed for this new beamline.

II.1 Ion Cluster Sources

There are many techniques for generating charged clusters for a beamline with each technique being better suited for different cluster compositions. As such, no single source can be used to produce the whole breadth of possible cluster combinations. This instrument is capable of using three different ion sources: DC magnetron sputtering, laser vaporization, and pulsed arc discharge. These will be discussed below with explanations of their pros and cons.

II.1.1 Magnetron Sputtering Source

Magnetron sputtering uses an electric discharge to generate a plasma near the surface of a material which gets evaporated into the gas phase via collisions with ionized particles in the plasma.[1,2] In a DC magnetron the target material being sputtered is held at a negative potential (-100V to -600V) relative to a shield in front of it which is usually grounded. The shield is spaced close to the target with a gap of 0.5 to 2mm between them. A gas mixture containing Ar, He, and, if desired, a reactant gas is introduced in between the shield and the target until a critical pressure (0.5 torr to 5 torr) is reached, and an arc sparks between the shield and the target.[1] This arc ionizes the gas mixture into Ar^+, He^+, e^-, and various ionized fragments of any reactant gas introduced. This resulting plasma is held close to the target via a magnetic field generated by a permanent magnet placed behind the target.[1] At this point the plasma will remain as long as the gas continues to flow and the voltage is applied to the target. (**Figure II.1.1-1**)

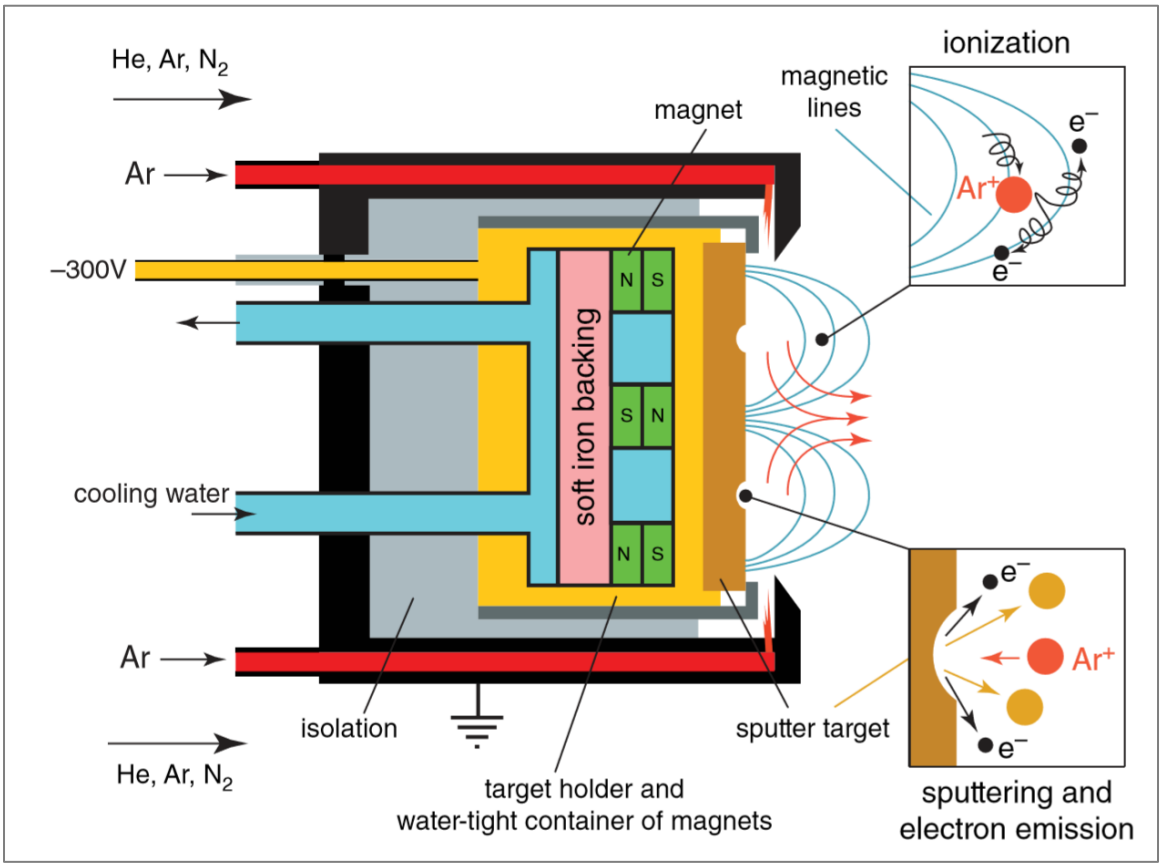

Figure II.1.1-1 Magnetron Schematic[3]

The cations in the plasma are attracted to the negative potential on the target causing them to be accelerated into the target, with a kinetic energy proportional to the voltage applied to the target, imparting energy into the target and sputtering the target material into the gas phase. The Ar^+ is the primary cation in this process due to its larger mass than He^+. The resulting gas phase target material can then undergo a range of processes in the plasma before leaving, including picking up a negative charge and being accelerated away from the target, picking up a positive charge and being accelerated back into the target causing more sputtering, or leaving the plasma as a neutral.[1,2,]

The area in front of the plasma contains mostly neutrals of every element introduced, as well as anions and some cations.[2] This region is not pumped on directly to allow for collisions

between the atoms to occur and clusters to condense, where the concentration of He has a large effect on how this process occurs and the cluster sizes produced. Most of the resulting clusters will be neutral and thus cannot be formed into an ion beam, however there is a large number of anions accelerated away from the target which can be extracted and formed into a beam.

By tuning the amount of each gas, the composition of the reactant gas, the distance between the target and the shield, the voltage applied to the target, and the length of the condensation region, the clusters produced can be changed in both size and composition.[1,2] The introduction of O_2 as a reactant gas will make oxides, CH_4 will make carbides, SH_2 will make sulfides, and NH_3 will make nitrides.

Due to the accumulation of positive charge on the target only conductive materials can be sputtered in a DC magnetron. A pulsed-DC or RF supply can be used for non-conductive materials at the cost of reduced duty cycle. Due to the importance of the magnetic field in confining the plasma to the surface, ferromagnetic targets are not sputtered well as the magnetic target dampens the confining magnetic field. Much of the material sputtered is wasted making this source cost prohibitive for expensive materials. The primary benefit to using a magnetron is the intense cluster beams it is capable of producing.

II.1.2 Laser Vaporization Ion Source (LVS)

In the LVS a pulsed laser is used to ablate a sample material into the gas phase.[4] The pulsed laser is focused onto a sample material to a critical energy density where the imparted energy heats the material locally, forming a plasma and ablating the material into the gas phase. From there the plasma is entrained in an expansion of gas from a pulse valve, thermalizing the plasma and allowing for cluster condensation while carrying the clusters down the beam axis with the timing between the laser pulse and the pulse valve controlled by a digital delay generator. In LVS the material is

not limited to conductive materials like in the other sources, and by varying the composition of the carrier gas different cluster types can be produced. (**Figure II.1.2-1**)

In LVS the laser must strike a fresh surface of the material every shot in order to get consistent signal and prevent the laser from digging into the material, requiring some form of mechanical motion to move the sample between every shot.[4] The kind of motion required is dependent on the shape of the material being ablated, where historically rods were used and a screw motion was applied to them to expose a fresh surface to the laser for every shot. This method can be costly depending on the material of the rod as only the surface of the rod is used and as such the bulk is wasted unless running for a very long time.

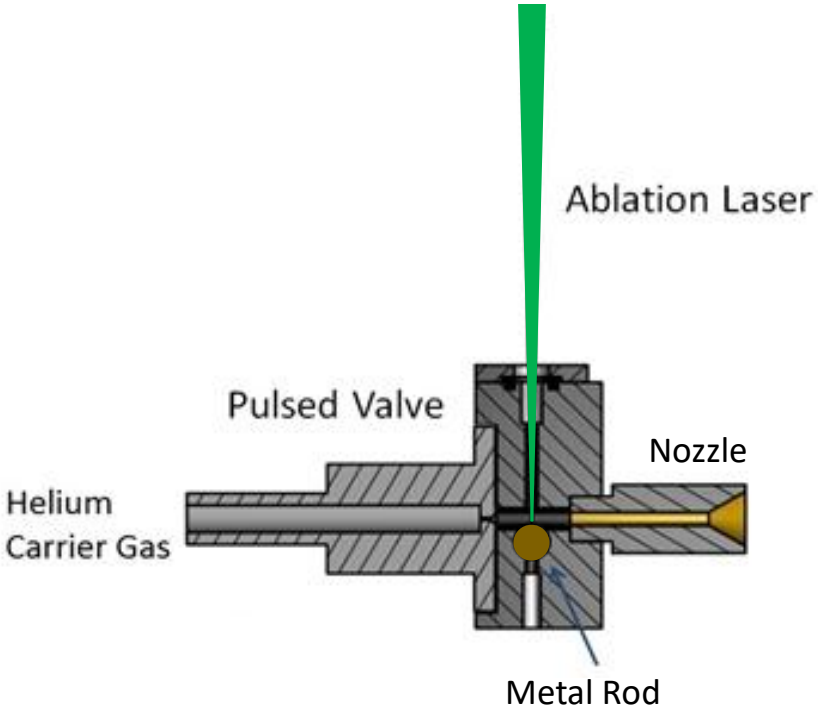

Figure II.1.2-1: LVS Rod Source Schematic[4]

Disk sources have been used with a hypocycloidal gear system that moves the disk in such a way that a laser shot normal to the plane of the disk etches a high petal number rose curve into the disk.[4,5,6,7] This setup is very efficient as the whole surface is used and reduces material costs as

one can use foil of an expensive material stretched over a disk. Hypocycloidal gear setups are technically challenging to implement due to the requirement of multiple axes of rotation.

A novel gear design was developed in this work. Presented here is a planetary gear system allowing for the same kind of motion as the hypocycloidal disk source, but with only a single axis of rotation. The gear system works as follows. The center gear (sun gear) is rotated via a motor attached to a rotary vacuum feedthrough which in turn rotates the planet gears inside the outer gear (ring gear). The sample is a disk mounted on a square peg pressed into one of the planet gears making the sample move with the planet gear. (**Figure II.1.2-2**) The sample is pressed and sealed against a front plate with a hole in it for the laser. The gear ratios are chosen so that the planet gear is not a direct ratio of the ring gear meaning that every time the planet gear makes a full rotation around the inside of the ring gear it does not return in the same orientation, but instead is indexed over some amount. As the target moves with the planet gear it rotates about its center and about the center of the gear system. (**Figure II.1.2-3**) Thus, if a pen where to be held in place touching the disk, as the disk moves it would trace a rose curve onto the face of the disk. This is the pattern the laser will trace into the disk and the greater the number of petals in the rose curve more of the disk's surface is ablated.

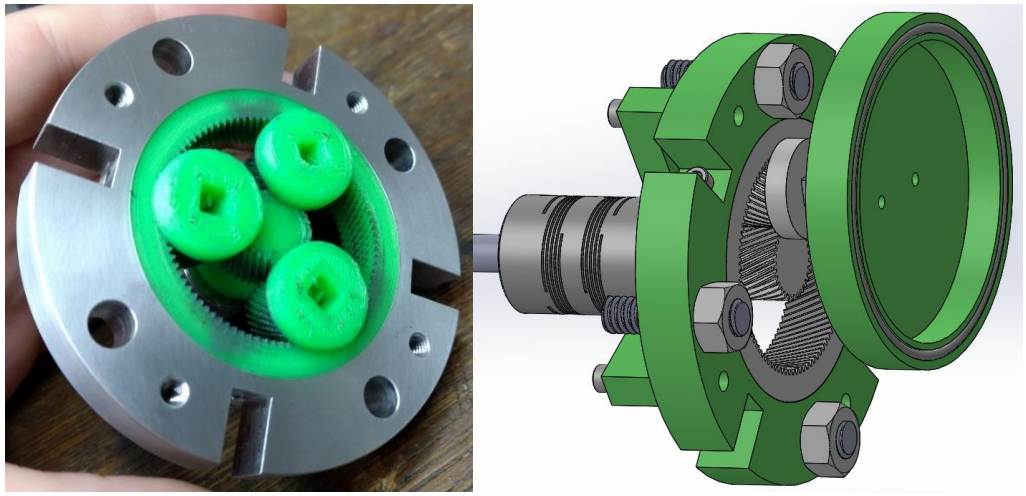

Figure II.1.2-2: Planetary Gear System

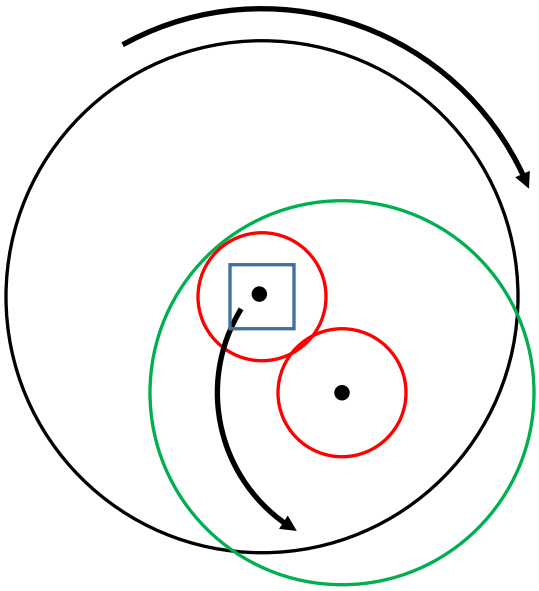

Figure II.1.2-3: Target Motion Schematic in Planetary Gear System (Target in Black)

The number of petals in the traced rose curve is dependent on the diameters of the ring (r) and planet (p) gear with the following equation, where D is the reference diameter of the respective gear. The greatest common denominator of the D_r and D_p is used in the calculation (GCD).

$$\#\ of\ petals = \frac{D_r}{GCD(D_r, D_p)}$$

Equation 1

In order for gears to mesh the gears must have the same module (M) which is defined as,

$$M = \frac{D}{T}$$

Equation 2

where T is the # of teeth the gear has. Combining the Equations 1 and 2, the # of petals can be determined by T rather than D as follows,

$$\#\ of\ petals = \frac{T_r}{GCD(T_r, T_p)}$$

Equation 3

This equation is convenient in that the number of teeth in a gear is always an integer value. The final gears chosen have the following parameters, T_r=91 and T_p=30, giving a 91 petaled rose curve. (**Figure II.1.2-4**)

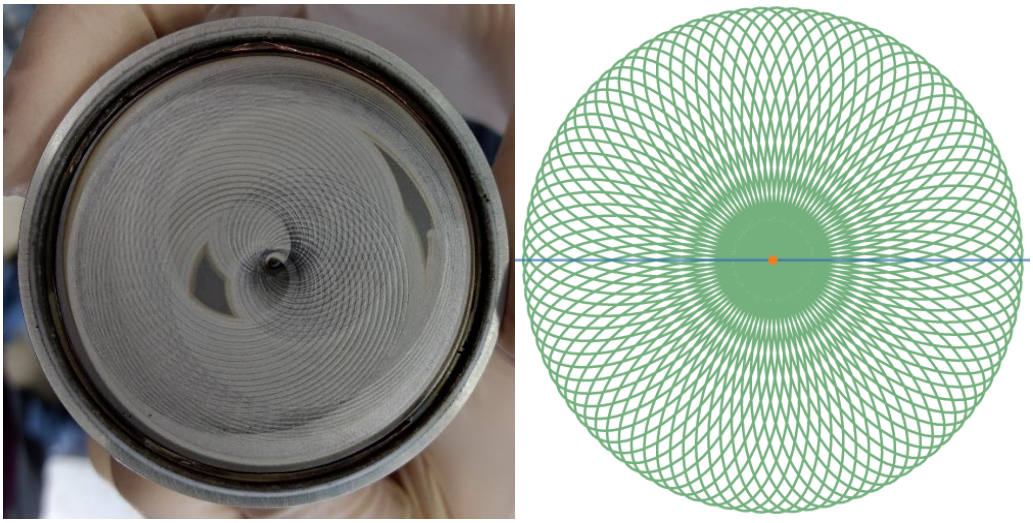

Figure II.1.2-4: 91 Petaled Rose Curve in Cobalt

The gear system was designed with a 2” diameter metal disk in mind, since going smaller than 2” resulted in gears so small they could not be produced. The geometry to accomplish this is as follows. The laser is aligned with the beamline axis in order to shoot the laser down the beamline and with the center of the LVS mounting flange, however the gear assembly is offset from the center of the flange by 0.5” and the distance of the planet gear center to the gear assembly center is 0.5”. (**Figure II.1.2-5**) This means that there is a point in the path of the planet gear where the two 0.5” offsets cancel each other out resulting in the center of the planet gear, and thus the center of the disk, being centered on the flange and the laser. At the other extreme, when the planet gear is on the opposite side of the ring gear the two offsets add together resulting in the center of the

planet gear, and thus the disk, being 1” from the flange and laser center meaning that on a 2” diameter disk the laser is now striking the edge of the disk. As the planet gear rotates the laser moves from the center of the disk to the edge and then back.

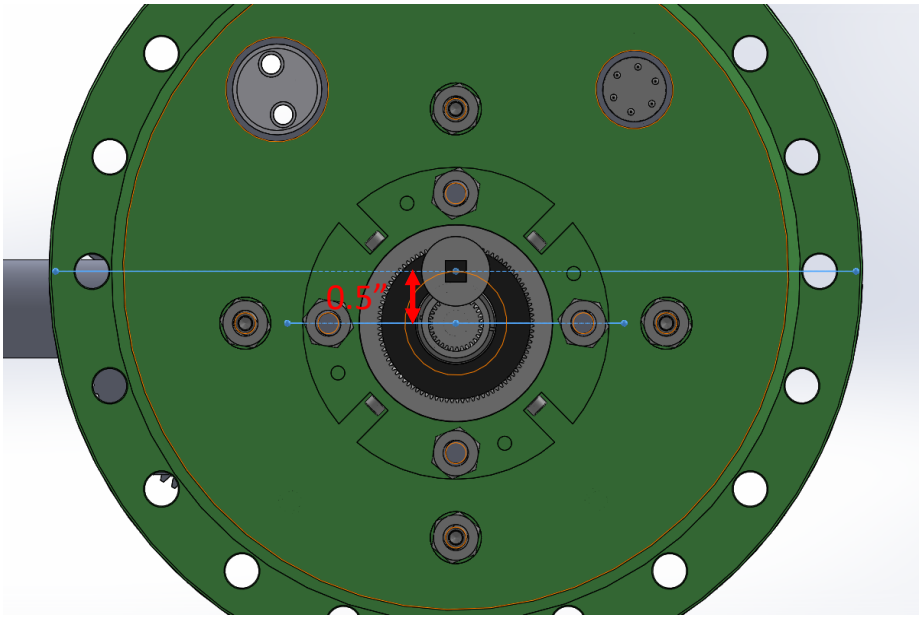

Figure II.1.2-5: Gear Placement in Instrument Frame

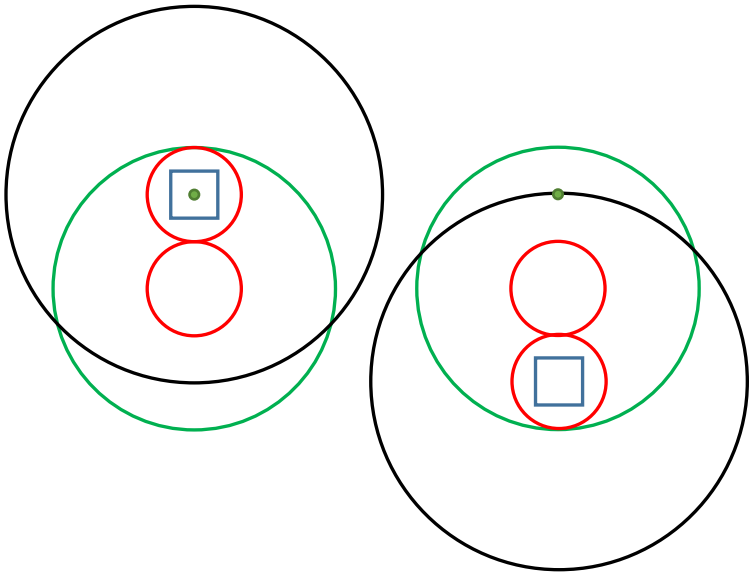

Figure II.1.2-6: Laser Movement on Target at Extremes (Green Dot is laser location, Black is 2”Ø Target)

To accomplish this 0.5” offset more gear equations are needed. In order for a planetary gear system to work the following equation must be met, with the center gear called the sun gear (s).

$$D_r = D_s + 2D_p$$

Equation 4

And consequently,

$$T_r = T_s + 2T_p$$

Equation 5

As established prior the following relationship is required for the 2” target to be used.

$$\frac{1}{2}(D_s + D_p) = 0.5"$$

Equation 6

After working this all out the resulting gears are as follows,

$$T_r = 91$$

$$T_p = 30$$

$$T_s = 31$$

$$M = 0.016”$$

These gears are very small and would be expensive to make conventionally, so 3D printed polylactic acid (PLA) was used to manufacture these gears. Nominally, PLA is not vacuum compatible,[8] however at the pressures a source chamber operates at it can be used. Upon experimental testing the source chamber has an ultimate pressure of $8*10^{-8}$ torr. The gears were

printed as helical gears instead of spur gears, as this allows for the planet gear to not need another support. The only way to disassemble a helical gear is to intentionally twist it out, which is not possible when the gear is not allowed to move in any direction parallel to the gear axis. If it was a spur the gear could fall out of the assembly on its own. This further simplified the mechanical design.

The entire LVS source was designed to be flange mounted so that it can be assembled on the bench and installed without needing to work inside the chamber. (**Figure II.1.2-7**) The flange is designed such that it is centered on the beamline axis, and thus the laser axis, when installed and has radial symmetry so that no matter how it is clocked on the flange it will be aligned. The design is explained as follows.

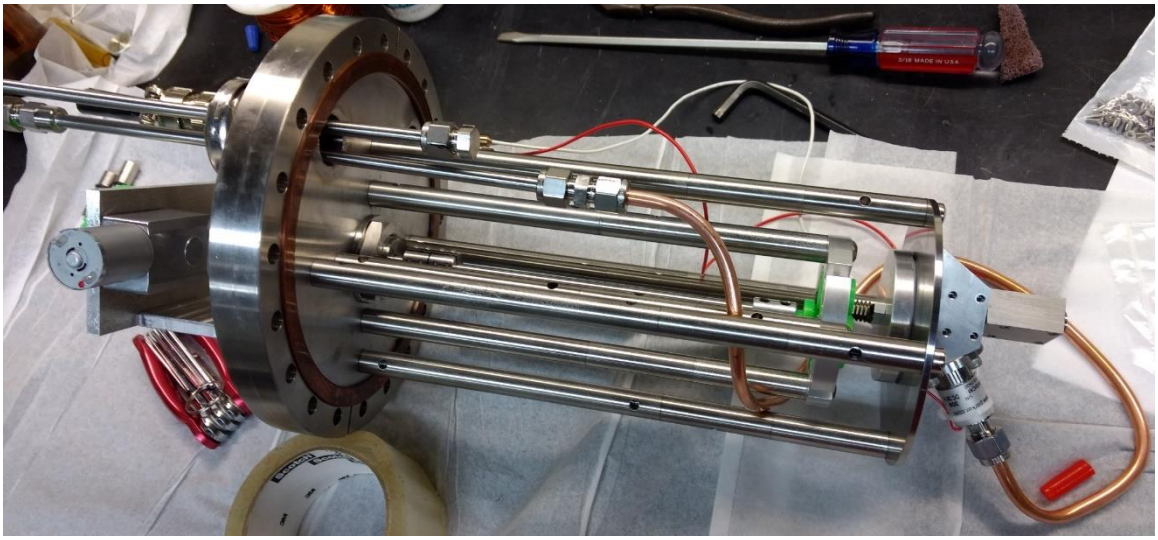

Figure II.1.2-7: LVS Source on Bench

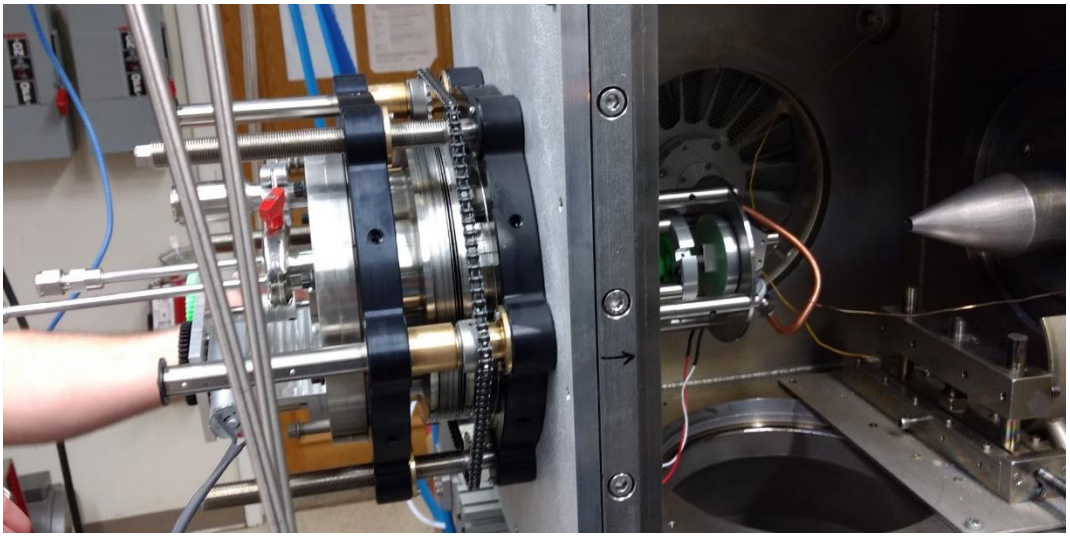

Figure II.1.2-8: LVS Source in Chamber

Starting at the back of the source, the LVS is mounted on an 8”CF flange that contains KF ports for gas (Lesker: #LFT8A22TESW) and a Mil-Spec 6-pin electrical feedthrough (Lesker: #IFTAG065108A) for the pulse valves, tapped holes for mounting the source’s support structure, and a hole for a baseplate mounted rotary feedthrough (Lesker: #KLFDBP02510-A). On the atm side of the flange a 12V DC motor and gear system is mounted that is used to apply the rotary motion to the feedthrough and thus later to the sun gear *in-vacuo*. (**Figure II.1.2-9,Figure II.1.2-10**)

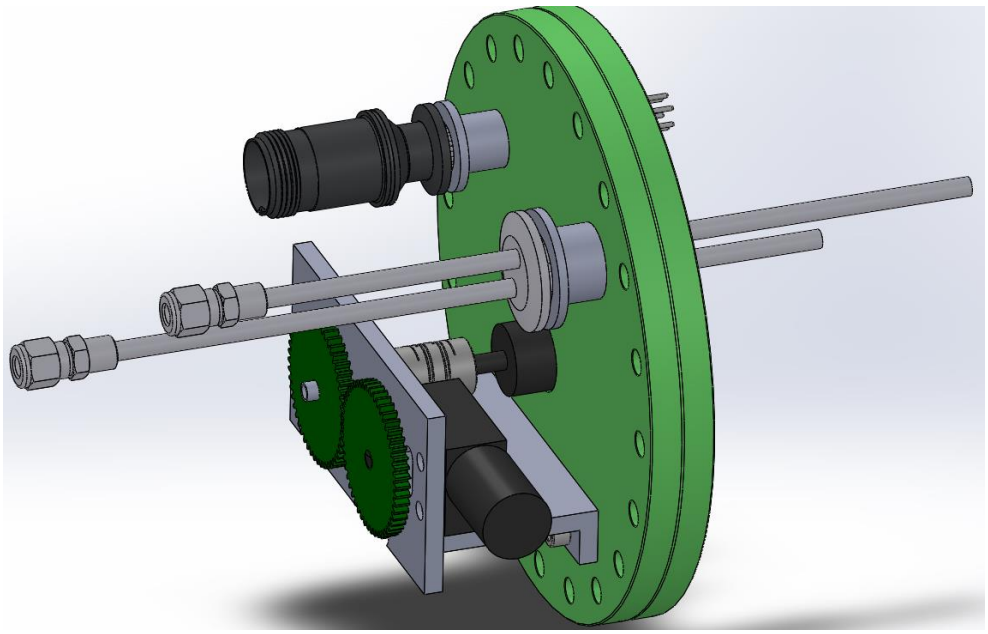

Figure II.1.2-9: Back of LVS Flange

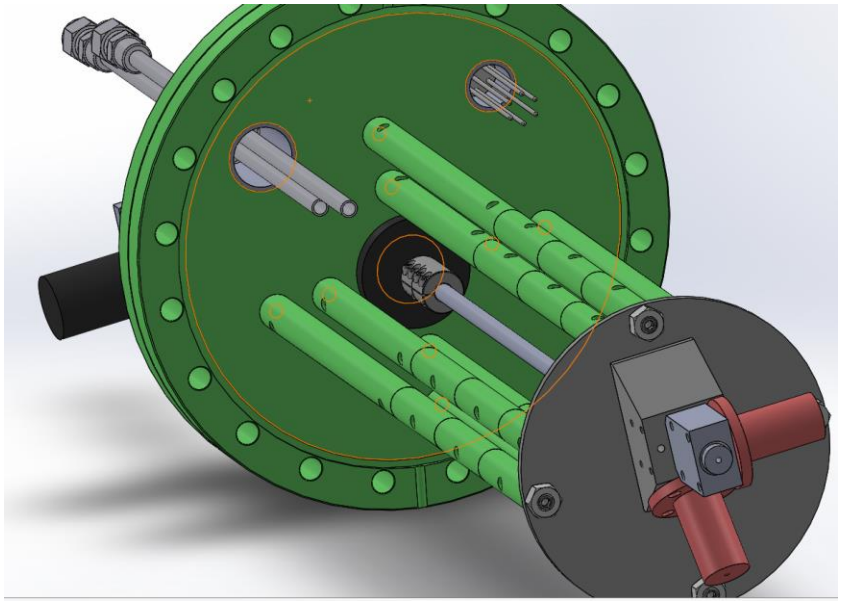

Figure II.1.2-10: Front of LVS Flange

The support structure is built from vented and end tapped 0.5” SS rods with four of them being 4.5” in length, another four being 6” in length, and the others being 2” in length. The rods are bolted together with ¼-20 set screws. The 6” and 4.5” rods hold the front plate and the gears,

respectively, thereby setting the distance between the gears and the front plate to 1.5". The 2" length rods allow for course adjustment of the distance of the source from the chamber's skimmer, meaning that the rods can be stacked to lengthen the source in 2" increments or removed to shorten it. At the end of the rods is the gear assembly press fit into its holder that is mounted on the rods and the front plate bolted to its rods. (**Figure II.1.2-11**)

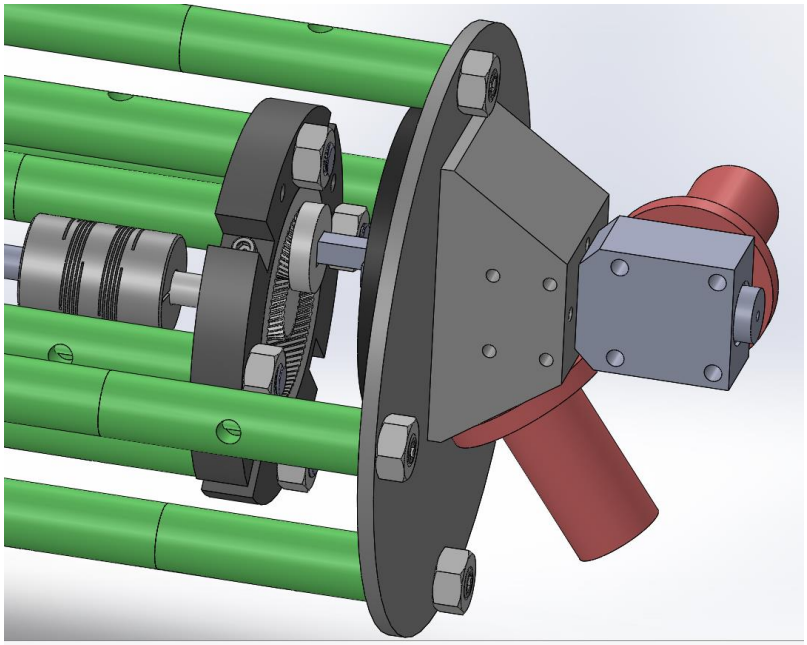

Figure II.1.2-11: LVS Support Structure

The target holder has a 6mm deep cup for accepting a 2" diameter target of a range of thicknesses up to 6mm. Around the edge of the target holder is a vacuum greased Teflon O-ring used to seal the target against the front plate and provide lubrication for its motion against the plate. On the back of the target holder is a square peg that slots into the planet gear allowing the motion of the planet gear to be applied to the target holder. This peg originally was made of aluminum, however the heat transfer from the target being struck by the laser was such that the planet gear was melting. To eliminate this problem a SCP-5000 Vespel peg was made with SCP-5000 having

a much lower thermal conductivity than aluminum.[9,10] A spring is placed around the peg in order to provide mechanical force to seal the target against the front plate.

A ¼" tube is connected to the rotary feedthrough and the sun gear via a flex coupling to account for any deviation in alignment. Multiple tubes were cut, differing in 2" lengths, for the various different lengths the source can be adapted to. The whole source is assembled in a stacking method allowing for easy setup.

The front plate has a housing with a mounting location for a pulse valve that points back at an angle to the target. The pulse valve used is a Parker Series 9 General Valve with a 0.020" orifice. Gas that is let out of this pulse valve travels down a 0.05" channel to the region where the laser strikes the target thereby mixing the plasma with the gas and expanding out the front of the housing. (**Figure II.1.2-12**)

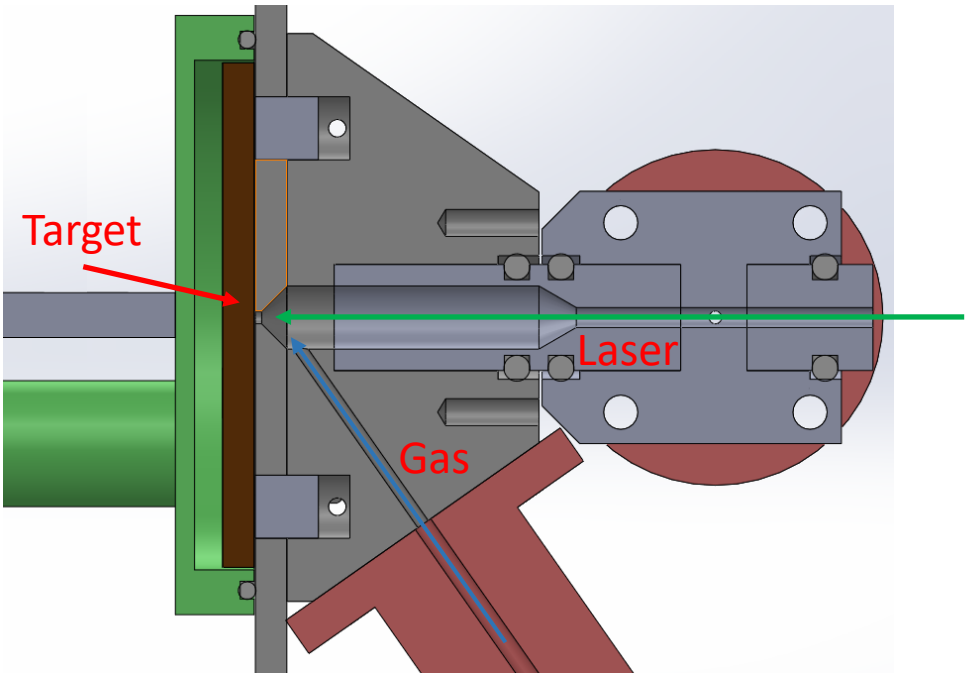

Figure II.1.2-12: Front Plate of LVS

The front plate has two regions: the mixing stage and the nozzle. The mixing stage is where the expansion gas and the plasma mix before being compressed into the nozzle where cluster condensation occurs. The length and diameter of these regions can be adjusted by installing different “click design” nozzles. The “click design” nozzles are precision machined tubes with 0.0005” clearance on either side that can be inserted or stacked in the housing where they are held in place by O-rings. This allows for a user to have a range of nozzles with the same outer shape, but varying inner shapes, allowing for them to mix and match the mixing stage shape, size, and nozzle geometries without needing to make a new nozzle for each setup. Also, in this vein is a reaction cell “click” housing that mounts another pulse valve or flow tube that can inject gas into a 2mm tube along the path of the carrier gas. This allows for another gas to be introduced into the clustering region separate from the expansion. This allows for two things: the secondary gas is introduced after the plasma has cooled, making it less likely to be decomposed, and this gas can be tuned independently of the carrier gas allowing for increased tunability.

Upon testing it was found to be sometimes beneficial to float the front plate to a positive voltage to aid in the extraction of the clusters into the first quadrupole ion guide. This was accomplished by isolating the front plate from its support rods with 4 Teflon washers of identical thicknesses between it and the rods and by replacing the threaded rods holding the front plate to the support rods with nylon bolts. From there a voltage was passed through a pin of the Mil-spec 6-pin feedthrough to the plate via a wire held against the front plate by one of its support bolts. 500VDC can be applied safely to this plate.

The whole LVS source is mounted on an 8” CF linear motion bellows (Mcallister Technical Services: #BTL86) that allows for the source to be moved forward and back in the chamber by 4” without needing to break vacuum and interrupt the experiment while running. This is useful because

varying the distance between the nozzle and skimmer of the next chamber may result in different clusters being produced or transported.

The laser used in this setup is a 2nd harmonic YAG Innolas DPSS 250 (25W, 150Hz, 145mJ). The laser is guided by two 90° coated mirrors mounted off a window normal to the beam axis. One mirror sends the laser up and the second mirror directs it into the chamber and down the beam axis, allowing for the beam to be walked using these two mirrors. Focusing the laser is critical to get the proper energy density at the target, so a dual lens system is mounted on the optical rails. (**Figure II.1.2-13**)

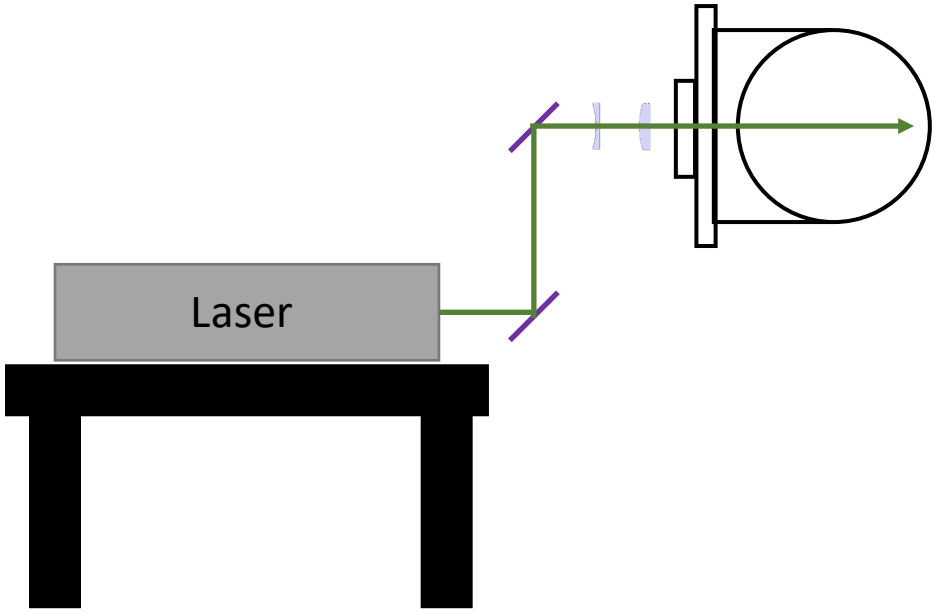

Figure II.1.2-13: Laser and Optics Orientation

The lens system is described as follows. The lens system is designed so that it can move forward and back as the source is moved forward and back with a distance between the focusing plane and the target of 1600mm. Focal point distance is described with the following equation, where a is the object distance, b is the image distance, and f is the focal length of the optic.

$$\frac{1}{a}+\frac{1}{b}=\frac{1}{f}$$

Equation 7

Lasers nominally can be described as having an object distance of infinity meaning a plano-convex lens with a focal length of 1600mm could be used. This is not ideal due to the focusing limit as described by the following equation, where λ is wavelength, w_0 is beam radius, and w_f is focal point radius.

$$w_f = \frac{\lambda f}{\pi w_0}$$

Equation 8

A 2nd harmonic YAG (532nm) with a 4mmØ being focused by a 1600mm lens would only focus to a 276µmØ at the best case. In order to improve this a dual lens setup was used consisting of a plano-concave lens (f_1 = -50mm) and a plano-convex lens (f_2 = 100mm). (**Figure II.1.2-14**)

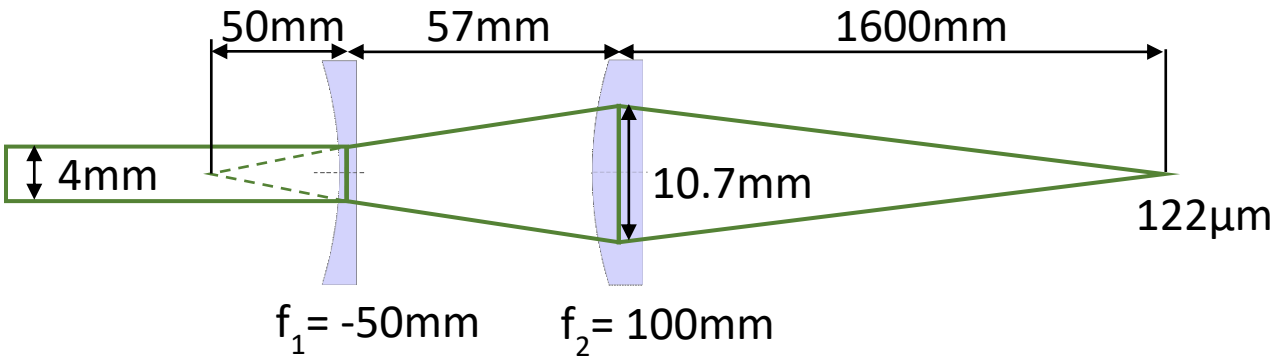

Figure II.1.2-14: Dual Lens Setup

The limitations of this setup are such that the plano-concave lens cannot diverge the beam much larger than 10mmØ due to it needing to pass through the 10mmØ apertures in the beamline. The required object distance for the 1600mm image distance of the plano-convex can be calculated

using **Equation 7** and then compared to the resulting image distance for the plano-concave lens from the laser giving a spacing between the lenses of 57mm. The beam waist at the convex lens can be calculated using trigonometry by knowing the angle of divergence of the plano-concave lens and the distance between the lenses, giving a size of 10.7mmØ which will have reduced enough to pass through the first aperture by the time it arrives. The angle of divergence of the plano-concave lens is determined with the following equation.

$$\theta = \frac{w_0}{|f|}$$

Equation 9

The effective focal length of the dual lens setup can be calculated with the following equation where *d* is the spacing between the two lenses.

$$\frac{1}{f'} = \frac{1}{f_1} + \frac{1}{f_2} - \frac{d}{f_1 f_2}$$

Equation 10

This gives an effective focal length of 725mm. Using **Equation 8** the focal spot size at the target is calculated to be 122µmØ which is a marked improvement over a single lens.

The lenses are mounted together in a holder that can be moved forward and backward as the source moves during signal tuning. The plano-convex lens is mounted in a high precision zoom housing allowing for it to be moved relative to the plano-concave lens for focus adjustment.

The timing between the laser and the pulse valve is controlled by an SRS DG645 Digital Delay Generator. The laser has a timed square pulse output corresponding to its pockel cell firing time which is used as an external clock for the DG645 setting its T_0. Another rising output is delayed off of T_0 and sent to the pulse valve controller thereby allowing for the time between the pulse valve and the laser to be adjusted. The actual value of the delay shown on the DG645 means little

in terms of what is actually happening as it does not account for electronic or physical (solenoid) delays inherent to the setup, but the values tend to be within 200μs-1ms with the pulse valve likely firing first.

II.1.3 Pulsed Arc Cluster Ionization Source (PACIS)

The PACIS uses pulsed electric discharge to evaporate materials into the gas phase.[11,12] The PACIS consists of an anode and cathode rods brought close together normal to the beam axis with a pulse valve expansion pointing in the direction of the beam axis. Using precise timing boxes, the pulse valve is fired, expanding gas into the region between the rods, where a 20kV pulse is then applied to the anode thereby causing an arc to form between the anode and cathode through the expanding gas. This voltage is then lowered once the arc forms so that a pulse of 1000-5000A with a duration of 1-20μs is generated.[12] This current evaporates the cathode into the gas phase where it is carried down the beam axis by the expanding gas. The arc also generates charged particles of the expanding gas, cathode material, and free electrons. The resulting plasma containing the material of interest is sent through a small nozzle channel where collisions occur allowing clusters to condense and is then expanded out of a nozzle and down the beam axis.[11,12] (**Figure II.1.3-1**)

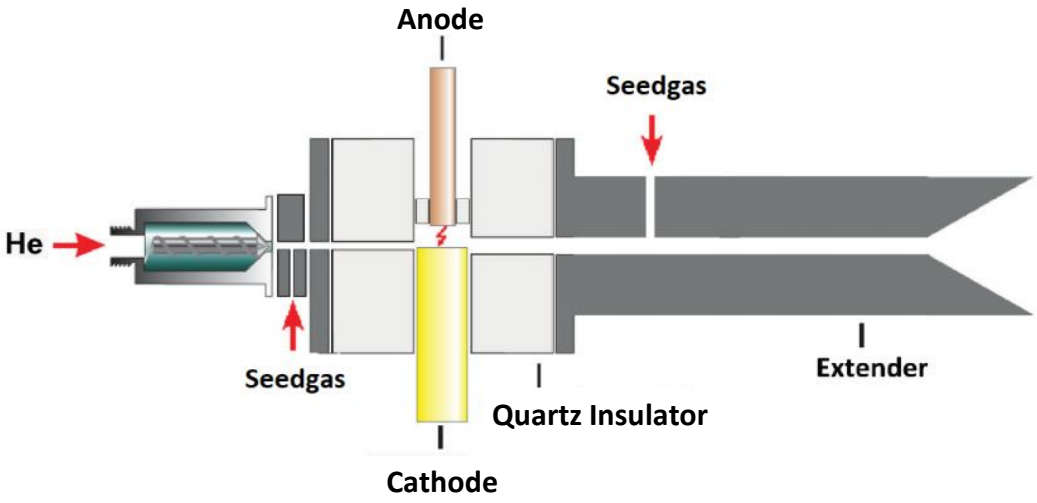

Figure II.1.3-1: PACIS Schematic[13]

[1] A. Majumdar, D. Köpp, M. Ganeva, D. Datta, S. Bhattacharyya, R. Hippler, Rev. Sci. Instrum., 2009, **80**, 095103.

[2] A. Vahl, J. Strobel, W. Reichstein, O. Polonskyi, T. Strunskus, L. Kienle, F. Faupel, Nanotechnology, 2017, **28**, 175703.

[3] Y. Huttel, "Gas-Phase Synthesis of Nanoparticles", Wiley, 2017. ISBN: 978-3-527-69840-0

[4] M. A. Duncan, Rev. Sci. Instrum., 2012, **83**, 041101.

[5] S. C. O'Brien, Y. Liu, Q. Zhang, J. R. Heath, F. K. Tittel, R. F. Curl, and R. E. Smalley, J. Chem. Phys., 1968, **84**, 4074.

[6] T. Masubuchi, J. F. Eckhard, K. Lange, B. Visser, M. Tschurl, U. Heiz, Rev. Sci. Instrum., 2018, **89**, 023104.

[7] U. Heiz, F. Vanolli, L. Trento, W.-D. Schneider, Rev. Sci. Instrum., 1997, **68**, 1986.

[8] A. P. Povilus, C. J. Wurden, Z. Vendeiro, M. Baquero-Ruiz, J. Fajans, J. Vac. Sci. Technol. A, 2014, **32**, 033001

[9] ASM Handbook: Vol 2: Properties and Selection: Nonferrous Alloys and Special-Purpose Materials, ASM International, 1990, pg181. ISBN 0-87170-378-5 (v.2)

[10] DuPont™ Vespel® SCP-5000 Datasheeet (2018).

[11] H. R. Siekmann, Ch. Lüder, J. Faehrmann, H. O. Lutz, K. H. Meiwes-Broer, Z Phys D - Atoms, Molecules and Clusters, 1991, **20**, 417.

[12] B. Klipp, M. Grass, J. Müller, D. Stolcic, U. Lutz, G. Ganteför, T. Schlenker, J. Boneberg, P. Leiderer, Appl. Phys. A., 2001, **5**, 547.

[13] Moritz Samuel Blankenhorn, "Zeitaufgelöste Photoelektronenspektroskopie an massenselektierten Eisen-Cluster-Anionen Fe_n^-", Master's Thesis, University of Konstanz, 2018.

II.2 Mass Spectrometers

Once the ion cluster beam is made, the ions must be mass selected. The new instrument only has one method of mass selection, a QMS, however the magnetic sector will be discussed, as it was present on the instrument being replaced.

II.2.1 Magnetic Sector

The magnetic sector uses ion trajectory, controlled by a magnetic field around a curve, to mass select ions. The ions are sent into a curved flight tube where a magnetic field perpendicular to both the curve and the beam axis is applied making the ion trajectory bend in a direction according to charge. The amount of bend is dependent on the strength of the magnetic field and the centripetal force of the ions. If these forces are matched, the ion is able to make the curve and continue down the beamline. The following equations describe this motion and can be converted to a m/z equation.[1]

$$F_B = zvB = F_c = \frac{mv^2}{r}$$

Equation 11

Equation 11 shows the equations for magnetic force on a moving charged particle and the centripetal force of the particle curving in the magnetic field and the condition that they must be equal for the ion to continue down the beamline and from manipulation of this relationship Equation 12 is derived.

$$v = \frac{Bzr}{m}$$

Equation 12

Equation 13 describes the relationship between kinetic energy, velocity, and charged particles accelerated in an electric field.

$$KE = zV = \frac{1}{2}mv^2$$

Equation 13

Subbing Equation 12 into Equation 13 allows for the determination of which m/z passes.

$$\frac{m}{z} = \frac{B^2r^2}{2V}$$

Equation 14

The radius of the flight tube (r) is constant and the mass selection is controlled by adjusting the strength of the magnetic field (B) or the ion's axial energy (V). Lighter ions will bend more, while heavier ions will bend less. The output of the tube usually has a slit in order to improve the resolution. And while having no theoretical upper mass limit, hardware will limit the magnetic field strength applied and thus the mass limit.

The resolution of a magnetic sector is increased by increasing the curvature of the sector or by increasing the V of the ion beam, however either of the changes require a larger B to be applied to the sector in order to pass the same mass, thereby lowering the upper mass limit. This tie between resolution and mass limit makes the magnetic sector limited for larger masses in a size selected study.

The instrument being replaced had a 20° magnetic sector with a resolution $M/\Delta M$ = 10-20 during normal operation. This resolution was limiting, in that the ability to resolve oxygen in a metal oxide cluster was lost around 160-320 amu.[2]

II.2.2 Quadrupole Mass Spectrometer (QMS) Theory

A QMS operates via the application of alternating RF and static DC voltages applied to a set of four parallel metal rods with an inscribed radius (r_0) described using the following equations, where V and ω are the RF voltage magnitude and frequency, U is the DC voltage magnitude, and t is time.[3,4,5] (**Figure II.2.2-1**)

$$N_{1,3} = +\left(U + Vcos(\omega t)\right)$$

$$N_{2,4} = -(U + Vcos(\omega t))$$

Equation 15

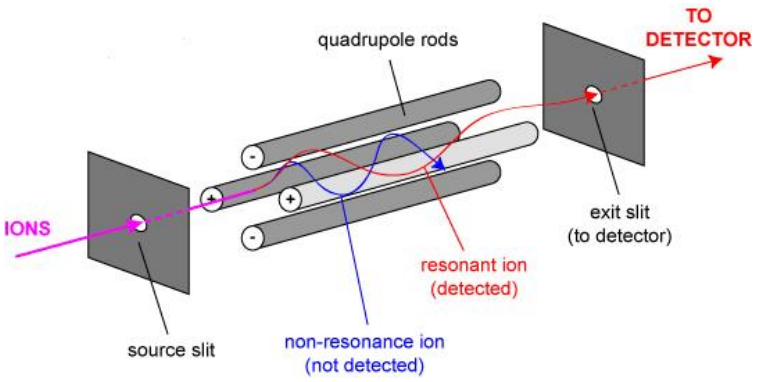

Figure II.2.2-1: QMS Schematic

The trajectory of ions through the field generated by these voltages can be described rigorously by solving the equations of motion of the ions, or thought of qualitatively. Qualitatively, the lower mass ions are able to resonate with the RF field until they gain enough energy to be ejected from the QMS making the RF a high-mass filter while higher masses don't resonate with the RF and will be defocused by the DC component making the DC a low-pass filter. When these are combined with a narrow overlap, the QMS can act as a mass filter for a given mass.

$$\frac{d^2x}{dt^2} = (\frac{e}{m})\frac{N_{2,4}}{r_0^2}x$$

$$\frac{d^2y}{dt^2} = (\frac{e}{m})\frac{N_{1,3}}{r_0^2}y$$

$$\frac{d^2z}{dt^2} = 0$$

Equation 16

Equation 16 shows examples of Mathieu's Equation,[6] which has an already determined solution. Two unitless parameters, a_u and q_u, are introduced, which allow for the calculation of ions with a stable trajectory, $r_{max} < r_0$. Equation 17 defines these parameters, where z is the charge of the ion and m is its mass. Note the linear independence between U and V for a stable trajectory.

$$a_u = \frac{8zU}{mr_0^2\omega^2}$$

$$q_u = \frac{4zV}{mr_0^2\omega^2}$$

Equation 17

With some conversion these equations can be manipulated to give regions of stability plotted as a function of U and V for a given m/z and ω. (**Figure II.2.2-2**)

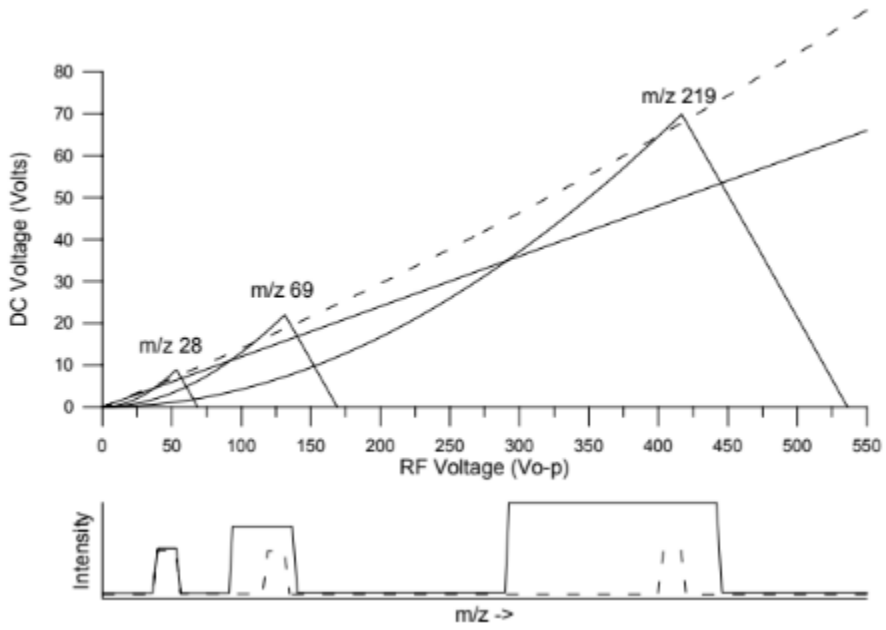

Figure II.2.2-2: QMS Stability Diagram with Different Slope Scan Line and Resulting Spectrum[7]

Plotting these diagrams together for a range of masses allows for the generation of a scan-line, where, in most QMSs, the ω and U/V are held constant, and the magnitude of the U and V are varied to determine the m/z resulting in a stable trajectory through the QMS.

II.2.3 Quadrupole Mass Spectrometer (QMS) Experimental Setup

The mass spectrometer setup consists of an analog controlled QMS (Extrel, 440kHz, 19mm rods) performing the mass selection and a GPIB-controlled Keithley 6514 Electrometer measuring current on a conductive surface. The control voltages and digital communication are handled by a NI PCI-6323 DAQ controlled via LabVIEW 2017.

An overview of the analog controls of the QMS is given below. The Mass Command (MC) is a 0-10 VDC applied through a ¼" Phono Connector, where 0 VDC is nominally 20 amu and 10 VDC is nominally 4000 amu. The actual mass values are subject to a small drift in the voltage, which is corrected for in calibration. The connector is wired up with the "Tip" as Lo (DAQ's Ground) and the "Ring" as Hi (0-10 VDC).

A DB15 connector contains the connections for the other controls. There are three analog controls, one analog output, and two TTL controls. The pinout of the DB15 is as follows:

1. Pin 2: **Pole Bias, ±5 VDC:** This applies a DC float to all four rods of the QMS scaled to ±200 VDC, such that +1 VDC is +40 VDC on the rods.
2. Pin 3: **Resolving DC On/Off:** Sending a TTL Lo to this pin turns off the resolving DC, and as a result the QMS acts as an ion guide. This is controlled via a digital output on the DAQ.
3. Pin 4: **ΔM, ±5 VDC:** This controls the *U* intercept of the mass scan line of the QMS.
4. Pin 5: **ΔRes, ±5 VDC:** This controls the slope of the mass scan line of the QMS thereby affecting the resolution of the QMS.
5. Pin 6: **Pole Bias Readback, ±5 VDC Output:** This reads back the applied DC float to the four rods of the QMS scaled to ±200 VDC, where +1 VDC is +40 VDC on the rods. This exists because the voltage requested at pin 2 may not be what is actually applied.
6. Pin 10: **Common:** This is the reference for all of the inputs. It is connected to the DAQ's ground.
7. Pin 11: **Pole DC Reverse:** Sending a TTL Lo to this pin flips the resolving DC on the rods. In a QMS rod pairs have a DC voltage equal but opposite in polarity applied to them. This switches which rod pair has the positive and which has the negative. For a perfect beam the QMS is not affected by the placement of this voltage, however an imperfect beam profile may make one condition have more intense signal than the other or even add precursor peaks. This is controlled via a DO on the DAQ.

These controls are wired up to the DAQ's Analog Outputs (AO), Analog Input (AI), and Digital Outputs (DO) with the common connected to the DAQ's common to assure the voltage outputs at the DB15 match the requested output at the DAQ.

How these voltages are used will be discussed with the LabVIEW program (See Appendix A). First the setup of the 6514 will be described. The 6514 is controlled via SERIAL communication using an IEEE-488 (GPIB) to USB where ASCII scripting commands are used to setup and run the 6514. A list of commands and programming structure can be found in the 6514's manual. The problem with serial communication is that it cannot be synched with the DAQ due to the READ-WRITE nature of SERIAL, and it will gradually drift over time. To overcome this issue the 6514 is setup to take a measurement upon receiving a trigger from the DAQ's Counter Output (CO), which is synched with the DAQ's other outputs that control the QMS. Even the act of transferring this measurement to the computer, which has to be done through SERIAL, would slow down the 6514. Instead, the measurement is stored in the "buffer" of the 6514 to be retrieved after the scan. The buffer of the 6514 can only hold 2500 data points, so when filled the ramp pauses and reads the buffer, empties the buffer, and then continues the ramp. This all ensures the mass scan and the signal measuring stay synced and operating as quickly as possible.

---

[1] C. Herbert, R. Johnstone, Mass Spectrometry Basics, CRC Press LLC, 2003 chapter 25, 26, 39

[2] X. Tang, Z. Hicks, L. Wang, G. Gantefçr, K. H. Bowen, R. Tsyshevsky, J. Sun, M. M. Kuklja, Phys. Chem. Chem. Phys., 2018, **20**, 4840–4850.

[3] P. H. Dawson, Quadrupole Mass Spectrometry and Its Applications, American Institute of Physics, 1997.

[4] F. H. Gross, Mass Spectrometry: A Textbook, Springer, 2011.

[5] Fachbericht Balzers BG 80003, Das Funktionsprinzip des Quadrupol-Massenspektrometers, 1990.

[6] J. Meixner, F.W. Schäfke, Mathieusche Funktionen und Sphäroidfunktionen, Springer, 1954.

[7] Extrel CMS, LLC, "Using Graphical Tools to Understand Quadrupole Theory", 2014.

II.3 Ion Optical Transport

II.3.1 Ion Guides

In order to transport an ion beam, the ions must remain collimated in the xy-axis as they travel down the z-axis from aperture to aperture. Maintaining collimation in a field-free environment is impossible for two reasons:[1] 1) Any initial transverse energy the ions have from their formation remains and causes expansion. (**Equation 18**) 2) Space-charge effects are a constant expanding force on the beam. (**Equation 19**) Where E is the energy of the beam, z is the axial component, r is the xy-axis defined radially, q is charge, and ρ is the charge density.

$$E_{total} = E_{axis} + E_{trans} = E_z + E_r$$

Equation 18

$$F(r) = qE_r = \frac{q}{\epsilon_0 r}\int_0^r \rho(r) r\, dr$$

Equation 19

Many ion optics are cylindrically symmetric and the beam can be treated as a cylinder making it prudent to define the beam and any equations in a polar form. The beam axis is the z-axis and the transverse axis is the radial component in a circular plane perpendicular to the z-axis. In order to maintain collimation, E_r must be 0 or counteracted with a focusing force, and in the case of an ion beam space-charge is always present resulting in the beam expanding. This means we must be able to focus in two dimensions.

Due to Earnshaw's Theorem,[2] a static DC field cannot be used to contain a charged particle because there does not exist a situation where DC fields can apply a potential well in a 2D system. The potential can either be flat in all directions or exist as a saddle point meaning there is always

an acceleration vector away from center. However, using alternating fields and the concept of strong focusing one can focus in two dimensions This is accomplished with multipole setups.[3]

Multipole setups consist of an even number of rods (2N), typically round or ideally hyperbolic, centered around an axis. Two 180° out of phase RF voltages, with magnitude *V* and frequency *w,* are applied to the rods in an alternating pattern.[3] (**Figure II.3.1-1**, **Figure II.3.1-2**)

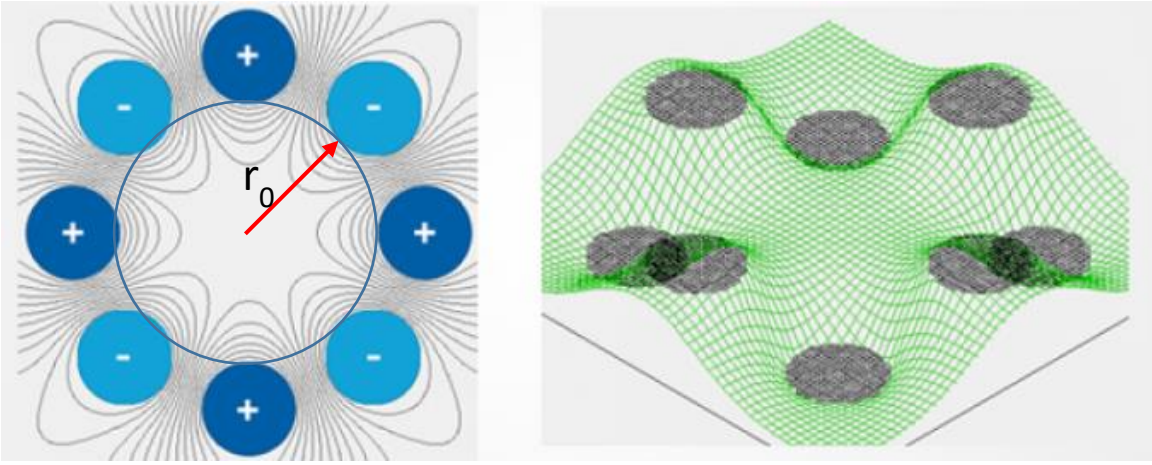

Figure II.3.1-1: Isopotential Fields on Octopole Ion Guide in r-plane[4]

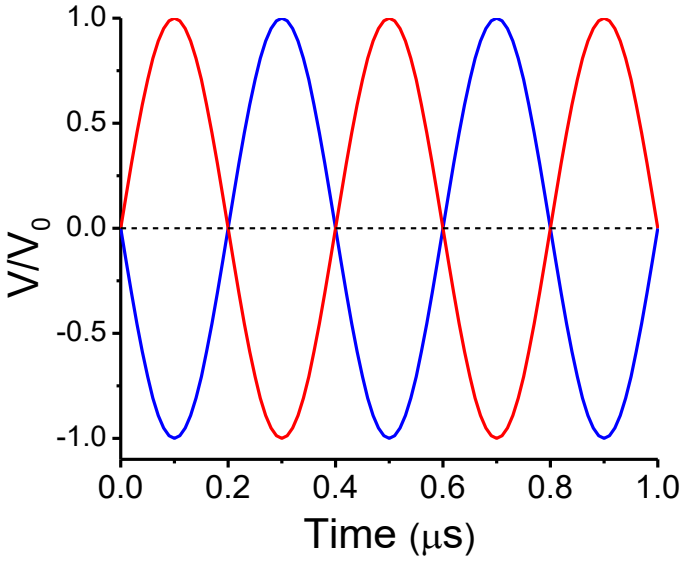

Figure II.3.1-2: 2.5MHz RF Waveform Plot in Time

The electric fields are described by **Equation 20**. The guide lengths, z, are irrelevant due to them having no axial field, so they can be short (cm) to very long (Dm).

$$\Phi_N(x,y) = V((x+iy)^N/{r_0}^N), \Phi_z = 0$$

Equation 20[3,4]

This alternating of the 180° out of phase RF voltages means there is alternating attractive and repulsive potentials as one approaches the edge of the "field radius," r_0, that returns to flatness and zero as $r \rightarrow 0$. Qualitatively, this field can be described as focusing the ions in the following way. At $t = 0$ the ion starts moving toward the attractive rod, but as it does so the rod switches to repulsive, pushing the ion to the center of the rods, and the neighboring rod becomes attractive, pulling the ion towards it. As these voltages continue to change, the ion makes a circular trajectory in the r-plane and is therefore constrained. Since there is no field in the z-axis, the ion can travel down the guide freely, resulting in the ions taking a screw trajectory down the length of the ion guide. (**Figure II.3.1-3**)

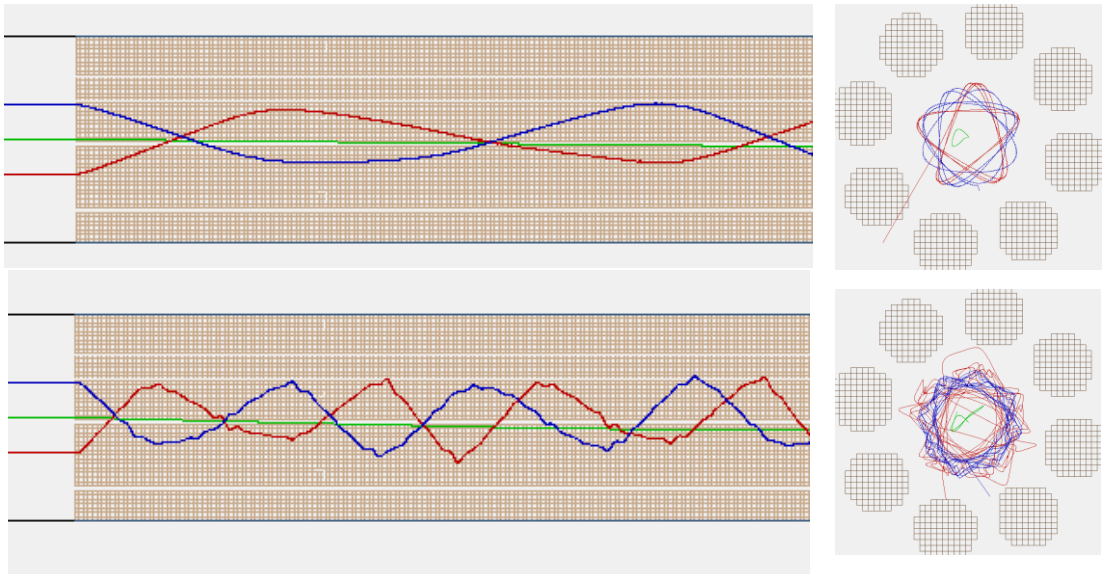

Figure II.3.1-3: Ion Trajectory in Ion Guide Side and End Profile via SIMION (1000amu top, 150 amu bottom)

In order to determine what happens on a longer time scale, a time average of the alternating field can be used to determine a constant restoring force to the center of the guide that happens over the time period of many cycles. This restoring force is called the effective potential (**Equation 21**).

$$V_{eff}(r) = V_0(r/r_0)^{(2N-2)}$$

Equation 21[3,4]

Plotting Equation 21 for a range of multipole orders results in a series of parabolic fields with the lower order multipoles having a more gradual slope to the peak voltage. (**Figure II.3.1-4**) This is the field that constrains the ions to the center of the guide. The ions fill the guide as a function of their transverse energy. For example, an ion with E_r of 0.2V will fill a quadrupole (N=2) up to $0.6r_0$ and would fill an octopole (N=4) to $0.75r_0$. This difference in filling between lower and high order multipoles is an important design consideration as it means that a high order multipole allows for a beam to have a larger diameter, which makes it harder to transfer through smaller apertures, but the effects of space-charge are reduced resulting in better overall transfer than lower order multipoles.

With known aperture sizes the maximum E_r an ion can have and still be passed through the aperture can be calculated using Equation 22[3], where r_m is the ratio between the aperture radius and the inscribed radius of the ion guide.

$$E_r = \frac{(NzV)^2}{4mw^2r_0^2} r_m^{2N-2}$$

Equation 22

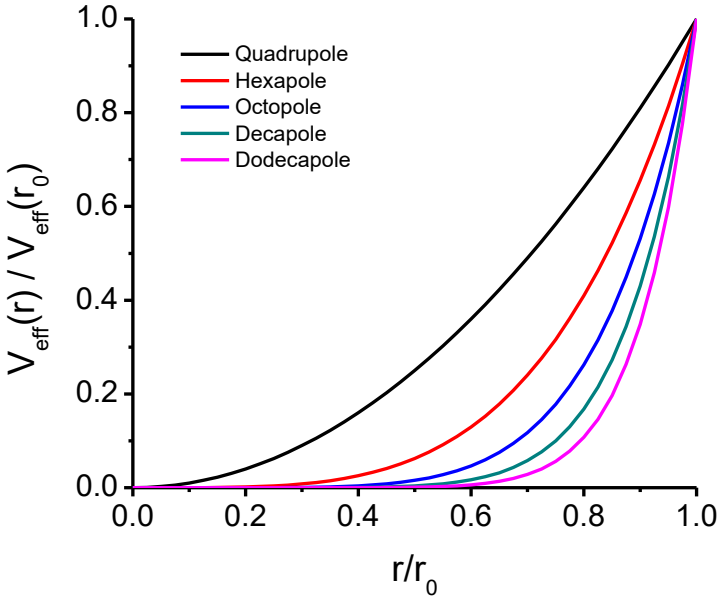

Figure II.3.1-4: Effective Potential for N-pole Guides

Having discussed the effective potential and how the ions' E_r determines their fill of the guide, the effects of collisional focusing can now be explained. Ions traveling in an ion guide are an adiabatic system, where their total energy is constant. If a gas is introduced into the system on the mtorr to torr regime, the system is no longer adiabatic, and collisions with the gas can change the total energy of the ions. This is the concept of collisional cooling.[3] If the ions are in a potential, it will shape the ion beam as collisions transfer energy to and from the system. If the ions are in a guide and energy is taken away from them, they are focused toward the center of the ion guide as they fall into the parabolic potential due to a loss of E_r. This is called collisional focusing. The figure below is a simulation of collisional focusing in a quadrupole performed in SIMION 8.1. (**Figure II.3.1-5**)

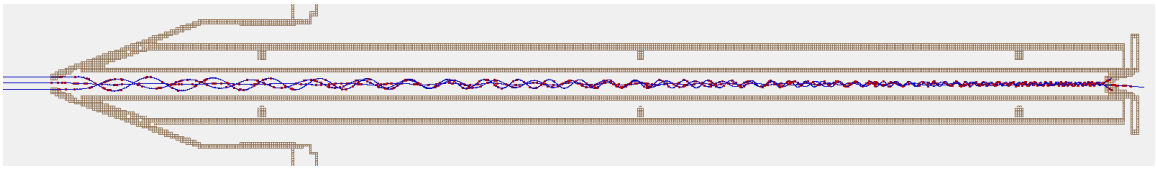

Figure II.3.1-5: Collisional Focusing Simulation SIMION 8.1 (Red Dot is a collision, 4 amu, 273K gas)

To this end the lower order multipole guides allow for collisional focusing to focus the beam to a smaller diameter due to the tighter potential they apply. (**Figure II.3.1-4**) Combining what is known about collisional focusing and transport in ion guides, a design consideration is to have a lower order multipole form the beam in the higher pressure regions closer to the ion source, and then use higher order multipoles to transport the ions through the beamline for minimal losses assuming the apertures are designed with the higher order multipole's filling in mind.

The equations for the quadrupole ion guide (n=2) have been rigorously solved using the same parameters used in the QMS described in **II.2.2**, where with U=0 all ions with q_u<0.905 will have stable trajectories. This sets a lower mass cutoff to the quadrupole ion guide that can be tuned by adjusting its V or its ω. The equations for higher order multipoles have not been solved rigorously but follow the same principles, where there is a lower mass cutoff tuned by adjusting V or ω.[3]

II.3.2 Electrostatic Bender

As established earlier, neutrals cannot be manipulated and therefore not be mass selected. This means they must be removed from the beamline so that they do not just travel forward and contaminate the sample. This is accomplished via a bend in the beamline, where the ions are turned 90°, while the neutrals continue straight. This bend is also what allows for the laser in the LVS to be used on axis.

The ions are bent around this 90° turn by an electrostatic bender optic. A bender consists of four rod sectors aligned perpendicular with the beam axis, where the ions enter the bender through a gap between a pair of the rods.[5,6,7] (**Figure II.3.2-1**)

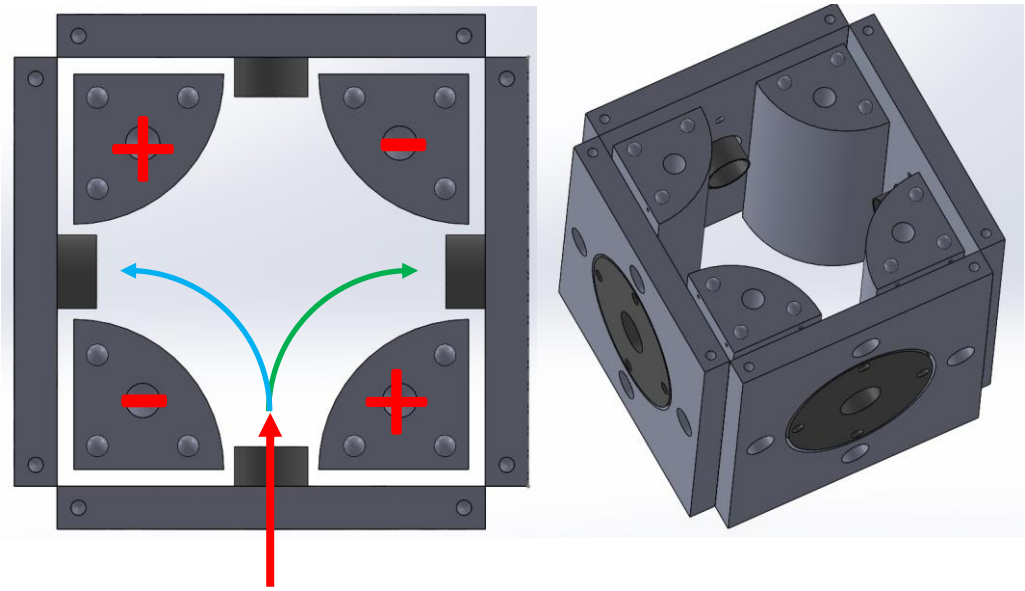

Figure II.3.2-1: Electrostatic bender Schematic

The rods diagonal from each other are held at the same DC voltage. This results in a quadrupolar field that has a saddle point in the middle of the bender. (**Figure II.3.2-2**)

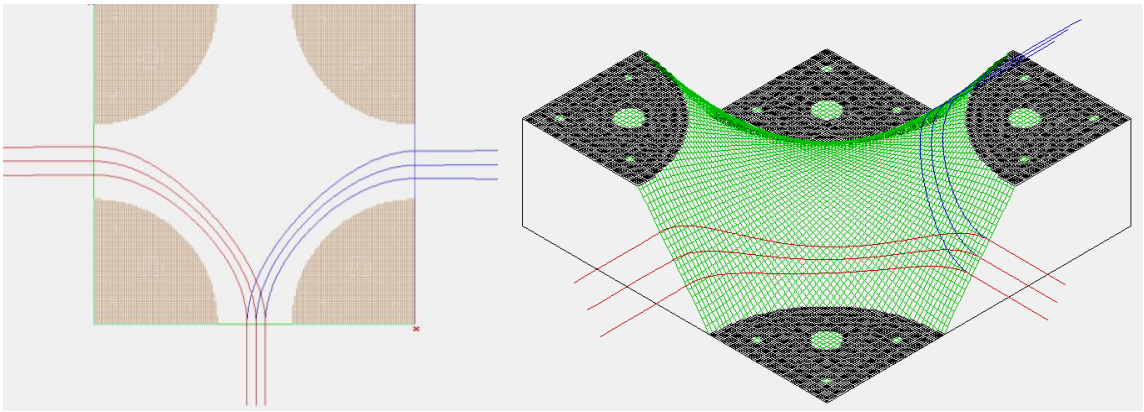

Figure II.3.2-2: Electrostatic bender in SIMION (Cations in Red, Anions in Blue, Iso-Energy)

As shown in the above picture, cations would experience this as a curved potential directing them to turn 90° to the left while anions would turn 90° to the right. The electrostatic bender, unlike the ion guides, has a strong dependence on axial beam energy, where ions with more energy may not bend enough to make the 90° turn, while lower energy ions may bend too much. (**Figure II.3.2-3**) This has to be considered for the various ion sources, as the LVS source is an iso-velocity source due to the gas pulse expansion, which means the heavier ions have a higher energy, while the magnetron generates a beam with a large energy dispersion due to the voltage applied to the target and the large number of gas collisions in the gas mixture.

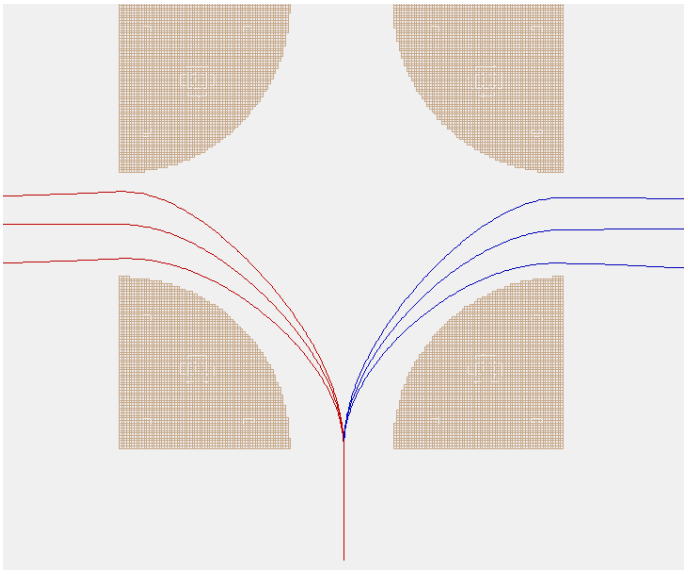

Figure II.3.2-3: Electrostatic bender in SIMION (8,10,12 eV, Cations Red, Anions Blue, Same Staring Point)

II.3.3 Thin Gate Valve (Thin-GV)

In order to modify the ion source, the source chamber has to be bled to atmospheric pressure, and ideally the rest of the instrument would remain under vacuum to maintain UHV conditions. In order to accomplish this, an in-line gate valve (GV) must be used to separate the two regions of the instrument.

Standard commercially available GVs can be placed between two chambers on a range of flange types, however they take up a lot of space both *in-vacuo* and *ex-vacuo*. The *in-vacuo* component consists of a region where the gate mechanism slides open and closed, which is usually around 0.75" thick. This region must remain clear for the GV to operate, creating a void in the ion optics, allowing the ions to defocus, and signal to be lost.

It is therefore prudent to make this region as small as possible. A thin-GV design was developed with a gap of only 0.1". This design was based on another design by Peter O'Connor at the University of Warwick.[8] The thin-GV is mounted inside a double-sided CF blank that has a pocket milled out for the GV mechanism and an O-ring groove for sealing. The holder/gate assembly is mounted into this pocket via bolts. The gate is 0.1" thick with a 1cmØ aperture and has wheels mounted on its edge that fit into a groove milled into the holder (**Figure II.3.3-1**). This groove is straight for most of the gate's range of motion until the end, where it pushes forward into the pocket thus pressing the gate into the O-ring and creating a seal (**Figure II.3.3-2**).

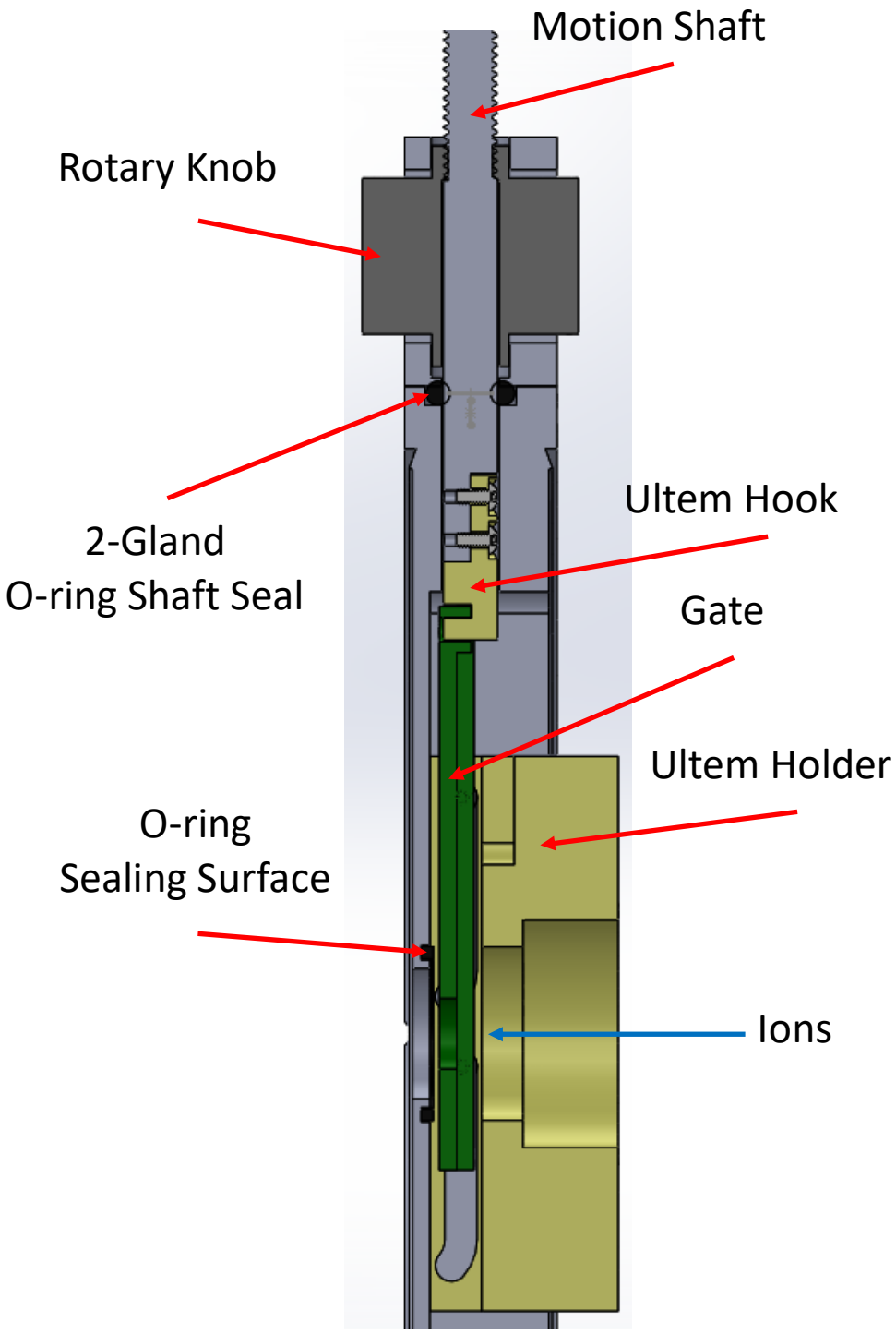

Figure II.3.3-1: Thin-GV Inner Workings Cross-Section

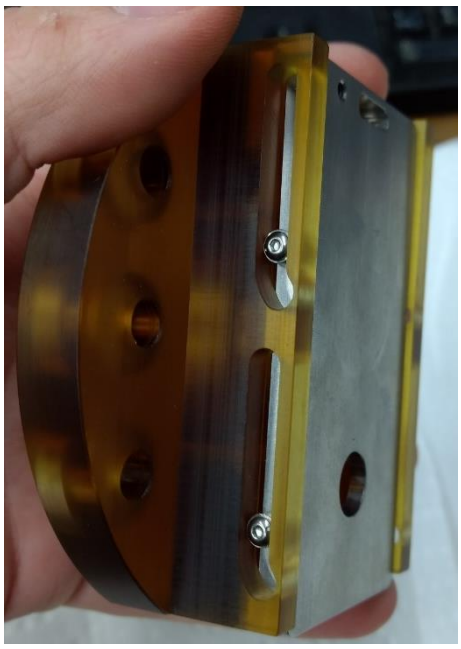

Figure II.3.3-2: Thin-GV Rails

The differences in our designs are as follows. O'Connor's design uses a UHV push-pull bellows manipulator, while this design uses a left-handed screw mechanism with a rod sealed via a 2-gland radial O-ring. This screw mechanism is a much gentler manipulation and removes the worry that a user's grip is lost, and the gate is pulled in via vacuum and damaged. Also, it allows for the gate to be partially opened, which is relevant to the last difference in design. O'Connor's design has the holder made out of stainless-steel meaning the gate is always grounded to the chamber. In this design the holder is made of a vacuum compatible plastic namely, Ultem. In this way the gate is electrically isolated from the chamber, and via an electrical feedthrough added radially to the gate's flange the gate can be floated to an applied voltage or grounded through an electrometer. This allows for the gate to act as an ion optical lens element thereby focusing the beam through it. If the gate is closed and connected to an electrometer, the full ion beam intensity can be measured as it strikes the gate.

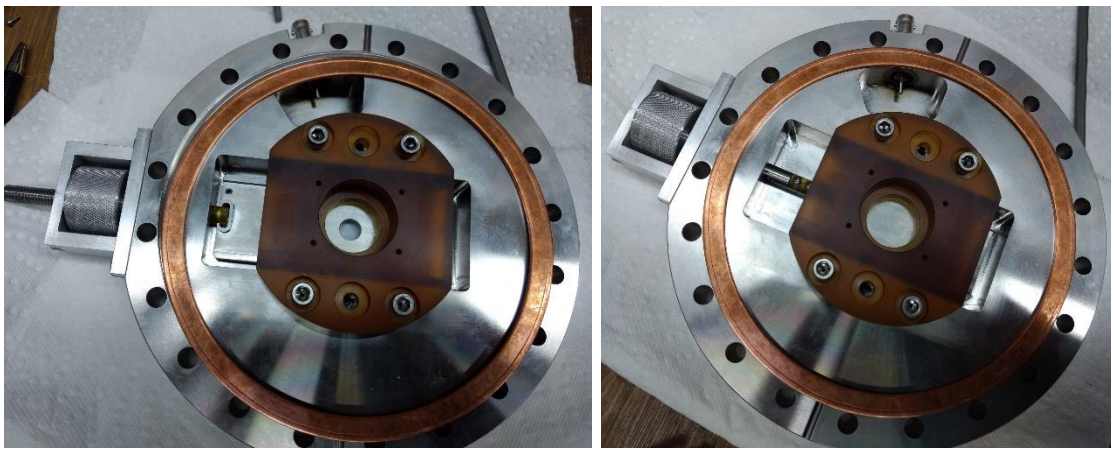

Figure II.3.3-3: Thin-GV Open and Closed (Radial Feedthrough not attached yet)

This design has been a success in that the gate is able to seal atm from $7x10^{-10}$ torr, the application of voltage to the gate versus ground has been able to increase the signal nearly two orders of magnitude, and at the time of this writing the GV has operated with no maintenance for over a year.

II.3.4 Beamline Ion Optics Setup

The ion optical layout for the instrument is shown below (**Figure II.3.4-1**). Each optical design and mounting will be described first. The optics will then be placed in order from the source to the deposition chamber, with every chamber after the source chamber being numbered starting at one (ch1, ch2, etc.) Unless otherwise noted, 316-Stainless Steel is the material used in manufacturing.

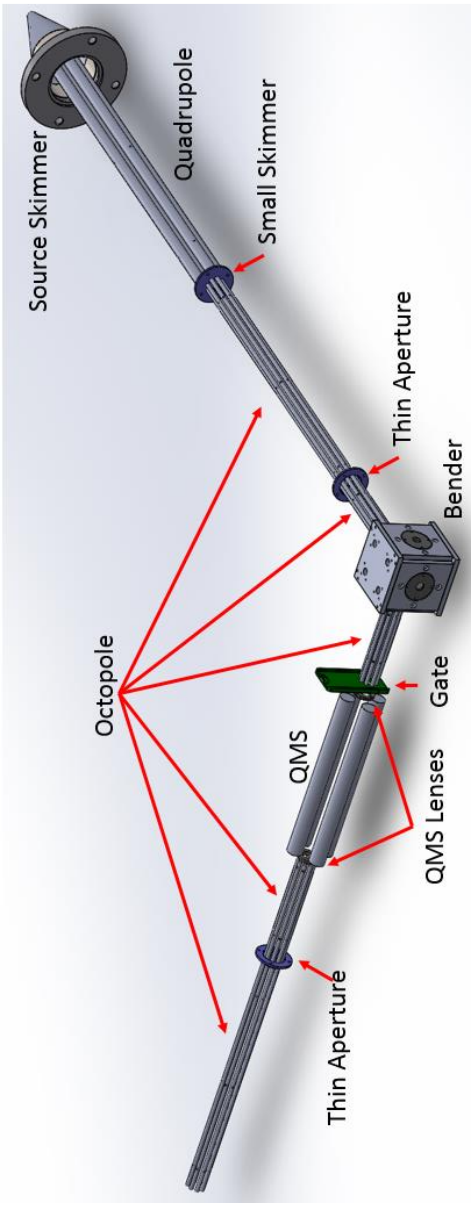

Figure II.3.4-1: Ion Optics

Note regarding all optics: Every optic is flange mounted. The benefit of this is that it assures alignment of the optic and every optic can be assembled on a bench and then inserted into the chamber thereby removing the need to ever work in the cramped space of a chamber and allowing for the smallest chambers to be used aiding in pump down.

Source Chamber Skimmer: (**Figure II.3.4-2**) This large skimmer has a 1cmØ opening and a 161° cone to a 2.5" OD. This skimmer is mounted on an ISO63 flange via weld. The ISO63 flange is then mounted on a double-sided ISO200 blank with an ISO63 center bore and bolt pattern. Alignment is maintained via a Delrin plastic centering ring which also electrically isolates the skimmer from the chamber allowing it to be floated. This skimmer acts to remove excess gas from the expansion and prevent turbulence as the ion packet passes through to the next chamber.

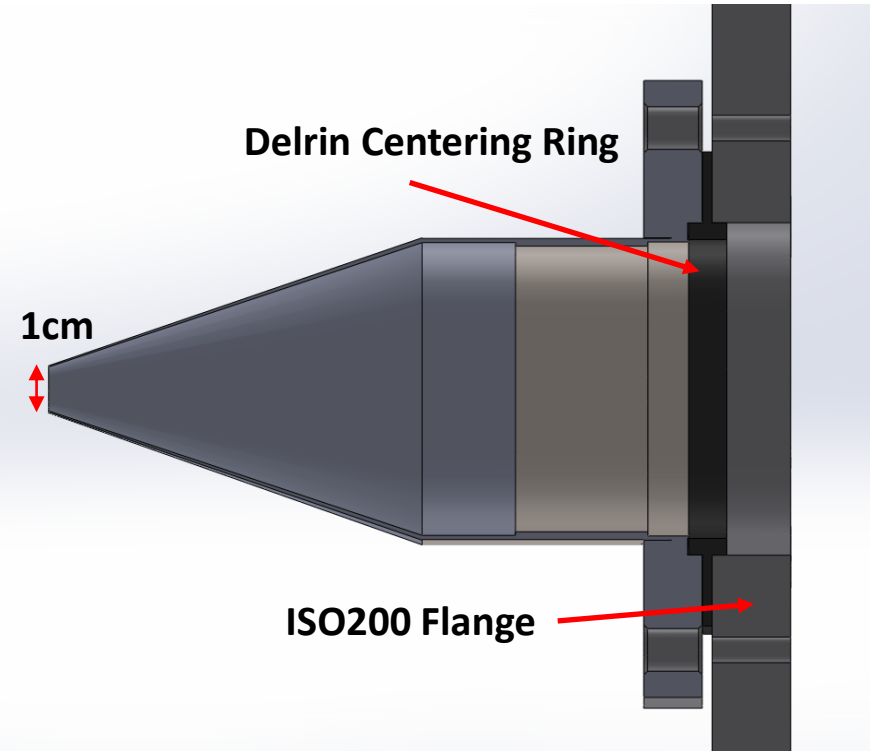

Figure II.3.4-2: Source Skimmer Assembly Cross Sectional View

Quadrupole Ion Guide Assembly: (Figure II.3.4-3) The quad is manufactured from 0.5"Ø and mounted to have an inscribed radius of 0.25". The rods are bolted radially to Ultem rings near the ends and at the middle of the rods to assure straightness and relative rod alignment. These Ultem holders are then attached radially to a vented shroud, which provides support for the length of the guide and alignment along the beam axis. The shroud is welded into a 3.375"CF flange. There is a 19° taper on the end of the rods allowing them to be inserted deep into the skimmer, thereby

reducing fringe field effects and allowing the ion to enter the guide earlier in their transport, which increases transport efficiency. Voltages are applied to the rods via the bolts that hold them to the Ultem, with the opposite pairs connected.

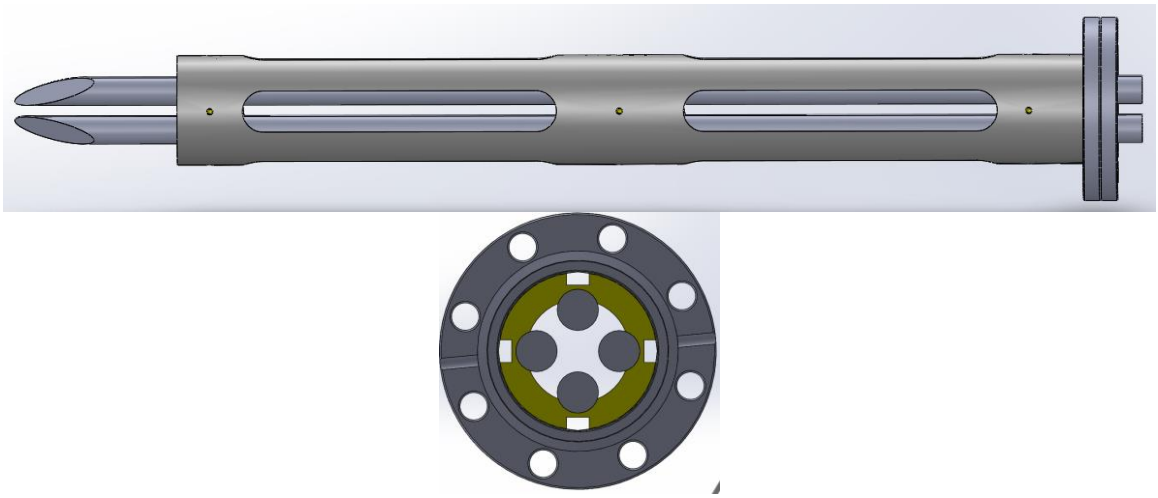

Figure II.3.4-3: Quadrupole Assembly (Yellow is Ultem)

Figure II.3.4-4: Quadrupole Mounted in Chamber (Radial Feedthrough Mounting flange on far right)

Octopole Ion Guide Assembly: (**Figure II.3.4-6**) There are multiple octopoles in the instrument with the only difference being their length and one of them being mounted on a different flange for the electrostatic bender.

The octopoles are made from 3/16” rods with an inscribed radius of 9/32”. The rods are then mounted on holders that bolt radially to every other rod. These holders are then each bolted to a separate Ultem holder. This creates an assembly where each set of rods is bolted to its own metal holder but attached to the same Ultem holder. Voltages can be applied to the metal holders in order to apply each phase of the RF to its respective rod set while remaining electrically isolated from the other set. (**Figure II.3.4-5**)

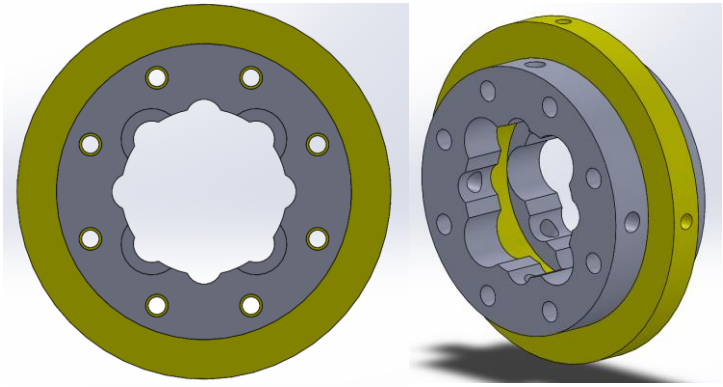

Figure II.3.4-5: Octopole Rod Holders (Yellow is Ultem)

The Ultem holder is then bolted radially to a shroud that provides structural support. This shroud is then welded into a 3.375”CF flange.

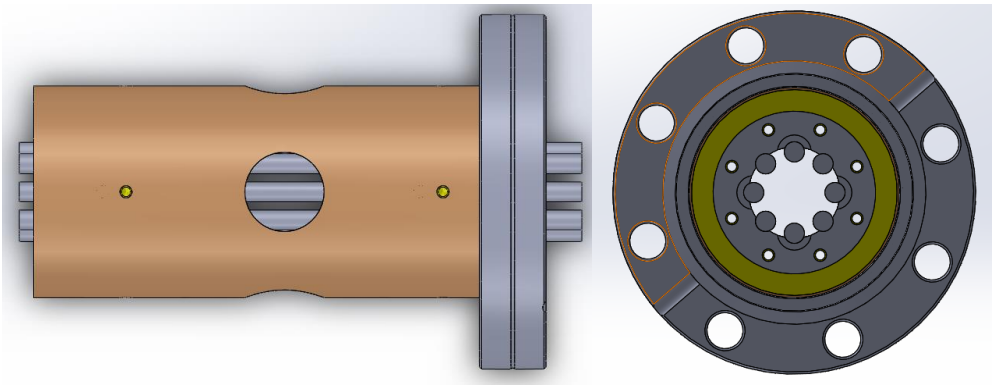

Figure II.3.4-6: Octopole Assembly of 2nd Octopole

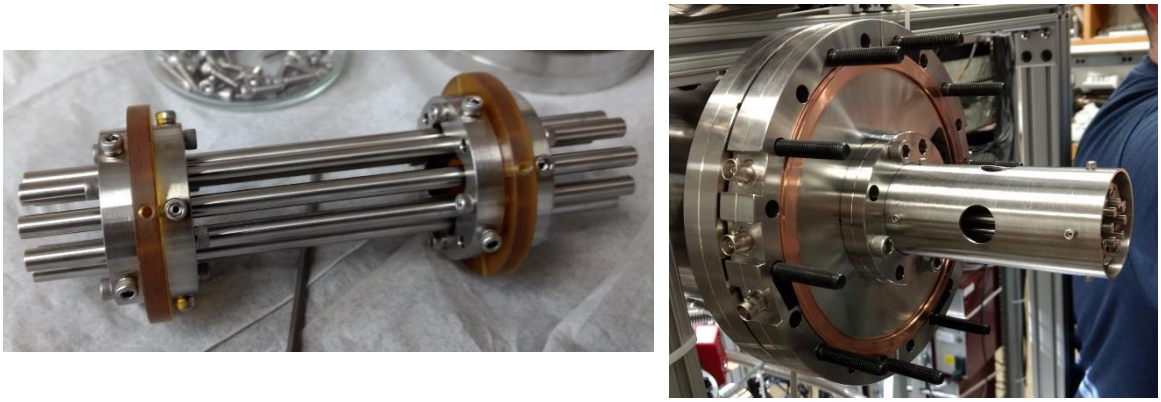

Figure II.3.4-7: Octopole Assembled and Mounted on Flange

Thin Apertures and Small Skimmer: Between each chamber is a floatable aperture. These allow for differential pumping and ion focusing between the chambers. There are two versions: a thin aperture and a small skimmer. The thin aperture is a thin 0.01" plate with a 1cmØ hole centered on it. (**Figure II.3.4-8**) The small skimmer has a tapered 1cmØ hole. Both have a bolt pattern used to attach them to their mounts.

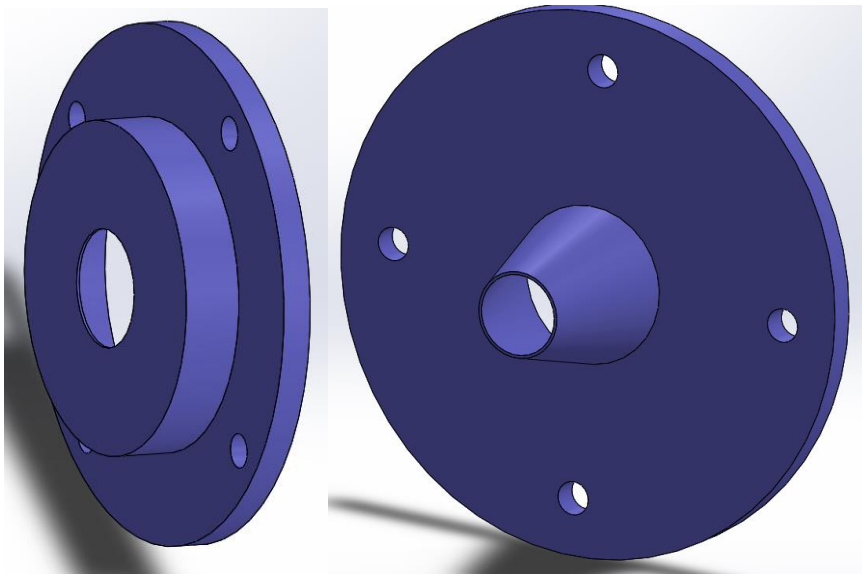

Figure II.3.4-8: Thin Aperture and Small Skimmer

Ion Guide Flange Mounts with Radial Feedthroughs: (**Figure II.3.4-9**) The guide assemblies and floated apertures are mounted onto double-sided CF flanges placed between the chambers.

These flanges contain matched MHV radial feedthroughs that allow for voltage to be applied to the guides and apertures. There is a center bored hole that allows the apertures to be attached with a centered bolt pattern via Teflon screws and a 0.01” thick Teflon ring for isolation. Around that is another centered bolt pattern corresponding to the bolt pattern of a 3.375”CF flange where the guide assemblies are attached. These flanges can either hold one guide on one side or two guides on each side. They also are manufactured on both 10”CF and 8”CF.

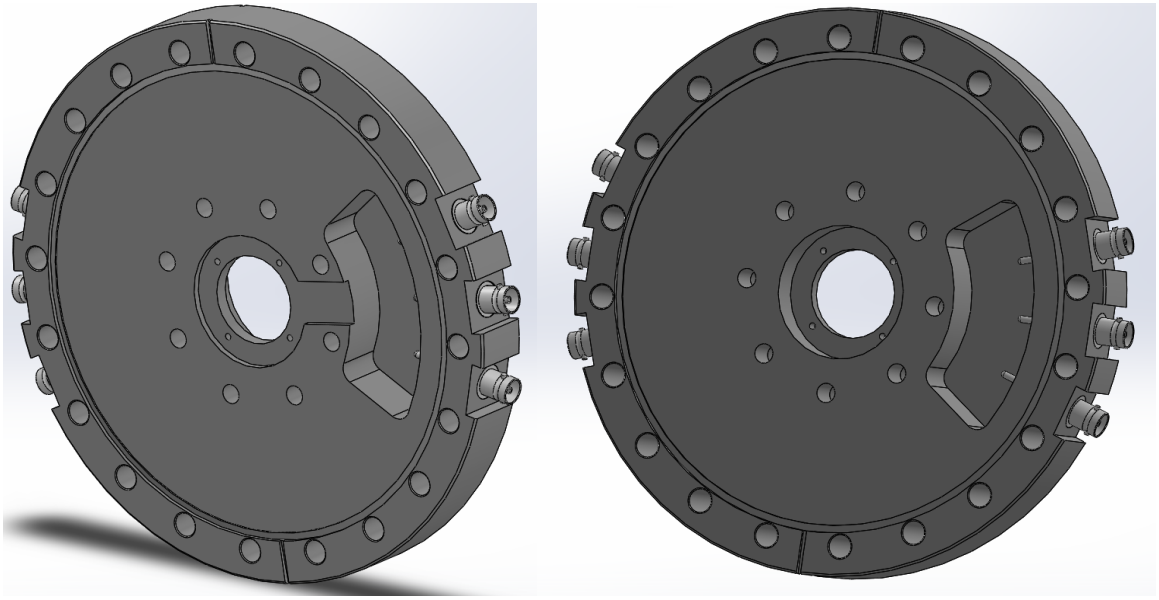

Figure II.3.4-9: 8"CF Double Ion Guide Flange (Front and Back)

Figure II.3.4-10: 8"CF Double Ion Guide Flange with Aperture and no Guides (Front and Back)

Electrostatic bender Assembly: The electrostatic bender assembly consists of six optics mounted on a grounded box formed via plates, with the box preventing RF from interfering with the bender. Four of the optics are the apertures which consist of plates with a 1cmØ ID tube and a bolt pattern. These bolt into the sides of the housing via Teflon bolts with a 0.01" thick Teflon ring isolating them from the housing, with the bore being made so that with the Teflon the plate faces are coincident with the face of the housing. The tubes stick into the bender housing deep enough to prevent fringe fields generated by the edge of the bender rods from interfering with the ion beam. (**Figure II.3.4-11**)

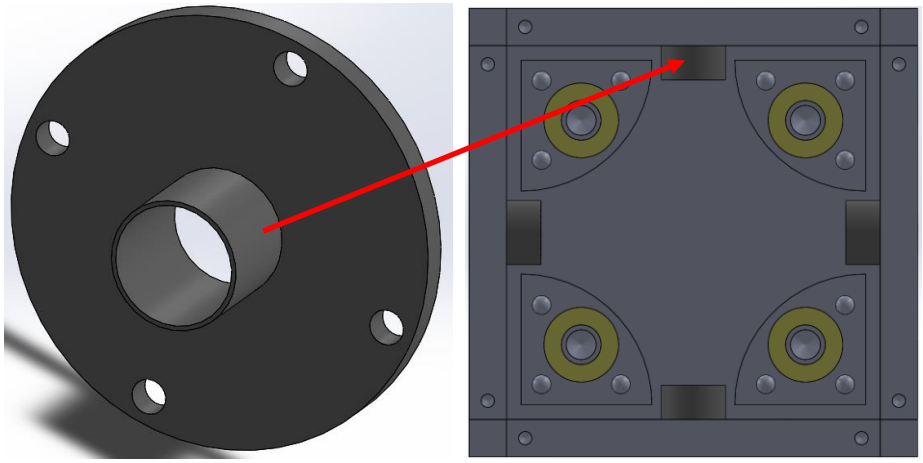

Figure II.3.4-11: Bender Apertures

The other two optics are the bender rod pairs. The rods are 1"Ø rod sectors spaced apart from one another with a 0.58" inscribed radius for an ideal quadrupolar field.[5,6,7] The alignment and the isolation of the rods are performed by the same feature. In the top and bottom of each rod sector is a triangle pattern of vented holes matching up to the same pattern of holes on the top and bottom plate of the housing. Precision ground 0.125" ruby balls are placed in these holes allowing the plate and rod to come together only if the holes on the plate and rod are aligned. A vented bolt is brought through an Ultem isolator in the plates to thread into the rod holding the plate and rod

together and creating a place where voltage can be passed through the housing to the rod. (**Figure II.3.4-12**)

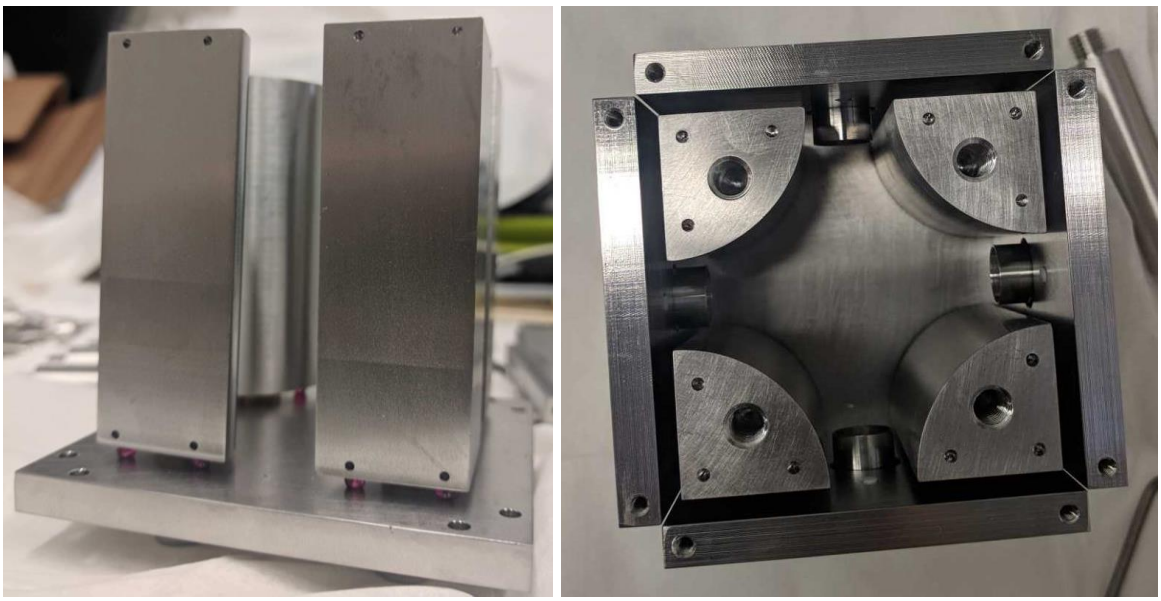

Figure II.3.4-12: Electrostatic bender Rod Alignment

The housing is then center mounted on a rotatable flange via rods cut to a precision length thereby centering the bender on the chamber and making rotation the only axis of alignment a user needs to perform. On the other side, an octopole ion guide is mounted to the bender with 0.05" spacing between the beginning of the rods and the output bender aperture. The flange contains a 6-pin feedthrough for the bender voltages as well as a 2-MHV feedthrough for the guide. (**Figure II.3.4-13**)

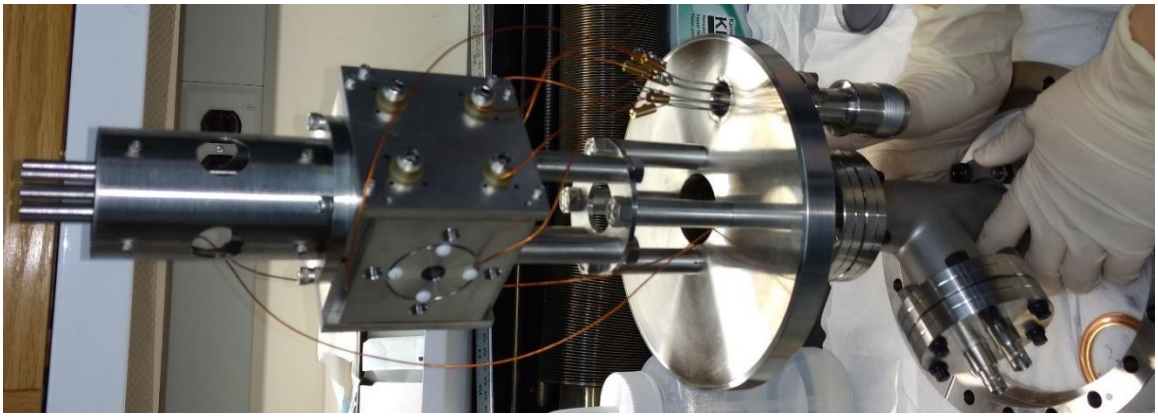

Figure II.3.4-13: Bender Assembly

II.3.5 Ion Optics by Chamber

This is a list of the ion optics by chamber. (**Figure II.3.4-1**)

Source Chamber: (**Figure II.3.5-1**) The source chamber contains two optics. The large skimmer sticks into the chamber 5” with its mounting flange held between the source chamber and ch1. The quadrupole tapered end sits inside the skimmer spaced by 0.05”. This spacing reduces the fringe fields from the quad and allows the ions to get into the guide sooner thereby improving ion transport.

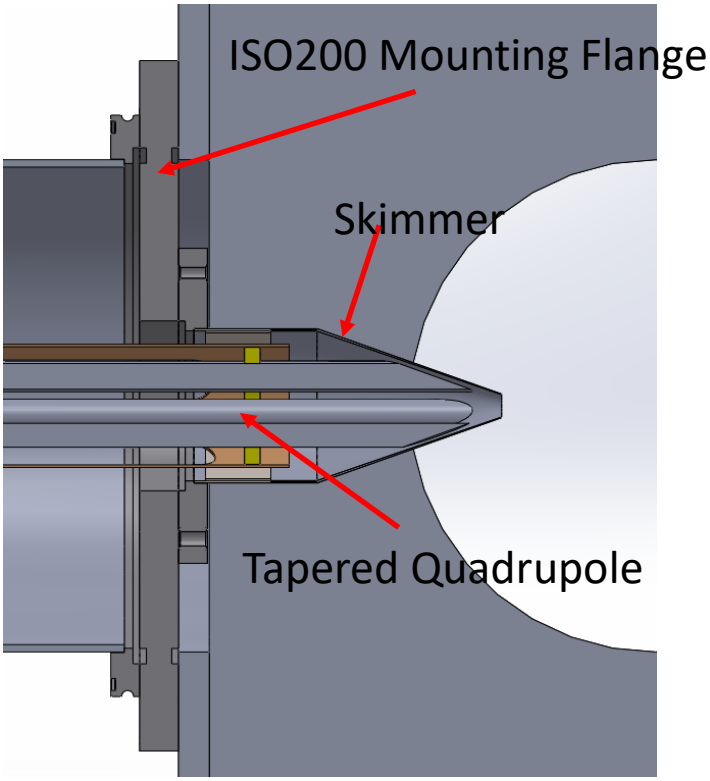

Figure II.3.5-1: Source Chamber Optics Schematics

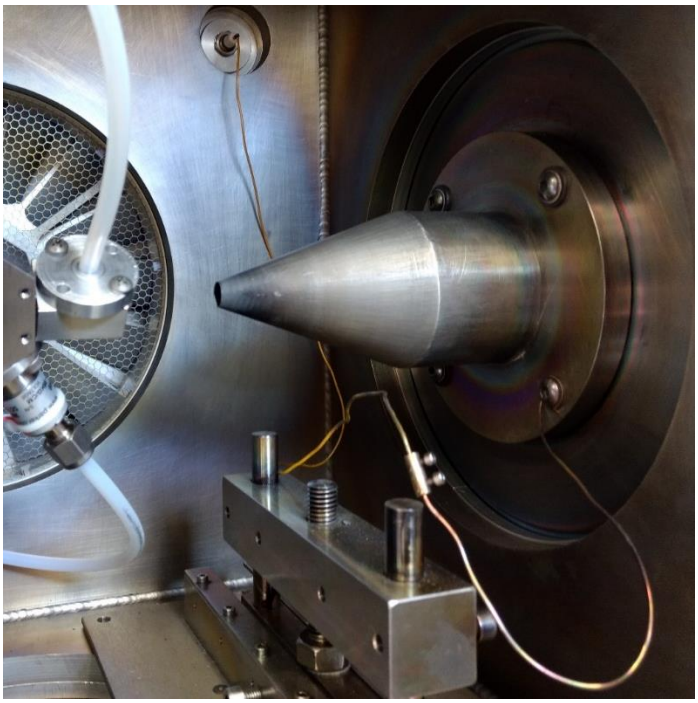

Figure II.3.5-2: Source Chamber Skimmer in Place

Ch1 Optics: (**Figure II.3.5-3**) Ch1 contains the quadrupole mounted on a dual ion guide flange between ch1 and ch2. A small skimmer mounted on the flange sticks into the quad with 0.05" clearance thereby removing fringe fields.

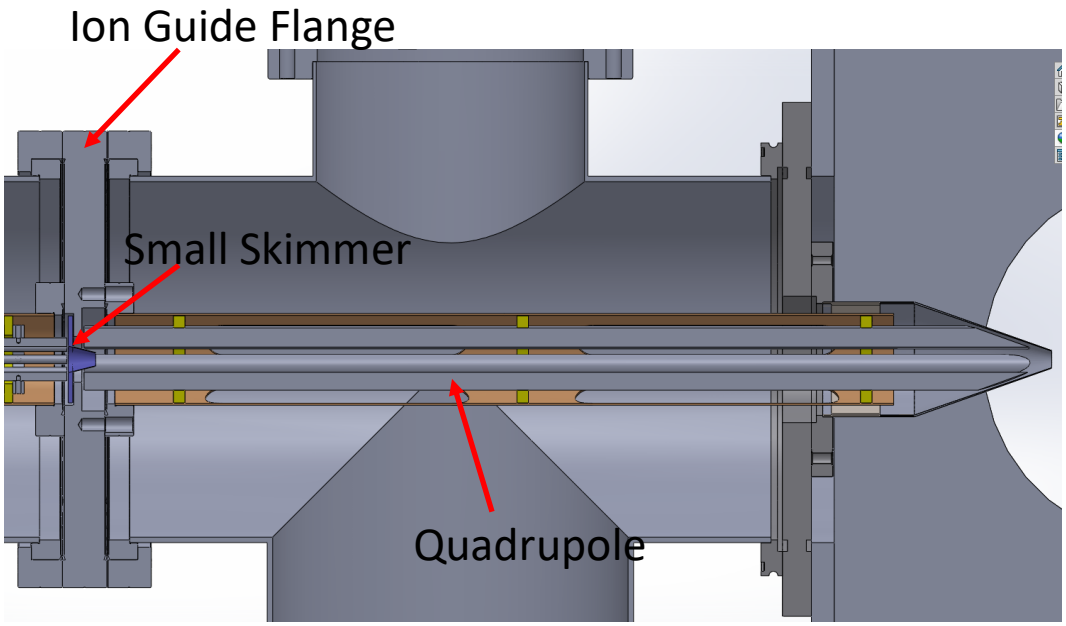

Figure II.3.5-3: Ch1 Optics (Ion Guide Flange holds the Quad and Ch2's Octopole) Also see Figure II.3.4-4.

Figure II.3.5-4: Small Skimmer Seen from Ch2 Side with Octopole Removed.

Ch2 Optics: (**Figure II.3.5-5**) Ch2 contains the first octopole guide. This guide is mounted on the source side flange with its rods being spaced out 0.05” from the back of the small skimmer. On its other end it approaches the entrance of a thin aperture between ch2 and ch3 with 0.05” spacing.

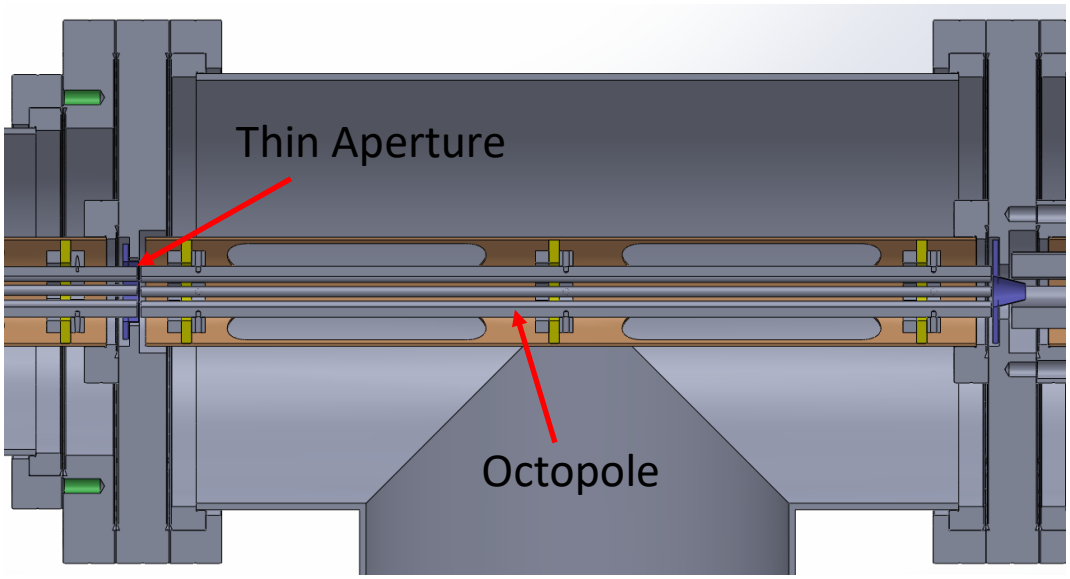

Figure II.3.5-5: Ch2 Optics Schematic

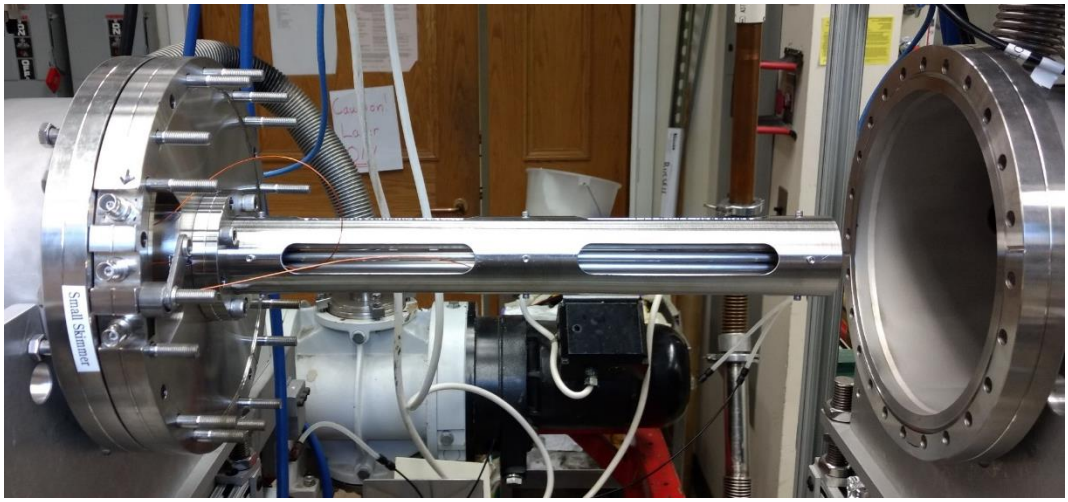

Figure II.3.5-6: Ch2 Octopole with Chamber pulled back.

Ch3 (Bender Chamber) Optics: (**Figure II.3.5-7**) Ch3 has four optics. Between ch2 and ch3 is a single ion guide flange that holds a guide going between the ch2 aperture and the entrance of the bender, both of which are 0.05" from the end of the guide. The bender and its output octopole are center mounted in this chamber. Between this chamber and the next is the thin-GV. When open, the gate is 0.05" from the end of the bender-mounted octopole.

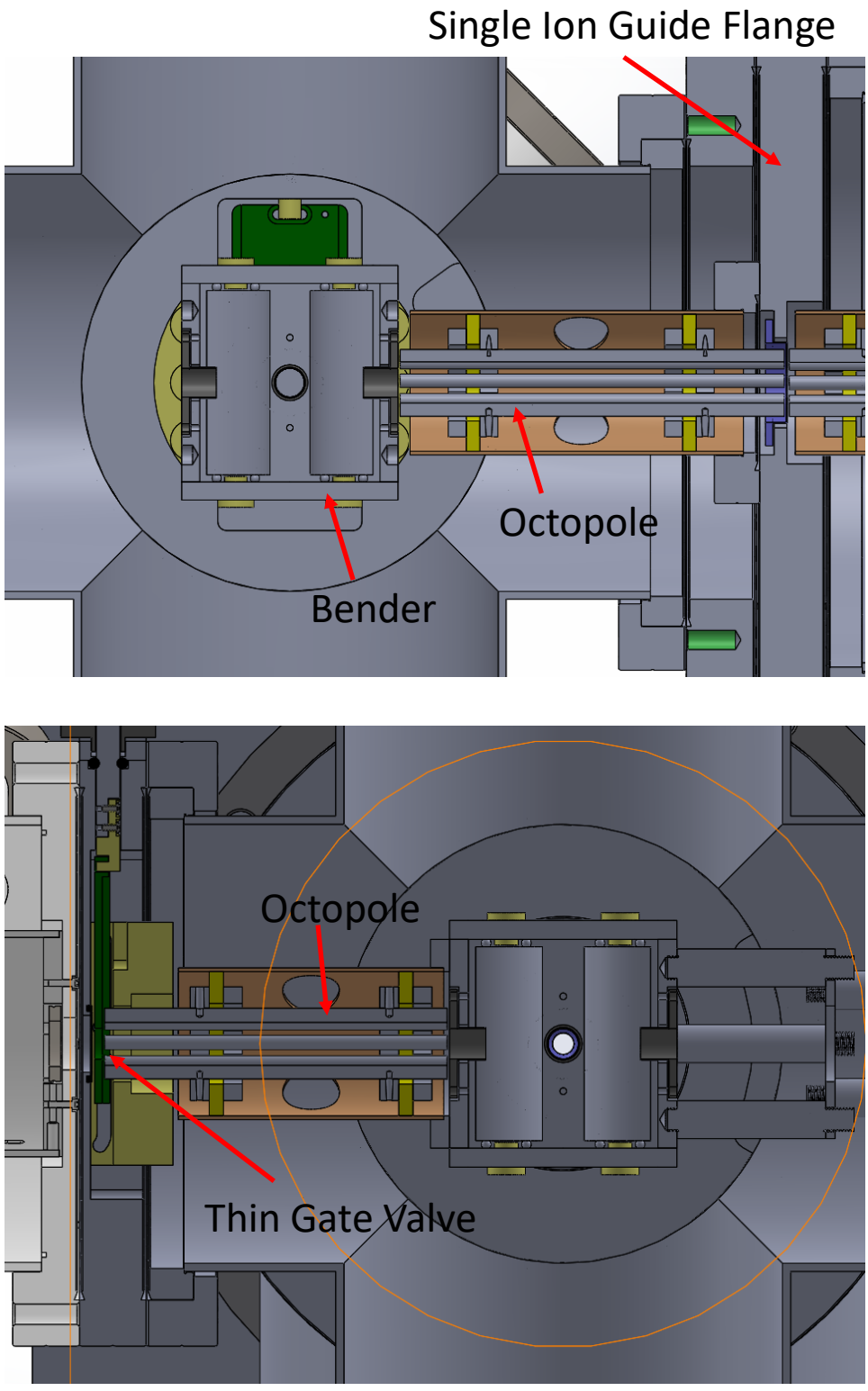

Figure II.3.5-7: Ch3 Optics Bender Inlet (Top) and Outlet (Bottom). Also see Figure II.3.4-13.

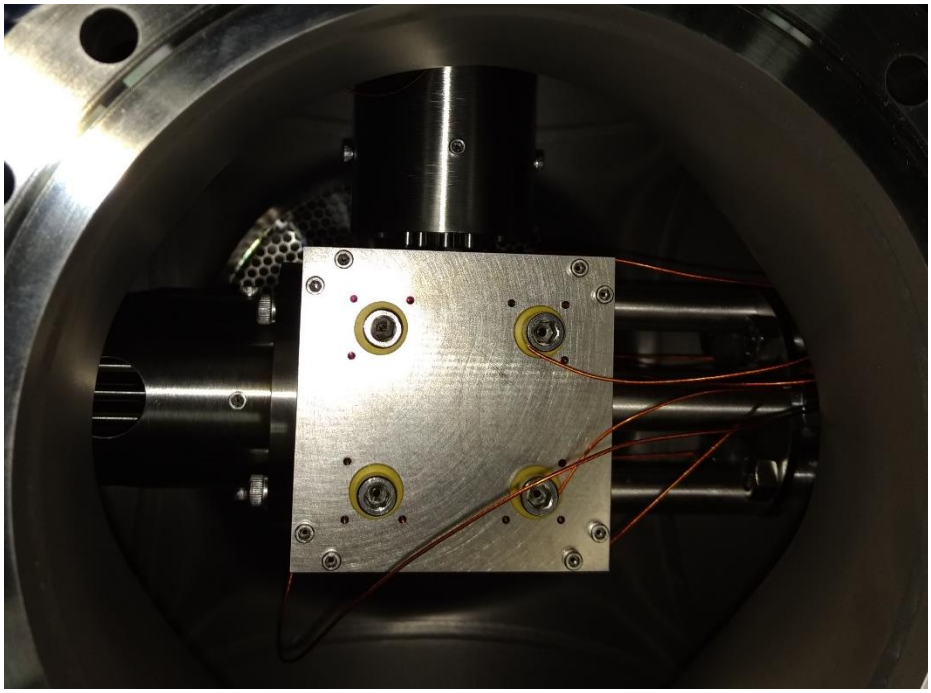

Figure II.3.5-8: Bender from Above

Ch4 (QMS Chamber) Optics: (**Figure II.3.5-9**) The beginning of this chamber is the flange mounted QMS that sticks about 75% of the way into the chamber. The QMS has an input lens and an output lens, and the thin-GV also aids with focusing into the QMS. The QMS housing has radially mounted feedthroughs for the rod voltages and lens voltages to be applied. On the other end of the chamber is the last dual guide mounting flange that holds an octopole that extends to the output of the QMS with 0.05" spacing and at the other end is spaced 0.05" from the last thin aperture.

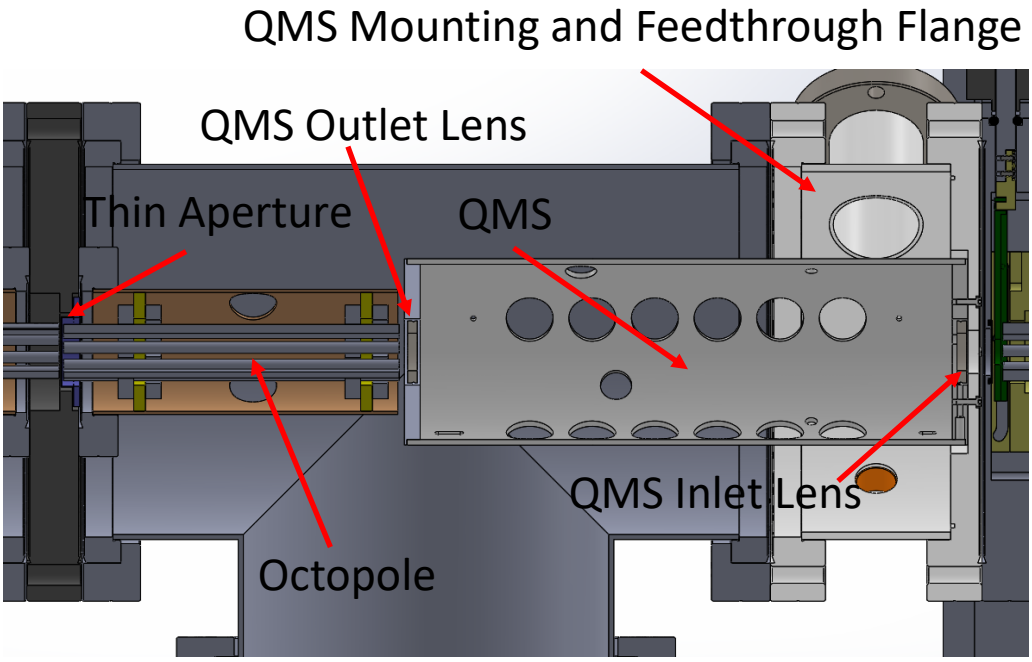

Figure II.3.5-9: Ch4 Optics. Also see Figure II.3.4-7.

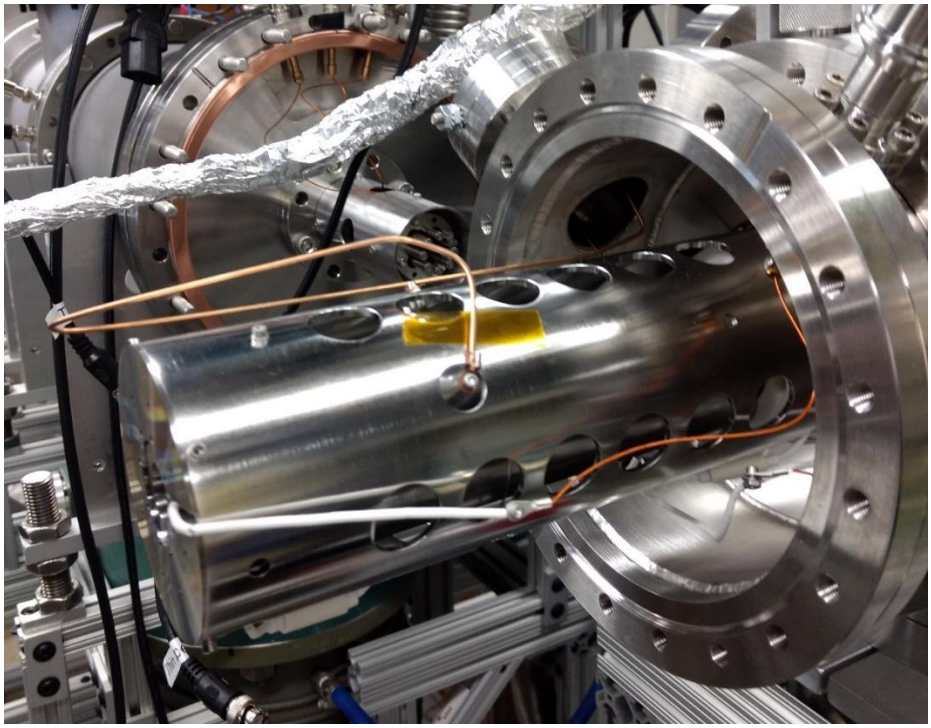

Figure II.3.5-10: QMS on Flange

Ch5 (Deposition Chamber) Optics: (**Figure II.3.5-11**) This is the last chamber and it contains an ion guide extending to near the center of the deposition chamber with an electrostatic lens assembly attached to its end for focusing the ion beam onto the surface of the substrate.

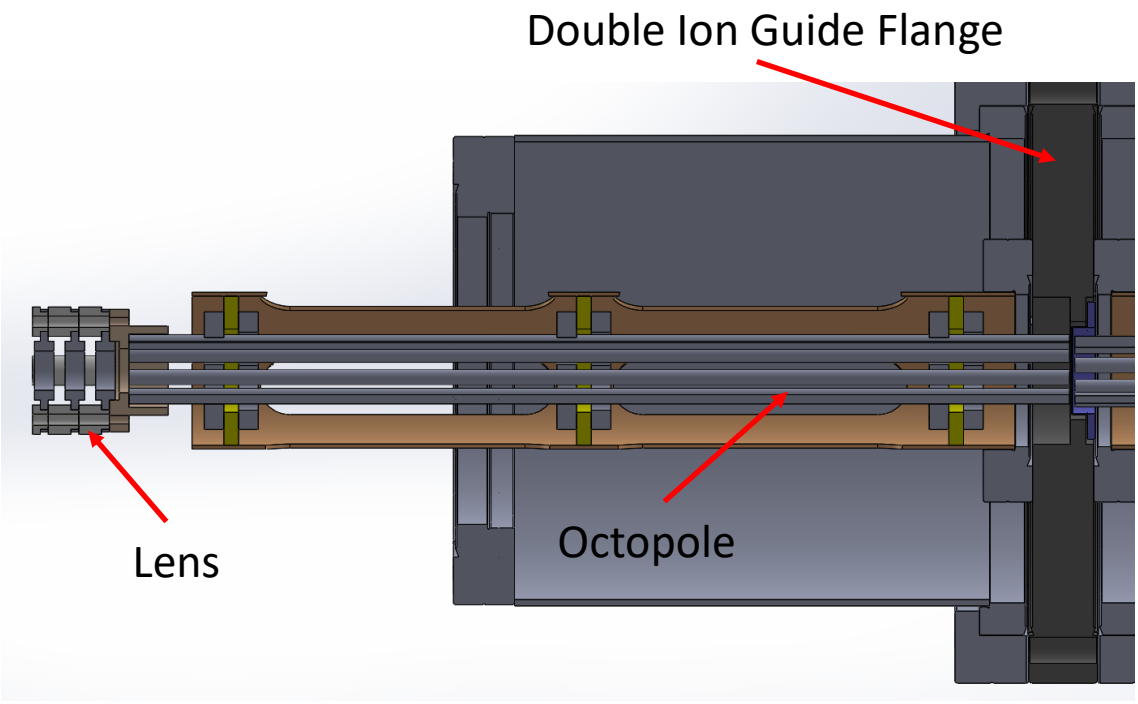

Figure II.3.5-11: Ch5 Optics

II.3.6 Ion Optic Voltage Generation

The voltages used in the instrument consist of a combination of RF and DC voltages. The RF is applied exclusively to ion guides while the DC is used to float every optic, including the guides. The RF is generated by an RF power supply developed by Scott Anderson at the University of Utah.[9] These supplies are cheap to make but require a high voltage and high wattage power supply to run. (500V, 50+W) These supplies have an RF chocked input where a DC float can be applied to the output of the supply without feeding any RF back into the DC power supply. (**See Appendix B**) This allows for the guides to be floated to a DC voltage as well as have their RF.

The DC voltages are generated by a home-built voltage divider box capable of outputting -48 to +148V using 14 individually adjustable outputs. A separate home-built power supply is used for the bender. The bender power supply has 6 individually adjustable outputs of ±250V that are floatable to ±100V. This allows the bender to operate independent of the axial voltage the beam feels. (**See Appendix B**)

---

[1] I. Bozsik, I. Hofmann, Nuclear Instruments and Methods, 1981, **187**, 305.

[2] S. Earnshaw, Trans. Camb. Phil. Soc, 1842, **7**, 97.

[3] D. Gerlich, "Inhomogeneous RF Fields: A Versatile Tool for the Study of Processes with Slow Ions," John Wiley & Sons Inc., 1992.

[4] Mass Spec Pro, Multipole Ion Guides, http://www.massspecpro.com/technology/ion-optics/multipole-ion-guide, Accessed 2019.

[5] J. W. Farley, Rev. Sci. Instrum., 1985, **56**, 1834.

[6] H. D. Zeman, Rev. Sci. Instrum., 1977, **48**, 1079.

[7] B. Elger, T. Schmidt, S. Krähling, F. Neuberger, R. Schäfer, Rev. Sci. Instrum., 2017, **88**, 063303.

[8] J. L. Pittman, P. A. A. O'Connor, J. Am. Soc. Mass Spectrom., 2005, **16**, 441-445.

[9] R. M. Jones, S. L. Anderson, Rev. Sci. Instrum., 2000, **71**, 4335.

II.4 Vacuum System

Both the beamline and the analytical work are done under UHV conditions. This prevents the beam from scattering off of or reacting with gas molecules in the chambers. On the analytical side many of the techniques involve measuring electron kinetic energies and any inelastic scattering of these electrons will affect measurement accuracy, and the sample itself needs to be kept isolated as clusters are very reactive and oxidize readily in the presence of O_2 or H_2O.

This vacuum is maintained by a series of UHV pumps that are either diffusion pumps or turbomolecular pumps. The diffusion pumps are installed closer to the source side of the instrument as they are oil based and inherently "dirty" since they slowly coat everything in their chamber with oil, however they have a very large pumping speed capable of handling the gas load from the source, specifically the helium used in all of the sources. The QMS and analytical side of the instrument are exclusively turbo pumps, which are oil free and capable of handling the occasional gas load brought about by dosing a reactant.

Neither diffusion nor turbo pumps are capable of compressing gas to atm, so they must be backed by a pump that can. The source side of the instrument is backed by oil pumps, while the analytics are backed by a low speed oil free scroll pump thereby preventing oil contamination. The chamber pressure drops in each consecutive chamber due to differential pumping.

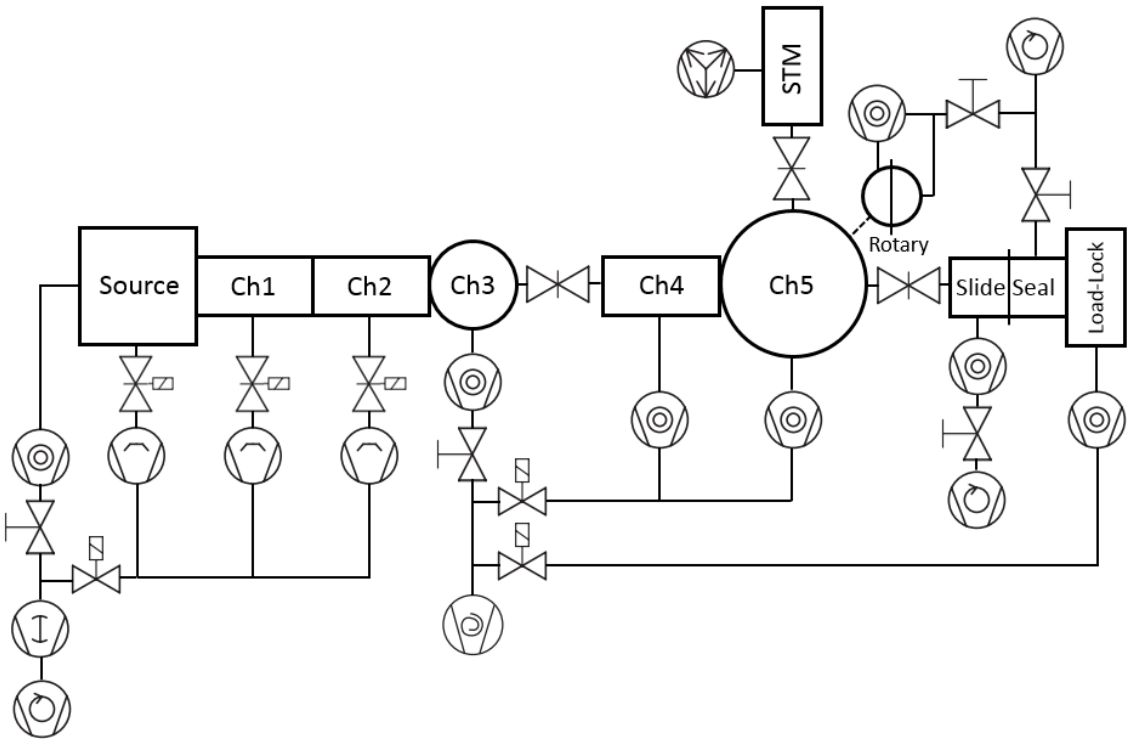

Figure II.3.6-1: Instrument Pumping

II.4.1 Chambers and Pumps

Source Chamber: This chamber has the highest gas load and that is considered in its design. This chamber is pumped by either a Pfeiffer TPU1201 P turbo pump (1250 l/s helium) or a Varian VHS-10 diffusion pump (5200 l/s helium). The VHS-10 can be isolated from the chamber via an interlocked, pneumatic gate valve.

The choice of pump depends on the pressure in the chamber. While the diffusion pump has a higher nominal pumping speed, the speed of a pump is pressure dependent, and this speed drops to near zero around $5*10^{-3}$ torr. At that point diffusion pump oil gets pulled into the chamber. The turbo pump however maintains a large pumping speed into the high single digit torr regime.

Experimentally, both the magnetron and the LVS source have run in the 1-50 mtorr range making the turbo pump the most used pump. Both pumps maintain a base pressure in the 10^{-8} torr.

Ch1: This chamber is pumped by a Varian VHS-6 diffusion pump. (2000 l/s helium) Due to differential pumping, this chamber runs at $1*10^{-4}$ to $2*10^{-3}$ torr while having a base pressure of 10^{-8} torr.

The gas density inside the quadrupole of this chamber is higher than the pressure in the surrounding chamber volume, due to the quadrupole being in line with the aperture to the source chamber. This is important as it allows for collisional focusing as described in the ion guide section.

Ch2: This chamber is pumped by a Varian VHS-6 diffusion pump (2000 l/s helium). Due to differential pumping, this chamber runs at $1*10^{-6}$ to $1*10^{-5}$ torr while having a base pressure of 10^{-8} torr.

Foreline of Source, ch1, and ch2: These three chambers share a foreline pumped on by a Pfeiffer WPK-500-A roots blower (490 m^3/h), which in turn is backed by a Alcatel 2063 direct drive (50 CFM). The roots blower is used because it has higher throughput capabilities at the pressures the instrument runs at. The roots blower input is connected in parallel between the four UHV pumps with a pneumatic valve between the pump and the three diffusion pumps as part of the vacuum interlock and a manual valve to the turbo.

Ch3 (Bender): This chamber is pumped on by a Pfeiffer HiPace 700 (655 l/s helium). The chamber operates in the 10^{-7} torr regime with a base pressure in 10^{-8} torr.

Ch4 (QMS): This chamber is pumped on by a Pfeiffer HiPace 700 (655 l/s helium). The chamber operates in the $10^{-(8-9)}$ torr regime with a base pressure in high 10^{-10} torr.

Ch5 (Deposition): This chamber is pumped on by a Pfeiffer HiPace 300 (255 l/s helium). The chamber operates in the 10^{-9} torr regime with a base pressure in the high 10^{-10} torr.

Load-Lock Chamber: This chamber is pumped on by a Pfeiffer HiPace 80 (58 l/s helium). The chamber has a base pressure of the high 10^{-8} torr.

Foreline of ch3, ch4, ch5, and Load-lock: These pumps are backed by an Edwards XDS5 scroll pump (4 CFM). This is an oil free pump for vacuum cleanliness. There are two pneumatic valves on this foreline as part of the vacuum interlock: one before the HiPace 80 and another before ch4 and ch5's turbos. The ch3 turbo has a manual valve between it and the scroll pump.

Rotary Flange: The rotary manipulator for the sample has two stages of differential pumping to prevent leaking during motion. The inner stage requires 2 l/s at 10^{-6} torr pumping and this is performed with a Pfeiffer HiPace 30. The foreline of this turbo and the outer differential are pumped on by a Precision Scientific 10985 direct drive (20 CFM), which, after accounting for the length of bellows, provides the >1.6 cfm pumping speed at pressures <10mtorr required for the outer region pumping.

STM Chamber: This chamber is pumped on by a 250 l/s ion pump and maintains a base pressure of high 10^{-10} torr.

II.4.2 Vacuum Interlock

The entire vacuum system is interlocked to prevent damage to pumps, ensure vacuum cleanliness, and allow full bleed to atm on the source side of the apparatus. The interlock is separated into two sections; before and after thin-GV. (For full explanation of the mechanics of the interlock see **Appendix C**)

Before the thin-GV, the major concern is the three diffusion pumps, as the source and ch3 turbo pumps have their own built-in protections. The conditions monitored by this section of the interlock include diffusion pump foreline pressure (<500mtorr, Edwards APG100), diffusion pump temperature (monitored by calibrated overheat switch), diffusion pump cooling water flow (via calibrated flow meter on water lines), and power loss. If any of these conditions are manifest, the diffusion pumps shut off, the gate valves close, and the diffusion pump's foreline valve shuts, thereby isolating the diffusion pumps.

After the thin-GV, there are only turbo pumps and their oil free backing pump. The pumps included is this part of the interlock are the ch4, ch5, and load-lock chamber's turbo pumps. This part of the interlock is not for protecting the pumps, as they have built-in protections, but rather for protecting the vacuum. If there is a loss of power, or the foreline pressure raises too high (caused by failure of backing pump), the foreline valves of these pumps shut. In the case of lost power, the turbos will eventually spin down and the chamber will leak into the low mtorr regime over the span of a few hours. This is better than leaking to atm, as once the problem is fixed the pump time back to 10^{-10} torr is a week or two less starting from the mtorr regime than from atm. If the backing pump fails, but power is maintained, the turbos will continue to spin and due to the low leak rate into the chambers and the high compression ratio of turbo pumps, the UHV conditions will be maintained for theoretically days, allowing for a user to fix or replace the backing pump.

II.4.3 Chamber Rail System

The chambers are mounted on two pairs of parallel rails, with each pair offset 90° from one another corresponding to before and after the electrostatic bender. This allows for the chambers to be moved away from each other when they are disconnected. This was implemented for two reasons; 1) On axis "sandwich" flange mounted optics are easier to take apart when the chambers can separate with chamber alignment being conserved while doing so. 2) The ion guides fill the length of the chambers with 0.05" tolerance making it only possible to insert or remove them axially.

These rails are made of precision ground hardened stainless steel and coupled to the chambers with precision bearings all produced by Thomson Linear. The rails are attached to the stand made from 80/20 extruded aluminum.

II.5 Deposition and Analytics

After the ions have been mass-selected, they are then deposited onto a surface where further studies of their composition and reactivity can be performed. By combining multiple techniques, a given system can be studied thoroughly. Ideally, this range of techniques can be used on a single sample in order to ensure the relative accuracy of the studies and to remove the need to deposit multiple samples, which is the most time-consuming part of an experiment. This is accomplished via a chamber with multiple techniques mounted on it and a sample holder that can be moved *in-vacuo* between these different techniques. (**Figure II.4.3-1**)

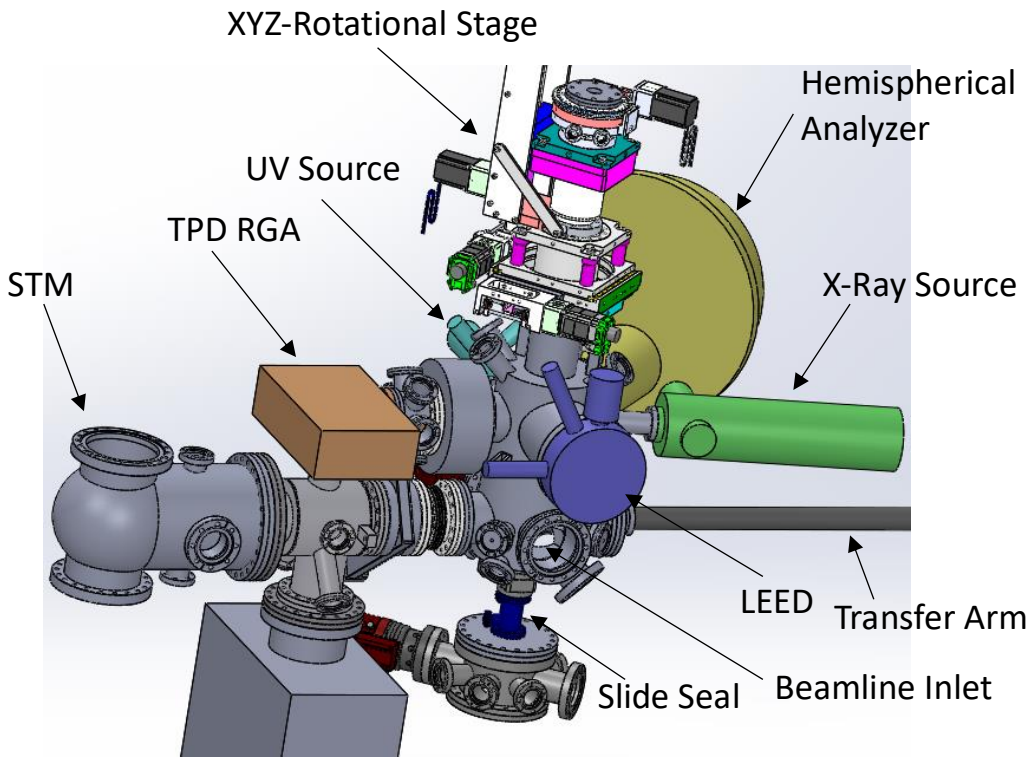

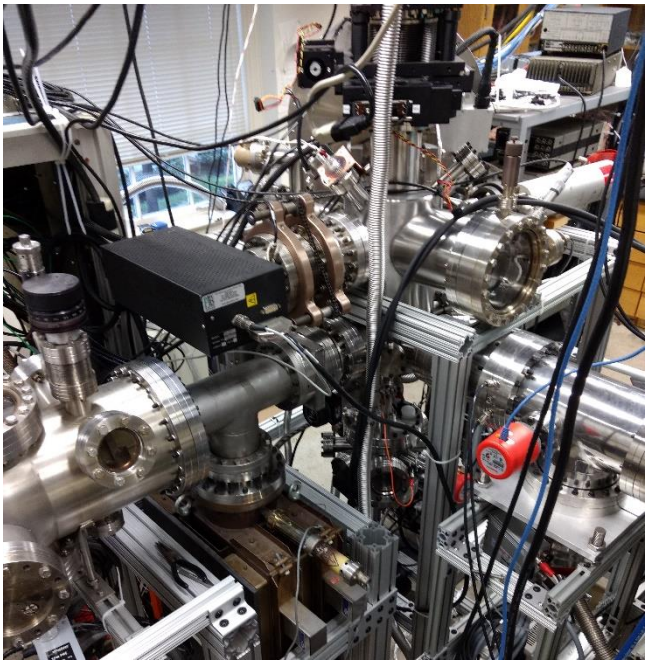

Figure II.4.3-1: Deposition and Analytics

The amount of clusters deposited can be determined via an electrometer. This allows for a user to determine when they have deposited enough clusters and to ensure that experiments are repeatable and comparable to each other if a comparison experiment is performed. If a conductive sample is connected via vacuum feedthrough to an electrometer, when the ion interacts with the sample it will give up its charge to the sample, which is measured as current by the electrometer.

Current is measured in amperes which is equivalent to Coulombs per second (C/s), and, by using the relationship between coulomb and number of electrons, the number of electrons per second can be determined. Programmatically, the amount of time between each measurement can be determined, and therefore the number of electrons given to the sample can be determined.

The charge of the clusters can be determined via the QMS, as it filters by *m*/*z*.

$$\#\ of\ Clusters = (6.242 * 10^{18})\frac{I * t}{z}$$

Equation 23

II.5.1 Sample Holder and Current Measurements

The sample holder consists of a 48” long tube (1.375” OD, 1.175” ID, <0°10’ deviation from straight) welded normal to the vacuum side of a 4.5”CF flange. At the end of this rod is a 1.33”CF half nipple. The bottom 9” is mirror polished to <0.15μm average roughness, R_A. Mounted to the 1.33”CF flange is an inverted 2-pin power/thermocouple feedthrough (Kurt J Lesker Part#: TFT1KY2C302). The sample is mounted between the two power pins, and a K-type thermocouple is spring loaded to the sample’s back. Inside the tube, Teflon-insulated 10 AWG copper wire connects to the power pins of the feedthrough, while a Teflon-coated K-type thermocouple wire pair connects to the thermocouple feedthrough. Surrounding these wires is a 1” ID tinned copper braid isolated from the walls of the tube by a 1.125” OD 1/16” thick Teflon tube. These wires and braid continue up and out of the 48” long tube.

This holder’s 4.5”CF flange is bolted to the chamber through a 360° rotational stage, which is mounted on a 30” travel linear manipulator sitting on top of a 2” xy-manipulator. (McAllister Technical Services) This setup allows for the sample to be moved anywhere in the chamber. These manipulators are moved via stepper-motors controlled via RS-432 SERIAL. (**Figure II.5.1-1**)

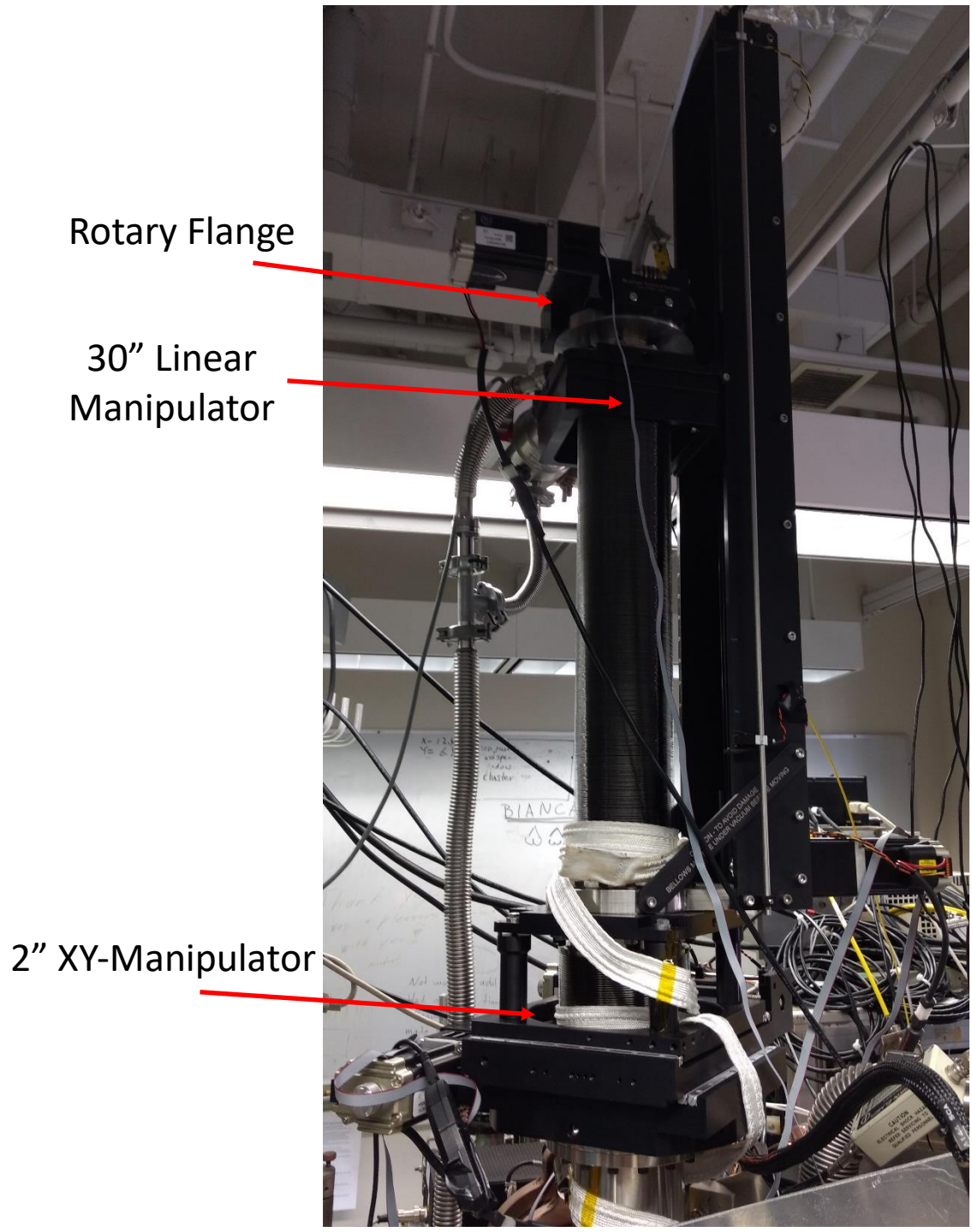

Figure II.5.1-1: Sample Manipulators

The sample can be heated via resistive heating by applying a current across the power leads, while the temperature is monitored by the thermocouple. The electrometer can be hooked up to one

of the power leads in order to measure the current on the sample. By filling the tube with liquid nitrogen on the atm side, the sample can be cooled via conduction through the power leads to near -170°C.

The reason for the isolated copper braid is for shielding purposes. It is desirable to float the sample during deposition in order to slow the ions down for soft landing (<1eV), as this prevents the clusters from falling apart upon landing. To pull this off and still be able to measure current with the electrometer, the electrometer must be floated as well. The Keithley 6514 electrometer is designed to be floated. The setup involves a triaxial output with a floated guard and a 1Hz Low Pass RC filter (2200pF, 75kΩ) for noise reduction. In this case the braid and sample are floated to the float voltage. (**Figure II.5.1-2**)

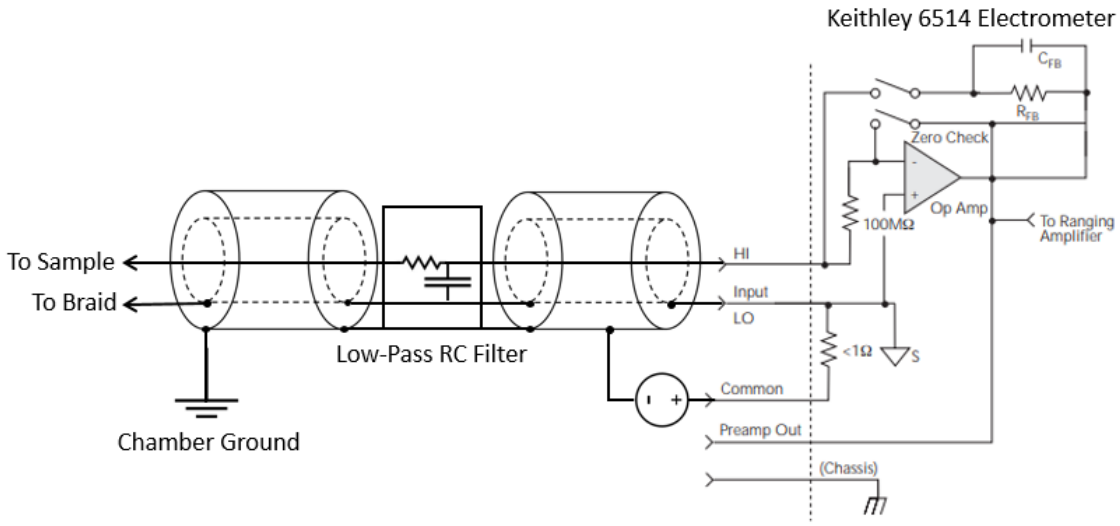

Figure II.5.1-2: Electrometer Circuit

II.5.2 Slide Seal

It is ideal that the deposition chamber be bled to atm rarely due to the length of time required to pump back down to operating pressure. This means the sample needs to be changed without breaking vacuum. Traditionally this has been done either with a transfer arm or with a load-

lock chamber, where the sample is raised into a load-lock region at the manipulator side that can be separated from the UHV chamber via a gate valve.

The transfer arm is not ideal in this application, as it would require a larger sample holder to make room for the clipping mechanism that holds the sample in and allows for transfer. This larger sample holder would contribute background noise to our TPD/R studies (**II.5.4**) as reactant or product gases come off of the holder rather than the sample.

The load-lock region located at the top of the manipulation system is non ideal as well, as the manipulator system is the source of the largest surface area in the deposition chamber due to the edge-welded bellows that allow for the motion of the manipulator. If this is bled to atm, the pump down would be long as well due to residual gas from the surfaces of the bellows. While this can be mitigated via baking or bleeding with nitrogen, ideally the load-lock region would be isolatable from the deposition chamber, which is not possible at the manipulator side of the instrument, as the sample rod has to pass through there and prevents the closing of a gate-valve.

The solution found was to have the load-lock at the bottom of the chamber with differentially pumped O-ring seals, sealed against the sample holder tube, used to maintain vacuum in the deposition chamber as the load-lock is bled to atm. The sample can then be accessed through a quick-access door on the bottom chamber. After the sample work is completed, the load-lock chamber is then pumped out ($2*10^{-7}$ torr in 15 minutes) and the sample holder is raised back to the deposition chamber, and a gate-valve is shut between the two chambers removing the need for the load-lock chamber to attain the same vacuum has the deposition chamber. Another benefit of this design is that the load-lock chamber can be used for high pressure dosing or for the dosing of a destructive chemical that should not be exposed to the sensitive analytical equipment.

The slide-seal consists of a custom 2.75”CF nipple with three spaced out internal O-ring grooves with a 1.33”CF half nipple between the 1st and 2nd O-ring and between the 2nd and 3rd O-ring acting as ports for differential pumping. (**Figure II.5.2-1**)

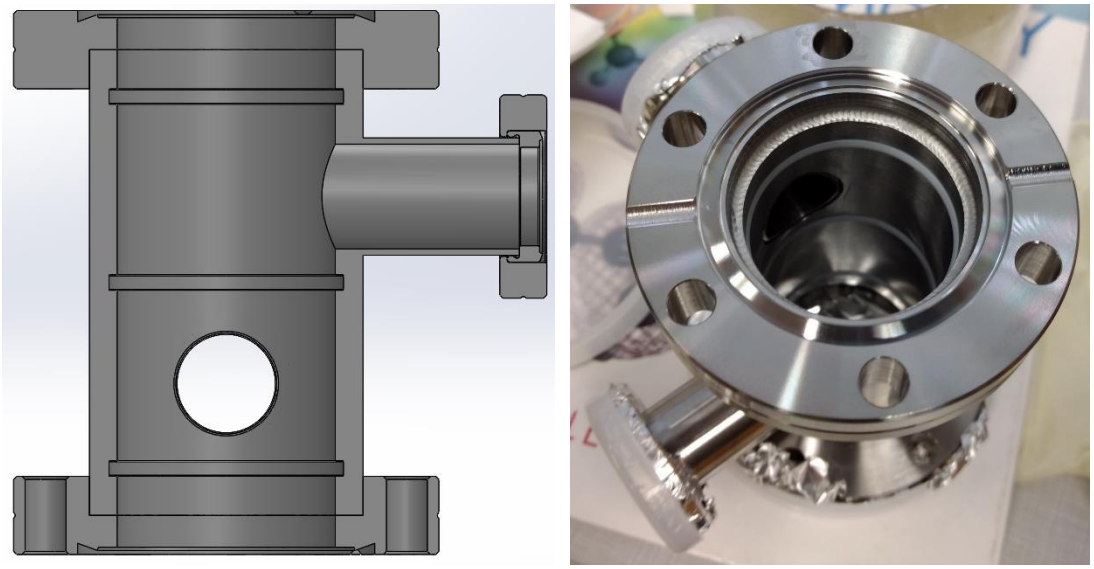

Figure II.5.2-1: Slide Seal Cross-section and O-rings.

The pumping on the two regions is the following. The region closer to the load-lock is pumped on by a Precision Scientific 10985 direct drive (20 CFM) while the region closer to the deposition chamber pumped on by a Varian TV250HT turbo pump (250 l/s) backed by another 10985.

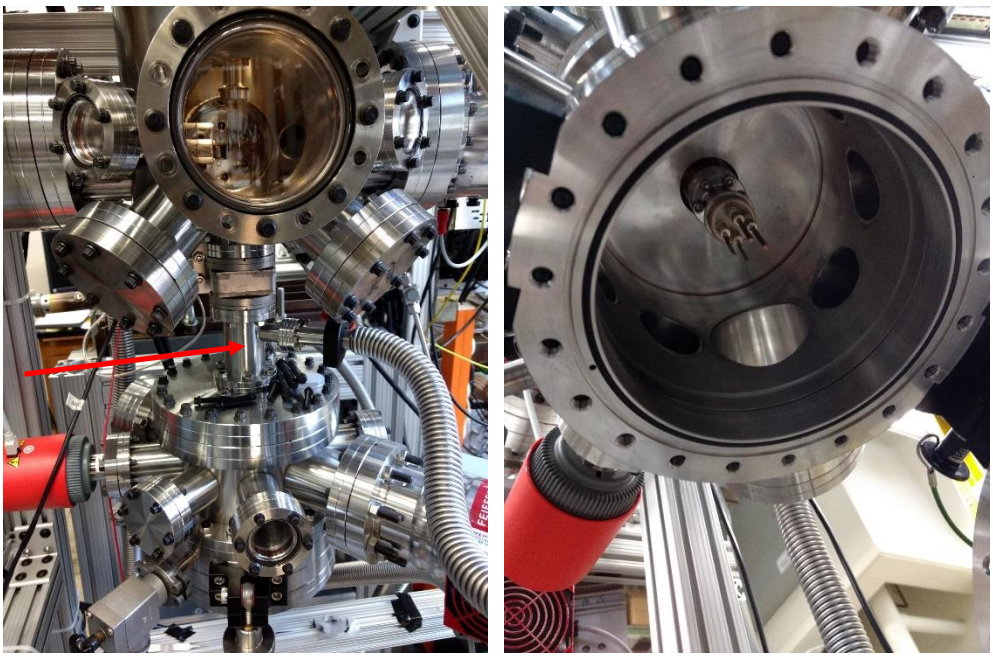

Figure II.5.2-2: Slide Seal in Place and Sample as Seen from Load-Lock Chamber

The O-rings placed in the groove are Parker FlexiSeal O-rings. These O-rings contain a spring that presses the sealing surface outwards creating a more solid seal. The O-ring itself is U-shaped over this spring with the open side on the atm side of the seal causing the atm pressure to expand the O-ring outwards into its sealing surface thereby creating a better seal.

The part number breaks down the individual parameters of the given O-ring. The Parker FlexiSeal O-ring catalog explains the pros and cons of each available option and was used to determine the O-ring used. (P/N 0100FBN06201375083SH).

0100: Material is Virgin PTFE. This was chosen for its cryogenic and chemical resistivity.

FB: Gland type. This is a piston seal used to seal ID and OD.

N: Lip Style. Default Lip Style.

062: O-ring's gland cross section is 0.062". The smaller the cross section of the O-ring the more flexible it is, which was required to insert the O-ring into the single-gland design of the slide-seal.

01375: O-ring ID of 1.375". This matches the sample holder tube's OD.

083: O-ring's gland height is 0.083". Used in manufacturing the O-ring groove in the slide-seal.

S: Spring material is stainless steel for vacuum compatibility and chemical resistance.

H: The spring is of a helical design. This spring design applies the most force to the sealing surface thereby creating a better seal. Since the sealing surface is for static/momentary slow motion, this should not generate a wear problem.

In practice the slide-seal has been a success. After a procedure for aligning the sample holder to the seal was developed, the slide-seal has been shown to seal $7*10^{-9}$ torr from atm while a user is manipulating the sample. The total time for sample replacement/cleaning is 30 minutes. This a marked improvement over the older instrument, where it took overnight just to attain $1*10^{-8}$ torr in the deposition chamber.

II.5.3 X-Ray and Ultraviolet Photoelectron Spectroscopy (XPS/UPS)

XPS and UPS are two techniques installed on this instrument. These techniques are able to characterize the chemical composition of the clusters and the reactants dosed onto the clusters.[1]

XPS and UPS both utilize the photoelectric effect, where light of a known wavelength is absorbed by an electron in a sample and, if the energy of the light is greater than the electron binding energy (*eBE*) and work function (Φ) of the material, the electron is ejected from the sample with any excess energy given to the electron as kinetic energy *(eKE*). (**Figure II.5.3-1**)

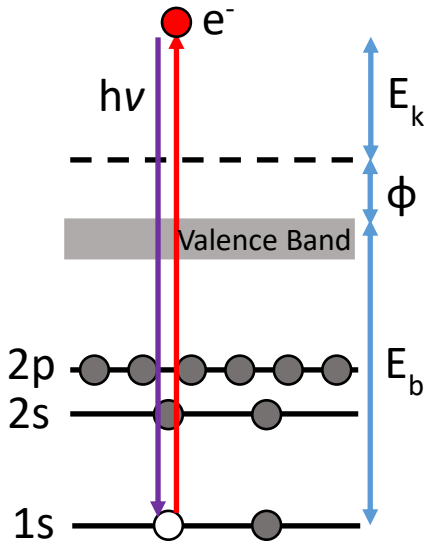

Figure II.5.3-1: Photoelectron Levels

$$h\nu = eKE + eBE + \Phi$$

Equation 24

If the *eKE* is measured, the $h\nu$ is known, and the Φ is calibrated, the *eBE* can be determined via **Equation 24**. The *eKE* is measured via a hemispherical analyzer which consists of an inner and outer hemisphere with radii of R_1 and R_2, respectively. The inner hemisphere is held at a more positive potential than the outer hemisphere thereby creating a field with $1/R^2$ dependence and making any electrons that enter the hemisphere bend around its curvature. The amount of bending is dependent on *eKE* with slower moving electrons bending more, resulting in the dispersion of electrons along *R* as a function of their *eKE*.[1,2] (**Figure II.5.3-2**)

Electrons entering the hemispheres with an energy E_0 at the midpoint between the hemispheres take a path with constant radius are defined to be at the "pass energy" of the hemisphere. The resolution of the hemisphere is dependent on the pass energy and the angle of acceptance of the hemisphere, with the resolution inversely proportional to both. The angle of acceptance is controlled via an adjustable aperture at the entrance of the hemisphere, while the pass

energy is controlled by the voltages applied to the hemispheres. Ideally, the hemisphere would have a constant resolution across its energy scan, so instead of changing the pass energy to scan the *eKE,* an input lens is used to decelerate or accelerate the electrons. As this acceleration sweeps, the electrons with the correct pass energy change as a function of their ejected *eKE*.[1,2]

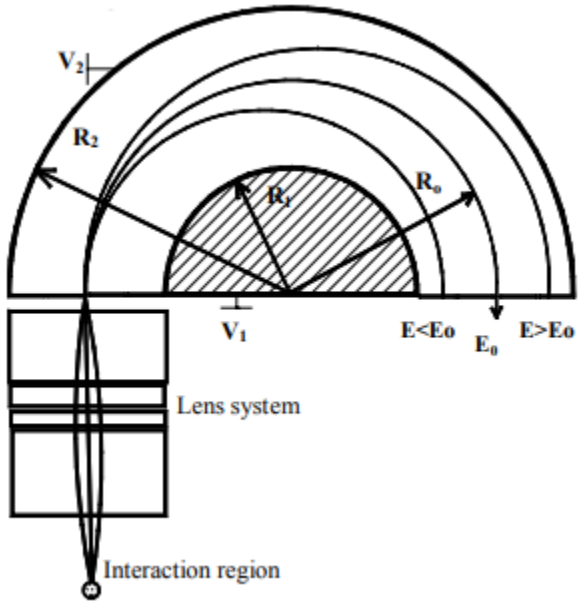

Figure II.5.3-2: Hemispherical Analyzer

XPS ejects core electrons and UPS ejects valence electrons. In XPS the eBE for a given core orbital electron is characteristic to the element it was ejected from, allowing for the determination of elements present in a sample. Further, the chemical environment of the atom it was ejected from will affect the *eBE* of the electron, where an oxidized atom will shift its core levels to a lower energy resulting in an increase in eBE and vice versa for a reduced atom. The magnitude of the chemical shift is determined by the level of oxidation, allowing for the determination of elements present in the sample and their oxidation state. UPS probes the valence electrons, and therefore the molecular orbitals of a sample, making it able to derive information on the bonds present in a sample.

This instrument is equipped with a Perkin-Elmer Φ Model 5100 10-360 Energy Analyzer with an extended lens system paired with a Φ 04-548 Dual Anode X-Ray Source (Mg 1253.6 eV and Al 1486.6 eV) and a 232 UV Lamp. This system is sold by RBD Instruments. This system works, but has large room for improvement. Replacing the single-point detector with a position-sensitive detector would go a long way toward increasing the sensitivity of hemisphere, allowing for the pass energy and angle of acceptance to be reduced and thereby increasing the resolution of the hemisphere. Further, sending the x-rays through a monochromator would increase the resolution; however, this would have to be paired with the position sensitive detector as the signal would drop do to the loss in x-ray intensity brought about by the monochromator.

II.5.4 Temperature Programed Desorption/Reaction (TPD/R)

In order to study the reactivity of the clusters, TPD/R is installed on the instrument. The basics of TPD/R are as follows. A sample on which the clusters of interest is deposited is dosed with a reactant gas, where the reactant can bind to the clusters. The sample is moved in front of a high sensitivity Residual Gas Analyzer (RGA) which consists of an electron bombardment ionizer, QMS, and detector. The sample is then heated at a linear rate, while the RGA monitors the gases that leave the surface by their *m*/*z*. This allows for spectra of desorption products as a function of temperature to be taken, and from this information about the thermodynamics and kinetics of a reaction can be determined as well as what the reaction products are, if there are any.[2,3]

Experimentally, this is setup as follows. The sample is mounted on the end of the sample holder (**See II.5.1**) between two power leads, with a thermocouple "spring-loaded" into the back of the sample. The sample is heated via resistive heating as current, supplied by a Sorensen DCS 55-55 power supply, is flowed through the sample via the power leads. Counter to the heating is a cooling force supplied via immersion of the power feed's atm side in liquid nitrogen which cools the sample via conduction, allowing the sample to reach ~ 170°C with no heating applied. By

balancing this heating and cooling force, a temperature ramp can be obtained. The sample holder is designed with a minimalist approach consisting of only the thermocouple behind the sample, the power leads, and the sample pressed into Ta clips wrapped around the power leads. This minimalist approach serves to reduce the amount of material, aside from the sample, that is heated up during the TPD, as desorption products from locations other than the sample are not desirable.

The temperature ramp is produced and controlled via a Eurotherm 2408 PID controller which uses feedback measurements to control the power supply.[4] In order to keep the 2408 electrically isolated from the heating voltage, the thermocouple is run through a DAT 4531A isolation converter which reads the temperature and outputs it on an isolated 0-10VDC scale with -200°C as 0VDC and 500°C as 10VDC. The 2408 accepts this 0-10VDC and is calibrated to convert this scale back to temperature, which it then compares to its ramp. Based on the controller's calibrated PID values and the difference between the actual and expected temperature, the 2408 outputs 0-20mA to a remote control on the power supply, where the current applied to this control is proportional to the power supply's current output.

The RGA is a Hiden 301/3F PIC. This is a 300 amu range QMS with a pulse counting detector able to detect $< 4x10^{-15}$ torr partial pressures at >650 measurements per second. The high sensitivity of this RGA is critical for the detection of reaction products from deposited cluster samples, as it reduces the amount of clusters that need to be deposited to produce a measurable signal as well as making it easier to detect products from samples with poor catalytic efficiency. The rapid acquisition rate is important for a multi-ion-detection (MID) setup allowing for many masses to be monitored at one time as the ramp progresses (up to 15 different m/z), as the number of data points per time, and therefore per temperature, decreases as more masses are monitored during a scan. The RGA is covered in a quartz shroud with a 5mmØ hole in front of the ionizer in order to prevent desorption products from locations that are not the sample from entering the RGA.

Quantitative results or desorption energy and reaction order can be derived from TPD/R. The rate law governing the desorption of a molecule from the surface is given below, where r_{des} is the rate of desorption, Θ is the surface coverage of the molecule, and n is the order of the reaction.[2,3]

$$r_{des} = -\frac{d\Theta}{dt} = k_n \Theta^n$$

Equation 25

The rate constant (k_n) can be described via the Arrhenius equation, where v_n is the frequency factor, E_{des} is the activation energy of desorption, and T is temperature.

$$k_n = v_n * \exp(-\frac{E_{des}}{RT})$$

Equation 26

Substituting **Equation 25** into **Equation 26** gives the Polanyi-Wigner rate law.

$$r_{des} = -\frac{d\Theta}{dt} = v_n(\Theta) * \exp\left(-\frac{E_{des}(\Theta)}{RT}\right) * \Theta^{n(\Theta)}$$

Equation 27

Some of these parameters are dependent on surface coverage, which is dynamic during the TPD/R experiment, making this equation difficult to use on actual experimental results as written. Many techniques and approximations have been developed to overcome this problem, and one of these approximations is used often in the experiments performed in this work. This approximation is called Redhead Analysis. [2,3]

Redhead assumed that activation parameters are independent of surface coverage and that desorption followed 1st order kinetics (n=1). This allowed for the derivation of an equation that only needed the temperature at the peak of desorption (T_{max}), the ramp rate (β), and an approximate frequency factor (v_1), in order to give an approximate E_{des}.

The temperature ramp rate can be described as follows.

$$\beta = \frac{dT}{dt}$$

Equation 28

Upon substitution into the Polanyi-Wigner equation and with the assumption of surface coverage independence and 1st order kinetics,

$$\frac{d\Theta}{dT} = -\frac{v_1}{\beta} * \exp\left(-\frac{E_{des}}{RT}\right) * \Theta$$

Equation 29

At the peak of the desorption profile $d\Theta/dT=0$, where the T at that point is called T_{max}. Upon substitution into the above equation and solving for E_{des} the Redhead Equation is derived.[3]

$$E_{des} = RT_{max}\left[\ln\left(\frac{v_1 T_{max}}{\beta}\right) - \ln\left(\frac{E_{des}}{RT_{max}}\right)\right]$$

Equation 30

The E_{des} dependent ln() parameter is small compared to the first parameter and is approximated to be 3.64, while the v_1 parameter is typically estimated to be 10^{13} s^{-1}. The Redhead analysis allows for the derivation of an approximate E_{des} from a single desorption spectrum, which is required in this work as a fresh deposition is performed before each TPD/R experiment due to cluster aggregation during the temperature ramp.

Again, the E_{des} is the activation energy of desorption from the surface and not the activation energy of any reaction that occurs on the surface. However, if desorption occurs immediately upon reaction, where the reaction is the rate-limiting step of the desorption process, then the E_{des} is the E_{rxn}. In other cases, the product may have already formed at a lower temperature and remains bound to the surface until given enough energy to leave. In this case, the E_{des} acts as an upper limit to E_{rxn}.

II.5.5 Dosing and Molecular Dosers

Dosing gas onto a sample is normally performed by introducing a static background of gas pressure into the chamber through a high precision leak valve for an amount of time. The dose is measured in the Langmuir unit ($L=1*10^{-6}$ torr for 1 s), where one Langmuir is nominally a mono-layer assuming a perfect sticking coefficient. Due to the inherent imprecision of pressure gauges, this is usually reported with 1 significant figure.[2]

Two methods were used to improve the accuracy of the dosing. First, instead of relying on a hot filament ionization gauge to monitor pressure, the RGA was used to track the pressure of the dose. The RGA is much more sensitive and consistent than the ionization gauge, due not only to the RGA's capability to determine the total pressure of the dose, but to its ability to break it down into its partial pressures allowing for the determination of any contaminate in the dose. Second, the static background approach to dosing has some uncertainties and runs the risk of contaminating the chamber or its analytical equipment, so ideally a lower pressure dose for a shorter time would be ideal, however there still needs to be enough reactant dosed onto the sample to measure any reaction. This can be achieved by keeping the local pressure on the sample high but reducing the dose overall. For this purpose, a molecular doser was manufactured.

A molecular doser consists of an uncoated micro-channel plate mounted in front of a diffusion region. The gas is leaked through a leak valve into this diffusion region, where it does not have line-of-sight to the sample but instead leaves through holes in the side of the tube. The gas flows around in this region and eventually diffuses out through the MCP. The act of moving through the MCP forces the gas to collimate as it leaves. If a sample were placed in front of the molecular doser, the local pressure there would be higher than the rest of the chamber and the gas would be directed onto the sample. The molecular doser is mounted on a double-sided 2.75"CF through a VCR fitting, with the leak valve mounted on the back of it. (**Figure II.5.5-1**)

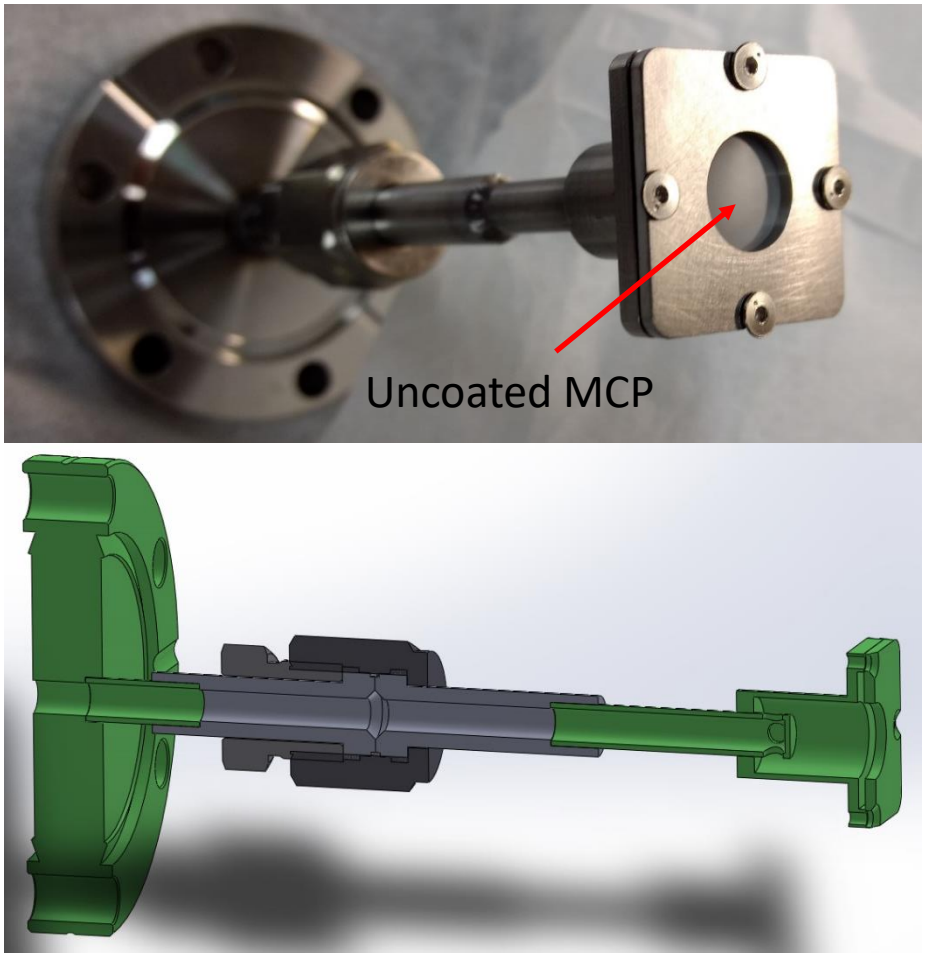

Figure II.5.5-1: Molecular Doser

Another method of dosing used in these studies is called matrix-method dosing. In this method, before depositing clusters the sample is cooled to liquid nitrogen temperatures followed by the introduction of a low pressure dose ($<1*10^{-7}$ torr) for a long time (>100s). Due to the cooling the sticking coefficient of the gas increases, both to the surface and to itself, condensing the gas and forminga multi-layer matrix of physi-adsorbed reactant on the surface. The clusters are then deposited into this matrix thereby guaranteeing that the clusters interact with the reactant and preventing aggregation. This has the benefit of both increasing the signal in our TPD/R experiments thereby requiring less clusters to be deposited as well as preventing cluster aggregation.

Integrated XPS signal was used to determine the ratio of reactant to cluster, and that ratio was used to determine if full cluster/reactant interaction took place. An example of this is work reported herein on the three clusters $(MoO_3)_3$, $(WO_3)_3$, and $(ZrO_2)_3$ with dimethyl-methylphosphonate (DMMP). DMMP contains a single P atom while the clusters each contain 3 metal atoms. Below is a plot of the ratio of P:Metal for the as-deposited clusters and at increasing temperatures.[5,6] (**Figure II.5.5-2**) The sample was heated up to room temperature in order to remove the unreacted physi-adsorbed DMMP molecules, so that only the chemi-adsorbed clusters remained. Both the $(MoO_3)_3$ and $(WO_3)_3$ samples had a 1:3/P:M indicating one DMMP molecule to one cluster. Theoretical calculations showed that the energy for binding a second DMMP molecule was endothermic with minimal potential barrier to the DMMP drifting away. The $(ZrO_2)_3$ was not studied with theory.

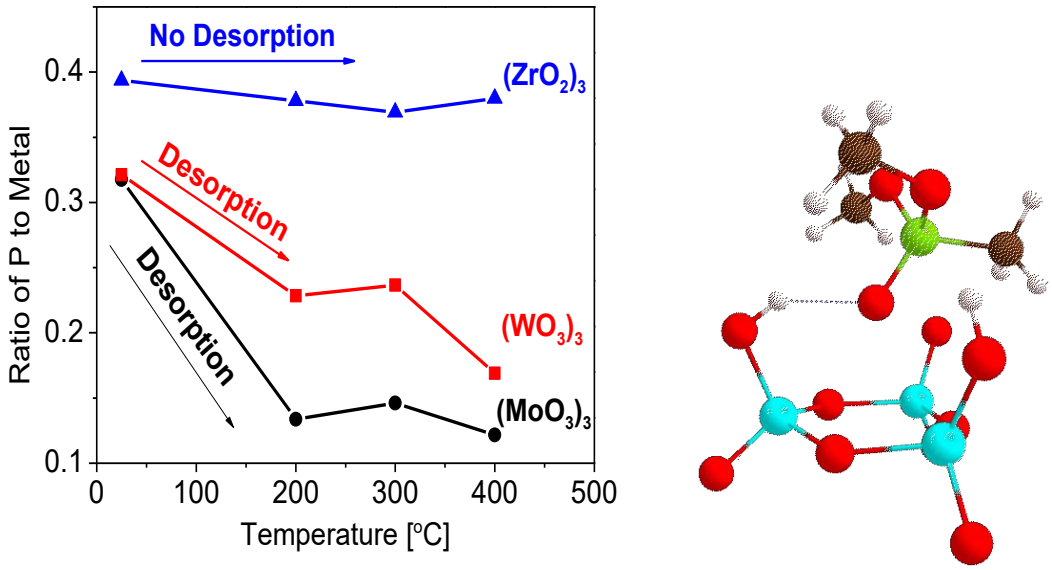

Figure II.5.5-2: P:M vs Temperature and Theoretical Structure of DMMP/$(MoO_3)_3$

II.5.6 Low-Energy Electron Diffraction (LEED)

A Specs ErLEED 1000-A is installed on the instrument. LEED uses the diffraction pattern of elastically scattered electrons to determine 2D periodicity of a sample surface. An electron gun creates electrons of 20-200eV that are directed at a sample, where they are scattered elastically or inelastically backwards. Grids with applied potentials are used to remove inelastically scattered electrons and to accelerate the electrons into a phosphor screen where the phosphorescence is detected by a camera. Due to diffraction of the electrons off of periodic patterns in the surface a diffraction pattern appears on the screen. This pattern is only a 2D diffraction due to the surface sensitivity of electrons resulting in low penetration into the sample.[2] (**Figure II.5.6-1**)

In experiments performed on this instrument, the primary application of the LEED would be in determining the quality of crystalline surfaces deposited onto, as clusters do not usually aggregate into periodic structures on the scale detectable by LEED.

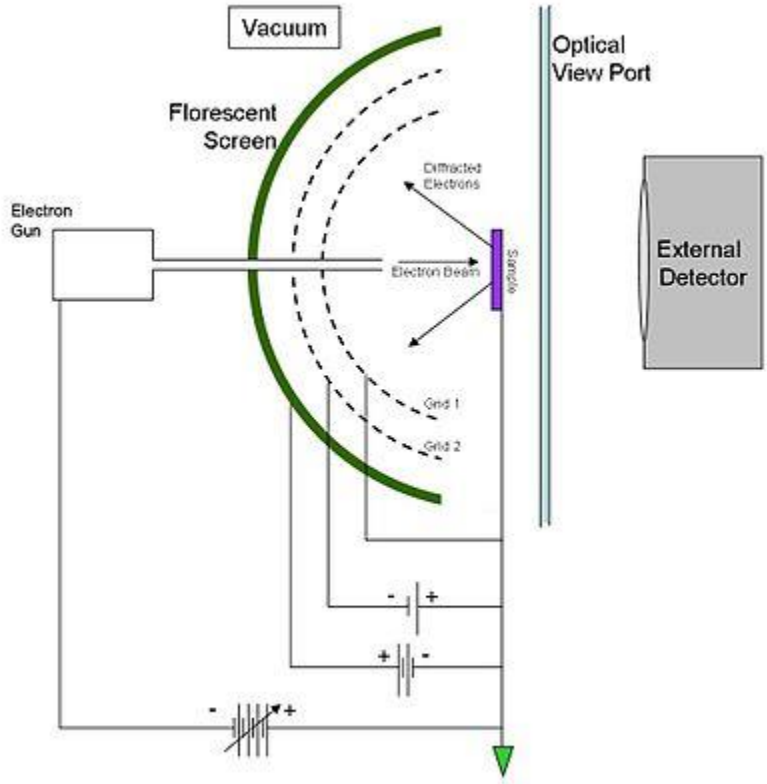

Figure II.5.6-1: LEED Schematic

II.5.7 Scanning Tunneling and Atomic Force Microscopy (STM/AFM)

Microscopy techniques are useful tools in determining how clusters migrate around the surface of a sample and if they aggregate.[1,2] Aggregation is a problem, as the clusters would lose their unique size effects, so STM and AFM are used to determine the presence and extent of aggregation in experiments performed on this instrument. The instrument is equipped with an *in-situ* STM (OMNICRON 1) and the samples can be removed for *ex-situ* AFM.

---

[1] Y. Leng, "Materials Characterization: Introduction to Microscopic and Spectroscopic Methods 2nd ed.", Wiley, 2013. ISBN: 3527334637

[2] J. T. Yates, "Experimental Innovations in Surface Science: A Guide to Practical Laboratory Methods and Instruments 2nd ed", Springer, ISBN: 978-3-319-17667-3

[3] P. A. Redhead, Vacuum, 1962, **12**, 203–211.

[4] Xin Tang, "Mass Selected Metal and Metal Oxide Clusters as Catalysts", PhD diss., Johns Hopkins University, 2016

[5] X. Tang, Z. Hicks, L. Wang, G. Gantefçr, K. H. Bowen, R. Tsyshevsky, J. Sun, M. M. Kuklja, Phys. Chem. Chem. Phys., 2018, **20**, 4840–4850.

[6] X. Tang, Z. Hicks, L. Wang, G. Gantefor, K. H. Bowen,

R. Tsyshevsky, J. Sund, M. M. Kuklja, Phys. Chem. Chem. Phys., 2018, **20**, 4840.

III. Results

This section will include work performed on the older instrument and experimental studies showing the improvements of the newer instrument as compared to the older instrument.

III.1 Adsorption and Decomposition of Dimethyl Methyl phosphonate on Size-Selected $(MoO_3)_3$ Clusters

Xin Tang[1], Zachary Hicks[1], Linjie Wang[1], Gerd Ganteför[2], Kit H. Bowen[1] Roman Tsyshevsky[3], Jianwei Sun[4], Maija M. Kuklja[3]

[1] Department of Chemistry, Johns Hopkins University, Baltimore, Maryland 21218, USA

[2] Department of Physics, University of Konstanz, 78464 Konstanz, Germany

[3]Department of Materials Science, University of Maryland, College Park, Maryland 20742, USA

[4] Department of Physics, Tulane University, New Orleans, Louisiana 70118, USA

The adsorption and decomposition of dimethyl methylphosphonate (DMMP), a chemical warfare agent (CWA) simulant, on size-selected molybdenum oxide trimer clusters, i.e. $(MoO_3)_3$, was studied both experimentally and theoretically. X-ray photoelectron spectroscopy (XPS), temperature programmed reaction (TPR), and Density Functional Theory (DFT)-based simulations were utilized in this study. The XPS and TPR results showed both, desorption of intact DMMP, and decomposition of DMMP through the elimination of methanol at elevated temperatures on $(MoO_3)_3$ clusters. Theoretical investigation of DMMP on $(MoO_3)_3$ clusters suggested that, in

addition to pure $(MoO_3)_3$ clusters, reduced molybdenum oxide clusters and hydroxylated molybdenum oxide clusters also play an important role in catalyzing DMMP decomposition via a "reverse Mars–van Krevelen mechanism". The present study, which focused on oxide clusters, underlines the importance of surface defects, e.g., the oxygen vacancies and surface hydroxyls, in determining the reaction pathway of DMMP, in agreement with previous studies on thin films. In addition, the structural fluxionality and the Lewis acidity of molybdenum oxide clusters, i.e. $(MoO_3)_3$, may make them good candidates for adsorption and decomposition of chemical warfare agents with similar structures to DMMP.

III.1.1 Introduction

Protection from chemical warfare agents (CWAs) requires the development of functional materials and catalysts to remove and/or decompose CWAs in an efficient manner. Regardless of the CWA, its concentration, and method of deployment, a mask or chemical-defense kit remains the best individual protection against chemical agents with the mask being used to protect the face, eyes, and respiratory tract against the hazardous chemical agents. The key component of the mask is the filter material, which is responsible for adsorption and degradation of the chemical agents. Unfortunately, despite its importance to the design of new materials and the improvement of current protective equipment, a detailed understanding of the processes, occurring both on and within the filter material during CWA exposure, is still lacking on the molecular level.

Gas masks have traditionally consisted of carbon-based and metal/metal-oxide-based filter materials and while a range of carbon-based filter material structures and compositions have been heavily studied,[1] most of the experimental studies of the adsorption and decomposition of CWAs and their simulant compounds on metal oxides have been performed on single crystals, polycrystalline films and nanoparticles. [2-15] In many of these experiments it was shown that the

mechanisms of adsorption and decomposition depend strongly on the surface structure of the filter material and the presence of contaminants.

Sub-nano clusters, chemical species consisting of a relatively small number of atoms, have been widely studied in the field of heterogeneous catalysis both as catalysts and as model systems used to help explain catalytic processes. Despite their intriguing size-dependent catalytic properties, which are attractive for creating new efficient filter materials, and their uses as model systems, which can help explain reactions at a molecular level, attempts to explore the ability of well-defined clusters to adsorb and degrade CWAs have not been reported.

In this research, we explore the adsorption and decomposition of dimethyl methylphosphonate (DMMP), a CWA simulant, on size-selected $(MoO_3)_3$ trimer clusters deposited on a Highly-Ordered Pyrolytic Graphite (HOPG) support by means of a joint experimental and theoretical study.

Dimethyl methylphosphonate belongs to the large class of organophosphate compounds well known for their toxicity,[16,17] but due to its low vapor pressure, its lower toxicity than other compounds in its class, and its structural similarity, it is commonly used as a simulant compound of more hazardous nerve agents such as sarin and soman. $(MoO_3)_3$ trimer clusters have already become the object of many experimental and theoretical studies due to their activity and selectivity in activation of some alkane molecules and dehydration of alcohols.[18,19,20]

In this work, x-ray photoelectron spectroscopy (XPS) and temperature programmed reaction (TPR) were used to investigate the fate of DMMP on $(MoO_3)_3$ clusters. Density function theory (DFT)-based calculations were used to simulate the adsorption configurations and the decomposition pathways of the DMMP molecule on $(MoO_3)_3$ clusters. The XPS and TPR results showed desorption of intact DMMP and decomposition of DMMP on $(MoO_3)_3$ clusters under elevated temperatures with methanol found to be the major gas-phase product. The theoretical

investigation suggested a “reverse Mars–van Krevelen mechanism” where reduced oxide clusters and hydroxylated oxide clusters were the active species leading to the decomposition of DMMP associated with the elimination of methanol.

III.1.2 Methods

Experimental Method

Molybdenum oxide trimer clusters $(MoO_3)_3$ were prepared as negative cluster anions by a magnetron sputtering source. The magnetron setup consisted of a molybdenum target placed in a magnetic field and biased to -500 V while a mixture of argon, helium and oxygen gases was introduced. The argon gas was ionized to create argon cations, which sputtered the metal target to produce molybdenum atoms and electrons. After reacting with the oxygen to form oxides, the resulting metal oxides aggregated, attached electrons, and formed molybdenum oxide cluster anions. The added helium served to cool and transport the cluster anions down the beamline, where they were then electrostatically accelerated before entering a magnetic sector mass spectrometer (25◦ sector magnet with resolution of $m/\Delta m = 20$). By tuning the magnetic field strength, $(MoO_3)_3^-$ cluster anions were mass-selected and focused by ion optics before entering the deposition chamber, where they were soft-landed (<1eV) onto a freshly peeled HOPG substrate (1cm × 1cm) in an ultra-high vacuum (UHV) environment (1×10-9 torr). The graphite-based substrate was specifically chosen to mimic the carbon support traditionally used for MoO_3 based catalysts. The resulting sample can be cooled to approximately -160 °C by liquid nitrogen (LN2) or heated via resistive heating by passing current through the HOPG, with the temperature of the sample being monitored by a K-type thermocouple spring-loaded to the back of the HOPG.

Once clusters had been deposited onto the HOPG substrate, a TPR set-up, using a Hiden HAL/3F PIC quadrupole mass spectrometer (QMS), was used to characterize their activity. The reaction products that desorbed from the surface during a linear temperature ramp were detected

and identified by a QMS which was positioned normal to the plane of the substrate and at a distance of 5 mm. To minimize the contribution from background gases and maximize the sensitivity towards species desorbing directly from the substrate, the QMS ionizer was surrounded by a custom-built glass shroud. Typically, in the TPR experiment, 0.2 Langmuir of DMMP was first dosed onto a freshly peeled HOPG surface cooled to -160 °C. The DMMP was purified by several freeze-pump-thaw cycles before being background dosed through a UHV compatible leak valve. After that, 3.0×1012 $(MoO_3)_3$ clusters were deposited into the multilayers of DMMP formed on the cooled HOPG. By depositing $(MoO_3)_3$ clusters into DMMP layers, the clusters will preferentially interact with the surrounding DMMP molecules rather than sintering. The number of clusters deposited is calculated by integrating the ion current over the deposition time. During the TPR temperature ramp, the surface temperature was first raised to 0 °C to desorb the vast majority of physisorbed DMMP, and eventually to 450 °C with a ramping rate of 2 °C/s.

In addition, the deposited samples could also be transferred in situ to an adjacent UHV analytic chamber, where they were characterized by X-ray Photoelectron Spectroscopy (in situ XPS) with non-monochromatic Mg Kα-rays (1253.6 eV), with the ejected electron kinetic energy analyzed via a high energy hemispherical analyzer. In the XPS analytic chamber, the sample was in situ heated by e-beam heating with the temperature measured by a K type thermocouple connected to the sample holder. For the XPS studies, a higher pressure of DMMP (5×10-7 torr) was dosed during the cluster deposition in order to saturate the adsorption sites on $(MoO_3)_3$ before being transferred to XPS analytic chamber. In this case the deposition was performed with the substrate at room temperature to minimize the adsorption of DMMP onto the sample holder.

Density Functional Theory Calculations

Calculations were performed with DFT[21,22] using a series of modern hybrid functions including, the B3LYP functional,[23,24] its long-range corrected version CAM-B3LYP,[25] and a

B3LYP+D3 functional including Grimme's empirical dispersion.[26] In addition to the three variations of the B3LYP functional, a recently developed meta-generalized-gradient (meta-GGA) functional SCAN[27,28] was also employed for calculations of desoprtion energies. The double-ζ 6-31+G(d,p) basis set was used for the H, C, O, and P atoms. The LanL2DZ basis set,[29,30,31] including the Los Alamos effective core potential, was used for the Mo atoms. Vibrational frequencies were calculated for relevant atomic configurations to distinguish energy minima and transition states. The stationary points corresponding to the energy minima were positively identified by having no imaginary frequencies, and the transition states were confirmed to have exactly one imaginary frequency. Reaction paths were investigated by conducting intrinsic reaction coordinate computations using the Hessian-based Predictor-Corrector integrator algorithm[32,33] for each transition state. All calculations were carried out with the Gaussian09 code.[34] The modified version of the Gausian 03 code[35] was used to perform calculations with the SCAN functional.

III.1.3 Results

XPS characterization of DMMP on $(MoO_3)_3$ Clusters

The temperature dependent XPS spectra of the P(2p) region for DMMP on $(MoO_3)_3$/HOPG are displayed in **Figure III.1.3-1**. As shown in the **Figure III.1.3-1(a)**, the P(2p) peak of DMMP on $(MoO_3)_3$ at room temperature was centered at 133.5 eV, compared to the 134.0 eV in the control case of DMMP adsorbed on clean HOPG. The slightly lower binding energy of the P(2p) peak indicates that the phosphorus present in DMMP was partially reduced at room temperature after the DMMP bound to the $(MoO_3)_3$ cluster. After heating the sample to 200 °C and allowing it to cool back to room temperature, the binding energy of the P(2p) peak shifted slightly to an even lower binding energy of 133.1eV (**Figure III.1.3-1(b)**). Further annealing to higher temperatures (300 °C and 400 °C) shifted the P(2p) peak back to the original position (**Figure III.1.3-1(c)(d)**),

possibly due to the formation of a PO_x species, which was previously seen with DMMP on other oxides.[7]

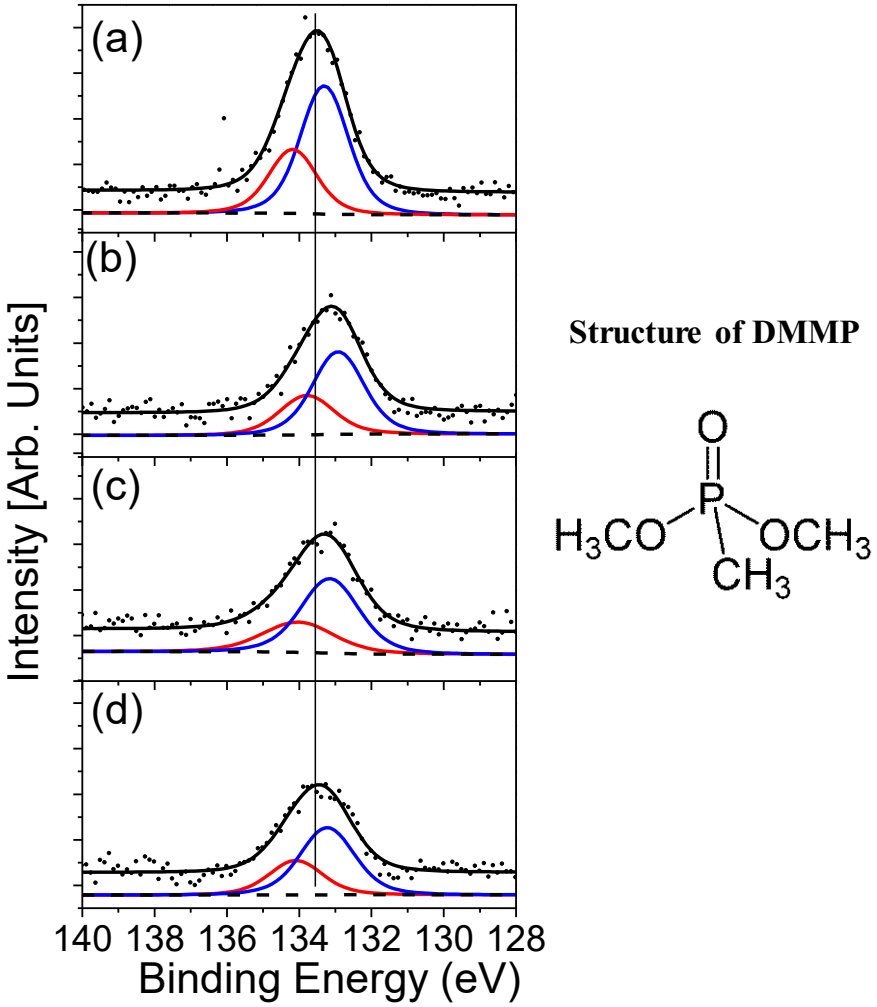

Figure III.1.3-1: XPS spectra of the P(2p) envelope of DMMP adsorbed on $(MoO_3)_3$ clusters on HOPG as a function of annealing temperature (a) Room Temperature (b) 200 °C(c) 300 °C(d) 400 °C. The structure of DMMP is shown on the right.

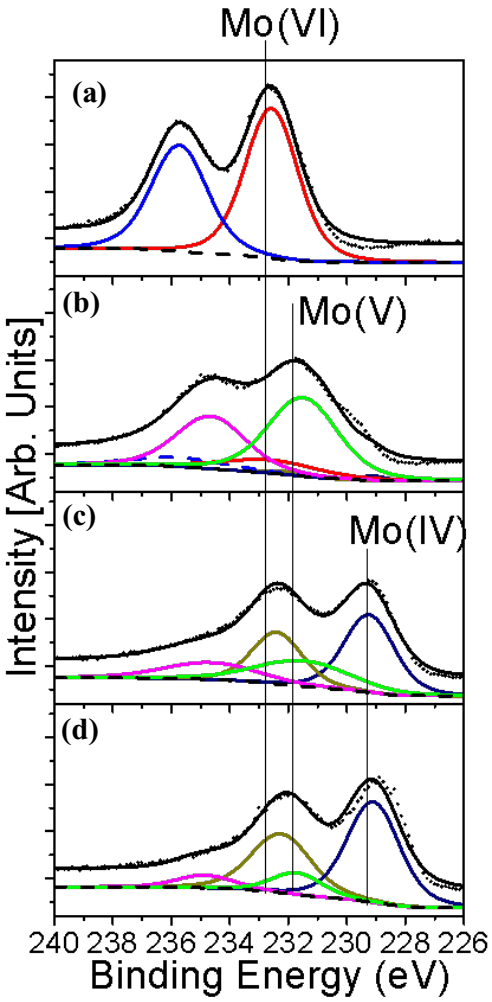

Structure of $(MoO_3)_3$

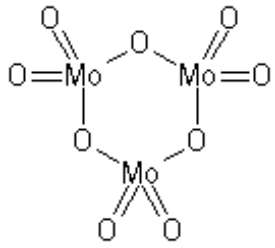

Figure III.1.3-2: XPS spectra of the Mo(3d) envelope of $(MoO_3)_3$ clusters on HOPG as a function of annealing temperature (a) Room Temperature (b) 200 °C(c) 300 °C(d) 400 °C. The structure of the $(MoO_3)_3$ cluster is shown on the right.

The temperature dependent XPS spectra of the Mo(3d) region for $(MoO_3)_3$/HOPG with DMMP adsorption is shown in **Figure III.1.3-2**. The XPS spectra for the Mo(3d) of $(MoO_3)_3$ at room temperature displayed a doublet peak, $3d_{5/2}$ and $3d_{3/2}$, centered at 232.5 eV and 235.6 eV, respectively (**Figure III.1.3-2(a)**). The binding energy of Mo($3d_{5/2}$) is consistent with the binding energy of Mo($3d_{5/2}$) in Mo(VI), indicating the presence of MoO_3.[36] After heating to 200 °C (**Figure III.1.3-2(b)**), the binding energy of Mo(3d) shifted to a lower binding energy, which indicates that

MoO_3 was reduced. Further annealing to 300°C and 400 °C caused more reduction, resulting in a mixture of lower oxidation species, i.e. Mo(IV) and Mo(V). (**Figure III.1.3-2(c)(d)**) It has to be noted that the reduction of MoO_3 was also observed in the absence of DMMP adsorption on an HOPG surface, indicating an abundance of reduced Mo species under elevated temperature.

Since the size of the clusters deposited on HOPG are smaller than the inelastic mean free path of photoelectrons generated in XPS, the XPS data can be used to quantize the speciation and concentration of the DMMP on $(MoO_3)_3$ clusters. The relative atomic ratio of P to Mo at different temperatures was calculated and is shown in **Figure III.1.3-3**. This ratio is calculated by dividing the peak area of P(2p) and Mo(3d) with their respective relative sensitivity factor (R.S.F.) and comparing the resulting values. The as-deposited DMMP on $(MoO_3)_3$ ratio of P to Mo is around 0.32. This indicates that for every $(MoO_3)_3$ cluster, about one DMMP molecule (~0.96) is adsorbed to it. It's worth noting that the ratio of P to Mo decreased with increasing temperature from room temperature to 200 ^oC. The loss of phosphorus upon heating is possibly due to the desorption of intact DMMP and other phosphorus-containing products. The decrease in the P to Mo ratio is dramatic from room temperature to 200 ^oC, and flat from 200 ^oC to 400 ^oC, indicating the majority of DMMP and other phosphorous containing species desorbed during the temperature range of room temperature to 200 ^oC.

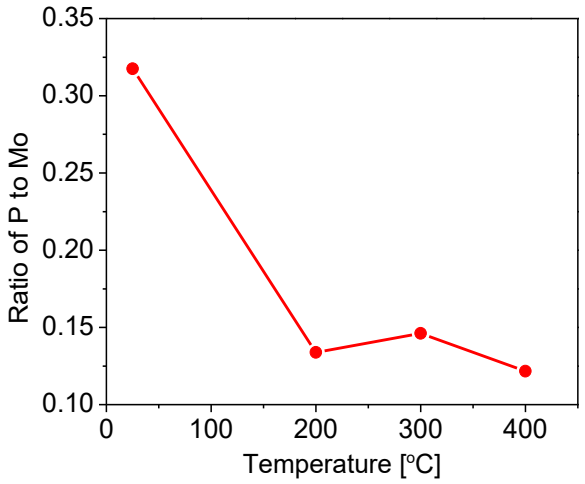

Figure III.1.3-3: The relative atomic ratio of P to Mo of DMMP on $(MoO_3)_3$ Clusters as a function of annealing temperature.

Temperature programmed reaction of DMMP on $(MoO_3)_3$

The TPR profiles of DMMP on $(MoO_3)_3$ clusters are recorded in **Figure III.1.3-4**, for the masses of 124 amu, 79 amu, 46 amu, 32 amu, 31 amu, 16 amu, 15 amu, and 2 amu. The mass of 124 amu corresponds to the parent ion of DMMP, while the mass of 79 amu is ascribed to the major fragment of DMMP under electron impact ionization in the QMS. The mass of 46 amu corresponds to dimethyl ether, while 32 and 31 amu are the masses for methanol and its deprotonated form, methoxy, respectively. Masses 16, 15, and 2 amu are methane, methyl, and hydrogen respectively.

Both 124 and 79 amu showed the same desorption profiles, with a desorption peak centered at 100 °C. This is consistent with the XPS result showing that the majority of DMMP desorbed in the temperature range of RT to 200 °C. Using the Redhead Analysis [37] a desorption energy of 23.4 kcal/mol was determined for DMMP. For the masses of 32 and 31 amu, a broad desorption peak was observed in both cases, indicating the production of methanol upon heating. The peak position, centered around 200 °C, gives a desorption energy of 29.8 kcal/mol for methanol. The lower temperature shoulder at 107 °C in the 31 amu profile is a minor fragment from DMMP. No peaks

were observed resulting from H_2 (2 amu), CH_4 (16 amu), and dimethyl ether (46 amu). The desorption profile of 15 amu replicated the desorption profile of DMMP and is a minor fragment of DMMP. Subtraction of the DMMP contribution reveals an additional shoulder around 198 ^{o}C, corresponding to a desorption energy of 29.7 kcal/mol for the methyl group. It is worth mentioning that the TPR experiment has been repeated multiple times for $(MoO_3)_3$ clusters and similar peak shape and positions were observed during these experiments.

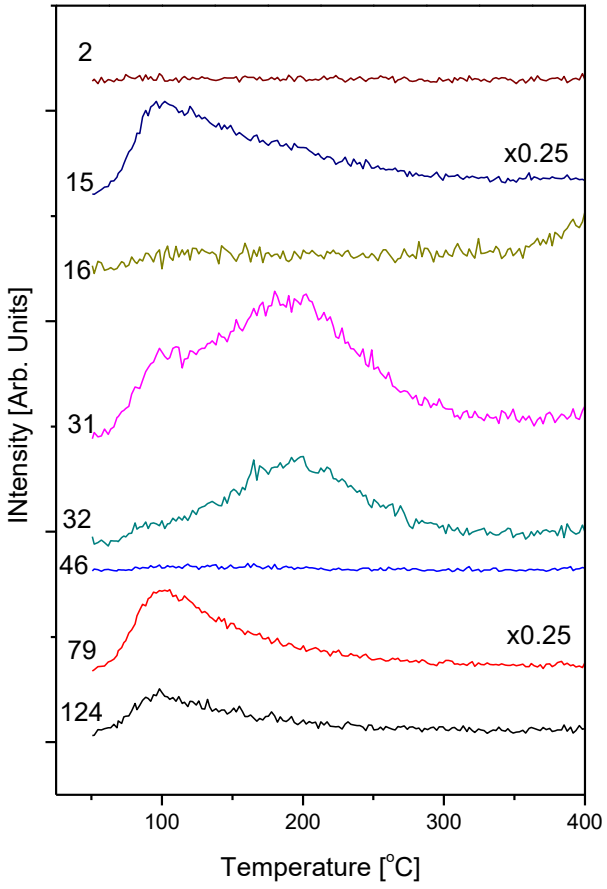

Figure III.1.3-4: Temperature programmed reaction profile of DMMP on (MoO3)3

DFT modeling of DMMP adsorption on Molybdenum Oxide Clusters

Oxygen vacancies and hydroxyl groups are common defects on metal oxide surfaces. In previous studies of DMMP on stoichiometric MoO_3 and on defect-rich MoO_3 surface, it was found

that the oxygen defects and surface hydroxyls are critical to drive the adsorption and decomposition process of DMMP on the reduced metal oxide surface. At the same time, the stoichiometric oxide surface shows little or no activity and is characterized by a low binding strength to DMMP due to the lack of Lewis acid sites.[13,14] As indicated in XPS measurements (**Figure III.1.3-2 (b),(c),(d)**) $(MoO_3)_3$ can be easily reduced to nonstoichiometric molybdenum oxide on the graphite support upon exposure to elevated temperatures. In addition, the reduced Mo center can readily promote the dissociation of water at vapor pressure below 10^{-8} Torr,[38] leading to the formation of hydroxylated molybdenum oxide clusters.[13,14] Therefore, in the simulations of adsorption and decomposition of DMMP on molybdenum oxide clusters, several models were considered. The models include a DMMP molecule adsorbed on: (1) a stoichiometric cluster, $(MoO_3)_3$ (**Figure III.1.3-5 (b)**), (2) a reduced cluster, Mo_3O_8 (**Figure III.1.3-5 (c)**), and (3) a series of hydroxylated clusters $Mo_3O_9H_n$ (n=1-3, **Figure III.1.3-6 (a)-(h)**).

Adsorption of DMMP on $(MoO_3)_3$

Calculations show that the most stable configuration of DMMP adsorbed on the $(MoO_3)_3$ cluster corresponds to the structure in which the DMMP molecule is oriented with its phosphoryl oxygen inside the cluster ring with the methyl and methoxy groups placed between the oxygen atoms of the cluster (**Figure III.1.3-5 (b)**). This is consistent with previous studies on Al_2O_3, MgO and WO_3,[6] where the phosphoryl oxygen binds to Lewis acid sites, i.e. the metal ion center. The resulting structures indicate that there is no additional adsorption sites available on the $(MoO_3)_3$ clusters for adsorbing another DMMP molecule, leaving one DMMP adsorbed on one $(MoO_3)_3$. This is consistent with XPS measurements and additionally explains the estimated the as-deposited DMMP on $(MoO_3)_3$ ratio of P to Mo (that is ~0.32).

Figure III.1.3-5 (b) shows a noticeable elongation of the P-O bond (by ~0.04 Å) and shortening of the P-OCH_3 bond (by ~0.02-0.04 Å) in DMMP adsorbed on $(MoO_3)_3$ clusters, as compared with

the gas-phase molecule. The distances of the P-CH_3 and O-CH_3 bonds change slightly (by ~0.01 Å) when DMMP is adsorbed on $(MoO_3)_3$.

The desorption energy of DMMP on $(MoO_3)_3$, calculated using B3LYP, is 17.7 kcal/mol (**Table III.1.3-1**). The desorption energy obtained using the long range corrected CAM-B3LYP functional (24.1 kcal/mol) is ~6 kcal/mol higher than B3LYP estimation, whereas the inclusion of van-der-Waals interactions via Grimme's empirical dispersion tends to increase the resulting desorption energy by additional ~8 kcal/mol (32.0 kcal/mol). A similar trend is observed for the different adsorption configurations of DMMP on the stoichiometric and reduced clusters (**Table III.1.3-1**). The desorption energies, recalculated using the meta-GGA SCAN functional, developed for an accurate prediction of weak nonbonding interactions, are consistent with B3LYP+D3 estimations. We therefore will refer in our discussion of the desorption energies to the numbers obtained with the B3LYP+D3 functional.

Adsorption of DMMP on Mo_3O_8 and $Mo_3O_9H_n$ (n=1-3)

The DMMP adsorption on the reduced Mo_3O_8 cluster was simulated (**Figure III.1.3-5 (c)**). The DMMP adsorbed molecule has a slightly shortened P-OCH_3 (by ~0.015 Å) and elongated PO-CH_3 (by ~0.015 Å) bonds as compared to the DMMP molecule adsorbed on an ideal $(MoO_3)_3$ cluster (**Figure III.1.3-5 (b)**). The calculated desorption energy is 40.0 kcal/mol (**Figure III.1.3-5 (c)**, **Table III.1.3-1**), which is 8.0 kcal/mol higher than that on pristine $(MoO_3)_3$. The trend is consistent with previous studies on MoO_3 thin films, where oxygen defects were found to strengthen the binding of DMMP to molybdenum oxides.[13,14]

There is a negligible change in bond distances of the DMMP molecule adsorbed on the hydroxylated cluster in comparison to DMMP adsorbed on an ideal cluster (**Figure III.1.3-5 (b) and (d)**). The desorption energy of the DMMP molecule from the hydroxylated cluster is calculated to be 28.6 kcal/mol (**Figure III.1.3-5 (d)**, **Table III.1.3-1**). The desorption energies obtained for

different configurations of DMMP on $Mo_3O_9H_2$ and $Mo_3O_9H_3$ clusters fall in the range 19-28 kcal/mol (**Figure III.1.3-6 (b)-(h)**, **Table III.1.3-1**). Regardless of the number of hydrogens on the clusters, the binding of DMMP to hydroxylated clusters happens to be comparable or even weaker than the binding to the stoichiometric $(MoO_3)_3$ clusters. This observation differs from the previous studies on MoO_3 thin films, where the hydroxylated MoO_3 surface was found to provide much stronger adsorption, as compared to the pristine MoO_3 surface.[13,14] It was suggested that the pristine MoO_3 surface binds weakly to DMMP due to the lack of Lewis acid sites at the terminal oxygen layer.[13,14] Given the substantial structural difference between the pristine MoO_3 surface and the $(MoO_3)_3$ clusters, a different binding energy with DMMP should be expected for $(MoO_3)_3$ clusters. A direct comparison of the calculated desorption energies from MoO_3 surface and $(MoO_3)_3$ clusters is problematic because different computational schemes were used. Nonetheless, it's plausible that the strong Lewis acidity and also the open six-member ring structure of $(MoO_3)_3$ accommodate the DMMP molecule better than the pristine oxide surface both sterically and energetically.

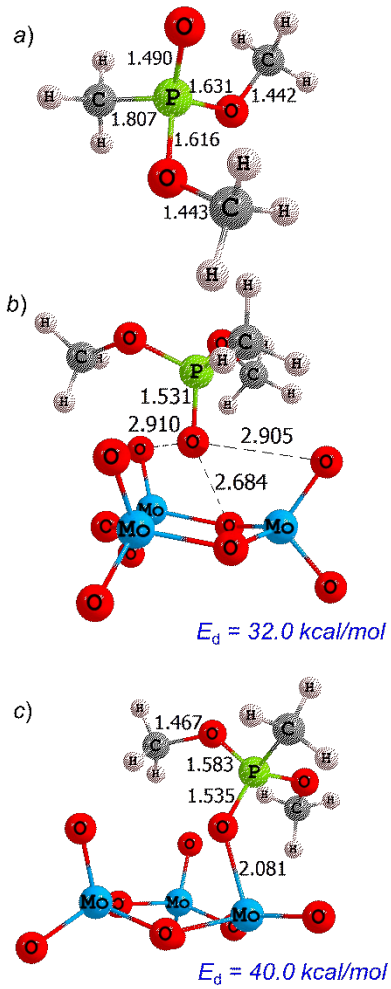

Figure III.1.3-5: The structures of the DMMP molecule (a) in the gas-phase, (b) adsorbed on a (MoO3)3 cluster, and (c) adsorbed on a reduced Mo3O8 cluster. Desorption energies (shown in blue) were calculated using B3LYP+D3 functional and included ZPVE corrections.

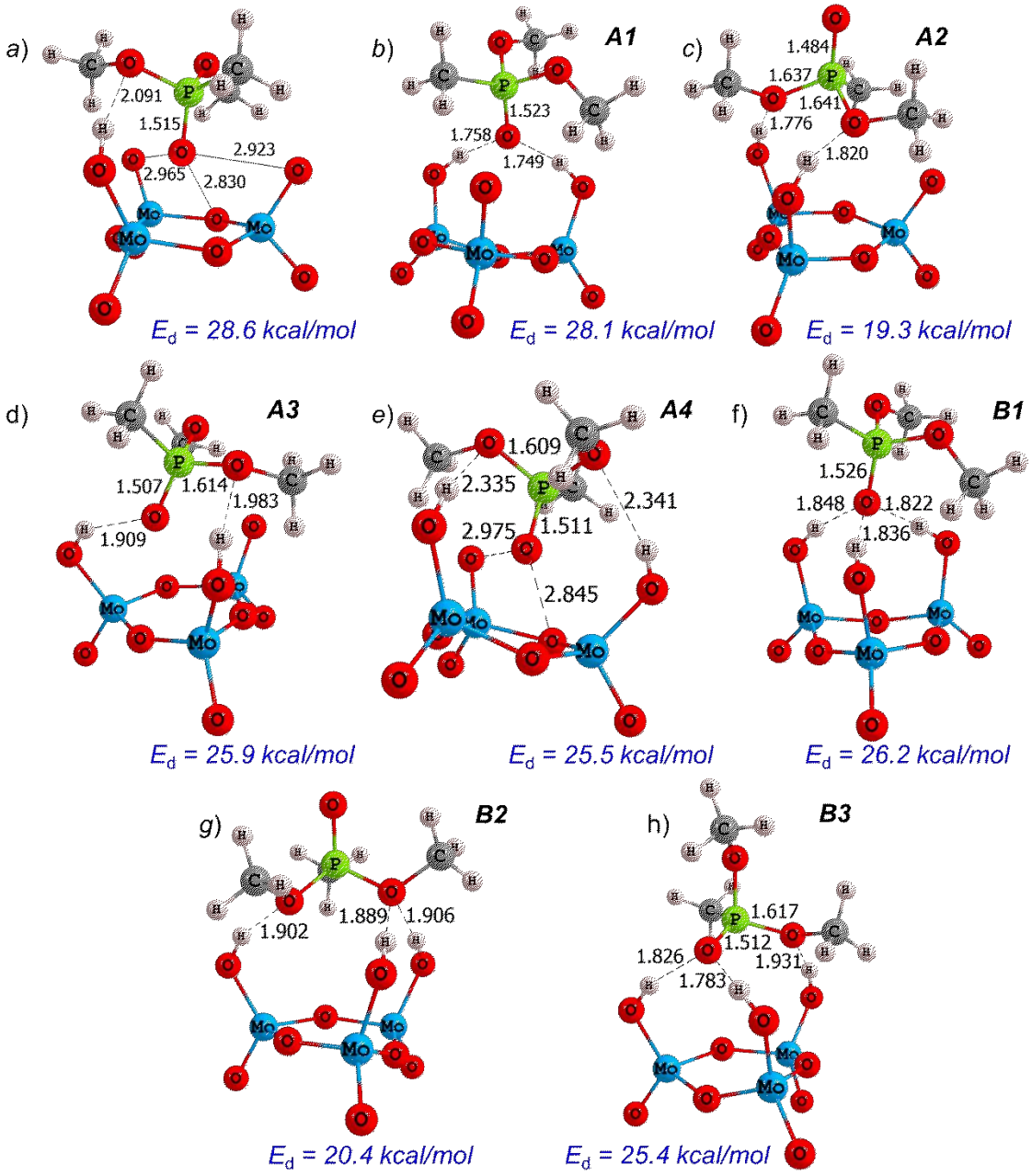

Figure III.1.3-6: The structures of the DMMP molecule adsorbed on the hydroxylated clusters in several configurations are shown: (a) Mo3O9H, (b) - (e) Mo3O9H2, and (f) - (h) Mo3O9H3 clusters. Desorption energies (shown in blue) were calculated using B3LYP+D3 functional

Table III.1.3-1: Calculated and experimental desorption energies (in kcal/mol) of the DMMP molecule from the molybdenum oxide clusters

Cluster/ Configuration		Theory							Exp.
		B3LYP		CAM-B3LYP		B3LYP+D3		SCAN[a]	
		E	E+ZPVE	E	E+ZPVE	E	E+ZPVE	E	
Mo_3O_9		19.1	17.7	25.6	24.1	33.8	32.0	35.7	
Mo_3O_8		29.5	28.6	35.4	34.2	41.4	40.0	35.8	
Mo_3O_9H		15.5	13.8	21.9	19.9	30.7	28.6	31.4	
$Mo_3O_9H_2$	*A1*	19.1	17.1	22.9	20.6	30.1	28.1	25.6	23.4
	A2	9.6	7.8	12.3	10.2	21.3	19.3	15.7	
	A3	15.9	14.0	20.3	18.2	28.0	25.9	23.5	
	A4	-		20.0	17.9	27.2	25.5	26.9	
$Mo_3O_9H_3$	*B1*	19.2	17.4	27.4	25.4	28.3	26.2	23.8	
	B2	11.2	9.6	19.8	18.0	22.6	20.4	15.0	
	B3	19.5	17.6	20.7	18.5	27.6	25.4	21.9	

[a] Total energies were refined through a single point calculation using the geometry structure optimized with B3LYP+D3 functional

III.1.4 DFT modeling of DMMP decomposition on Molybdenum Oxide Clusters

The decomposition mechanisms of an isolated DMMP molecule and adsorbed on a molybdenum oxide clusters were studied using the CAM-B3LYP functional. Although the CAM-B3LYP functional underestimates energies of the DMMP desorption from $(MoO_3)_3$ relative to the B3LYP+D3 method, the decomposition energies obtained using these functionals were found to be in good agreement.

To simulate the decomposition of DMMP, we analyzed the six most feasible reactions. They include (**Figure III.1.4-1**): (1) the cleavage of the P=O (Eq. 1, Path 1), (2) P-CH_3 (Eq. 2, Path 2), (3) O-CH_3 (Eq. 3, Path 3), and (4) P-OCH_3 (Eq. 4, Path 4) bonds, (5) the concerted intramolecular elimination of methanol (Eq. 5, Path 5), and (6) the methanol elimination involving the intermolecular (cluster-to-molecule) hydrogen transfer that can occur on the hydroxylated

$Mo_3O_9H_n$ (n=1,2) clusters (Eq. 6, Path 6). The obtained activation barriers and reaction energies are collected in **Table III.1.3-2**.

$(CH_3)PO(OCH_3)_2 \rightarrow (CH_3)P(OCH_3)_2 + {}^3O_{(atom)}$ (1)

$CH_3)PO(OCH_3)_2 \rightarrow {}^{\bullet}PO(OCH_3)_2 + {}^{\bullet}CH_3$ (2)

$(CH_3)PO(OCH_3)_2 \rightarrow (CH_3)PO(OCH_3)O^{\bullet} + {}^{\bullet}CH_3$ (3)

$(CH_3)PO(OCH_3)_2 \rightarrow (CH_3)P^{\bullet}O(OCH_3) + {}^{\bullet}OCH_3$ (4)

$((CH_3)PO(OCH_3)_2 \rightarrow (CH_2)PO(OCH_3) + HOCH_3$ (5)

$H_n(MoO_3)_3\text{-}(CH_3)PO(OCH_3)_2 \rightarrow H_{n-1}(MoO_3)_3\text{-}(CH_3)PO(OCH_3) + HOCH_3$ (6)

In the isolated DMMP molecule, the P=O bond breaking requires the highest energy (130.7 kcal/mol) among all probed reactions. The P-OCH_3 bond cleavage is a noticeably less costly process (93.1 kcal/mol), whereas the P-CH_3 and O-CH_3 bond breaking requires ~10 kcal/mol less energy (84.0 and 83.3 kcal/mol, respectively). The elimination of methanol is the most energetically favorable process with an activation barrier of 67.5 kcal/mol. These findings are consistent with results of the recent study reporting methyl and methanol, among other products, of DMMP pyrolysis in the gas-phase.[39]

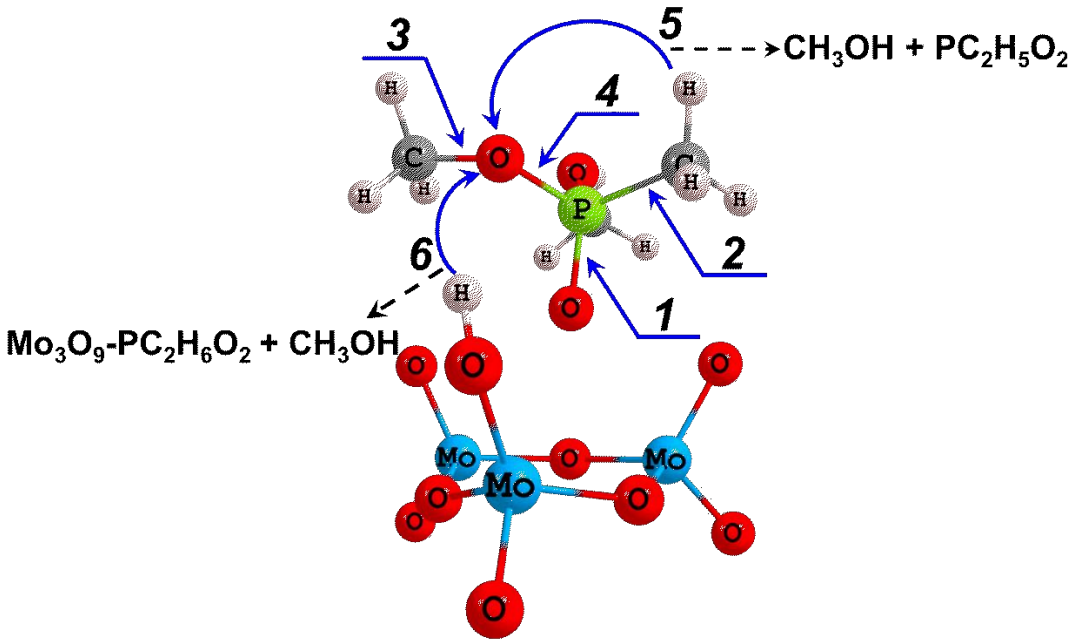

Figure III.1.4-1: Schematic representation of decomposition channels of DMMP: fission of (1) P=O (Eq. 1), (2) P-CH3 (Eq. 2), (3) O-CH3 (Eq. 3), (4) P-OCH3 (Eq. 4) bonds, (5) the methanol elimination through a concerted intramolecular hydrogen transfer (Eq. 5), and (6)

Table III.1.4-1: Calculated and experimental activation barries (in kcal/mol) of DMMP decomposition in gas phase and adsorbed on molybdenum oxide clusters.

Reaction		DMMP	DMMP adsorbed on Mo oxide cluster				EXP
			Mo_3O_9	Mo_3O_8	Mo_3O_9H	$Mo_3O_9H_2$	
1	P=O	130.7	-	-	-	-	-
2	P-CH_3	84.0	90.5	56.4	75.8	75.5	-
3	O-CH_3	83.3	91.3	22.1	30.7	20.6	29.7
4	P-OCH_3	93.1	95.9	68.1	87.6	70.3	-
5	CH_3OH loss (intramolecular)	67.5	72.3	70.7	71.5	71.4	29.8
6	CH_3OH loss (intermolecular)	-	-	-	23.9	20.0	

Once DMMP is adsorbed on ideal $(MoO_3)_3$ clusters, its decomposition requires even higher energy than decomposition of the isolated DMMP molecule (**Table III.1.3-2**). For example, the energy required for the cleavage of P-CH_3 and O-CH_3 bonds increases by ~6-8 kcal/mol. The methanol elimination remains the most favorable process and requires ~20 kcal/mol lower energy (72.3 kcal/mol) than the homolysis of the P-CH_3 (90.5 kcal/mol), O-CH_3 (91.3 kcal/mol) and P-

OCH_3 (95.9 kcal/mol) bonds. Thus, the ideal stoichiometric $(MoO_3)_3$ clusters would serve to stabilize the adsorbed DMMP molecule rather than degrading it.

Reduced Mo_3O_8 clusters behave notably differently. Significantly lower energies are characteristic for the decomposition of DMMP on the reduced Mo_3O_8 clusters as compared to the isolated molecule and ideal clusters (**Table III.1.3-2**). For instance, the O-CH_3 bond cleavage needs only 22.1 kcal/mol instead of 91.3 kcal/mol on the ideal $(MoO_3)_3$ cluster, showing a dramatic drop in activation energy. **Table III.1.3-1** shows a ~30 kcal/mol decrease of the P-CH_3 and P-OCH_3 bond energies relative to similar reactions of the DMMP molecule on an ideal cluster. Unlike these, the methanol loss reaction is barely affected by the lack of oxygen atom in the cluster configuration. The activation barrier predicted for methanol elimination from the DMMP molecule on Mo_3O_8 cluster (70.7 kcal/mol) is only 1.6 kcal/mol lower than in the molecule adsorbed on the ideal $(MoO_3)_3$ cluster (72.3 kcal/mol) and 2.8 kcal/mol higher than in gas-phase (67.5 kcal/mol). Interestingly, the O-CH_3 bond cleavage is the dominating reaction (rather than the methanol elimination) on the Mo_3O_8 clusters.

The decomposition of the DMMP molecule adsorbed on a hydroxylated Mo_3O_9H cluster via bond cleavage pathways requires lower energies than the gas-phase DMMP or DMMP on the ideal cluster (**Table III.1.3-2**). The energies of the P-OCH_3 (87.6 kcal/mol), P-CH_3 (75.8 kcal/mol), and O-CH_3 (30.7 kcal/mol) bonds cleavage are 8.3, 14.7, and 60.6 kcal/mol lower relative to the DMMP molecule adsorbed on an ideal cluster. The methanol elimination via intramolecular hydrogen transfer (Eq. 5, Path 5) requires 71.5 kcal/mol and is only 0.8 kcal/mol lower than the activation barrier calculated for DMMP on the ideal cluster (72.3 kcal/mol).

Hydroxylated clusters bring about an opportunity for intermolecular hydrogen transfer activated reactions. Thus, the methanol loss from DMMP on hydroxylated clusters may also proceed via intermolecular hydrogen transfer (Eq. 6, Path 6) unlike the similar reaction proceeding

through intramolecular hydrogen transfer in the isolated molecule, on the ideal or reduced clusters. **Table III.1.3-2** shows that this reaction channel dominates DMMP decomposition in the presence of hydroxyl groups and requires the activation energy as low as 23.9 kcal/mol on the hydroxylated Mo_3O_9H clusters and 20.0 kcal/mol on the $Mo_3O_9H_2$ clusters.

The O-CH_3 bond dissociation, the reaction competing with the methanol loss, in the DMMP molecule adsorbed on the $Mo_3O_9H_2$ cluster (20.6 kcal/mol) needs 10 kcal/mol lower energy than that on a Mo_3O_9H cluster (30.7 kcal/mol), whereas the activation barrier of intermolecular methanol elimination (Eq. 6, Path 6) is 20 kcal/mol. The intramolecular elimination of methanol remains high energy reaction that requires 71.4 kcal/mol and can be triggered at high temperature.

We conclude here that methanol loss reactions are dominating decomposition mechanisms in the isolated DMMP and DMMP on ideal stoichiometric clusters; the reactions are activated with a fairly high energy of ~70 kcal/mol, implying that DMMP is rather stable in these configurations and does not decompose well. The reduced clusters favor the O-CH_3 fission decomposition pathway with the low activation barrier of ~22.1 kcal/mol and barely affects the methanol elimination barrier. The hydroxylated clusters catalyze two competing channels, the O-CH_3 fission and the methanol loss through intermolecular hydrogen transfer with low activation energies of 20-30 kcal/mol while the intramolecular hydrogen transfer reaction would be still viable at high temperature (~70 kcal/mol).

III.1.5 Discussion

Adsorption and Desorption of DMMP on $(MoO_3)_3$

Our results allow us to analyze the adsorption characteristics of DMMP on $(MoO_3)_3$. The XPS results indicate that the initial adsorption of DMMP onto $(MoO_3)_3$ can occur at room temperature. The XPS spectra of the P(2p) region of DMMP on $(MoO_3)_3$ at room temperature already contained partially reduced phosphorus as shown in **Figure III.1.3-1 (a)**, although our

theory shows that stoichiometric $(MoO_3)_3$ clusters do not decompose DMMP well. In addition, previous studies in UHV suggested little or no decompositions of DMMP on stoichiometric MoO_3 at low pressure.[14] We speculated that the presence of partially reduced phosphorus at room temperature could be caused by some nonstoichiometric Mo_3O_{9-x} cluster species present on HOPG, which have the capability to decompose DMMP, similar to the reduced MoO_3 surface.[13] It is interesting to note that each $(MoO_3)_3$ cluster adsorbs about one DMMP molecule evident from a 1:3 P to Mo ratio from XPS envelope fitting, possibly due to steric effects and limited adsorption sites on the clusters. This is in good agreement with the results of our theoretical modeling, which show that the binding energy of a second DMMP molecule (12.5 kcal/mol) is ~8 kcal/mol lower than that of the first (19.5 kcal/mol). In addition, the P to Mo ratio observed here is significantly higher than that observed in MoO_3 thin films,[13] probably due to the high dispersion of these isolated $(MoO_3)_3$ clusters as well as their higher binding affinity to DMMP resulting from their increased Lewis acidity as compared to bulk MoO_3.[20]

Additionally, the decreasing of the P to Mo ratio in XPS upon heating (**Figure III.1.3-3**) and the TPR results (**Figure III.1.3-4**) provide some insight into the desorption behavior of DMMP on these clusters. The TPR profile of both the DMMP parent ion (124 amu) and its major fragment (79 amu) exhibited a desorption peak around 100 ^oC, which is consistent with the large decrease in the P to Mo ratio from RT to 200 ^oC. This resulted in a desorption energy, as calculated via Redhead Analysis, of about 23.4 kcal/mol (**Table III.1.3-1**). Upon comparing to theory, the desorption energy of DMMP from $(MoO_3)_3$ clusters falls in the range of theoretically calculated values for DMMP desorbed from stoichiometric $(MoO_3)_3$ clusters (32 kcal/mol), Mo_3O_9H clusters (28.6 kcal/mol), $Mo_3O_9H_2$ clusters (19.3-28.1 kcal/mol), and $Mo_3O_9H_3$ clusters (20.4-26.2 kcal/mol), (**Table III.1.3-1**). The experimentally determined desorption energy is calculated from the peak center of the DMMP desorption profiles (124 and 79 amu), but when the broadness and skewness of the peaks are considered it indicates the presence of a range of desorption energies (**Figure**

III.1.3-4). Given the little information known about the nature and energetics of adsorption sites, a direct spectral deconvolution will be premature here. However, the broad range of desorption energies can be explained by a non-homogenous composition in the deposited clusters. Such non-homogenous composition for the deposited clusters will consequently affect the decomposition of DMMP as discussed below.

Decomposition of DMMP on Molybdenum Oxide Clusters

What are the reaction pathways and the reaction products of DMMP on $(MoO_3)_3$ and its reduced forms?

First, the reduction of the phosphorus of DMMP on $(MoO_3)_3$ was seen in XPS at elevated temperatures, indicated by a shift of P(2p) peak to lower binding energy (**Figure III.1.3-1 (b)**). Previous studies on titania and ceria assigned the reduced phosphorus species to methyl methylphosphonate and methyl phosphonate due to a stepwise loss of methoxy groups.[7,40] The TPR results in this work showed the evolution of methanol indicating that methoxy groups pick up a hydrogen and evolve into the gas phase leaving behind methyl methylphosphonate, which is similar to the case of DMMP on titania and ceria.[7] This also agrees well with previous ambient pressure XPS studies on defect-rich MoO_3 surface, which suggested a loss of methanol during DMMP decomposition.[13] However, the desorption energy of methanol from Redhead Analysis of TPR (29.8 kcal/mol) is significantly lower than the calculated activation barrier of methanol elimination from the DMMP molecule adsorbed on the stoichiometric $(MoO_3)_3$ (72.3 kcal/mol) and the non-stoichiometric Mo_3O_8 (70.7 kcal/mol) clusters (**Table III.1.3-2**). This discrepancy between the experimental value and theoretical prediction is still substantial even after taking the underestimation of the frequency factor used in Redhead analysis into account. Alternatively, according to the results of our theoretical modeling, the presence of hydroxyls on the cluster may cause an approximately four-fold reduction of the energy required for methanol elimination (**Table**

III.1.3-2, **Figure III.1.5-1**). The calculated activation barrier for methanol loss via cluster-to-molecule hydrogen transfer (Eq. 6) requires 20-24 kcal/mol which are comparable to the experimentally estimated activation energy of 29.8 kcal/mol (**Table III.1.3-2**).

The proposed intermolecular hydrogen transfer mechanism is in agreement with earlier results on metal oxide surfaces indicating the important role of surface hydroxyls as nucleophiles in methanol elimination from DMMP.[6] Recent XPS studies from Head *et. al.* also suggested the presence of neighboring surface hydroxyls is responsible for the methanol elimination.[13] We note, although the initial clusters deposited onto the graphite surface are stoichiometric $(MoO_3)_3$, the elevated surface temperature can easily lead to the formation of the reduced metal center, which promotes the dissociation process of residual water molecules to form hydroxylated metal oxide even at UHV conditions. It is evident from our study that the importance of surface defects and hydroxyl groups is also applicable to the corresponding cluster species.

An analysis of the decomposition energies, collected in **Table III.1.3-1**, revealed that the loss of a methyl group from DMMP seen in the TPR (**Figure III.1.3-4**) with an activation energy of 29.7 kcal/mol can be explained by the O-CH_3 bond cleavage in the DMMP molecule adsorbed on a reduced Mo_3O_8 and hydroxylated $Mo_3O_9H_n$ (n=1,2) clusters. Our calculations determined the decomposition energy of this bond cleavage are 22.1 (Mo_3O_8), 30.7 (Mo_3O_9H) and 20.6 ($Mo_3O_9H_2$) kcal/mol (**Table III.1.3-2**), in good agreement with experiment. This indicates some level of structure sensitivity in the decomposition of DMMP between the different stoichiometries of clusters with the non-stoichiometric Mo_3O_8 cluster preferentially removing a methoxyl methyl group and the Mo_3O_9H cluster preferentially removing an intact methoxy group via methanol elimination, while the $Mo_3O_9H_2$ cluster supports DMMP decomposition along either pathway.

The results of our joint experimental and theoretical study revealed the effect of surface hydroxyl and reducible metal centers on the reaction pathway and product distributions of DMMP

decomposition. The activation energies required for methanol and methyl loss from DMMP adsorbed on $Mo_3O_9H_n$ (n=1,2) and Mo_3O_8 clusters are 3-4 times lower compared to the gas-phase and decomposition on the ideal stoichiometric cluster. Practically, reduced Mo_3O_8 can be easily generated by thermal reductions of Mo_3O_9 clusters on graphite support and hydroxylated clusters are immediate products of residual water and reduced metal oxide clusters. A full catalytic cycle can be viewed as a water-assisted "reverse Mars–van Krevelen mechanism".[41,42] The bond cleavage of DMMP is driven by reduced metal oxides (Mo^{4+} and Mo^{5+}) and the presence of water facilitates the formation of the methanol via an intermolecular hydrogen transfer mechanism. The reduced metal oxides can be easily regenerated under thermal treatment due to a high reducibility of Mo metal center within the clusters on graphite support.[43] It is interesting to note that in previous studies regeneration of metal oxides is usually carried out by thermal annealing under oxygen environment.[41,44] This procedure usually resulted in a higher affinity to DMMP but a lower activity toward decomposition.[44] The higher affinity to DMMP is likely due to an increase in Lewis acidity from the presence of PO_x.[45] According to the mechanism we proposed here, oxygen annealing would not recover the oxygen vacancies thus a low activity toward DMMP decomposition was found. To further verify the proposed mechanism, two different metal oxide clusters, i.e. $(WO_3)_3$ and $(ZrO_2)_3$ were chosen to study the relationship between the reducibility of metal center and their reactivity toward DMMP. The study is currently ongoing. Last, a possible inference with the proposed catalytic route is the potential poison effect of the residual PO_x species left on the MoO_3 surface. However, this may not be practically significant given the relatively cheap cost of MoO_3 oxides and also the low concentrations of the phosphorus species.

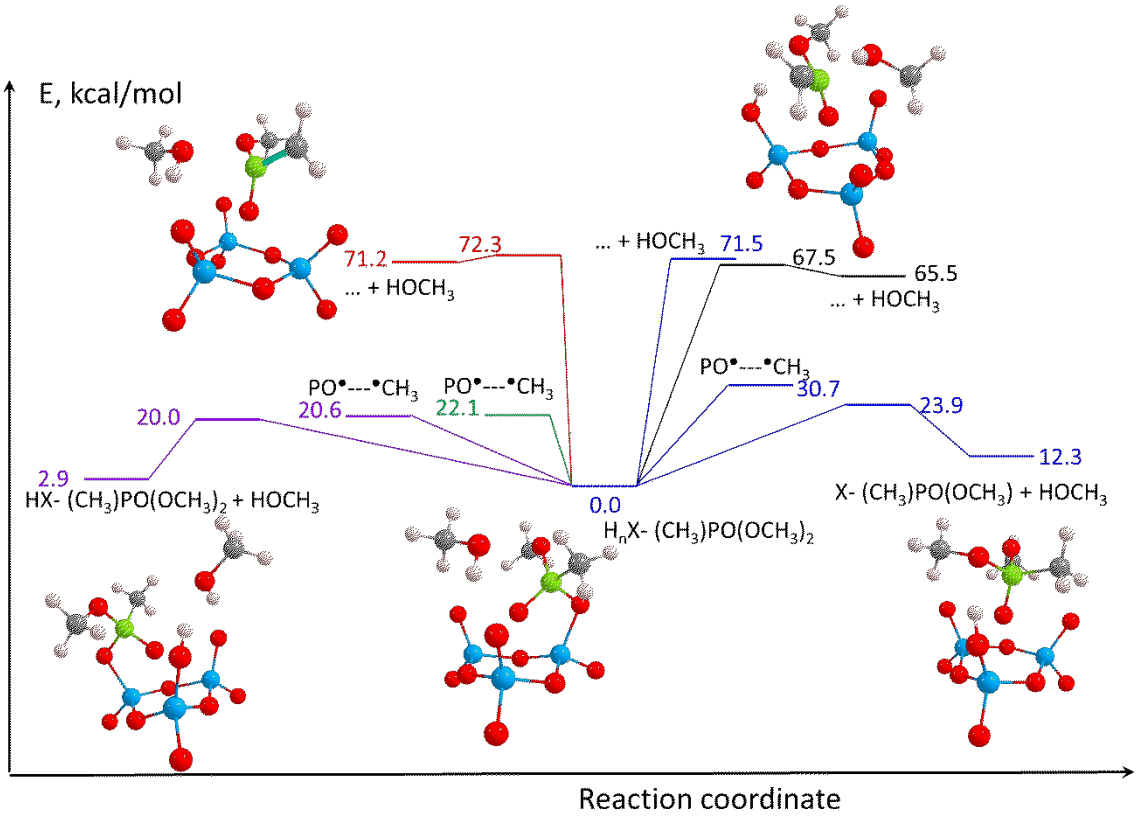

Figure III.1.5-1: Schematic energy diagram for the decomposition of DMMP. Blue lines correspond to decomposition pathways of DMMP adsorbed on a Mo3O9H cluster, purple - Mo3O9H2, green – Mo3O8 cluster, red – (MoO3)3 cluster, and black – gas phase.

III.1.6 Conclusion

The adsorption and decomposition behaviors of DMMP on size-selected $(MoO_3)_3$ clusters were studied experimentally by XPS and TPR and theoretically by DFT calculations. The experimental results indicated the decomposition of DMMP on $(MoO_3)_3$ involves the loss of methoxy groups leading to the elimination of methanol during the reaction, and the experiments provided the measured desorption energies that helped validate the theoretical calculations. The theoretical calculations determined that hydroxyl groups on the cluster and partially reduced, non-stoichiometric, clusters had significantly lowered activation barriers for DMMP decomposition, showing the importance of the reducibility of a metal center and the presence of residual hydroxyl groups in metal oxide catalysis. The Group VI transition metal oxide based cluster materials are

potential candidates for adsorption and decomposition of CWA with similar structures to DMMP due to their structural fluxionality and Lewis acidity. A combination of XPS and TPR measurements coupled with DFT modeling is a powerful methodology to explore how chemical activity and selectivity of the clusters towards decomposition of CWA compounds depends on their structure and chemical composition. This knowledge could be further used for rational design of new materials with targeted catalytic properties.

III.1.7 Acknowledgments

This material is based upon work supported by the Defense Threat Reduction Agency (DTRA) under grant number HDTRA1-15-1-0005. R.T. and M.M.K acknowledge support from NSF XSEDE resources (Grant DMR-130077) and DOE NERSC resources (Contract DE-AC02-05CH11231) and computational resources at the Maryland Advanced Research Computing Center (MARCC).

---

[1] S. Yenisoy-Karakas, A. Aygun, M. Gunes, E. Tahtasakal, Carbon, 2004, **42**, 477-484.

[2] B. Aurianblajeni, M.M. Boucher, Langmuir, 1989, **5**, 170-174.

[3] C.N. Rusu, J.T. Yates, Journal of Physical Chemistry B, 2000, **104**, 12292-12298.

[4] L. Yang, D. Tunega, L. Xu, N. Govind, R. Sun, R. Taylor, H. Lischka, W.A. DeJong, W.L. Hase, Journal of Physical Chemistry C, 2013, **117**, 17613-17622.

[5] Bermudez, V. M. Quantum-Chemical Study of the Adsorption of DMMP and Sarin on γ-Al_2O_3. J. Phys. Chem. C, 2007, **111**, 3719-3728

[6] M.B. Mitchell, V.N. Sheinker, E.A. Mintz, Journal of Physical Chemistry B, 1997, **101**, 11192-11203.

[7] D.A. Chen, J.S. Ratliff, X.F. Hu, W.O. Gordon, S.D. Senanayake, D.R. Mullins, Surface Science, 2010, **604**, 574-587.

[8] A.R. Wilmsmeyer, J. Uzarski, P.J. Barrie, J.R. Morris, Langmuir, 2012, **28**, 10962-10967.

[9] A.R. Wilmsmeyer, W.O. Gordon, E.D. Davis, D. Troya, B.A. Mantooth, T.A. Lalain, J.R. Morris, Journal of Physical Chemistry C, 2013, **117**, 15685-15697.

[10] D.E. Taylor, K. Runge, M.G. Cory, D.S. Burns, J.L. Vasey, J.D. Hearn, K. Griffith, M.V. Henley, Journal of Physical Chemistry C, 2013, **117**, 2699-2708.

[11] D. Troya, A.C. Edwards, J.R. Morris, Journal of Physical Chemistry C, 2013, **117**, 14625-14634.

[12] Y. Paukku, A. Michalkova, J. Leszczynski, Journal of Physical Chemistry C, 2009, **113**, 1474-1485.

[13] A.R. Head, R. Tsyshevsky, L. Trotochaud, Y. Yu, L. Kyhl, O. Karslioglu, M.M. Kuklja, H. Bluhm, Journal of Physical Chemistry C, 2016, **120**, 29077-29088.

[14] A.R. Head, et al., Catalysis, Structure & Reactivity, 2017, **3**, 112-118.

[15] L. Trotochaud, R. Tsyshevsky, S. Holdren, K. Fears, A.R. Head, Y. Yu, O. Karslıoğlu, S. Pletincx, B. Eichhorn, J. Owrutsky, J. Long, M. Zachariah, M.M. Kuklja, H. Bluhm, Chemistry of Materials, 2017, **29**, 7483-7496.

[16] Y.C. Yang, J.A. Baker, J.R. Ward, Chemical Reviews, 1992, **92**, 1729-1743.

[17] K. Kim, O.G. Tsay, D.A. Atwood, D.G. Churchill, Chemical Reviews, 2011, **111**, 5345-5403.

[18] G. Fu, X. Xu, X. Lu, H. Wan, J. Am. Chem. Soc., 2005, **127**, 3989-3996

[19] G. Fu, X. Xu, X. Lu, H. Wan, J. Phys. Chem. B., 2005, **109**, 6416-6421

[20] X. Tang, D. Bumueller, A. Lim, J. Schneider, U. Heiz, G. Ganteför, D. H. Fairbrother, K.H. Bowen, J. Phys. Chem. C, 2014, **118**, 29278−29286

[21] P. Hohenberg and W. Kohn, Phys. Rev. B: Condens. Matter Mater. Phys., 1964, 136, B864.

[22] W. Kohn and L. J. Sham, Phys. Rev., 1965, **140**, 1133.

[23] C. T. Lee, W. T. Yang and R. G. Parr, Phys. Rev. B: Condens. Matter Mater. Phys., 1988, **37**, 785–789.

[24] A. D. Becke, J. Chem. Phys., 1993, **98**, 5648–5652.

[25] T. Yanai, D. P. Tew and N. C. Handy, Chem. Phys. Lett., 2004, **393**, 51–57.

[26] S. Grimme, J. Antony, S. Ehrlich and H. Krieg, J. Chem. Phys., 2010, **132**, 154104.

[27] J. W. Sun, A. Ruzsinszky and J. P. Perdew, Phys. Rev. Lett., 2015, **115**, 036402.

[28] J. Sun, J. Sun, et al., Nat. Chem., 2016, 8, 831–836et al., Nat. Chem., 2016, **8**, 831–836.

[29] P. J. Hay and W. R. Wadt, J. Chem. Phys., 1985, **82**, 270–283.

[30] P. J. Hay and W. R. Wadt, J. Chem. Phys., 1985, **82**, 299–310.

[31] W. R. Wadt and P. J. Hay, J. Chem. Phys., 1985, **82**, 284–298.

[32] H. P. Hratchian and H. B. Schlegel, J. Chem. Phys., 2004, **120**, 9918–9924.

[33] H. P. Hratchian and H. B. Schlegel, J. Chem. Theory Comput., 2005, **1**, 61–69.

[34] M. J. Frisch, et al., Gaussian 09, Gaussian, Inc., Wallingford, CT, USA, 2009.

[35] M. J. Frisch, et al., Gaussian 03, Revision D.02, Gaussian, Inc., Wallingford CT, USA, 2004.

[36] X. Li, K.A. Wepasnick, X. Tang, Y. Wang, K.H. Bowen, D.H. Fairbrother, G. Gantefoer, J Vac Sci Technol B, 2012, **30**, 031806.

[37] J.L. Falconer, J.A. Schwarz, Catalysis Reviews-Science and Engineering, 1983, **25**, 141-227.

[38] H. Bluhm, Journal of Electron Spectroscopy and Related Phenomena, 2010, **177**, 71-84.

[39] S.Y. Liang, P. Hemberger, N.M. Neisius, A. Bodi, H. Grutzmacher, J. Levalois-Grutzmacher, S. Gaan, Chemistry-a European Journal, 2015, **21**, 1073-1080.

[40] J. Zhou, K. Varazo, J.E. Reddic, M.L. Myrick, D.A. Chen, Analytica Chimica Acta, 2003, **496**, 289-300.

[41] T.M. Tesfai, V.N. Sheinker, M.B. Mitchell, Journal of Physical Chemistry B, 1998, **102**, 7299-7302.

[42] A.V. Mironenko, D.G. Vlachos, Journal of the American Chemical Society, 2016, **138**, 8104-8113.

[43] Z.J. Li, Z.T. Fang, M.S. Kelley, B.D. Kay, R. Rousseau, Z. Dohnalek, D.A. Dixon, Journal of Physical Chemistry C, 2014, **118**, 4869-4877.

[44] D.A. Panayotov, J.R. Morris, Langmuir, 2009, **25**, 3652-3658.

[45] M. Ai, S. Suzuki, Journal of Catalysis, 1973, **30**, 362-371.

III.2 Adsorption and Decomposition of DMMP on Size-Selected $(WO_3)_3$ Clusters

Xin Tang[1], Zachary Hicks[1], Gerd Ganteför[2], Bryan W. Eichorn[3], Kit H. Bowen[1]

[1] Department of Chemistry, Johns Hopkins University, Baltimore, Maryland 21218, USA

[2] Department of Physics, University of Konstanz, 78464 Konstanz, Germany

[3]Department of Materials Science, University of Maryland, College Park, Maryland 20742, USA

The adsorption and decomposition behaviors of dimethyl methylphosphate (DMMP) on size-selected $(WO_3)_3$ clusters were studied by a combination of X-ray Photoelectron Spectroscopy (XPS) and Temperature Programmed Reaction (TPR). The fate of DMMP adsorbed on $(WO_3)_3$ clusters was found to be very similar to its fate on $(MoO_3)_3$. In contrast to DMMP on $(MoO_3)_3$, however, dimethyl ether was observed as a product in the reaction of DMMP with $(WO_3)_3$, in addition to methanol, due to the higher Lewis acidity of $(WO_3)_3$ clusters as compared to $(MoO_3)_3$.

III.2.1 Introduction

The surface chemistry of chemical warfare agents is of critical importance to the rational design of sensors to detect chemical warfare agents and sorbents to decontaminate them.[1] Organophosphorus compounds are commonly used as chemical warfare agents,[2] and therefore, the adsorption and decomposition behaviors of organophosphates are widely studied by many research groups.[3,4,5,6,7] Of all the organophosphates, dimethyl methylphosphate (DMMP) has attracted considerable attention, since it has a similar structure to many nerve agents but a much lower toxicity, allowing for easier study. Thus, DMMP is frequently used as a structural simulant in many

related studies of chemical warfare agents.[2,8,9,10,11,12,13] Using DMMP as a model molecule, the reactivity of many metals and metal oxides toward DMMP has been studied, i.e. MoO_3,[14] Cu,[15] CuO,[16] MgO,[17] ZnO,[18] CeO_2,[13] TiO_2,[10] $Y2O_3$,[19] etc.. As illustrated in these studies, DMMP usually undergoes a stepwise loss of methoxy groups on the metal oxide surface, resulting in methanol being observed as a common hydrolysis reaction product for DMMP on many oxide surfaces.[20] In addition to the hydrolysis reaction, reduction processes are also observed when surface defects, i.e. oxygen vacancies, are present.[10] It has also been noted that both the acidity and reducibility of metal oxides are known to affect the adsorption behavior and the decomposition pathway of DMMP molecules.[16,21,22] The acidity of metal oxides can affect the binding strength of the DMMP molecule to Lewis and/or Brønsted acid sites on the surface of metal oxides, while the reducibility of metal oxides enables the production of oxygen vacancies, which act as potential active sites to decompose DMMP molecules via a redox mechanism.[16] In this work, the adsorption and decomposition behaviors of DMMP on tungsten oxide trimer clusters, $(WO_3)_3$ were studied via a combination of X-ray Photoelectron Spectroscopy (XPS) and Temperature Programmed Reaction (TPR). Prior work has been performed studying the adsorption of DMMP on bulk WO_3.[12] However, there is a lack of detailed understanding on the interaction between DMMP and nanostructured tungsten oxides with structural controls, despite the fact that tungsten oxide nanoclusters are well-known structure-sensitive catalysts.[23] Our previous studies on the decomposition of DMMP on $(MoO_3)_3$ clusters indicated that the adsorption and decomposition of DMMP on metal oxide clusters depend heavily on the Lewis acidity of metal oxides and the oxygen vacancies within the clusters.[22] Since tungsten oxide clusters are usually used as strong solid acid catalysts industrially,[24] a study of their interaction with DMMP can shed light on the role of the Lewis and Brønsted acidity on both the adsorption and decomposition behaviors of DMMP. The $(WO_3)_3$ clusters were size-selected and soft-landed into a frozen matrix of DMMP multilayers supported on Highly Oriented Pyrolytic Graphite (HOPG) and their interactions with DMMP were studied by spectroscopic tools.

III.2.2 Results and Discussion

The XPS spectra of P(2p) regions of DMMP on $(WO_3)_3$ are shown in **Figure III.2.2-1**. In comparison to previous studies on $(MoO_3)_3$,[22] the evolution of the P(2p) peak exhibited a similar trend: Initial annealing from room temperature to 200 °C resulted in the shift of P(2p) peak to a lower binding energy, indicating a reduction of phosphorous species; Further annealing to 300 °C did not significantly change the spectral envelope and their intensity; Finally, after annealing to 400 °C, the P(2p) peak shifted slightly back to the higher binding energy, indicating a possible re-oxidation of phosphorous species. Additionally, during heating, the tungsten oxide was also reduced as indicated by the shift of the W(4f) peak to a lower binding energy as well as the broadening of the spectral envelopes as shown in **Figure III.2.2-2 (b)**. Interestingly, the reduction of WO_3 was observed at as low as 200 °C, resulting in the formation of low valency tungsten species. It is suggested that the underlying graphite support may promote the reduction of the $(WO_3)_3$ cluster.[25] It is worth noting that the initial reduction of WO_3 appears to synchronize with the reduction of phosphorous species, as indicated in **Figure III.2.2-1**. It is known from previous studies on TiO_2, that the annealing process introduces the oxygen vacancies as well as conduction band electrons in reducible metal oxides, which act as the active species for reducing phosphorus.[4]

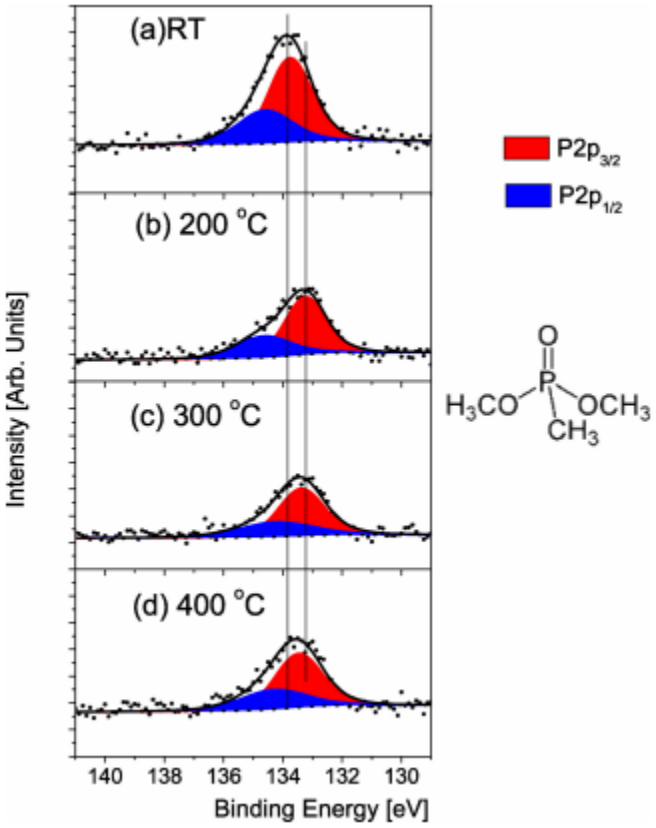

Figure III.2.2-1: P(2p) envelope of DMMP/ (WO3)3: (a) Room Temperature (b) 200 °C (c) 300 °C (d) 400 °C; The structure of DMMP is shown on the right.

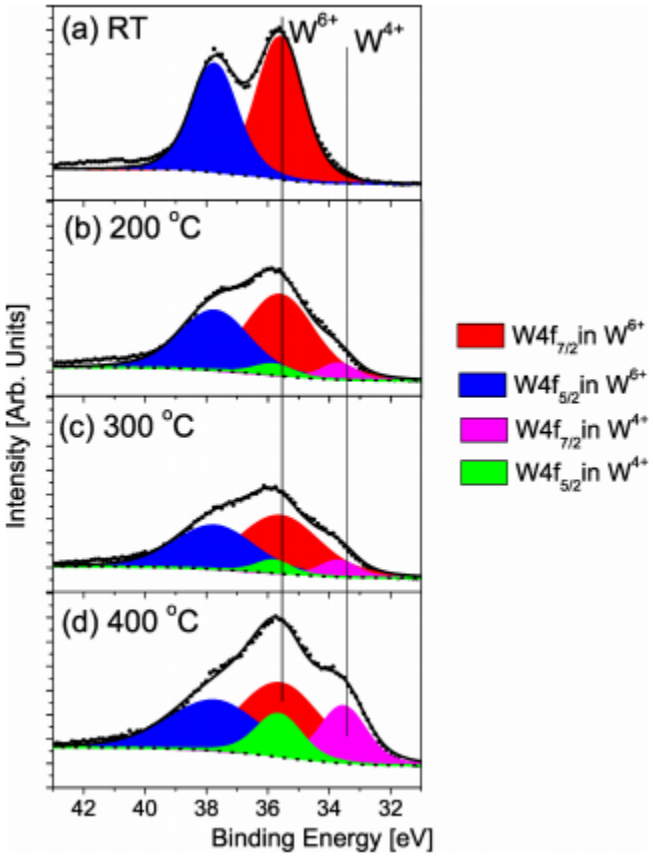

Figure III.2.2-2: W(4f) Envelope of DMMP/ (WO3)3: (a) Room Temperature (b) 200 °C (c) 300 °C (d) 400 °C

The loading of DMMP per tungsten atom as a function of the annealing temperature was also calculated and displayed in **Figure III.2.2-3** by dividing the integrated spectral area with the relative sensitivity factor for both W(4f) and P(2p) regions. The initial ratio of P to W was calculated to be 0.33, indicating that only one DMMP molecule can adsorb to each $(WO_3)_3$ cluster. As shown in the plot, the vast majority of DMMP desorbed upon heating to 200 °C, and then remained mostly constant from 200 °C to 300 °C. Further annealing to 400 °C resulted in additional loss of phosphorous species.

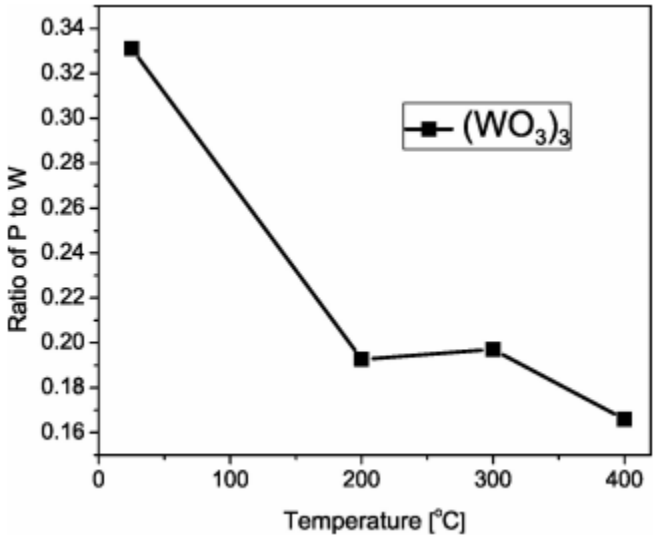

Figure III.2.2-3: Ratio of P to W as a function of the annealing temperature

The TPR results of DMMP on $(WO_3)_3$ clusters are shown in **Figure III.2.2-4**. The intact DMMP was observed to desorb at a lower temperature around 100 °C as shown in the desorption profile at 79 amu, which is the mass of the major fragment of DMMP. This is consistent with the fact that the vast majority of DMMP desorbed between room temperature and 200 °C, as indicated in the XPS experiment (**Figure III.2.2-3**). Methanol and dimethyl ether were also observed as major desorption products at higher temperatures. The desorption of dimethyl ether is reflected by the desorption peak around 245 °C at 46 amu, which is the mass of the parent ion of dimethyl ether. The desorption of methanol is indicated by the desorption peak around 275 °C at both 31 amu and 32 amu. By assuming a frequency factor of 10^{13} s^{-1}, the desorption energy of DMMP, dimethyl ether and methanol are calculated to be 23.4, 32.8 and 34.8 kcal/mol, respectively, using a simple Redhead analysis.[26] It is suggested by many studies that methoxides are intermediates that lead to the formation of methanol and dimethyl ether.[13] Therefore, the activation barrier from methoxy to dimethyl ether seems lower than that to methanol.

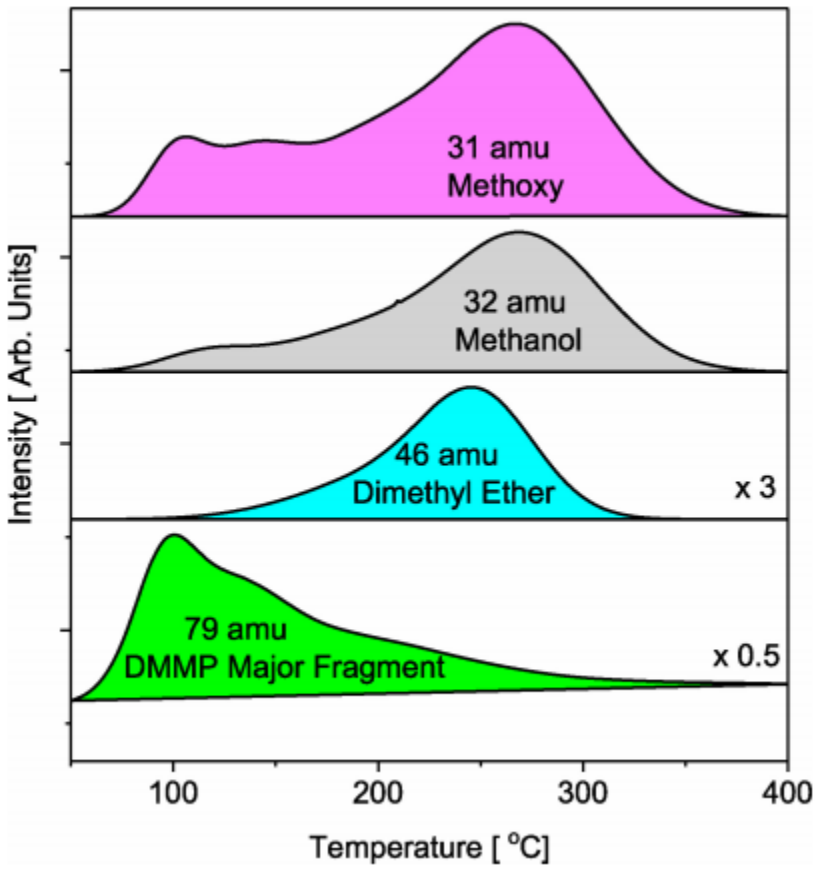

Figure III.2.2-4: TPR Profiles of DMMP on (WO3)3

III.2.3 Conclusions

The adsorption behavior of DMMP on $(WO_3)_3$ is very similar to that on $(MoO_3)_3$ clusters. The interaction between DMMP and $(MO_3)_3$ (M= Mo, W) both resulted in a metal to P ratio of 3:1 at room temperatures, indicating that, for each $(MO_3)_3$ cluster, only one DMMP molecule can adsorb to it. It's suggested by Wang[27] and Dixon[28] that $(WO_3)_3$ and $(MoO_3)_3$ clusters share a similar six-member ring structure and that their electronic structures are comparable. Thus, a similar adsorption geometry and steric interaction with DMMP may be expected for both $(MO_3)_3$ (M= Mo, W) clusters. The decomposition of DMMP on $(WO_3)_3$ was also revealed by XPS and TPR. As indicated in the XPS studies, reductions of both the phosphorous species and the metal oxides were observed after annealing to 200 °C, which is also similar to DMMP on $(MoO_3)_3$ clusters. Very

likely, the reduction of the phosphorous species may have to do with the production of oxygen vacancies, caused by the annealing of metal oxides on the graphite support. Previous studies on both molybdenum oxide thin films and clusters suggested that the oxygen vacancies present on the metal oxide surface may hydroxylate and facilitate both the adsorption and decomposition of DMMP on metal oxides.[14,21,22] The resulting intermolecular hydrogen transfer between hydroxyls on the cluster and the methoxy groups can lead to the loss of methoxy groups and the formation of methanol, which is supported by in situ XPS[14] and TPR[22] studies. Since the desorption of methanol was also observed for DMMP on $(WO_3)_3$ clusters, the pathway of DMMP on $(WO_3)_3$ may follow a similar route, starting with the thermal annealing of $(WO_3)_3$ clusters, resulting in the formation of reduced tungsten species, i.e. W^{5+} and W^{4+}. The reduced metal centers can not only interact with residual water to form surface hydroxyl groups, but also can reduce the phosphorous species in DMMP as indicated in the shift of P(2p) peak to a lower binding energy. It is suggested that methyl methylphosphate (MMP) and methylphosphate (MP) are formed on the oxide surface during the step-loss of the methoxy groups.[29] The production of methanol was also believed to be caused by an intermolecular hydrogen transfer from an adjacent hydroxyl group to methoxides.[29] Further annealing to 400 °C resulted in the P(2p) peak shifting back to a slightly higher binding energy. This is usually attributed to the formation of PO_x species due to the cleavage of P-CH3 bond at higher temperatures.[29] Moreover, different from that on $(MoO_3)_3$, the formation of dimethyl ether was observed for DMMP on $(WO_3)_3$ clusters. It's well-known that solid acid catalysts can facilitate the dehydration reaction of methanol to dimethyl ether.[30,31] It is suggested by Neurock and Iglesia that the strong acid catalysts will favor the reaction pathway to dimethyl ether from surface methoxides by stabilizing the transition state to form dimethyl ether.[31,32,33] Indeed, the $(WO_3)_3$ cluster is a strong Lewis acid, as indicated by its ability to dehydrate 2-propanol to propene.[34] In addition, the interaction of DMMP and metal oxide surfaces is known to form surface methoxides.[14] Therefore, the stronger Lewis acidity of $(WO_3)_3$ relative to $(MoO_3)_3$ can readily lead to the

desorption of dimethyl ether as a consequence of the reaction between DMMP on $(WO_3)_3$ clusters. The different fate of DMMP on these two metal oxide clusters underlined that the difference in Lewis acidity of metal oxide clusters can lead to different product distributions of DMMP possibly by providing different degree of the stabilization of transition states. In summary, the adsorption behavior and the decomposition pathways of DMMP on $(WO_3)_3$ clusters were studied by in situ XPS and TPR. Overall, both the adsorption and the decomposition of DMMP on $(WO_3)_3$ are very similar to that on $(MoO_3)_3$. Only one DMMP molecule can adsorb to each $(WO_3)_3$ cluster. The reduced tungsten species are responsible for decomposing the DMMP molecules. Furthermore, in addition to methanol, dimethyl ether was also observed as the reaction product due to the strong Lewis acidity of $(WO_3)_3$ clusters.

III.2.4 Acknowledgments

This material is based upon work supported by the Defense Threat Reduction Agency (DTRA) under grant number HDTRA1-15-1- 0005.

---

[1] Y. C. Yang, J. A. Baker, J. R. Ward, Chem. Rev., 1992, **92**, 1729–1743.

[2] O. P. Korobeinichev, S. B. Ilyin, T. A. Bolshova, V. M. Shvartsberg, A. A. Chernov, Combust. Flame, 2000, **121**, 593–609.

[3] A. R. Wilmsmeyer, J. Uzarski, P. J. Barrie, J. R. Morris, Langmuir, 2012, **28**, 10962–10967.

[4] D. A. Panayotov, J. R. Morris, Langmuir, 2009, **25**, 3652–3658.

[5] M. K. Ferguson-McPherson, E. R. Low, A. R. Esker, J. R. Morris, J. Phys. Chem. B, 2005, **109**, 18914–18920.

[6] J. S. Ratliff, S. A. Tenney, X. Hu, S. F. Conner, S. Ma, D. A. Chen, Langmuir, 2009, **25**, 216–225.

[7] S. Ma, J. Zhou, Y. C. Kang, J. E. Reddic, D. A. Chen, Langmuir, 2004, **20**, 9686–9694.

[8] G. Wang, C. Sharp, A. M. Plonka, Q. Wang, A. I. Frenkel, W. Guo, C. Hill, C. Smith, J. Kollar, D. Troya, J. R. Morris, J. Phys. Chem. C, 2017, **121**, 11261–11272.

[9] Y. Wang, Z. Zhou, Z. Yang, X. Chen, D. Xu, Y. Zhang, Nanotechnology, 2009, **20**, 345502.

[10] D. A. Panayotov, J. R. Morris, Langmuir, 2009, **25**, 3652–3658.

[11] A. Mattsson, C. Lejon, V. Sˇtengl, S. Bakardjieva, F. Oplusˇtil, P. O. Andersson, L. sterlund, Appl. Catal., B 2009, **92**, 401–410.

[12] S. M. Kanan, A. Waghe, B. L. Jensen, C. P. Tripp, Talanta, 2007, **72**, 401–407.

[13] M. B. Mitchell, V. N. Sheinker, W. W. Cox, E. N. Gatimu, A. B. Tesfamichael, J. Phys. Chem. B, 2004, **108**, 1634–1645.

[14] A. R. Head, R. Tsyshevsky, L. Trotochaud, Y. Yu, L. Kyhl, O. Karslıogˇlu, M. M. Kuklja, H. Bluhm, J. Phys. Chem. C, 2016, **120**, 29077–29088.

[15] S. Ma, J. Zhou, Y. C. Kang, J. E. Reddic, D. A. Chen, Langmuir, 2004, **20**, 9686–9694.

[16] L. Trotochaud, R. Tsyshevsky, S. Holdren, K. Fears, A. R. Head, Y. Yu, O. Karslıogˇlu, S. Pletincx, B. Eichhorn, J. Owrutsky, J. Long, M. Zachariah, M. M. Kuklja, H. Bluhm, Chem. Mater., 2017, **29**, 7483–7496.

[17] Y. X. Li, K. J. Klabunde, Langmuir, 1991, **7**, 1388–1393

[18] Y. Paukku, A. Michalkova, J. Leszczynski, J. Phys. Chem. C, 2009, **113**, 1474–1485.

[19] W. O. Gordon, B. M. Tissue, J. R. Morris, J. Phys. Chem. C, 2007, **111**, 3233– 3240.

[20] D. A. Trubitsyn, A. V. Vorontsov, J. Phys. Chem. B, 2005, **109**, 21884–21892.

[21] A. R. Head, X. Tang, Z. Hicks, L. Wang, H. Bleuel, S. Holdren, L. Trotochaud, Y. Yu, L. Kyhl, O. Karslıoglu, K. Fears, J. Owrutsky, M. Zachariah, K. H. Bowen, H. Bluhm, Catal. Struct. React., 2017, **3**, 112–118.

[22] X. Tang, Z. Hicks, L. Wang, G. Gantefçr, K. H. Bowen, R. Tsyshevsky, J. Sun, M. M. Kuklja, Phys. Chem. Chem. Phys., 2018, **20**, 4840–4850.

[23] D. G. Barton, M. Shtein, R. D. Wilson, S. L. Soled, E. Iglesia, J. Phys. Chem. B, 1999, **103**, 630–640.

[24] D. G. Barton, S. L. Soled, E. Iglesia, Top. Catal., 1998, **6**, 87–99.

[25] X. Tang, K. H. Bowen, F. Calvo, Phys. Chem. Chem. Phys., 2017, **19**, 31168– 31176.

[26] P. A. Redhead, Vacuum, 1962, **12**, 203–211.

[27] X. Huang, H. J. Zhai, B. Kiran, L. S. Wang, Angew. Chem. Int. Ed., 2005, **44**, 7251–7254.

[28] S. Li, D. A. Dixon, J. Phys. Chem. A, 2006, **110**, 6231–6244.

[29] D. A. Chen, J. S. Ratliff, X. Hu, W. O. Gordon, S. D. Senanayake, D. R. Mullins, Surf. Sci., 2010, **604**, 574–587.

[30] F. Yaripour, F. Baghaei, I. Schmidt, J. Perregaard, Catal. Commun., 2005, **6**, 147–152.

[31] W. Alharbi, E. F. Kozhevnikova, I. V. Kozhevnikov, ACS Catal., 2015, **5**, 7186–7193.

[32] R. T. Carr, M. Neurock, E. Iglesia, J. Catal., 2011, **278**, 78–93.

[33] A. J. Jones, R. T. Carr, S. I. Zones, E. Iglesia, J. Catal., 2014, **312**, 58–68.

[34] X. Tang, D. Bumueller, A. Lim, J. Schneider, U. Heiz, G. Gantefçr, D. H. Fairbrother, K. H. Bowen, J. Phys. Chem. C, 2014, **118**, 29278–29286.

III.3 Testing of New Instrument

III.3.1 Cluster Ion Formation and Mass Spectra

The instrument was first tested using the magnetron sputtering source as this was a working source on the older instrument. In order to determine the amount of improvement in the resolution of the mass spectrometer systems preformed on the older instrument were duplicated on the newer instrument. Below are comparison mass spectra between the two instruments for MoO_x and WO_x. (**Figure III.3.1-1**)

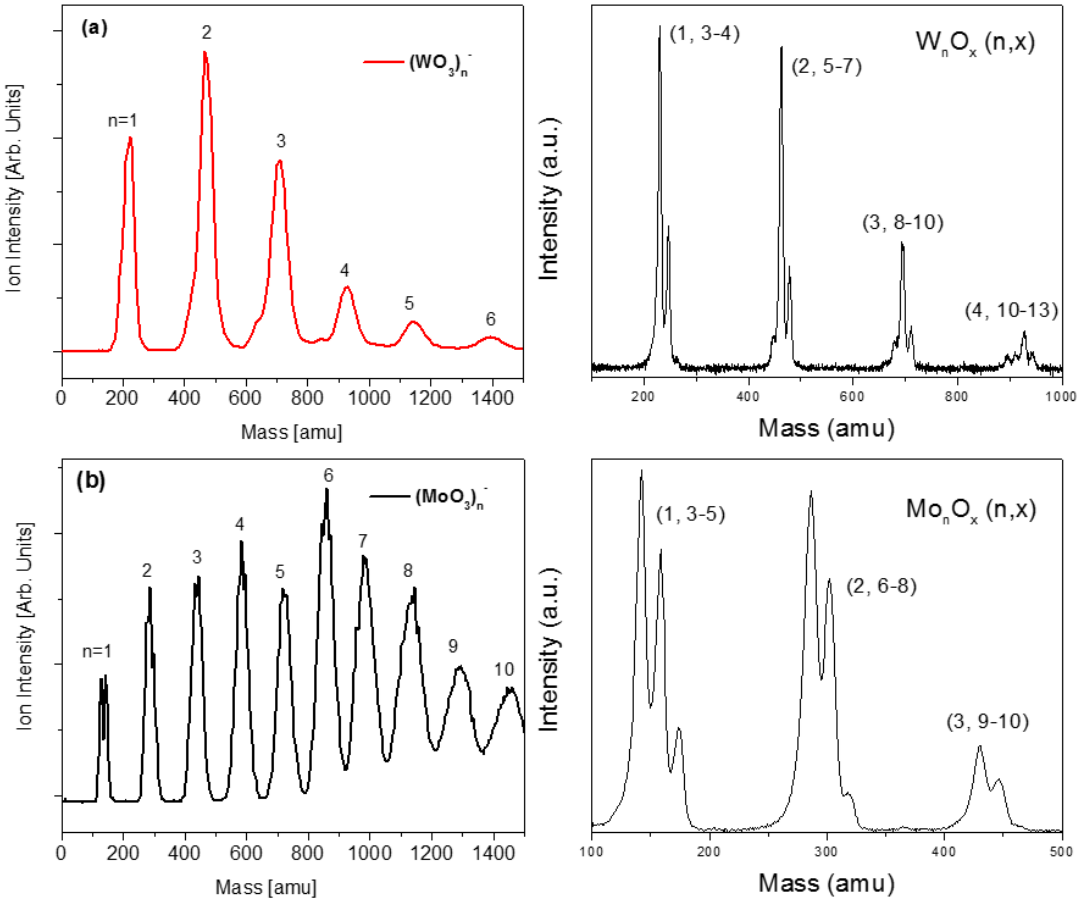

Figure III.3.1-1: Mass Spectra of $(WO_3)_n$ and $(MoO_x)_n$ (Top, Bottom) on older and newer instruments (Left, Right)

The new instrument shows marked improvement in resolution and specifically allows for the determination of the number of oxygens present in the metal oxide clusters. One observation

from this is that the distribution of oxygen amounts in the clusters, while centered on the stoichiometric amount of MO_3, tends to have a not insignificant amount of over-oxidized species where, in the case of the MoO_x clusters, the +1O peak is of nearly the same intensity of the stoichiometric peak. Further, by tuning the oxygen level the distribution could be shifted to under-oxidized clusters. The old instrument would have been depositing a range of oxidation numbers rather than just the stoichiometric cluster. When looking at data collected on the old instrument, the effects of these superoxide and under-oxidized clusters must be considered. Moving forward these experiments can be repeated with this better resolution to determine the effect of the number of oxygens on their results.

In the work on the $(MoO_3)_3$ catalytic decomposition of DMMP (**III.1**) discussed above, the formation of methanol as a decomposition product is attributed to the step-wise loss of methoxy from the DMMP. Another possibility is the cleaving of the P-C bond on the methyl group attached to the phosphonate and the loss of that methyl to the superoxide oxygen, which can then desorb as methoxy or methanol upon gaining a hydrogen. The presence of the superoxide was not considered when theoretical calculation were performed and they might have a measurable effect on the reaction.

In order to study mixed-metal-oxides (MMO) a high resolution spectrometer is needed as the more elements added to a beam, the more convoluted a spectrum becomes with the increased chances of near-mass coincident peaks being present. On the older instrument an attempt was made to study $Mo_xCu_yO_z$ species in the decomposition of DMMP. As described in the introduction the Mo_2CuO_z cluster showed different TPD results as compared to $(MoO_3)_3$ as well as a reduced Mo^{+5} oxidation state as seen by XPS. However the quality of mass spectrum was such that it was not possible to determine what our cluster specifically was and could not rule out a reduced oxidation

state caused by underoxidation. An attempt at repeating this spectra was taken on the newer instrument and is shown below. (**Figure III.3.1-2**)

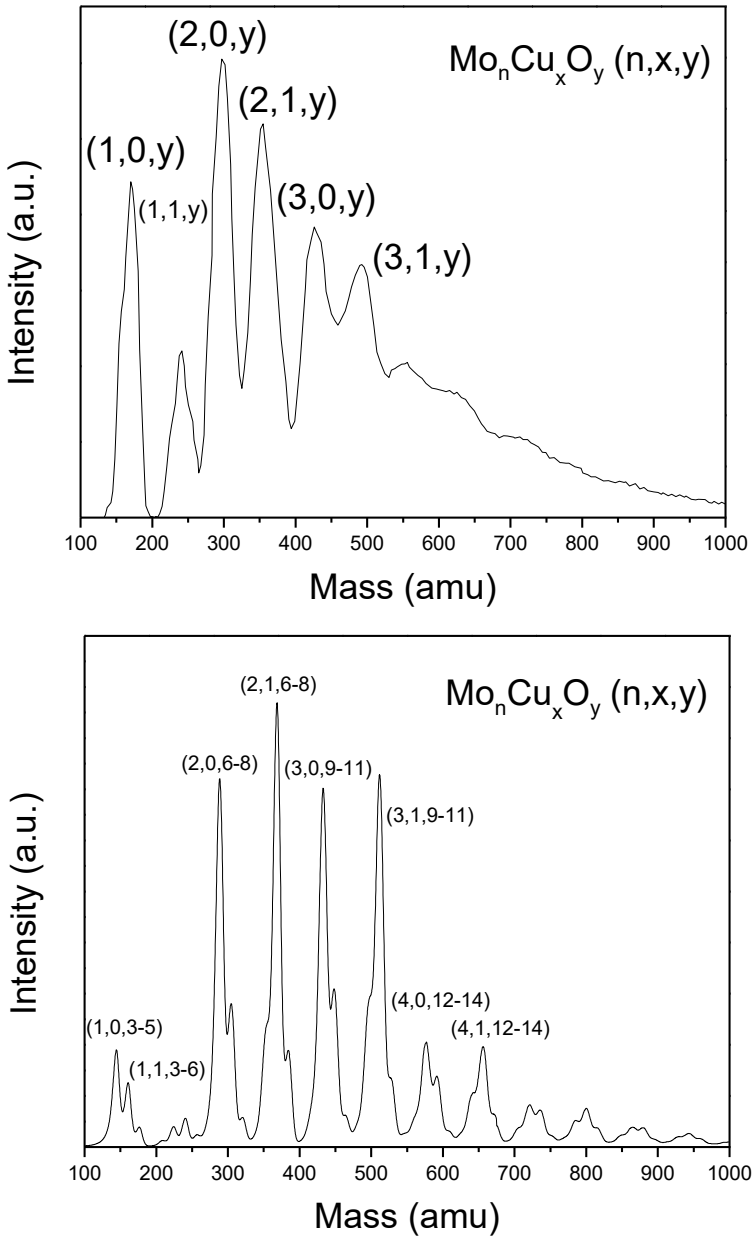

Figure III.3.1-2: $Mo_xCu_yO_z$ Mass Spectra taken on old and new instrument (Top, Bottom)

The newer instrument showed a significant resolution increase. However the exact number of oxygens present in the cluster cannot be determined from just the mass spectrum alone due to the near-mass coincident overlap between Cu and O_4. The addition of XPS to the experiment allows for the determination of ratios between the elements present in the cluster as described in **III.1, 0**. For example, the peak centered at 224 amu can be either MoO_8, $MoCuO_4$, or, $MoCu_2$. While MoO_8 is unlikely to be stable, the other two could exist but have different ratios of Mo:Cu, so XPS can be used to determine if it is near completely one or the other or a mixture of the two. Another way to get a qualitative estimate of the number of oxygens vs copper in the cluster is to look at the peak distributions as compared to the pure MoO spectrum. A peak at 208 amu can either be $MoCuO_3$ or MoO_7 where in a pure MoO spectrum there is no evidence of MoO_7.

The stated resolution of the QMS ($M/\Delta M=1000$) should be able to resolve the difference between the 16 amu oxygen and the 63 and 65 amu of the copper isotopes, however for each increase in resolution the overall signal decreases until it cannot be detected by the Keithley 6514 and such a loss would make a deposition of the cluster impossible. A future improvement of the instrument would be the addition of a multiplier for detecting small signals in the mass spectrum allowing for the resolution to be increased. (**Appendix III.3.3D**) While this will not help with deposition being limited due to signal, it will allow for checking what is present in the beam in high resolution. If the 224 amu centered peak is looked at closely it could possibly contain an isotope pattern matching only one of near-mass coincident possibilities and then upon worsening the resolution to increase the signal for deposition the peak can be said to contain only that cluster.

Other samples were tested with the magnetron including Ta seen in the mass spectra below. (**Figure III.3.1-3**) As seen in the spectra there is a low level of oxidation present in spectrum even when oxygen is not added to the magnetron. On the older instrument this oxide would not have been resolved and would have been included in any metal deposition performed.

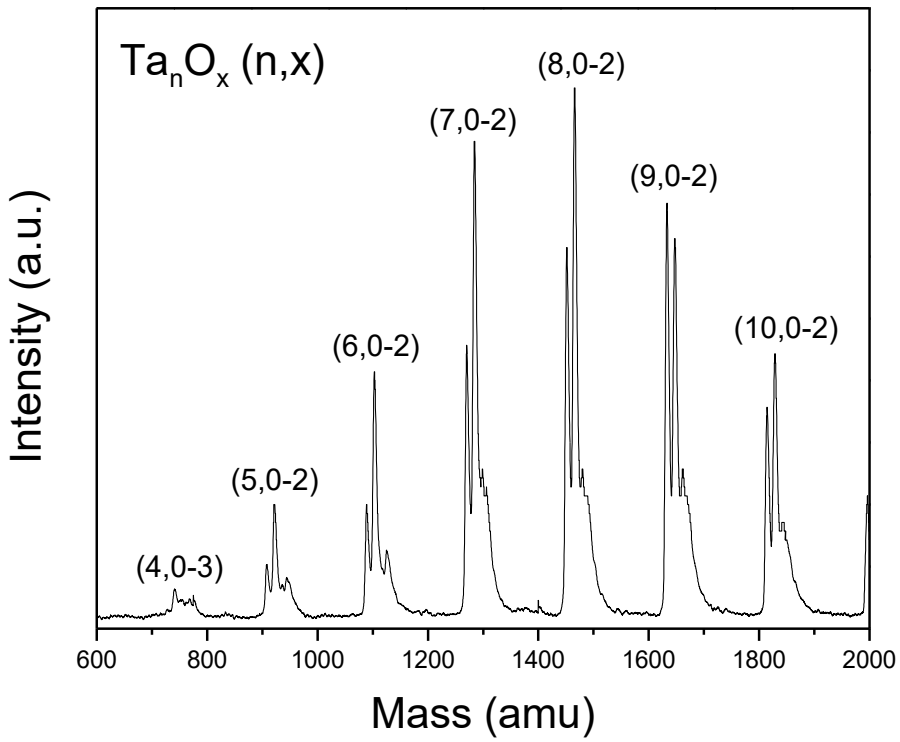

Figure III.3.1-3: Ta Mass Spectrum from Magnetron

An analysis of all of these spectra show a marked increase in resolution as compared to the older instrument, however due to this increased resolution and the lower transport efficiency of a QMS vs a magnetic sector overall intensities are lower. For a deposition experiment the amount of clusters deposited is directly proportional to the intensity of signal measured in any analytical techniques used after deposition. This means that a sample that would generate quality results for 1nA of signal deposited over an hour, would take 10 hours to deposit if the signal is only 100pA. On top of that some studies would need more or less clusters than others depending on the cluster and the reaction being studied. A user can tune the resolution of the QMS to achieve what they believe to be the acceptable signal to resolution ratio for a given experiment. Upon experiment it was determined that messing with the resolution of the QMS had near negligible effects on the

distribution and relative intensities of the clusters, however peak shape was very affected giving them a more Lorentzian shape. With careful fitting, using a Lorentzian fit, the exact overlap of the peaks can be determined and therefore the composition of the deposited beam at the selected mass. The use of a Lorentzian fit is evident from the scan line passing through the QMS stability diagram in **Figure II.2.2-2**.

III.3.2 Laser Vaporization Source Testing

The new LVS design was installed and tested starting with cobalt. Cobalt was chosen for the initial test as it is a system that cannot be performed in the magnetron sputtering source as Co is magnetic. This magnetism results in the dampening of magnetic fields in the magnetron, specifically in front of the target which are necessary to hold the plasma close to the surface of the target to induce sputtering. The resulting mass spectrum is below. (**Figure III.3.2-1**) Co_n n=1-18 is seen in the spectrum as well as these clusters with one oxygen.

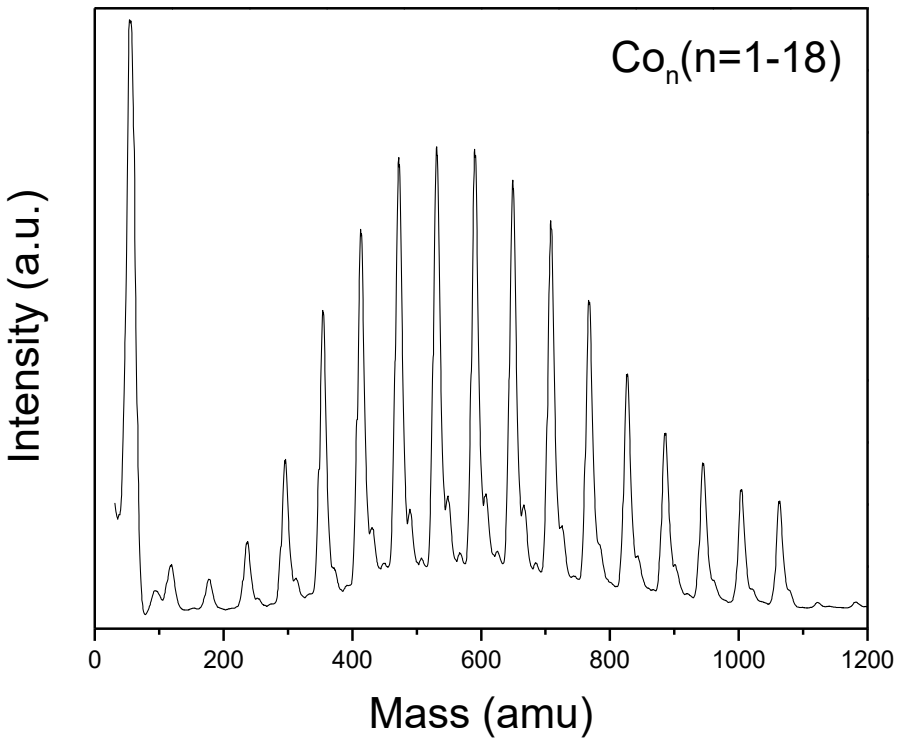

Figure III.3.2-1: Co Laser Vaporization Source Mass Spectra

The LVS source can also be used with the same samples used on a magnetron sputtering source with the goal of producing a different distribution of cluster sizes. Due to the nature of magnetron sputtering certain materials like to produce clusters around a given size. For example sputtering copper in this magnetron produces Cu_n n>50 in studiable quantities while smaller clusters are very weak in intensity. LVS is a great source for producing small clusters. Below is a mass spectra of Ta from the LVS. (**Figure III.3.2-2**) When compared to the Ta mass spectrum generated by a magnetron sputtering source seen in **Figure III.3.1-3** the differences in cluster distribution can be seen where the magnetron is distributed around Ta_8 the LVS has a distribution around the smaller cluster sizes with Ta_1 and Ta_4 being the most intense.

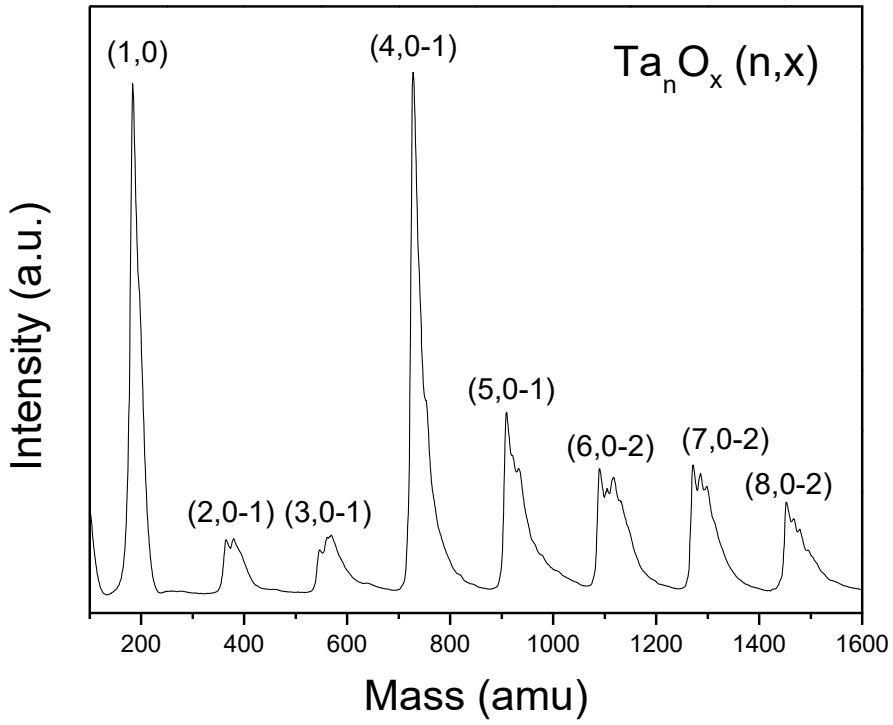

Figure III.3.2-2: Ta Mass Spectrum from LVS

III.3.3 WO_3 DMMP Decomposition Experiment

Once the mass spectrometer and beamline were working, a full catalytic experiment analogous to the experiments reported in **III.1 and 0** was performed in order to test the analytical capabilities of the instrument and thereby show the full application of the instrument being viable.

The experiment chosen was the decomposition of dimethyl methyl phosphonate, DMMP, with WO_3 monomer. Previously this has been done on the older instrument with $(WO_3)_3$ where it is now know that the clusters deposited were likely a combination of W_3O_x (x=9-11) due to the low resolution of the magnetic sector. The monomer was chosen for this experiment due to its high signal allowing for more rapid experimentation, thereby making finding the proper experimental procedures for the new instrument faster. This experimental procedure is described in detail.

HOPG Preparation: The HOPG sample was lowered through the slide-seal and cleaned via the Scotch-Tape Method where tape is used to remove the top layer of the HOPG. Upon being returned to UHV ($<1*10^{-9}$ torr) conditions in the deposition chamber, the sample was cooled to near LN2 temperatures (-170 °C) and annealed to 500 °C to remove any gases or other contaminates such as water or O_2 from the surface. This process was monitored via the RGA (Hiden 301/3F PIC) where upon heating there was a rise in pressure in the chamber as gases devolved and this was detected by the RGA. Once the RGA's background had returned to pre-annealing levels the sample was deemed cleaned. The sample was cooled back down to LN2 temperatures.

Dosing: A leak valve was loaded with a drop of DMMP in a Swagelok cap. This sample was purified with 5 cycles of the freeze-pump-thaw method, where the DMMP was cooled to just above its freezing point with an water/dry ice mixture and then pumped out. After a few minutes of pumping, the pumping was stopped and the DMMP heated to ~50 °C with a heat gun and the process was repeated. Previously the RGA was used to determine that this process was effective at removing the large H_2O contamination present in the DMMP sample as well as some other minor contaminates. When the leak valve is opened to the chamber, the RGA is used to monitor both the purity of the dose and the quantity of the dose.

Since the RGA contains an electron bombardment ionizer any neutral molecule that enters it can be fragmented in the ionization process. The ratio of the fragments are fixed for a given molecule with the largest mass being the intact parent ion and the most intense mass being called the major fragment. Knowing these ratios and monitoring multiple masses as a function of time it is possible to determine the quality of a dose. For DMMP 124 amu is the parent ion while 94 amu is the major fragment. In this work the second major fragment 79 amu was used due to 94 amu being too intense. 79 amu is also larger than most contaminants in a clean UHV chamber thereby removing the possibility of it being from any other source than the DMMP.

In this case a 150k counts/s (79 amu fragment) dose for 300s was used. (**Figure III.3.3-1**) This dose is around 10L as judged by the ionization gauge pressure reading, giving us a multi-layer of DMMP on the LN2 cooled HOPG. This large of a dose ensures that each WO_3 deposited will interact with a DMMP molecule, thus increasing the sensitivity of the experiment. (A note here for future users is that as the RGA multiplier or filament ages, the count reading will drift, so while this is a very accurate method for dosing and doing relative dosing (15k counts/s for 300s is exactly a 10^{th} of the dose) experiments done across years may not be completely comparable so be astute in searching for potential changes over time.) The masses in the RGA spectra are as follows; 15 amu–methyl, 16–methane, 29-HCO, 30-H_2CO, 31-methoxy, 32-methanol, 46-dimethyl ether, 79-phosphonate. In previous studies the parent ion 124 amu was included to confirm that 79 amu followed the same profile. After confirmation 124 was omitted to speed up the RGA collection rate.

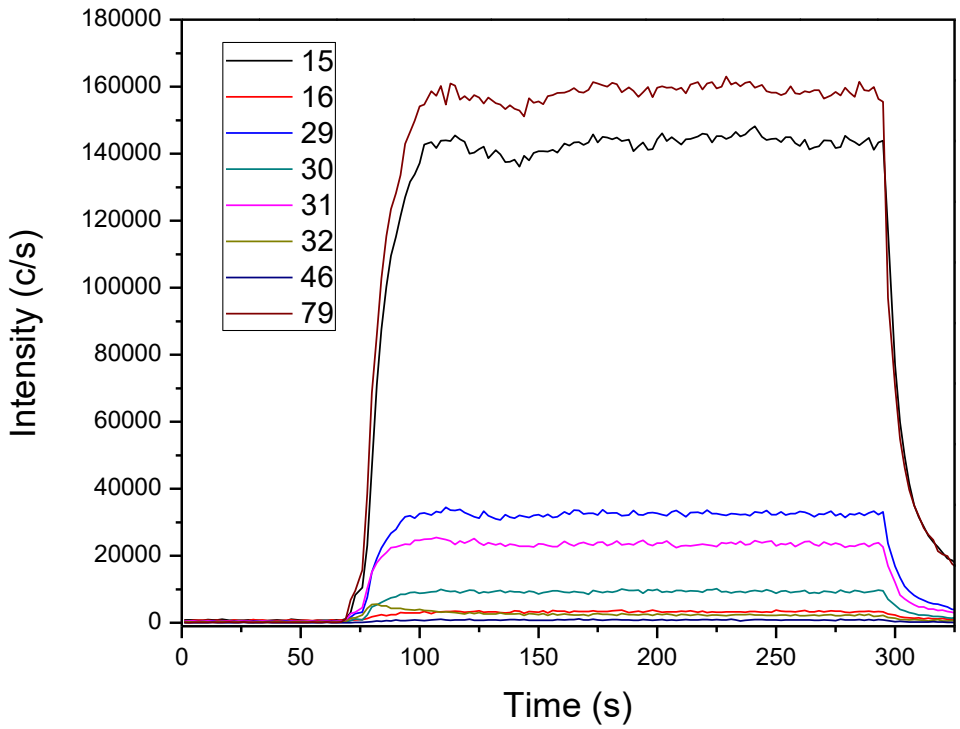

Figure III.3.3-1: WO3 DMMP Dose (Fragments in amu)

Before depositing clusters onto the DMMP dosed sample, a background TPD/R was collected to confirm that any effects seen after cluster deposition were from the clusters themselves. (**Figure III.3.3-2**) The only peak in the background is the desorption of intact DMMP at 95 °C.

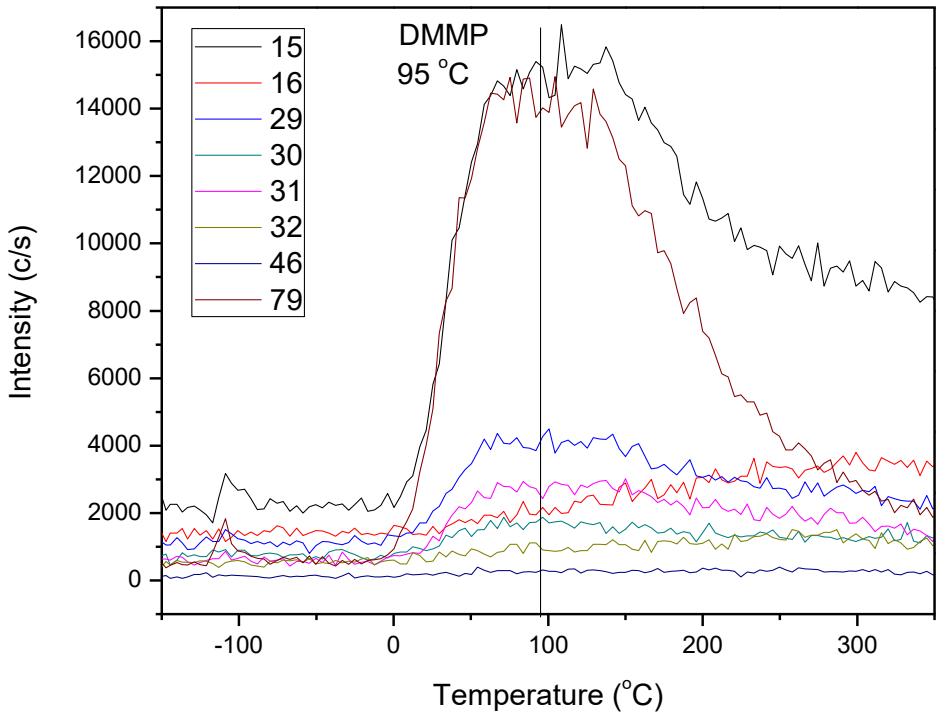

Figure III.3.3-2: DMMP on HOPG Background

Cluster Deposition: The WO_3 cluster was produced with the magnetron sputtering source. The resulting mass spectra with the resolution used for the deposition is located in a previous section and reproduced here for ease of access. (**Figure III.3.3-3**) The overlap between WO_3 and WO_4 was determined to be <5% at the center of the WO_3 peak, and future experiments on WO_4 should be performed to rule out any possible deconvolution in the results. The WO_3 was deposited on the DMMP coated surface while monitoring the cluster current to determine the exact number of clusters deposited ($1.5*10^{14}$ clusters) as described in **II.5.1**. (At the time of this experiment the Keithley 6514 was not floatable so beam energy profiles were not taken and soft-landing was not

attempted. Future users should float the HOPG sample with the same polarity of the clusters being deposited in order to slow the clusters down for soft-landing. To accomplish this the current should be monitored while the voltage is increased from ground. Eventually the current will drop to zero. Plotting this current as a function of voltage will give a plot with a drop-off. The mid-point of this drop-off is the average axial beam energy of the clusters. The less steep this drop-off the wider the energy spread of the ions in the beam. From here statistics can be used to determine the soft-landing conditions <1eV/atom for a given cluster.)

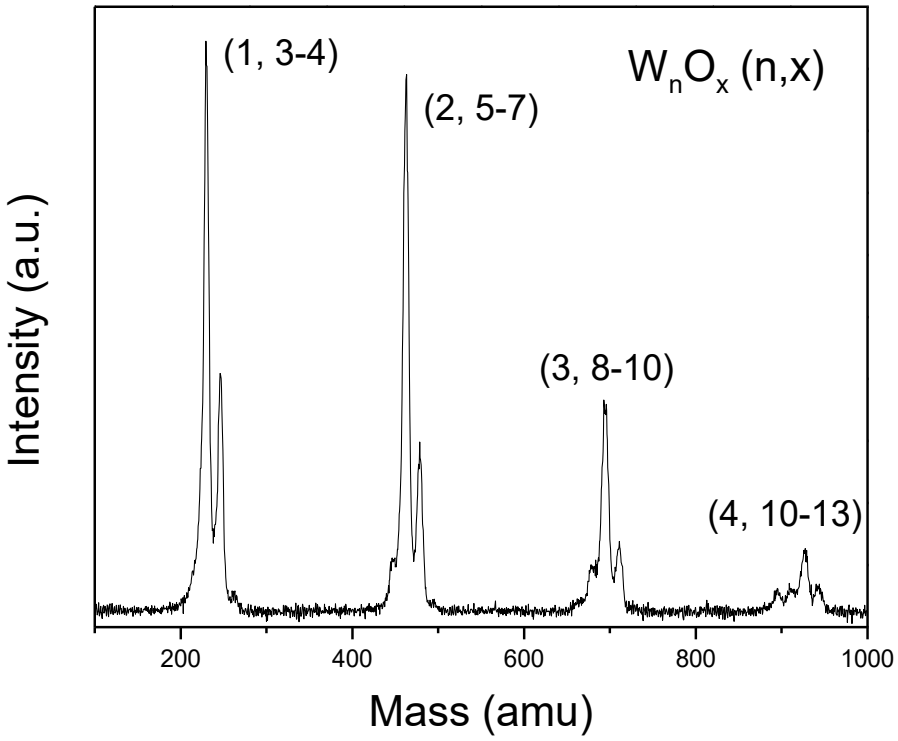

Figure III.3.3-3: WO3 with DMMP Experiment Mass Spectrum

XPS of Deposited Sample: After the deposition, but before XPS, the sample was heated to 50 °C. This desorbs any DMMP not interacting with a cluster (physi-adsorbed) which there is much of due to the orders of magnitude difference in the dose vs the cluster deposition. During the initial

ramp to 50 °C, the RGA is kept off as the amount of DMMP desorbing at this point is a lot and it is unnecessary to expose the RGA to this. Once 50 °C is reached, the RGA is turned on and used to monitor the DMMP background. Due to kinetic limitations of the physi-adsorbed DMMP desorbing off of the sample, the background observed on the RGA drops slowly. Once the background is back to <200 counts/s of the 79 amu signal, the sample is allowed to cool back to LN2. The 50 °C temperature was chosen because this experiment was performed multiple times and it was determined that no chemi-adsorbed DMMP desorbs at 50 °C via TPD. The removal of this physi-adsorbed DMMP is required before XPS as the many layers of DMMP act to perturb the ejected photoelectrons resulting in shifted and broad peaks.

The hemisphere was calibrated previously using a pure sample of gold and copper to correct for spacing across its whole energy range and the work function of the instrument. (See RBD's online description of calibration for the procedure used.) It is important that the sample be grounded and grounded to the same point used during the calibration, as failing to ground it will shift the peaks to a higher BE as the sample charges up and grounding it to a different point will result in a different work function than what was calibrated for and thereby shifting the peaks. This ground point is bolted to the instrument on one end and a gator clip on the other is used to attach it to the shorter of the power-feeds. Further the peak position of HOPG carbon (284.5 eV) can be used to check for any problems in the XPS calibration.

Below is the XPS profiles of the as-deposited WO_3 and DMMP for W(4f). P(2p), and C(1s). (**Figure III.3.3-4, Figure III.3.3-5, Figure III.3.3-6**) The peak center of the C(1s) was at 284.57eV and therefore was used to calibrate peak positions by shifting the binding energies by 0.07eV bringing the C(1s) to 284.5eV. The tungsten is fully oxidized at W^{6+} in the as deposited clusters as expected for WO_3. The P(2p) peak is centered at 134eV which is slightly higher than as reported for the $(WO_3)_3$ clusters in the previous work. Using Relative Sensitivity Factors (RSF) for W(4f)

(3.523) and P($2p_{3/2}$) (0.39), and given the areas under the peaks in the XPS spectra, a ratio of P:W of 1.0 is determined indicating one adsorbed DMMP molecule per cluster. This result is consistent with the $(WO_3)_3$ results where the ratio was ~0.33 P:W.

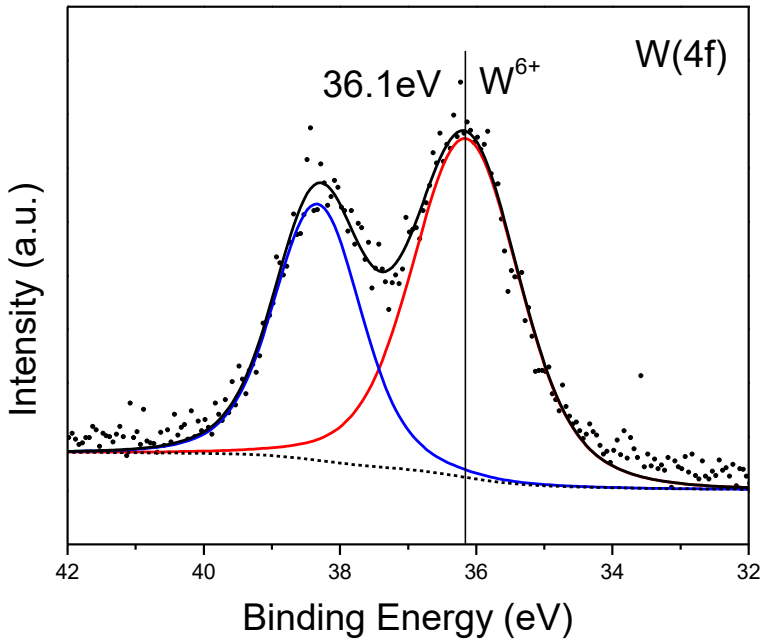

Figure III.3.3-4: W(4f) XPS Envelop of As-Deposited Clusters

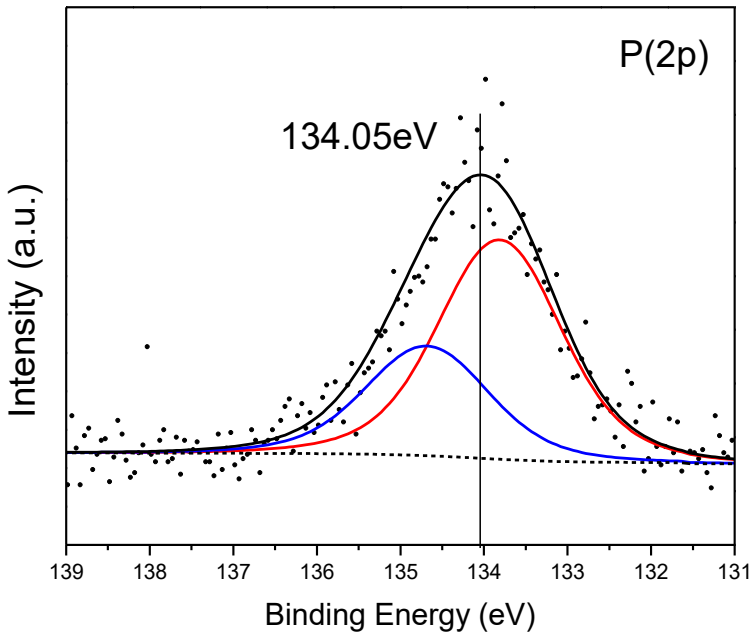

Figure III.3.3-5: P(2p) XPS Envelop of As-Deposited Clusters

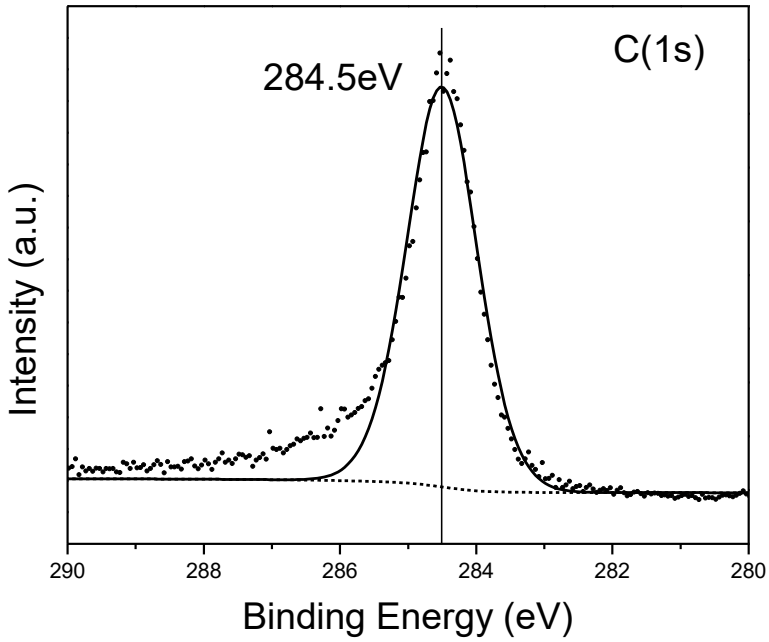

Figure III.3.3-6: C(1s) XPS Envelop of As-Deposited Clusters

TPD/R Results: After XPS was performed on the as-deposited sample the sample was turned towards the RGA and TPD/R was performed. The same masses were monitored as in the dose profile above. (**Figure III.3.3-1**) The sample started at near LN2 temperature ~-170 °C and was ramped up to 500 °C at a rate of 2 °C/s. The RGA tracks both ion signal and temperature as a function of time allowing for the ion signal as a function of temperature to be plotted. (**Figure III.3.3-7**)

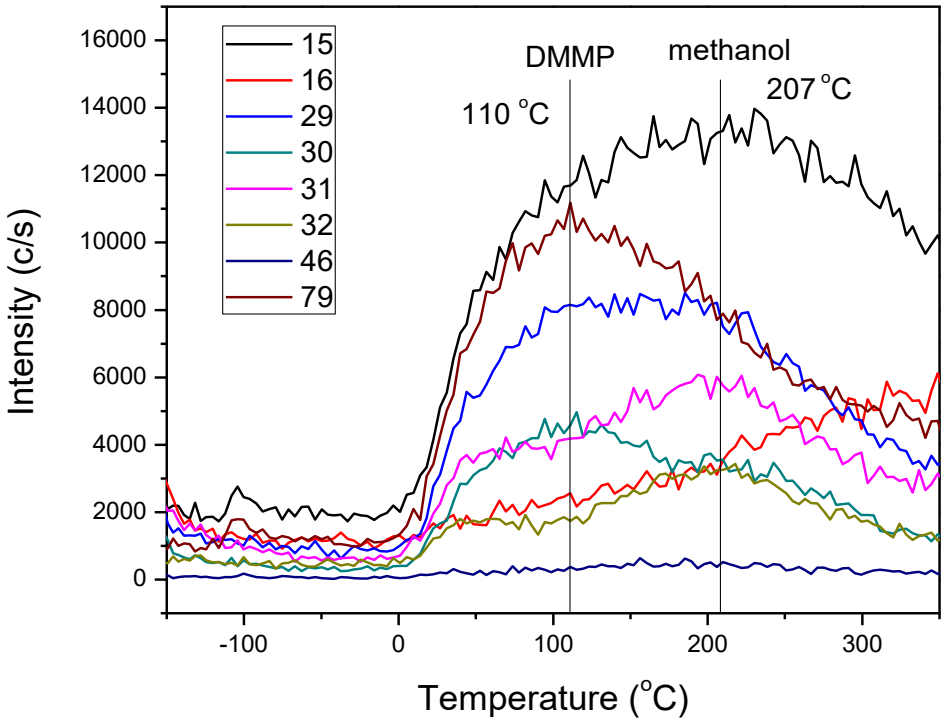

Figure III.3.3-7: TPD/R Results of WO_3 with DMMP

The first peak is attributed to DMMP (79, 31, 30, 29, 15 amu) and desorbs at 110 °C. A second peak at 207 °C is attributed to methanol (32, 31, 30, 29, 15 amu). No dimethyl ether is seen in the spectra (46 amu). While both DMMP and methanol share many fragments, the lack of 32 amu in the 110 °C peak and the lack of a 79 amu peak in the 207 °C peak support the profile

assignments. Further the trends of the fragments should match each other if only coming from one molecule, and it can be seen that while the 79 amu signal (DMMP) is dropping starting at 110 °C, the 29, 30, and 31 amu profiles do not follow that drop, indicating they are originating from a different molecule, in this case methanol. A Redhead Analysis of these peaks (**II.5.4**) gives desorption energies of 24.0 kcal/mol for DMMP and 30.3 kcal/mol for methanol.

Comparison to Previous Work: On the older instrument $W_3O_{9\text{-}11}$ was deposited and studied for its catalytic effects for the decomposition of DMMP. The resulting TPD/R showed the following; DMMP desorption at 100 °C giving an E_{des} of 23.4 kcal/mol, dimethyl ether desorption at 245 °C giving an E_{des} of 32.8 kcal/mol, and methanol desorption at 275 °C giving an E_{des} of 34.8 kcal/mol.

The first major difference is the lack of dimethyl ether formation in the WO_3 experiment. A possible explanation for this result is that the overoxidation of the $W_3O_{9\text{-}11}$ allows for a reaction pathway to form dimethyl ether. Further studies should be performed on WO_4 to confirm. The desorption of the DMMP was identical between the two experiments indicating similar binding strength to the two clusters. There is a dramatic difference between the two systems in the E_{des} of the methanol well beyond the uncertainty of Redhead Analysis, indicating either a lower E_a for DMMP decomposition in WO_3 or $W_3O_{9\text{-}11}$ having a higher binding energy to methanol. Quality theoretical work will be needed to explain these differences.

Conclusion: A full WO_3 with DMMP decomposition experiment was performed using the new instrument. The experimental procedure was developed and fine-tuned and was able to give repeatable results on a new cluster system.

A LabView Program

The LabVIEW program is large and complicated, so in this section it will be broken down into its parts and explained piecemeal. It might be beneficial to follow along while looking at the whole program. Math functions and data manipulation will not be explained in detail in this writing, assuming once told what a function performs a reader can determine how it is performed while studying the VI.

Some tips to help understand LabVIEW:

1. LabVIEW is a visual programming language and is read left to right just like a book. At no point in the program is data moved to the left. The program will be described left to right.
2. A given node in LabVIEW will not begin to run until it has received all of its inputs. In many cases this is used to time the events in the program. This includes structures.
3. A given node won't output any of its outputs until all outputs are ready.

While looking at a node all inputs are on the left and all outputs are on the right. For the lines leaving the top and bottom you can tell if it is an input or output if the wire runs left or right.

Setup: (1) The VIs to the left of the first while loop are hardware setup and only run once when the program is initialized. It is used to tell the program which pins on the DAQ to use and how to use them. There are 5 levels described as follows from top to bottom.

1. **Analog Output Setup:** This section takes the four AO on the DAQ and creates an "AO Task" referenced to DAQ Ground with a range of -10 to 10 Volts. This task is referenced when telling the DAQ what voltages to apply to the QMS controller. The task continues

into the while loop. AO0 is the Mass Command control. AO1 is the Pole Bias control. AO2 is the DM control. AO4 is the DRes control.

Note on AO: Many times in this document I will refer to "Writing to the AO". This works as follows. The AO is a 2D array with 4 rows and N columns where the rows correspond to the 4 channels and the N columns are the values the channels will take as the scan progresses. It starts on the first column and each clock cycle moves to the next column. In this way the computer is not telling the DAQ each step as the steps occur but it "wrote" the whole array to the buffer (i.e. storage) of the DAQ.

2. **Analog Input Setup:** This section sets up an AI that measures the actual applied voltage that AO0 sends to the QMS controller. It may have been told to output 2V but it may be different in actuality, so this AI takes that measurement. This is setup through internal channels in the DAQ as it directly measures "_AO0_vs_AOgnd" and has no external connections. This is a differential measurement for increased accuracy expecting a range from -10 to 10V. Later the whole program will be triggered to start, so here we delay it 6μs in order to give the AO0 time to change to the next voltage before taking a measurement.

3. **Counter Output Setup:** This section sets up a CO that outputs a square pulse train used to sync the 6514 with the DAQ. (See below) Here it is defined as "High (>3V)" is 0 and "Low (<0.3V) is 1. It is given an arbitrary 100 Hz frequency which is changed by parameters later in the program. Its duty cycle is 50% and it is delayed 6μs to give the QMS time to change masses before the 6514 takes a measurement.

4. **Keithley 6514 Setup:** The 6514 is controlled via a USB to GPIB adapter created by Agilent with drivers installed in such a way that NI-Max can recognize the GPIB port. By default, the 6514 is on channel 14 of the GPIB. Starting from the left the program takes remote control of the 6514, turns on zero check, sets it to read current, sets the scale to the 20pA

scale (lowest) while turning off auto-scaling, takes a measurement of instrument zero, sets that as the zero offset, turns off zero check, turns on zero correct so that the measurement is corrected for 6514 burden, sets the electrometer to only collect the reading (rather than reading, timestamp, and scale) and communicate with the computer via binary rather than converting to ASCII thereby decreasing the read time by 5 orders of magnitude, the front panel is turned off further increasing the speed as it doesn't need to update, and finally returned to idle.

Note on Binary: The 6514 normally takes and stores readings in binary but by default converts it to ASCII when transferring over the GPIB bus. Since the 6514's processor is much slower than the computer's, this conversion takes a long time. So instead it is set to remain in binary, and the program converts it with the computer's faster processor. With a full buffer the 6514 readings were taking 24 secs to be read. Reducing the data to only reading cut that to 8 secs. Changing that to binary and converting in the program cut that to <1sec.

5. **Digital Output Setup:** This sets up the DO (TTL) of the DAQ. Each line is controlled separately. This controls the "Flip DC" and "Resolving" controls of the QMS, where 1 is resolving and 0 is RF only mode.

Run Loop: The setup tasks are then sent into the run loop. This loop will run continually until the program is stopped.

1. **Scan Setup While Loop: (2)** This contains all of the controls for the program. This loop will continue to run and read the controls until the "Pause" button is released. This gives you time to set the controls to what you want. It derives the scan time from the inputted parameters. Finally, it determines if you are running a mass scan or sitting on a mass by

determining if you have more than one point in your mass array. This is output as a True or False. It also sets the "Running" light to off.

2. **Single Mass Mode (True Case):** Next is a case structure dependent on whether you are in single mass mode or in a mass scan.

Signal Integration Setup SubVI: (3) This SubVI tells the DAQ and 6514 what to do in single mass mode. This only needs to be performed once, so it is outside the **Single Mass Run Loop**. First off it sets the AO buffer to 2 (aka the 2D array has two columns). It then sets the AO to allow regeneration, which is when the end of the array is reached it will just start over rather than wait for another array to be written. The sample clock is set to change value every 10 secs.

The CO and AI are not used in single mass mode. The 6514 is setup as follows. It sets up the filter, then the scale, then integration time, turns off the 6514's buffer, and sets the trigger such that the 6514 does not wait for a trigger. (See 6514's manual for triggering scheme.)

The single mass mode takes the requested mass and converts it to a voltage for each of the 4 AOs by using the slope and intercept of the voltage vs. mass linear fit. This voltage array is duplicated to a two element 2D array where the two columns are identical. (This was a funny bit of programming, as once the DAQ is setup to output multiple changing values, such as in a scan, it could not be returned to single value. Instead it "switches" between two identical values at 0.1 Hz.) This 4Chan 2Samp array is then written to the AOs and the task automatically starts.

Single Mass Run Loop: (4) The computer time and previous indicator results are sent into this loop. The computer time is compared to the time in the previous loop thereby determining the time between each iteration of the loop. This is used to convert current

to # of clusters and as the climbing x-scale in the waveform. The 6514 is told to take a measurement (Makes it leave idle in the triggering scheme.) Two things happen to this reading.

The first is that it is placed on an indicator and added to a signal waveform. This waveform collects signal as a function of time creating a useful tuning resource. The average and std dev of the readings are also determined. This waveform can be cleared via a latching case structure that when true writes null values to the x and y of the waveform.

The other thing that happens is that, if the "Integration" switch is on the signal is converted to "# of clusters" and integrated over time. The integration can be paused by unclicking the integration switch and resumed by pressing it again. The integration can be cleared in a manner identical to the clearing of the waveform. The encased case structure is due to the signal reading spiking to 10^{36} when it goes off scale which would ruin the integration. If the signal is larger than 10^{-7}, that value is ignored giving the users time to change the scale to a higher scale.

At the bottom the DO can be updated in real time as a 2Chan 1Samp write.

This loop only stops for three reasons: 1) You hit "Pause". Making it return to the **Scan Setup While Loop**. 2) There is an error code. 3) One of the setup values changes. Making it so that it automatically runs through the setup procedure without pausing in the **Scan Setup While Loop** and continues collecting.

When leaving the loop the AO task is stopped and the 6514 is returned to idle.

3. **Mass Scan Mode (False Case):** If your setup has more than one mass, the mass scan mode is used.

Mass Scan Setup SuVI: (5) This VI sets the hardware for a mass scan. First, is sets the AO to allow regeneration (see above) and then sets it to clock at a rate that was determined empirically from the NPLC (integration time) of the 6514 as set by the user.

Then the AI and the CO are setup to start on a rising trigger, with that trigger being the start of the AO task. (Recall these two are then delayed by 6μs.) The AI is setup to run 2000x faster than all of the other tasks as determined by NPLC. The CO is setup to pulse at a rate as determined by the NPLC, where since it is a pulse of a set frequency its clock is implicit.

The 6514's filter is turned off, scale is set, integration time is set, and then setup so that it collects a data point on a trigger on Line6 in this case this is the CO. The arm layer is bypassed. (see 6514 manual for triggering scheme.)

Mass Scan Run Loop: (6) First off, the TTL for "Resolving" is set to true and the "Flip DC" TTL is set. Then immediately the program goes into the **Mass Scan SubVI.**

Mass Scan SubVI: (7) The mass scan subVI is where the scan is setup, timed, and read.

The first thing it does is build a "Mass Array" out of the "Start Mass," "Final Mass," and "Samples/Mass." For example, if you go from 1 to 5 with 1 S/amu it builds an array of 1, 2, 3, 4, 5. If you go from 1 to 5 with 2 S/amu you get 1, 1.5, 2, 2.5, 3, 3.5, 4, 4.5, 5. However, the 6514 is limited to a buffer of 2500 data points, meaning if your scan is more than 2500 points it has to be broken into chunks. This checks the requested array size and if larger than 2500 it takes the first 2500 points, carries the remainder to another iteration of the loop, and repeats until an array less than 2500 is sent through, where it will then stop the loop after it has passed through, as that would be the end of the scan. Each of these loop's data are concatenated via a concatenating tunnel at the end giving a seamless spectrum.

The resulting mass array is converted to a voltage array and combined into a 4Chan NSamp 2D array and written to the AO. The array size is used to set the buffer size of the AO and the 6514 as well as tell the 6514 how many triggers it will expect. The AI, CO, and 6514 are then initialized, but THEY DO NOT START! This is due to the trigger setup

earlier. Once they have all initialized, they wait for the start trigger which is the AO initialization, and the AO initialization is forced to be after the others via a "merge error" VI. This syncs the whole scan.

The AO, CO, and therefore the 6514 run at a matched and synced clock rate as the scan steps up. The AI runs 2000 times faster, so that it can take 2000 measurements of the AOvsAOgnd and average them. This builds an array of AO voltages, which is then converted to a mass array via the calibration parameters, giving the Mass (amu) axis of the mass scan.

The reading of the 6514's buffer is delayed by the error output of the for loop so it will not attempt to read the 6514's buffer until completed. This "Read 6514 Buffer" SubVI is a homemade VI ,which gets the buffer in a form of a single precision binary array and converts it to a single precision floating point array which is the y-axis of the mass scan.

Return to the Mass Scan Run Loop: The mass array and signal array are sent out of the Mass Scan SubVI, where the mass array is used as the x-axis on a plot. The signal array then could be averaged over a number of scans (this case structure is self-explanatory), or simply plotted with the mass array giving the mass spectra. The sign of the anions can be flipped giving an upwards spectrum. The resulting spectrum can then be saved with headings automatically added.

This loop will repeat unless; 1) The "Pause" button is hit. 2) A scan parameter is changed, which will then make it automatically run through the setup procedure. 3) There is an error.

Ending the Program: Hitting the "Stop" button will end the "Run Loop", release the tasks, and then display any errors. Alternatively, the program is setup to automatically end every loop and show an error whenever there is an error with no user input.

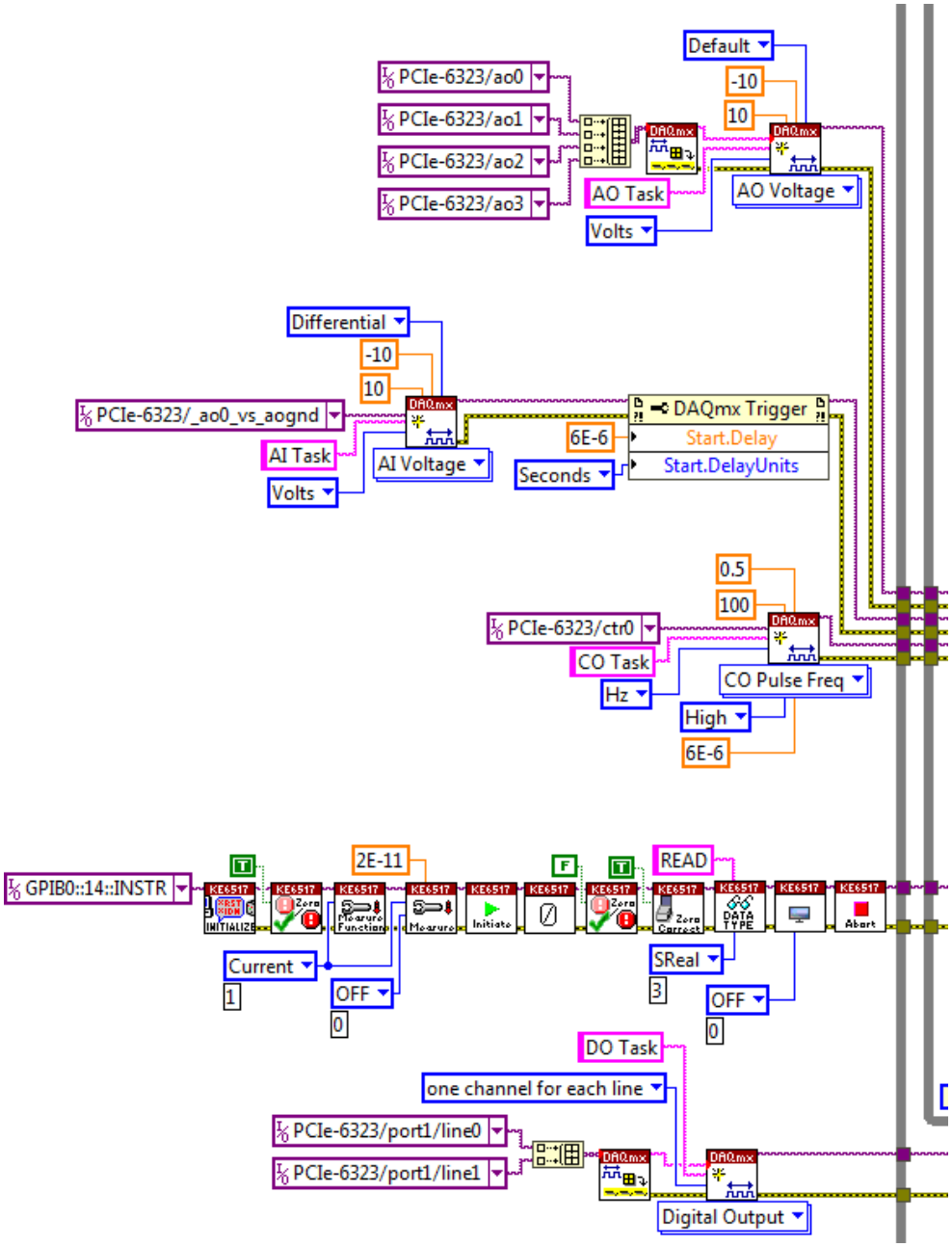
Default
PCIe-6323/ao0
PCIe-6323/ao1
PCIe-6323/ao2
PCIe-6323/ao3
-10
10
AO Task
AO Voltage
Volts
Differential
-10
10
PCIe-6323/_ao0_vs_aognd
AI Task
Volts
AI Voltage
6E-6
Seconds
DAQmx Trigger
Start.Delay
Start.DelayUnits
0.5
100
PCIe-6323/ctr0
CO Task
Hz
CO Pulse Freq
High
6E-6
GPIB0::14::INSTR
2E-11
READ
Current
1
OFF
0
SReal
3
OFF
0
DO Task
one channel for each line
PCIe-6323/port1/line0
PCIe-6323/port1/line1
Digital Output

(1) Setup

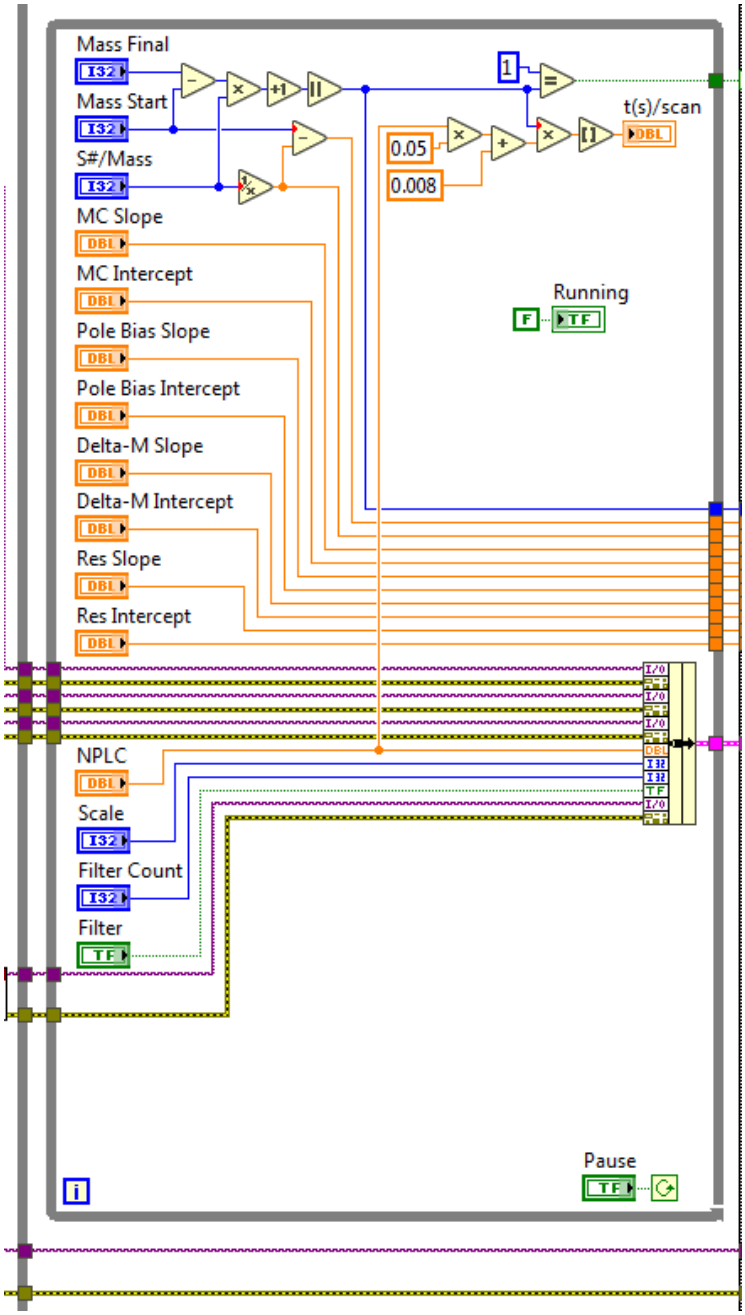

(2) Scan Setup While Loop

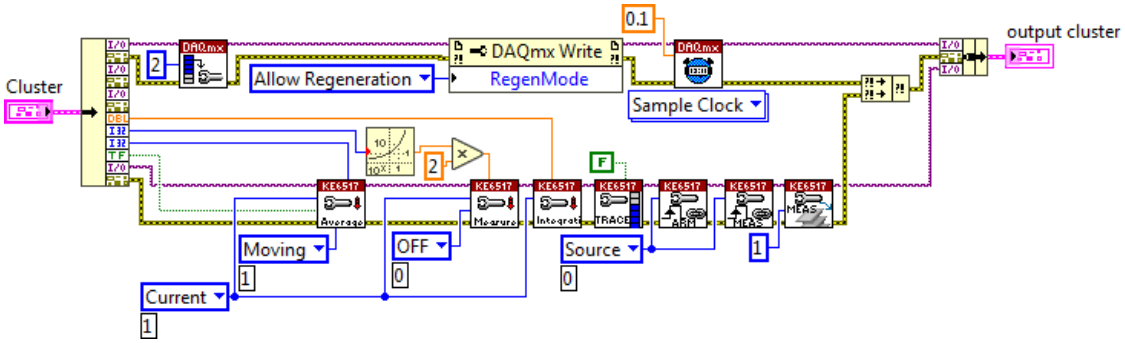

(3) Signal Integration Setup

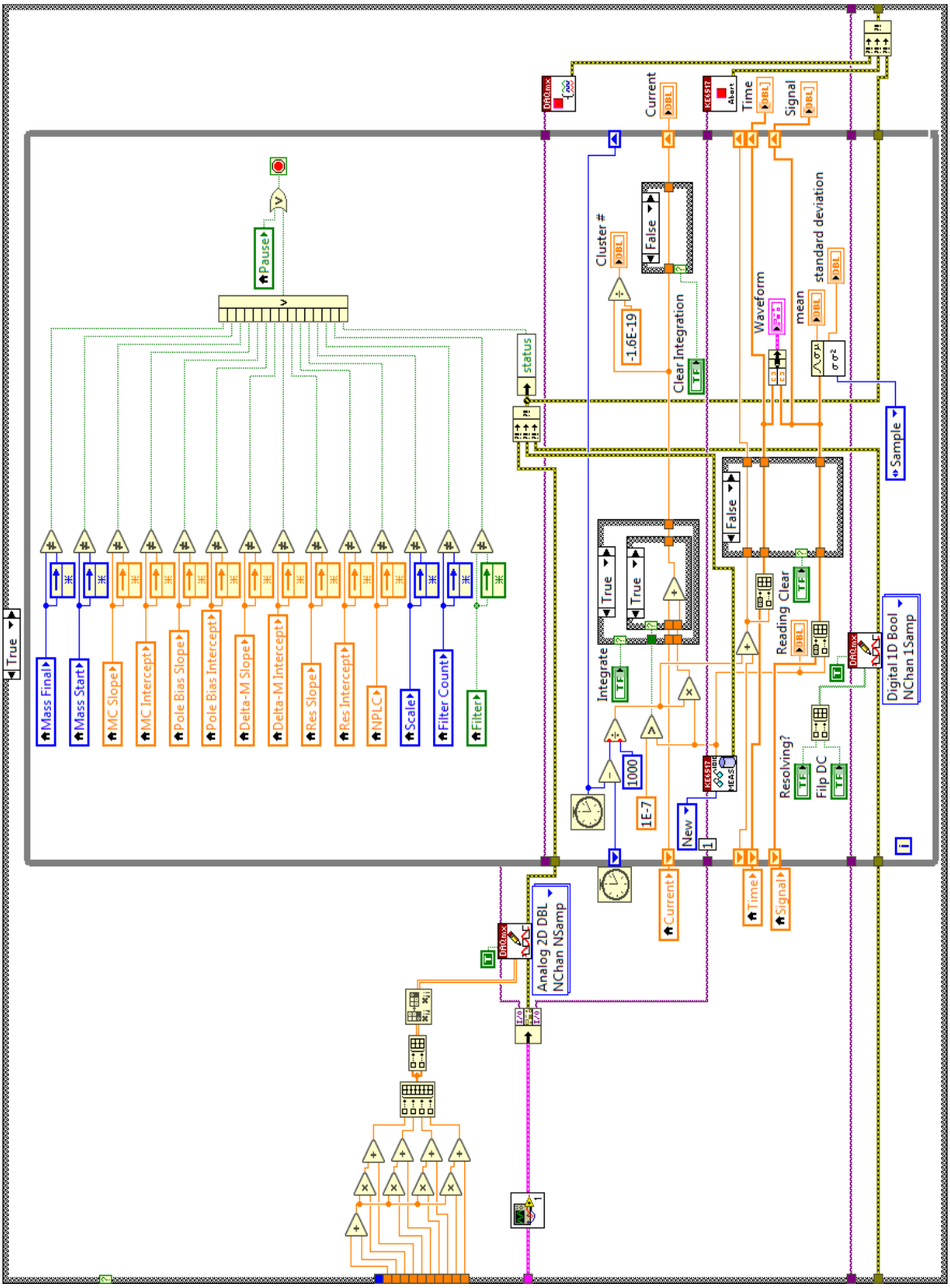

(4) Single Mass Run Loop

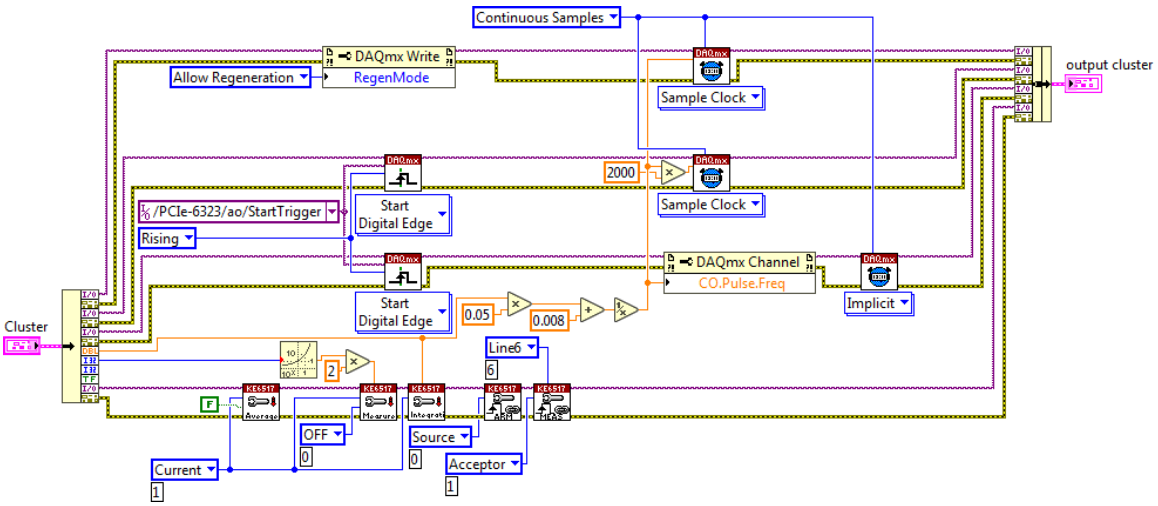

(5) Mass Scan Setup SubVI

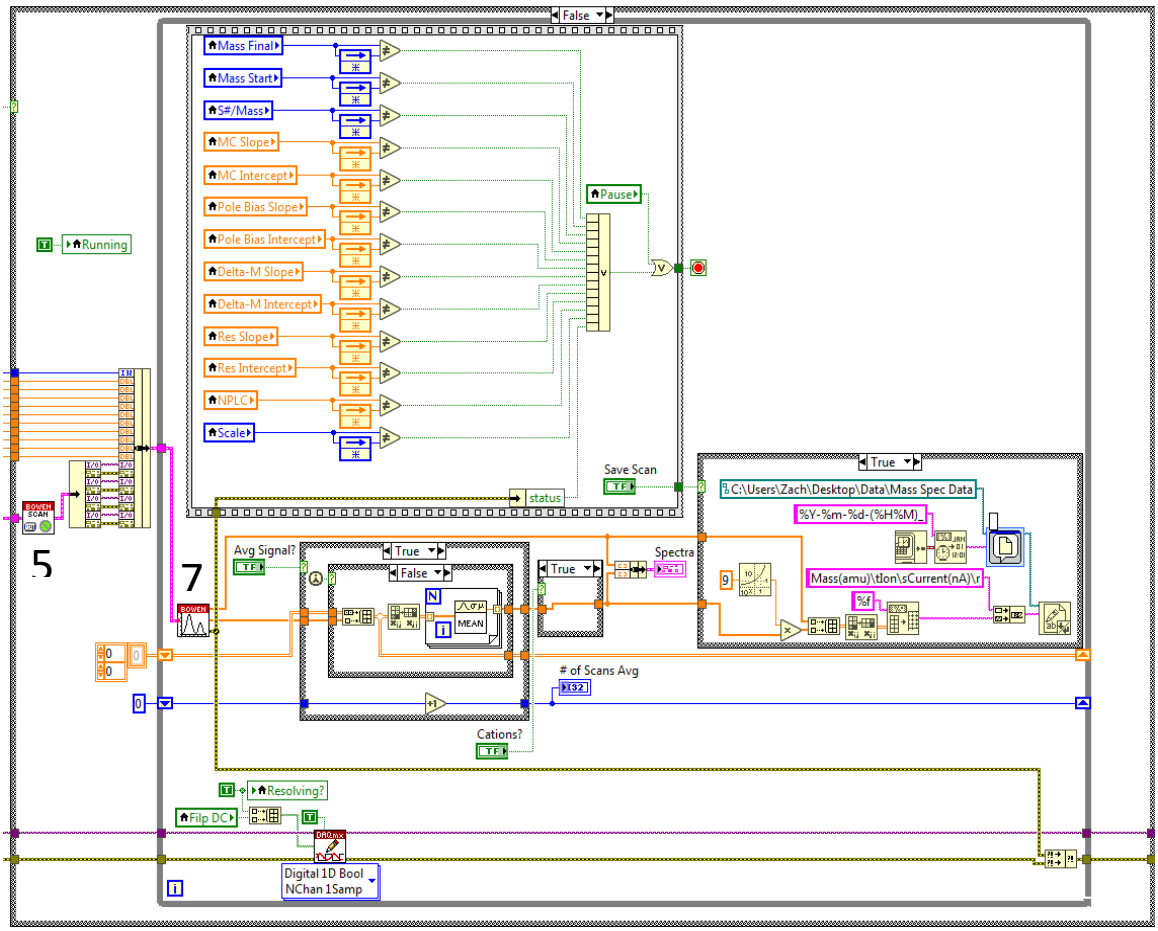

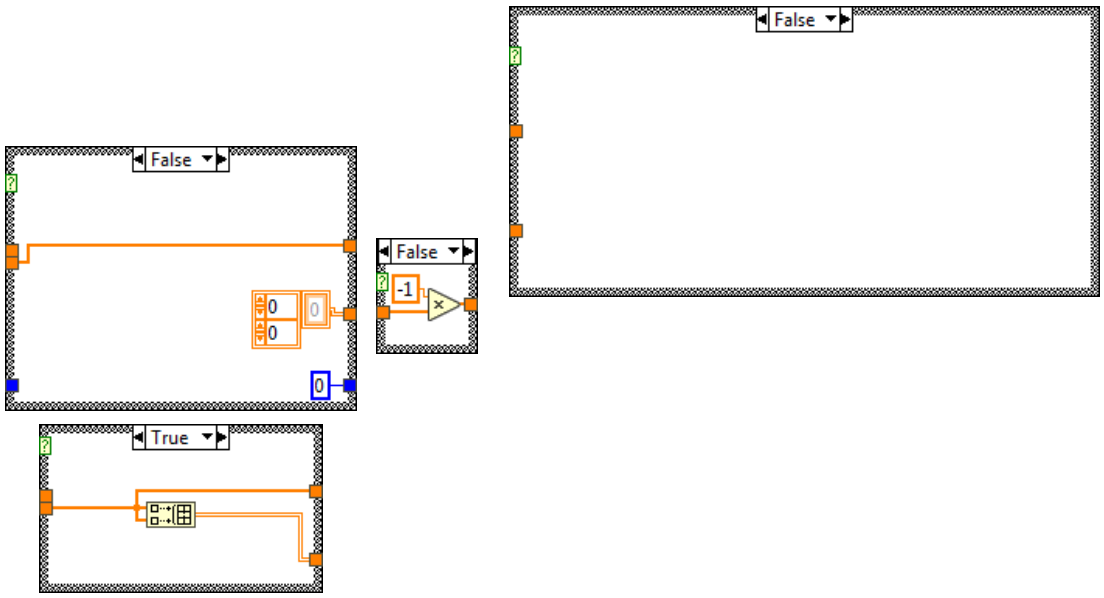

(6) Mass Scan Run Loop

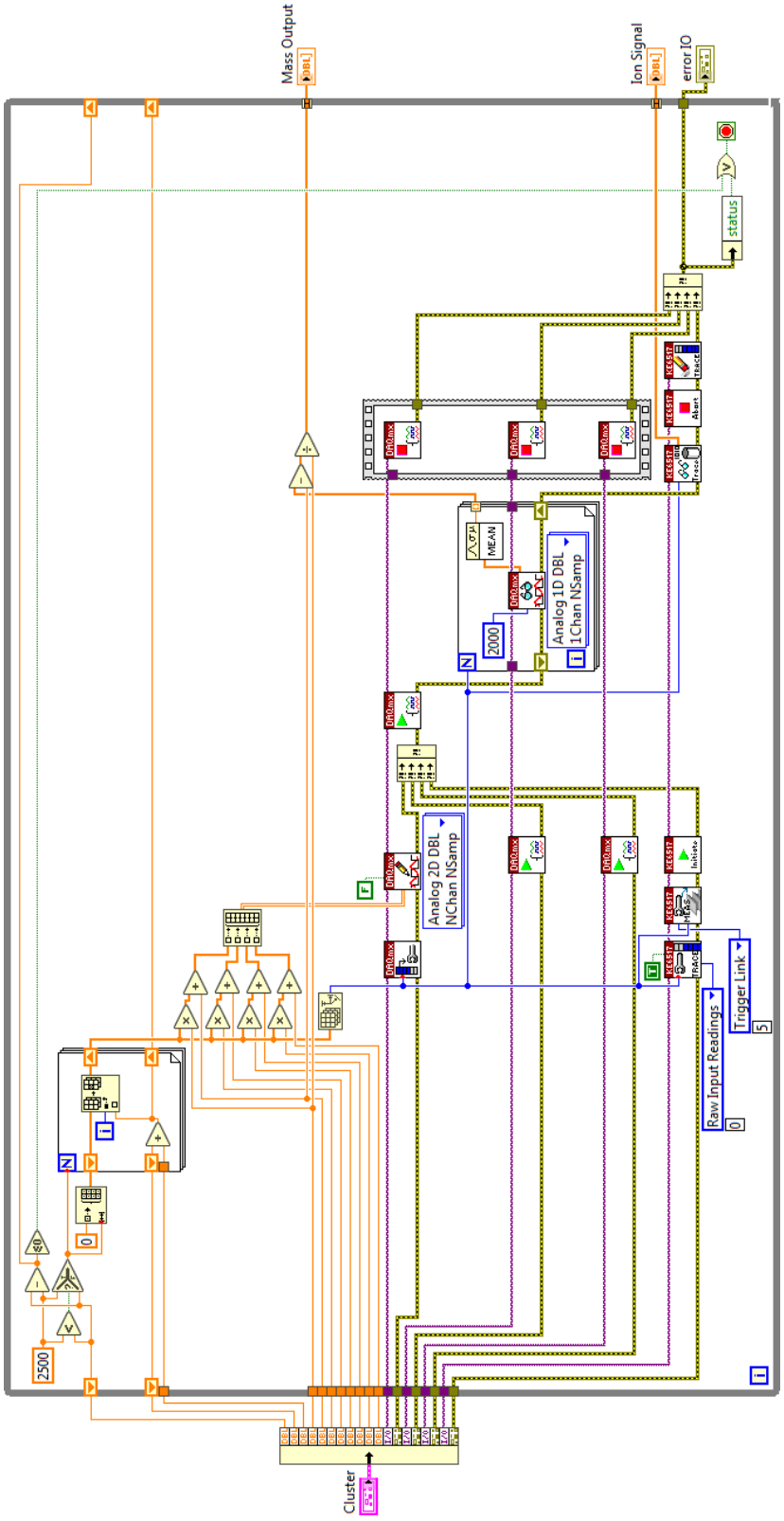

(7) Mass Scan SubVI

B Power Supply Schematics

Low Voltage DC Divider: This supply consists of two fixed output 48VDC power supplies with the + of one grounded to instrument ground, giving an output of -48VDC relative to this ground, and the other supply having its – floated by a 100VDC supply referenced to instrument ground, giving an output of +148VDC relative to instrument ground. The 100VDC supply is external to the box, as it was added later to increase the positive voltage, which was determined experimentally to be required. The 14 outputs are all identical consisting of a polarity switch that connects the high of the potentiometer to either the -48 or the +148VDC with the low of the potentiometer connected to instrument ground allowing the output to be adjusted from 0 to (-48 or +148) VDC. The output is run through a fuse to protect the circuit from accidental arcing in the chambers. Banana jacks at each output and at a ground reference allow for measurement of the outputs via multimeter. Current draw from the optics is minimal as they have a resistance of GΩ to instrument ground. The current draw across the circuit matters as it increases with each additional output, as you are adding a resistor in the form of a potentiometer in parallel. The resistance across the circuit at worst case scenario, when all of the switches are set to the same polarity, is determined by the 14 potentiometers (100kΩ) in parallel giving 7.2 kΩ. Then, 148VDC across this resistance gives a current draw of 21mA at the worst-case scenario. The power supplies must be able to handle this current. This has to be recalculated if a potentiometer is changed or another is added. Due to the low current application of this, no effort was made to correct for a ground loop that generates, in the worst case scenario, 3μV difference in the furthest optic. The ground loop is correctable but makes the supply harder to maintenance. The 48VDC power supplies have a fused 120VAC input for power.

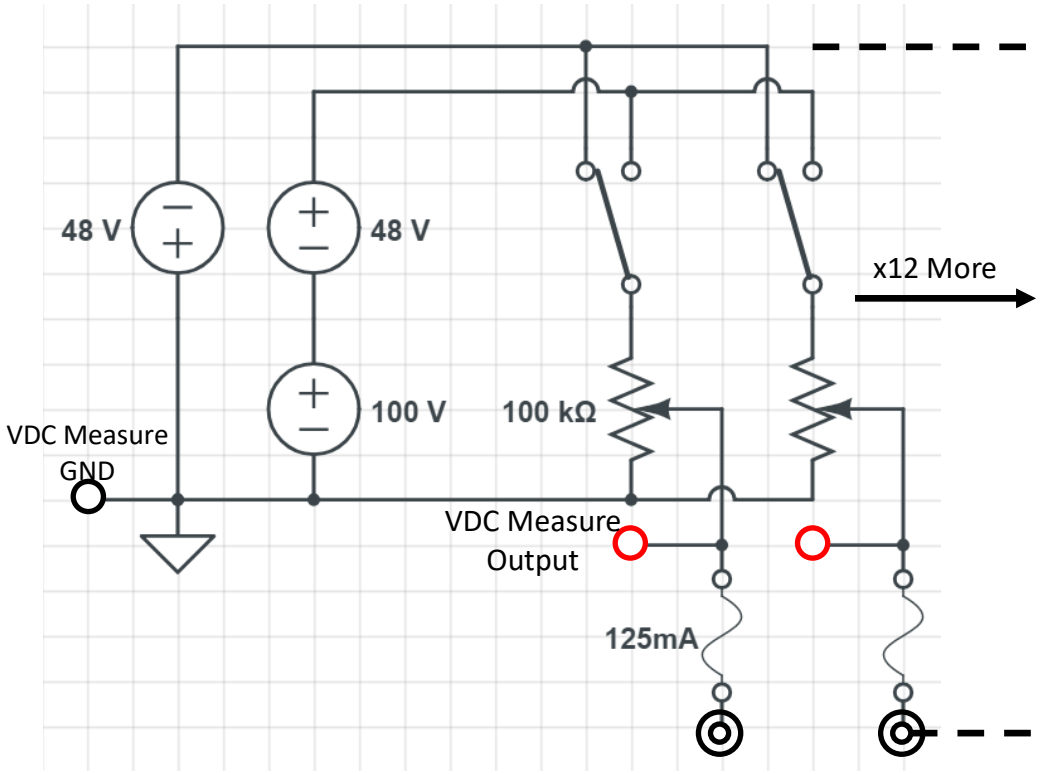

(1) Low Voltage DC Divider

Bender Power Supply: The idea behind this supply is to have a float that raises the entire bender (apertures and rods) together while still being individually adjustable. This allows for the beam path to be thought of as a series of sloping voltages. For example, if the source is -100 VDC and the bender is floated at -50 VDC and the sample is at 0 VDC the axial potential can be viewed as sloping downwards from -100 to -50 before the bend and then -50 to 0 after the bend regardless of the focusing voltages applied to the bender apertures or of the bending voltages applied to the bender rods.

The supply consists of a 100VDC power supply connected to a DPDT switch used to change its polarity. When the switch is up the – pole is grounded and the + pole is applied to the high of a potentiometer. When the switch is down the + pole is grounded and the – pole is applied to the high of the potentiometer. This means the potentiometer gets either ±100VDC referenced to

instrument ground. The potentiometer's low is connected to instrument ground. The output of this potentiometer is the bender's float. This float is applied to the + of a 250VDC power supply making it output -250VDC relative to the float and applied to the – of another 250VDC supply making it output +250VDC relative to the float. Further, the float is applied to the low of the 6 output potentiometers meaning that when they are turned all the way down the voltage applied to the optic is equal to the float. The outputs of the 250VDC supplies are sent to a switch allowing the high side of the potentiometers to be connected to either the + or – 250VDC making these polarity switches for the optics. The outputs of the potentiometers are then sent out to the instrument. In summary, this means the supply is capable of outputting six adjustable ±250VDC relative to a float voltage, with the float adjustable ±100VDC relative to instrument ground.

Currents and fuses were determined as described in the Low Voltage DC Divider description. All three power supplies receive 120VAC for power. A ground loop, creating at worst a 15mV difference in a bender rod output, is present and is ~0.0075% of total running output voltage (normally 200VDC), which has been deemed acceptable. This ground loop is correctable but makes the power supply much harder to maintenance.

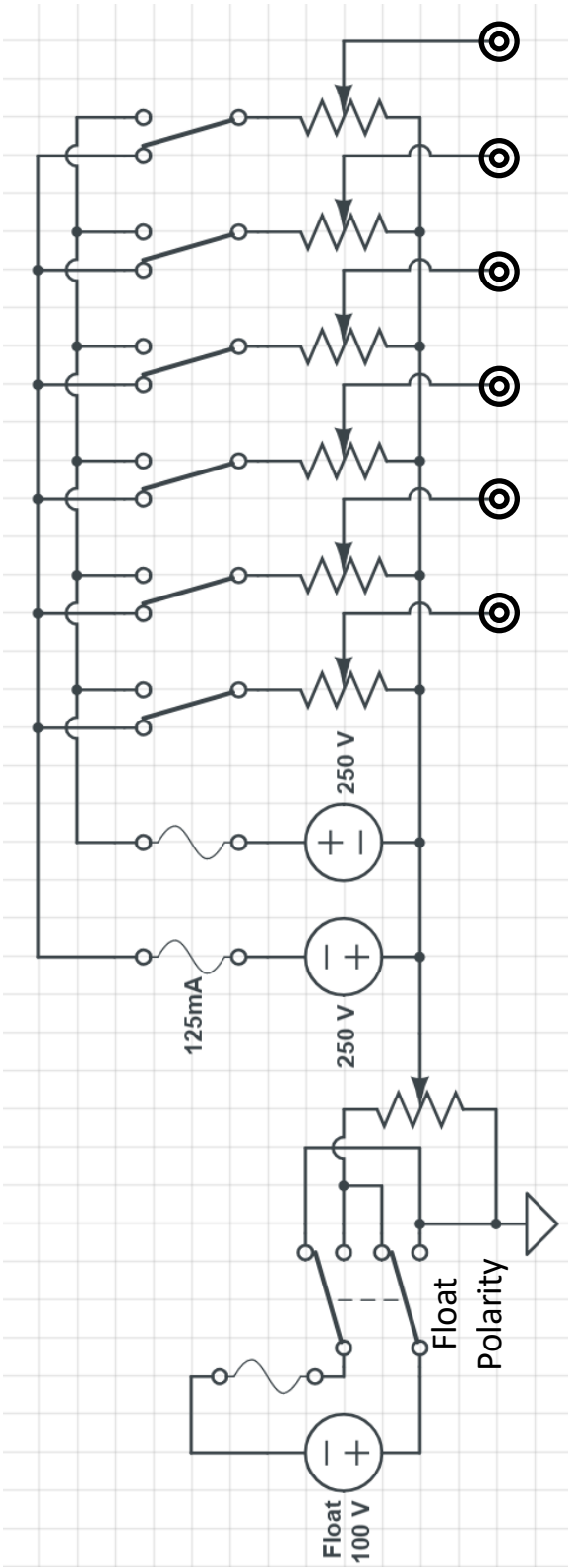

(2) Bender Power Supply

C Interlock Schematics

The interlock system is broken up into four sections: 1) Diffusion Pump Interlock, 2) Turbo Pump Interlock, and 3) Source Turbo Water Alarm; there is a separate interlock box for the magnetron denoted: 4) Magnetron Interlock.

First, a brief introduction to Automation Direct switches. These switches are unique in that a user can stack switches on a single knob or button. When the knob or button is actuated every switch attached to it is actuated as well. If there is a NO and 2 NC stacks on a knob, when switched the NO closes and the 2 NC open at the same time. The NO and NC are color coded green and red, respectively. These knobs and buttons can also be bought with LEDs in them. In the circuit diagrams anything in a box is part of the same switch. The exception to this is the two momentary switches found on the Diffusion Pump Interlock and Turbo Pump Interlock, as I was unable to place them close together in the diagram.

Diffusion Pump Interlock: Below is the diagram for the diffusion pump interlock. This controls the foreline valve for the diffusion pumps, their gate valves, and their on/off state. All of these are controlled with 24VDC. The foreline valve opens upon receiving air (which it always has), and voltage on its pilot valve. The gate valves open and close depending on which side of their pneumatic actuating system air pressure is applied, so the air is controlled by a pneumatic control valve that changes the direction of air flow depending whether or not voltage is applied to the valve. The diffusion pump voltages are run through contactors that are closed when voltage is applied and open when voltage is removed. All of these get voltage if and only if (iff) their switches are actuated. (Switches 1-5) These switches light up upon being turned on iff they are applying voltage to the object they control.

The interlock works by determining if the 24VDC is applied to the high side of the switch. If it isn't applied turning the switch does nothing. The switches get voltage iff the interlock relay is closed. When open, the relay shorts the high side of the switches to the return guaranteeing 0V across the switches. In this state an alarm gets 24VDC across it and it starts to beep. An alarm mute is used to interrupt the alarm, where when switched it lights up red. (Switch 6)

The on state is achieved by pressing the interlock on momentary button. This contains the "Interlock On", "Delay", and "Interrupt", as well as the light that is on when voltage is applied to the high side of the switches. When pressed this applies 24VDC to the relay coil closing the relay; the "delay" is opened to prevent accidental shorting during actuation; and the "interrupt" prevents any of the switches from receiving voltages until the pressure relay is checked (This was added because we found that, if a switch was actuated when the interlock on was pressed, the switch would receive voltage and act accordingly as long as the button was held). Once the button is released, the pressure relay is "checked". When the relay closes it also applies 24VDC to two possible paths: an interlock bypass (Switch 7) or the pressure relay. If either of these are closed, they supply a route for the 24VDC to be applied to the interlock relay's coil, i.e. the relay is powering itself with its output. If at least one of the two paths are not closed when the button is released, the relay opens and removes voltage from the line. The Interlock Bypass (Switch 7) provides an alternate route for the relay to stay on if the pressure condition isn't met.

The Pressure Relay is part of the Edwards Active Gauge Controller and is closed iff the diffusion pump foreline pressure is <500mtorr.

The reason a button is used for turning on the interlock is so that if the whole lab losses power the interlock system will not switch back on upon the return of power. A person MUST push the button, therefore a person must be present to make sure the system is okay to turn back on.

There are three overheat and three water flow meters on the return of the interlock. If any of these are tripped, the interlock shuts off and there is NO WAY to turn it on until the problem is fixed. There is never a time when a user wants to bypass these overheat and water flow safeties. To do so is dangerous.

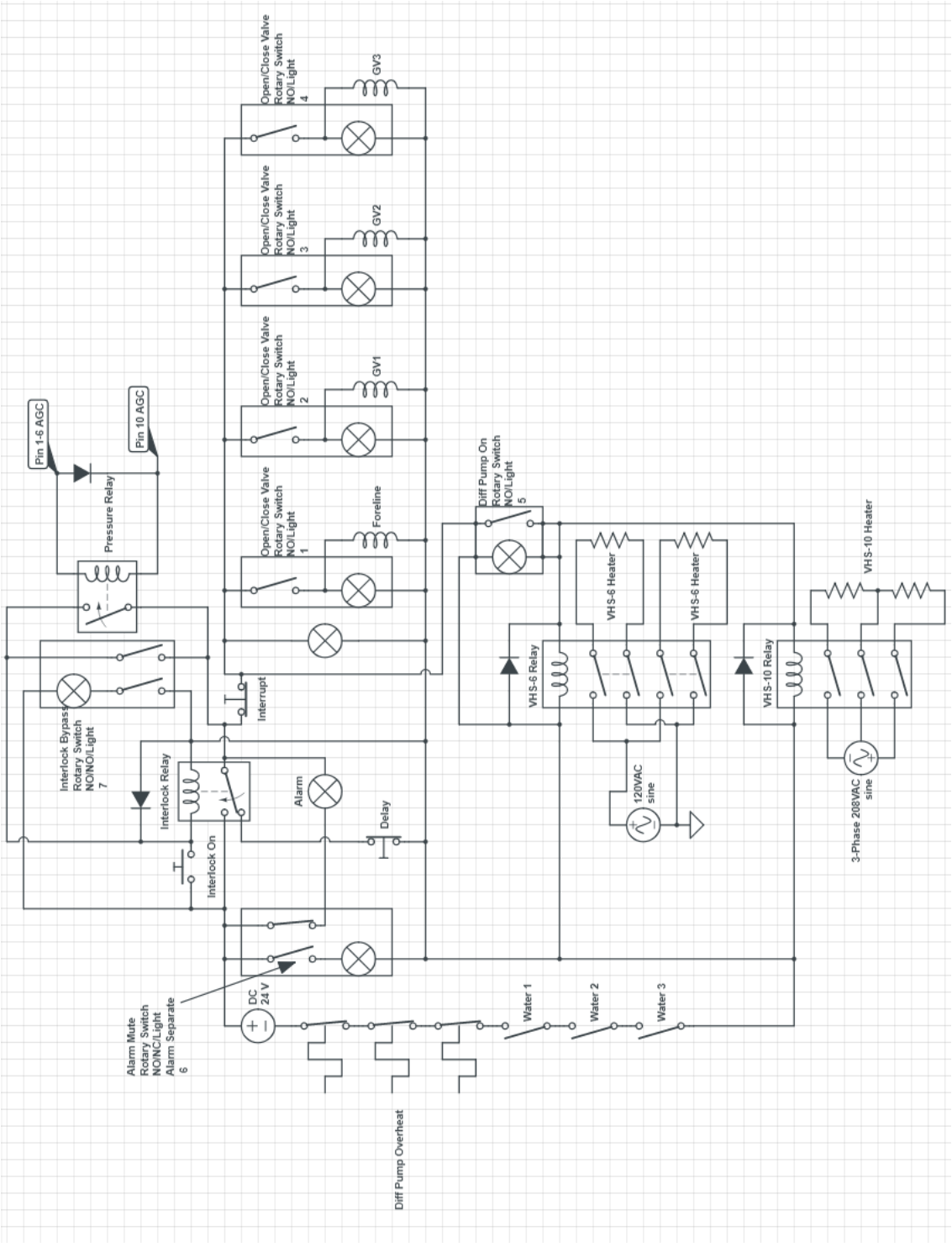

(1) Diffusion Pump Interlock

Turbo Pump Interlock: The turbo pump interlock operates on the same principles as the Diffusion Pump Interlock, only with less conditions and only two foreline valves. It does not have overheat or water flow conditions. The turbos are air cooled and monitor their own temperature. The turbos are designed to handle themselves. No modifications were made to the turbos. The only condition checked for in this interlock is the foreline pressure of the turbos. If it climbs above 200mtorr, the interlock shuts off. This circuit shares a 24VDC power supply with the Diffusion Pump Interlock.

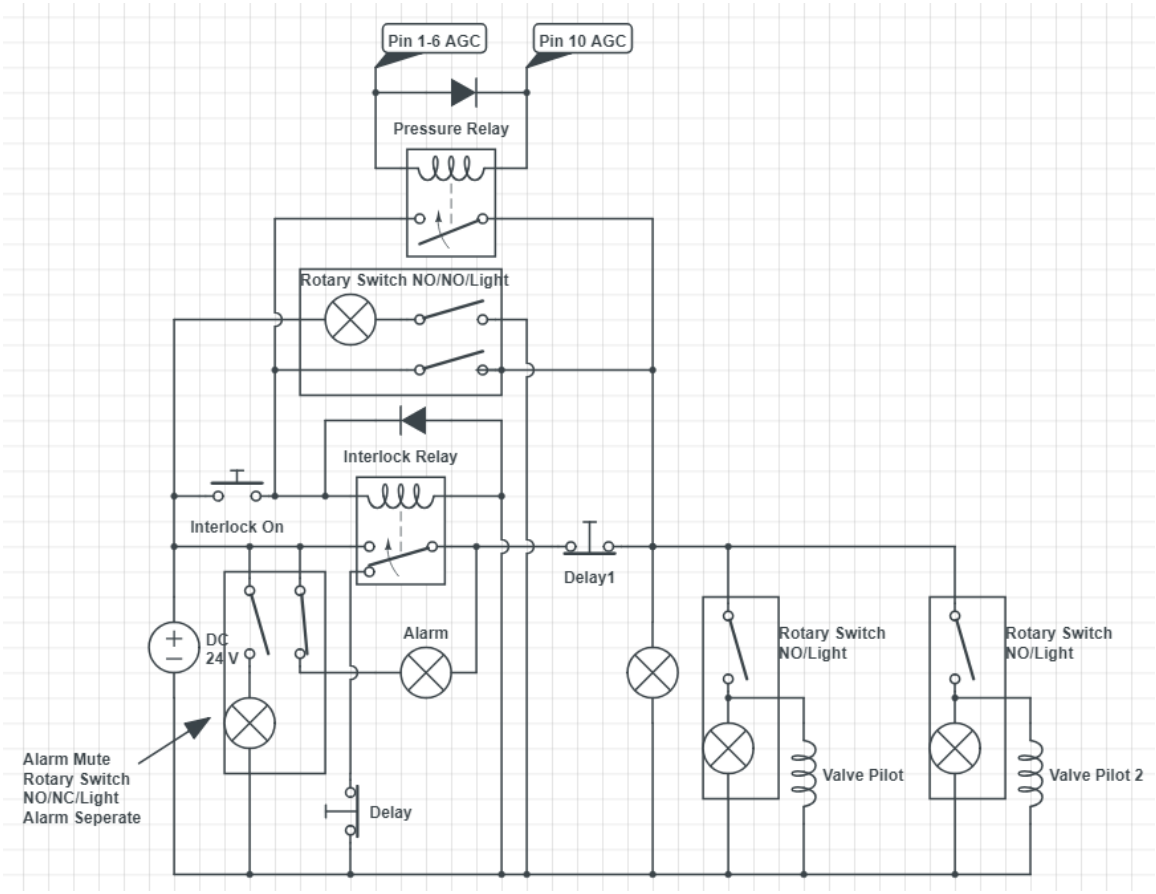

(2) Turbo Pump Interlock

Source Turbo Water Alarm: This is not an interlock. It simply sounds an alarm when the source turbo is not receiving its water cooling. This one is powered with wall 120VAC. It contains an alarm and a switch to mute the alarm.

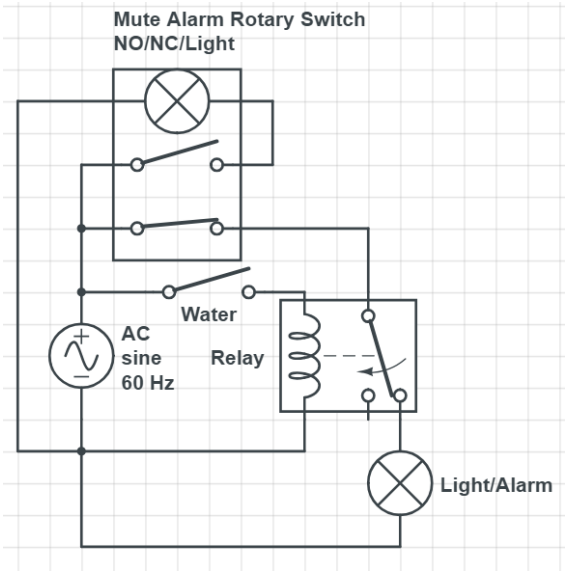

(3) Source Turbo Water Alarm

Magnetron Water Interlock: The magnetron requires water cooling lest the magnet losses its magnetism. This interlock checks that the water is flowing. If flowing the magnetron power supply will receive 120VAC on its IEC input. If not flowing the 120VAC is interrupted by a relay and an alarm sounds. There is also an alarm mute switch (This is not a bypass. There is no bypass because a user will NEVER want to run the magnetron without water.)

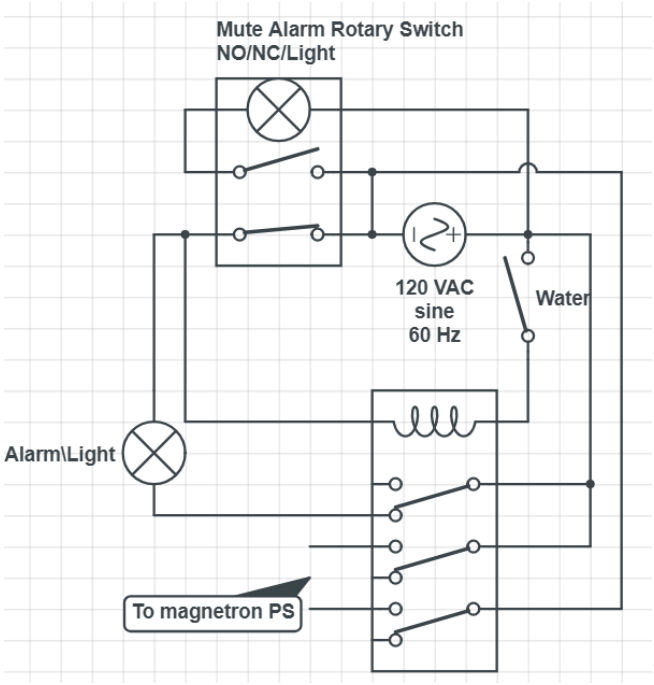

(4) Magnetron Water Interlock

D Electron Multiplier

Currently, the ion signal is measured by grounding an optic along the beamline through a Keithley 6514 electrometer where the ion current is measured. The sensitivity of this electrometer is very good, as it is capable of measuring 10s of aA when everything is running smoothly. More realistically, due to the RF noise brought about by the RF supplies and the resulting voltage burden from this noise, 1fA is a more attainable lower limit. While 1fA is not enough signal to deposit, there are times where current that low needs to be measured in order to tune up signal.

There are times when signal lower than 1fA needs to be measured, such as when the resolution of the QMS is increased to achieve unit mass resolution to determine what clusters are present in the beam. In order to measure these very low ion currents, an electron multiplier needs

to be used. While this multiplier has not been installed yet, the instructions and explanation for doing so are present in this section.

Due to the ion optics having no break between them, the multiplier must be installed in the deposition chamber. The multiplier is mounted on a linear translator where it can be moved into the path of the beam and pulled away from the path of the beam, so that the sample can be moved into place for deposition. The multiplier assembly is mounted on a 2.75”CF 2” linear translator that is in turn mounted on a 4.5”CF to 2.75”CF ZLR. This ZLR is mounted on a 4.5”CF Tee, with the collinear port attached to the deposition chamber through an angled 4.5”CF port with a focal point at the center of the chamber at beamline level. The other port on the 4.5”CF Tee will have four MHV feedthroughs for voltage application and reading output.

The multiplier purchased is a Photonis 4770B channeltron. This is an analog multiplier with a gain of $3*10^7$at -3kV (34μA draw, so a 0.1W minimum PS is needed). The amplified output current will be measured by the 6514. This multiplier also contains a conversion dynode for use with anions.

The multiplier housing contains four feedthroughs. One for the front-plate for drawing ions in, one for the conversion dynode (+1-5kV), one for the channeltron input (-3kV), and one for the collector which is the output to the 6514. The back end of the multiplier channel is held at chassis ground through the base-plate of the housing, meaning this plate must either be mounted on metal connected to chamber ground. On this note, the supplies imparting the voltages must be referenced to chamber ground, which is most easily accomplished through the MHV cable. Cations can be collected with the conversion dynode turned off.

The power supplies used are SRS PS350 (±5kV, 25W). The output reference is from the SHV shield on the output, so a coaxial cable can be used to reference the PS to chamber ground. (See PS350 manual for circuit diagram of output for confirmation of reference)

To repeat, this is not a pulse-counting multiplier that measures voltage pulses across a capacitor. This is an analog output multiplier where if 1fA gets sent into it 30nA is output to the collector (at -3kV on channel) which can then be measured by the electrometer.

A user must be wary not to put too much current into the multiplier as it will damage it! Also, the full gain at -3kV may not be required and can be tuned down to reduce the gain thereby increasing the life of the multiplier.

Zachary A. Hicks

909 W University, Apt 105
Baltimore, MD 21210

(703) 498-9681
zhicks2@jhu.edu

EDUCATION

May 2019	**Doctorate of Philosophy** Physical Chemistry	The Johns Hopkins University
October 2017	**Master of Arts** Physical Chemistry	The Johns Hopkins University
August 2013	**Bachelor of Science** ACS Chemistry **Minor** in Mathematics	James Madison University

EXPERIENCE

Fall 2013 – May 2019 **Graduate Research Assistant, Bowen Laboratory**

Dr. Kit H. Bowen Jr.'s laboratory at The Johns Hopkins University, Baltimore, MD

Focus: Designed and constructed a novel instrument that allows for the study of the reactivity and catalytic properties of clusters. Novel tools were developed in this pursuit, including a new laser vaporization ion source setup utilizing 3D printing in its construction, a 1.375" slide seal capable of sealing atmosphere from UHV, and a thin in-line gate valve that operates as an ion optic.

- Worked with and incorporated many experimental chemistry techniques including; Auger Electron Spectroscopy, X-ray Photoelectron Spectroscopy, UV Photoelectron Spectroscopy, Low-Energy Electron Diffraction, Temperature Programmed Reaction, Pulsed Laser Vaporization, and Magnetron Sputtering.
- Designed and constructed a novel molecular beam instrument capable of studying the chemical and structural properties of a wide range of molecular clusters of varying composition and size tuned at the atomic level.
- Improved upon existing, and designed novel, molecular beam technologies to incorporate into the instrument, including a new Pulsed Laser

Vaporization Ion Source setup and a Thin-Gate Valve incorporating ion optics to minimize loss of ions.
- Worked with vendors to develop and implement required technology for the instrument including modifying commercial equipment to fit my needs.
- Planned the layout of the electrical, exhaust, pneumatics, and water in the lab space where the instrument was constructed.
- Experience with designing vacuum pump systems, vacuum chambers, ion optics, anion/cation ion sources, analog interlocks, analog electronics, and signal processing.
- Performed a range of different troubleshooting efforts during the installation of this instrument including; electrical, mechanical, sub-picoamp signal processing, and serial and digital communication.
- Led and instructed a team of three graduate students in the assembly of and use of the instrument.

Spring 2015 **Teaching Assistant, Advanced General Chemistry**
The Johns Hopkins University, Baltimore, MD
Focus: Taught freshman entering JHU with advanced knowledge of chemistry. This class covered general chemistry topics at a much faster and more detailed pace than the regular class. While teaching this class I encouraged and helped undergraduates find research labs to work in including having two students join the Bowen lab as undergraduate researchers where one stayed his entire undergrad career before going to MIT pursuing a PhD in Physics.

Fall 2014 **Teaching Assistant, Inorganic Laboratory**
The Johns Hopkins University, Baltimore, MD
Focus: Taught a rot-vibration IR experiment where quantum mechanical theories of the anharmonic oscillator and rigid rotor were shown to students experimentally. Also taught an NMR experiment where not only were students taught to interpret NRM data they learned how the NMR functioned and how it is related to the uncertainty relationship between angular momentum components.

Fall 2013 - Spring 2014 **Teaching Assistant, Introductory Chemistry**
The Johns Hopkins University, Baltimore, MD
Focus: Introductory Chemistry is the standard first chemistry lecture and laboratory for most Johns Hopkins freshman, and familiarizes students with the

basic concepts of chemistry and chemical reactions, including acid-base chemistry, thermodynamics, and spectroscopy.

Spring 2011 - Spring 2013 **Undergraduate Research Assistant, Wright Laboratory**
Dr. Nathan Wright's laboratory at James Madison University, Harrisonburg, VA
Focus: Produce the myosin binding protein A via splicing DNA into *E. coli* and forcing expression. After determining best expression conditions the protein could be produced in an isotopically pure media resulting in a protein that's structure could be determined via 3D NMR studies.

PUBLICATIONS

"Mechanistic Studies of [AlCp*]4 Combustion", X. Tang, J. B. DeLisio, S. Alnemrat, **Z. Hicks**, L. Stevens, C. A. Stoltz, J. P. Hooper , B. W. Eichhorn, M. R. Zachariah , K. H. Bowen , and D. H. Mayo, Inorg. Chem. 57, 8181-8188 (2018)

"Adsorption and Decomposition of DMMP on Size Selected (WO3)3 Clusters", X. Tang, **Z. Hicks**, G. Gantefoer, B. W. Eichhorn, and K. H. Bowen, Chemistry Select 3, 3718-3721 (2018)

"Adsorption and Decomposition of Dimethyl Methylphosphonate on Size-Selected (MoO3)3 Clusters", X. Tang, **Z. Hicks**, L. Wang, M. Kukla, R. Tsyshevskiy, G. Gantefoer, and K. Bowen, Phys. Chem. Chem. Phys. 20, 4840-4850, (2018)

"Combined TPD and XPS Study of Ligation and Decomposition of 1,6-Hexanedithiol on Size-Selected Copper Clusters Supported on HOPG", L. Wang, N. Blando, **Z. Hicks**, M. Denchy, X. Tang, H. Bleuel, M. Zhang, G. Gantefoer, and K. Bowen, J. Phys. Chem. C 122, 2173−2183, (2018)

"Borane-Aluminum Surface Interactions: Enhanced Fracturing and Generation of Boron-Aluminum Core-Shell Nanoparticles", J. Yu, J. Boatz, X. Tang, **Z. Hicks**, K. H. Bowen, S. Anderson, J. Phys. Chem. C, 121, 14176-14190 (2017)

"Low-Overpotential Electroreduction of Carbon Monoxide Using Copper Nanowires", D. Raciti, L. Cao, K. J. T. Livi, P. F. Rottmann, X. Tang, C. Li, **Z. Hicks**, K. H. Bowen, K. J. Hemker, T. Mueller, and C. Wang, ACS Catal. 7, 4467-4472 (2017)

"Thermal desorption of dimethyl methylphosphonate from MoO3 ", A. R. Head, X. Tang, **Z. Hicks**, L. Wang, H. Bleuel, S. Holdren, L. Trotochaud, Y. Yu, L. Kyhl, O. Karslioğlu, K. Fears, J. Owrutsky, M. Zachariah, K. H. Bowen, H. Bluhm, Catalysis, Structure and Reactivity, 3, 112-118 (2017)

"Molecular Aluminum Additive for Burn Enhancement of Hydrocarbon Fuels ", P. M. Guerieri, S. DeCarlo, B. W. Eichhorn, T. Connell, R.A. Yetter, X. Tang, **Z. Hicks**, K. H. Bowen, Jr., and M. R. Zachariah, J. Phys. Chem. A, 119, 11084−11093 (2015)